UNIVERSITY OF SOUTHAMPTON

Faculty of Engineering and the Environment

Development of a New Class of Noise Environment Assessment Codes

by

Chuikuan Zeng

Submitted for the degree of
Doctor of Philosophy

August 2016

UNIVERSITY OF SOUTHAMPTON

ABSTRACT

FACULTY OF ENGINEERING AND THE ENVIRONMENT

Doctor of Philosophy

Development of a New Class of Noise Environment Assessment Codes

by **Chuikuan Zeng**

A novel linearised Navier-Stokes equations method including turbulence information is developed to simulate sound propagation especially considering the inhomogeneous medium with non-uniform flows. The emphasis is on the development of methodology and the applications to further the understanding of sound propagation in a turbulent flow. To govern the acoustic-vorticity interaction, which is important in shear flows, perturbation Reynolds stress is used to introduce the turbulent information. A linear hydrodynamic stability analysis demonstrates that the turbulence can stabilize the flow; therefore this method can overcome the instability issue associated with variants of the linearised Euler equations method. Numerical simulations are performed to validate the stability of the proposed method dealing with sound propagation in shear flows. An algebraic turbulence model is used in a benchmark case with a prescribed mean flow profile. Moreover, the turbulent viscosity solved numerically is employed to study turbofan aft noise radiation. The numerical experiments demonstrate the acoustic-vorticity interaction can be resolved by this linear acoustic propagation model to some degree. The resulting effects are evaluated in respect of the near-field and far-field results. Moreover, the attenuation of sound in fully developed turbulent pipe flows is solved and validated against experimental results. Subsequently, the acoustic damping induced by turbulence at high-order duct modes is investigated. Finally, this method is used to investigate the effects of the wall boundary layer on the external noise radiation in respect of two aspects, namely the engine noise impact on the fuselage at cruise conditions and the far-field noise distribution at take-off/landing conditions. These studies demonstrate the stability of the proposed method in the presence of shear layers and density gradients, while show the ability of the method to qualify the attenuation of sound by turbulence.

Contents

List of Figures

List of Tables

Declaration of Authorship

I, Chuikuan Zeng declare that the thesis entitled

Development of a New Class of Noise Environment Assessment Codes

and the work presented in the thesis are both my own, and have been generated by me as the result of my own original research. I confirm that:

- this work was done wholly or mainly while in candidature for a research degree at this University;
- where any part of this thesis has previously been submitted for a degree or any other qualification at this University or any other institution, this has been clearly stated;
- where I have consulted the published work of others, this is always clearly attributed;
- where I have quoted from the work of others, the source is always given. With the exception of such quotations, this thesis is entirely my own work;
- I have acknowledged all main sources of help;
- where the thesis is based on work done by myself jointly with others, I have made clear exactly what was done by others and what I have contributed myself;

Signed: _____

Date: _____

Acknowledgements

I would like to express my deepest gratitude to Professor Xin Zhang and Dr. Xiaoxian Chen, my research supervisors, for their patient guidances and useful critiques of this research work.

For the enjoyable experiences in University of Southampton, I would like to offer my thanks to my colleagues and friends Junjun, Suming and Yu Zhang. In particular, I am grateful for the assistance and friendship given by Xiaowan Liu, Yu Hou and Mark Blackwell. I would also like to especially thank Chenyang Weng for his help in the duct acoustics case, as well as for his encouragement to my research.

I would very much like to thank my parents, Yingmao Tan and Weigao Zeng, for their continued support throughout my time. Last, but certainly not least, I would like to thank my wife, Siting Shang, for her optimism and encouragement.

Nomenclature

Alphanumeric Symbols

$\boldsymbol{A}$	Vector potential	$m^2 \cdot s^{-1}$
A	Ratio of grid convergence index, $A = GCI_{32}/\left(r^o GCI_{21}\right)$	[-]
a	Attenuation coefficient	[-]
a_0	Attenuation coefficient in a quiescent fluid	[-]
c	Speed of sound	$m \cdot s^{-1}$
C_p	Heat capacity at constant pressure	$J \cdot K^{-1}$
C_s	Smagorinsky coefficient	[-]
C_v	Heat capacity at constant volume	$J \cdot K^{-1}$
D	Diameter of duct	m
e	Specific internal energy	$J \cdot kg^{-1}$
e_a	Approximate relative error	[-]
e_{ext}	Extrapolated relative error	[-]
$\boldsymbol{f}$	External force density vector	$N \cdot m^{-3}$
f	Frequency	s^{-1}
h	Specific enthalpy, $h = e + p/\rho$	$J \cdot kg^{-1}$
I	Turbulent intensity	[-]
k	Wave number	m^{-1}
k_a	Axial wave number	m^{-1}
k_r	Radial wave number	m^{-1}
l	Turbulent length scale	m
l_m	Mixing length	m

M	Mach number	[-]
p	Pressure	$N \cdot m^{-2}$
$\boldsymbol{q}$	Heat flux due to heat conduction	$W \cdot m^{-2}$
o	Order of convergence	[-]
R	Convergence ratio	[-]
$\boldsymbol{s}$	Strain-rate tensor	s^{-1}
S	Stokes number	[-]
s	Entropy	$J \cdot K^{-1}$
T	Temperature	K
t	Time variable	s
$\boldsymbol{u}$	Velocity vector, (u_1, u_2, u_3)	$m \cdot s^{-1}$
u_i''	Fluctuating velocity about the density-weighted part	$m \cdot s^{-1}$
u_τ	Wall-friction velocity	$m \cdot s^{-1}$
$\bar{u}_i^\rho$	Mass-averaged velocity	$m \cdot s^{-1}$
$\boldsymbol{x}$	Cartesian coordinate vector, (x_1, x_2, x_3)	m
y^+	Dimensionless wall distance	[-]

Greek Symbols

α	Wave number in $\boldsymbol{x}$ direction	m^{-1}
α_i	Imaginary part of α	m^{-1}
β	Wave number in $\boldsymbol{z}$ direction	m^{-1}
γ	Ratio of specific heats, $C_p/C_v = 1.4$ for air	[-]
δ	Thickness of mixing layer	m
δ_A	Thickness of acoustic boundary layer	m
δ_A^+	Non-dimensional thickness of acoustic boundary layer	[-]
δ_{ij}	Kronecker Delta	[-]
λ	Acoustic wavelength	m
μ	Molecular viscosity	$kg \cdot m^{-1} \cdot s^{-1}$

μ_e	Effective viscosity	$kg \cdot m^{-1} \cdot s^{-1}$
μ_t	Turbulent viscosity	$kg \cdot m^{-1} \cdot s^{-1}$
ν	Kinematic viscosity	$m^2 \cdot s^{-1}$
ν_e	Effective kinematic viscosity	$m^2 \cdot s^{-1}$
ν_t	Kinematic turbulent viscosity	$m^2 \cdot s^{-1}$
ξ	Prandtl number	[-]
ρ	Density	$kg \cdot m^{-3}$
$\mathbf{\Gamma}$	Turbulence stress tensor	$kg \cdot m^{-1} \cdot s^{-2}$
$\boldsymbol{\tau}$	Viscous stress tensor	$kg \cdot m^{-1} \cdot s^{-2}$
τ_w	Wall shear stress	$kg \cdot m^{-1} \cdot s^{-2}$
φ	Scalar potential	$m^2 \cdot s^{-1}$
ω	Angular frequency	$rad \cdot s^{-1}$
$\boldsymbol{\omega}$	Vorticity vector	s^{-1}

Subscripts

$()_i$, $()_j$, $()_{ij}$	Variable components in Einstein notation

Superscripts

$\acute{()}$	Turbulent quantity
$\bar{()}$	Time-averaged quantity
$\hat{()}$	Amplitude of variables in normal model
$\tilde{()}$	Organised perturbation quantity
$()'$	Perturbation quantity
$()^*$	Non-dimensional quantity

Symbols

Δ_x, Δ_y	Grid spatial dimensions
Δs	Nearest wall distance of grid
$\langle\rangle$	Phase average
$\overline{()}$	Time average

Abbreviations

ABL	Acoustic Boundary Layer
APE	Acoustic Perturbation Equations
B.C.	Boundary Condition
B.L.	Boundary Layer
CAA	Computational Aeroacoustics
CFD	Computational Fluid Dynamics
CFL	Courant-Friedrichs-Lewy
DES	Detached Eddy Simulation
DNC	Direct Noise Computation
DNS	Direct Numerical Simulation
ESM	Equivalent Source Method
FFT	Fast Fourier Transform
FW-H	Ffowcs Williams-Hawking
GCI	Grid Convergence Index
GTF	Gradient Term Filtering
GTS	Gradient Term Suppression
LDE	Linearised Divergence Equations
LEE	Linearised Euler Equations
LES	Large Eddy Simulation
LNS	Linearised Navier-Stokes Equations
PPW	Points Per Wavelength
PRS	Perturbation Reynolds Stress
RANS	Reynolds Averaged Navier-Stokes
RMS	Root Mean Square
SGS	Subgrid-Scale
SPL	Sound Pressure Level
SST	Shear-Stress Transport

Chapter 1

Introduction

1.1 Background

The field of aeroacoustics has become increasingly important due to the demand for noise reduction in contemporary human life. In the design of commercial aircraft [1], road vehicles [2] and building ventilation systems, the noise criterion has played an important role. In terms of the computational methodology towards noise predictions, conventionally analytical solutions and semi-empirical methods show good performance with an instant assessment. Their shortcomings, however, restrict their applications to simple configurations at standard operating conditions. Meanwhile, fully numerical methods can simulate the hydrodynamic and acoustic fields simultaneously with regard to arbitrary geometries and complicated flows, however, currently at a hardly affordable cost for industrial applications [1]. In the field of the external noise radiation study, such as the airframe noise and the sound emission from the engine duct, the hybrid method as a combination of the acoustic analogy and the numerical solution is advocated [1], where the sound generation and propagation in the near field are simulated by numerical methods, then the resulting sound radiation to the far-field is calculated by an acoustic analogy. Nevertheless, the acoustic analogy method presents issues when quadrupole sources are important, as well as when the propagation effects are considerable. To further reduce the computational cost, the linearised perturbation equations method is proposed to simulate the sound propagation in the near field, while the corresponding hydrodynamic field is solved by conventional computational fluid dynamics (CFD) methods. The proper extraction of source information from the hydrodynamic field to the propagation simulation is a difficult problem associated with this method. Nevertheless, when the incident acoustic source can be simply specified, such as in the problems of scattering of propulsion system noise and in duct acoustics, this method has an especial advantage.

Linear acoustic propagation models are generally based on the linearised Euler equations (LEE). Due to the inviscid assumption, these models face a serious challenge to properly govern the evolution of fluid instability. In particular, the Kelvin-Helmholtz instability arises in shear layers and may grows unlimitedly, as a result the simulations of

sound propagation can be corrupted in many cases. Current methods to solve this issue are reviewed in Section 1.2, and the instability issue itself is discussed in Section 1.3. Furthermore, from another point of view, the instability waves is actually triggered and influence the sound propagation in real life, although the effect is usually ignored in external acoustic propagation problems. However, in cases that acoustic-vorticity coupling is significant, the effect induced by instability waves becomes valuable to be resolved. The topic about the associated effect imposed on sound waves is reviewed in Section 1.4. Given these points, this thesis aims to develop a generalised and robust method to solve sound propagation problems, especially considering the shear layers and turbulent flows. The proposed method needs to simulate the acoustic scattering and propagation, and is required to solve the hydrodynamic interaction. Through a comprehensive review of acoustic propagation problems, the current issues and solutions are concluded in Section 1.5. Based on the complete understanding of the related physical mechanism, the potential methodologies are given and the linearised Navier-Stokes (LNS) equations including turbulence information is developed.

1.2 Modelling of Aeroacoustics

Efforts to model aerodynamic sound can be traced to the early 1950s, starting with the pioneering work of Lighthill [3]. Subsequently computational aeroacoustics (CAA) as a separate discipline acquired its identity in the early 1990s. Nowadays the simulation of sound generation and sound propagation have been usually tackled as separate topics due to their conceptual differences, and the so-called hybrid method has been generally adopted for the sake of practicality.

With regard to the aircraft noise community, researchers traditionally focused on high Mach number and high Reynolds number free-field jet flows, and unbounded flows with impacts on, such as high-lift devices and landing gears. Noise is produced in such flows by the unsteady and nonlinear interaction between hydrodynamic and acoustic quantities. The methodologies developed for sound generation, therefore, deal with flow and sound simultaneously. Direct numerical simulation (DNS) includes no turbulence models and can obtain thorough aerodynamic and acoustic information, but its application has been limited by the high computational cost. By introducing turbulence models, such as using the unsteady Reynolds averaged Navier-Stokes (RANS) approach, detached eddy simulation (DES) and large eddy simulation (LES), the computational cost becomes more affordable in practice. However these methods filter out small spatial and high frequency fluctuations to different degrees, thereby potentially leading to an inconvenient distortion of the acoustic waves [4]. Numerical simulation of sound generation is still a developing field.

A lesser-explored subject is on the sound wave propagates in an inhomogeneous medium based on arbitrary mean flows. This topic is prominently different from sound generation as herein the aerodynamic field can be considered independent of the acoustic field in general. The governing equations can therefore be linearised if the perturbations

relative to the mean flow are small enough in magnitude. The mean flow can be solved by traditional CFD methods without acoustic consideration, then the acoustic waves can be simulated by the perturbation equations. However, this two-step kind of approach has difficulties in simulating a shear mean flow wherein the instability waves could grow temporally. Some approaches have been proposed to address this issue. The acoustic perturbation equations (APE) method [5] employs a wave operator to exclude the vortical component from the solution. The linearised divergence equations (LDE) method [6] was developed to eliminate the solenoidal component of the momentum equations. Also, the gradient term filtering (GTF) method [7] attempts to address the instability issue by excluding the solenoidal component of the perturbed velocity. Alternatively, rather than these time-domain approaches, frequency-domain methods [8–11] can be employed to eliminate the unstable time-asymptotic components. In addition to this issue, efforts have been paid to resolving the viscous and turbulent effects on sound propagation, such as the frequency-domain wave equation solver incorporating a non-equilibrium turbulence model [12] is used to resolve the acoustic damping, also for example the LNS method including only the molecular viscosity is used to study the acoustic property in duct systems.

This section reviews the modelling of aeroacoustics and attempts to give a comprehensive understanding of these models and their connections.

1.2.1 Direct Noise Computation

The complete compressible Navier-Stokes equations can simultaneously solve unsteady flows and the resulting acoustic fields, as well as their interactions. With improved requirements for the numerical accuracy, in principle the numerical techniques used in conventional CFD can also be employed to solve aeroacoustic problems. This is referred as the direct noise computation (DNC). This approach generally simulates the source region and, at least partially, the near field of sound propagation. This method must concurrently deal with a wide range of scales/frequency in physical quantities; consequently the numerical schemes are subject to rigorous challenges and incur high costs. Usually DNC has been reserved for fundamental research purposes to tackle relatively simple cases with low Reynolds numbers, but it has gradually progressed owing to the improvements of computational methods and hardware. As summarised by Colonius [13], the method has been applied from idealized cases [14, 15] towards the nearly complete flow regions [16–21]. Although the Reynolds number is still modest and far away from engineering practices, the physical mechanisms that generate sound in more complex cases could be studied, thereby guiding the theoretical and numerical modelling.

The main methods of the DNC approach are DNS, LES and DES. DNS attempts to simulate the dynamics of all physical scales, and resolves the energy-containing range and the dissipative range of scales together. In LES, by contrast, the objective is to only capture a range of energy-containing eddies, and dissipative eddies are disposed in a

sub-grid model. DNC is usually conducted in a part of near field, and the acoustic field farther away can be obtained by simpler models with DNS data, commonly the acoustic analogy as well as the linearised Euler equations (LEE). There are two critical issues in relation to model transformation. Firstly, the accuracy and stability of information transfer is necessarily guaranteed at the domain (grid) interface. For instance, Freund [22] matched a convecting wave equation and the isentropic linearised Euler equations to the Navier-Stokes solver beyond the source region, and validated that interpolation at the interface could result in a significant numerical dispersion. Secondly, as the mesh suited for an extended domain (far-field) is usually different, the quality of interpolation schemes should be carefully considered.

1.2.2 Acoustic Analogy with Near-field Data

Generally, an acoustic analogy can reliably compute the sound radiation to the far-field with the near-field data. In an equation of acoustic analogy, the right-hand side represents equivalent sound sources (near-field results); the left-hand side holds a partial differential operator that describes sound propagation.

This concept was originally proposed by Lighthill [3] via rearranging the conservation equations of mass and momentum into the form of a linear wave equation for an idealized hypothetical medium at rest with quadrupole source terms, as follows:

$$\frac{\partial^2 \rho'}{\partial t^2} - \bar{c}^2 \nabla^2 \rho' = \frac{\partial^2 T_{ij}}{\partial x_i \partial x_j}, \tag{1.1}$$

where $T_{ij} = \rho u_i u_j + \left(p' - \bar{c}^2 \rho'\right) \delta_{ij} - \tau_{ij}$ is the Lighthill stress tensor. A simple Green's function can offer a solution to the sound propagation in the free space, and the double divergence of Lighthill's stress tensor T_{ij} represents the exact source terms. The equation demonstrates an exact analogy between the density fluctuations in any real flow and those resulting from the distribution of a quadrupole source in an ideal stationary flow. Simplifying the source terms as $T_{ij} = \rho u_i u_j$, can be justified when studying a low Mach number flow which ignores the viscous stresses τ_{ij}. The meaning of this simplification is that with the instantaneous density being replaced by ambient density the remaining flow variables can be resolved by conventional CFD methods.

Lighthill's analogy presents some drawbacks or shortages. The equivalent source terms of Equation 1.1 (namely the right-hand side terms) contain the sound generation as well as the propagation effects induced by mean flow, namely, it is not the true sound source but rather represents refraction and scattering as well. Various efforts have been made to develop alternative wave equations that include the interactions between the mean flow and the sound wave directly into the wave operator, thus the terms remaining on the right of the equation represent the more real acoustic sources. Early in 1960, Phillips [23] derived a convective wave equation to describe the generation and propagation of the pressure fluctuations in the turbulent shear layers with high Mach numbers. Powell [24] introduced the theory of vortex sound that proposes aerodynamic sound

as the result of vorticity movement, and formulated a new class of sound source as a modified version of the Lighthill stress tensor (extracting a dipole-like term involving the vorticity). Doak recognized the convenience of Lighthill's analogy might conceal the basic mechanisms of acoustic-aerodynamic interactions [25], and derived an inhomogeneous convective wave equation in which the inhomogeneity representing the source of acoustic disturbances would only rely on the vortical and thermal quantities [26]. More well-known, Lilley [27] and Goldstein [28] developed a shear flow analogy, in which an inviscid parallel shear flow replaces Lighthill's idealized medium at rest. From the practical point of view, the nonlinear propagation operator (D'Alembertian operator) on the left-hand side of the equation is replaced by the Pridmore-Brown operator [29] that represents the effects of sound propagation in a transversely sheared mean flow; the right of the equation can be approximated by the form given by Goldstein [30]. Furthermore, Goldstein sought to refine the form of the source-term by introducing new dependent variables and specific source terms [31].

In respect of another main shortage of Lighthill's analogy, namely the limitations on problems where solid surface effects can be neglected in sound generating, Curle [32] made the first significant extension which can take the effect of stationary solid surfaces into account, and showed that the solid boundaries induce dipole sound sources which are of greater efficiency than Lighthill's volume quadrupole at sufficiently low Mach numbers. Further extension developed by Ffowcs Williams and Hawkings [33] generalized the form of Lighthill's theory to include a moving surface immersed in the flow. The Ffowcs Williams-Hawkings (FW-H) equation enables treatment of an arbitrary rigid body, as well as the permeable surface that allows the flow to enter and/or leave the computational domain [34, 35]. An overview of the FW-H equation used in rotor noise studies was given by Brentner and Farrassat [36]. Gloerfelt [37] performed a far-field prediction with the FW-H equation coupled to DNS for studying two-dimensional cavity flow. Also, there is a similar approach derived from the viewpoint of electromagnetic wave theory, namely the Kirchhoff method. Both of the two approaches appear to be generalized and efficient, however, the FW-H method is proposed to be superior to the Kirchhoff method [38, 39]. The accuracy of the Kirchhoff methods degrades when the integral surface lies within the non-uniform flow region [36], with a reasonable justification given by Singer et al. [35].

In summary, the acoustic analogy can be reliable and efficient to predict sound far-field radiation when the near-field data is known in sufficient detail. The use of this method is generally coupled with a near-field solver, for example LES [40], DNS [41], and LEE [42].

1.2.3 Vortex Methods Coupled with Acoustic Solver

Vortex methods can be employed to compute unsteady flows [43, 44] as an alternative methodology access to sound sources data. The two techniques used in vortex methods

are the Navier-Stokes (or Euler) equations in vorticity-velocity form, and the Lagrangian discretization of the vorticity.

According to Helmholtz's theorem, the vorticity $\boldsymbol{\omega}$ can be defined as in Equation 1.2. Taking the curl of the momentum equation of Navier-Stokes equations yields the Helmholtz vorticity equation, as Equation 1.3.

$$\boldsymbol{\omega} = \nabla \times \boldsymbol{u}, \tag{1.2}$$

$$\frac{\partial \boldsymbol{\omega}}{\partial t} + \boldsymbol{u} \cdot \nabla \boldsymbol{\omega} = \boldsymbol{\omega} \cdot \nabla \boldsymbol{u} + \frac{1}{\rho^2} \nabla \rho \times \nabla p + \nabla \times \boldsymbol{F} + \nu \nabla^2 \boldsymbol{\omega}, \tag{1.3}$$

where $\boldsymbol{F}$ represents a conservation force. With respect to the essentially incompressible, constant-temperature, single-phase turbulent flows, Equation 1.3 can be simplified by dismissing the terms of pressure p and $\boldsymbol{F}$. Therefore the new governing equations in terms of vorticity form only depend on the vorticity and velocity. Subsequently the numerical schemes used to solve the Navier-Stokes equations are greatly simplified. Moreover, in many cases of interest, since the flows are essentially inviscid, the fluid containing significant vorticity accounts for only a small fraction of the total flow volume. Therefore the computing cost can be dramatically reduced. A comparison [45] illustrated that vortex methods can be faster by up to an order of magnitude, even when the volume is fully filled with vorticity. This means that a practical tool can be established to evaluate the impact of geometrical variables on the flow and its sound. The far-field acoustic field can be computed by incorporating a sound radiation solver to the vortex method [46].

Guo [47, 48] developed a vortex-method based model to simulate the noise generated by flow separation in the flap side edge regions of aircraft high-lift systems. A two-dimensional version of the FW-H formulation was coupled with this model [49]. The revised Brown & Michael equation [50, 51] was used to determine the strengths of the shed vortices, and a conformal mapping has been exploited for potential flows around the airfoil. Howe [52, 53] also demonstrated the use of a similar model to evaluate a two-dimensional vortex flow over an airfoil with a rounded trailing edge. These two-dimensional methods can significantly reduce computational expense by orders of magnitude both in the near-field and the far-field calculations [49], thus are available to provide an instant assessment of design variables on the acoustic features. Guo demonstrated quite encouraging comparisons with experimental data [49]. To deal with two-dimensional cases there are three classes of vortex methods in general, namely the vortex particle method, the vortex filament method, as well as the method combining vortex particles and a Poisson solver for the calculation of particle velocities. Vortex methods suffer more rigorous challenges in dealing with two-dimensional problems. Primarily, most unsteady two-dimensional vortical flows have instability and inevitably become turbulent or transitional, and in principle are rarely suitable to vortex methods. Moreover, vortex methods were proposed just for researching qualitative features of simple flow and its sound (this application is encouraging [54]), rather than more complex flow

or quantitative purposes, both of which would lead to demanding computation [54, 55]. From another aspect, Eldredge et al. [56] have extended vortex methods to fully compressible equations of motion. A vortex particle method for unsteady two-dimensional flow was developed for the purposes of, for instance, sound generation by co-rotating vortices.

1.2.4 Parabolized Stability Equations Coupled with Wave Equations

Parabolized stability equations (PSE) formulation can be derived from Euler equations or the complete viscous Navier-Stokes equations in the linear or nonlinear form, and was first introduced by Herbert and Bertolotti [57, 58]. PSE formulation has been proposed due to its parabolicity that enables the marching procedure to solve the problems of jet noise [59].

PSE methods are employed to compute streamwise evolution of instability waves, which are considered as the main sound source of jet noise. A wave equation is subsequently coupled with PSE to compute the sound radiation outside the jet. PSE methods may not be suitable for cases with spatially damped disturbance [59], as the corresponding difference equation needs to be extended to the complex plane thereby resulting in some technical difficulties. Also, although the PSE method has shown its efficiency to predict the spatial development of jet large-scale instabilities in both subsonic and supersonic case, the accuracy of acoustic predict is remarkably decreased in respect of subsonic cases for which the majority of the acoustic radiation is induced by small-scale structures associated to the turbulence that is not captured by the PSE method in subsonic mixing layers [59, 60]. This method can therefore be an efficient means for the study of supersonic jet noise [59].

1.2.5 Viscous/acoustic Splitting Method

Given the different requirements for numerical algorithms between simulating viscous effects (small space and time steps) and acoustic fields (large domains and long-time solutions) [61], Hardin and Pope [62] attempted to optimise the solution to acoustic processes (i.e. generation, propagation and radiation) by introducing a viscous/acoustic (also called hydrodynamic/acoustic) splitting technique.

The compressible Navier-Stokes equations are detached to govern the incompressible viscous flow and the compressible inviscid acoustic perturbations via the decompositions of flow variables as follows.

$$u_i = U_i + u_i', \tag{1.4}$$

$$p = P + p', \tag{1.5}$$

$$\rho = \bar{\rho} + \rho_1 + \rho', \tag{1.6}$$

where U_i and P are the velocity and pressure of the nearly incompressible flow, $\bar{\rho} + \rho_1$ is the corrected incompressible density, and ρ_1 is the hydrodynamic density fluctuations to be computed via the unsteady pressure of incompressible flow. The acoustic field is described by a set of first-order nonlinear equations by subtracting the terms of incompressible flow from continuity and momentum equations. After solving the incompressible part, the sound generation and propagation are computed by solving the perturbation equations based on an acoustic mesh. Furthermore, Shen and Srensen [63, 64] suggested a modified formulation to overcome the inconsistencies in the original equations and extended this method to allow for entropy variations in the base flow.

This method compared well with an asymptotic solution on classical problems [62], and was applied to a low Mach number cavity flow [65]. Still, there are some serious issues. Foremost, this method ignores the aerodynamic reactions on acoustic behaviour, therefore it is not applicable to cases in the presence of significant hydrodynamic-acoustic coupling. This coupling generally exists in the process of aerodynamic sound generation. Moreover, in some simple cases the splitting method can be a computational equivalent of Ribner's theory of aerodynamic sound generation [66]. Ribner's theory regards the dilatation of fluid elements as the primary factor of sound generation. Ribner's theory aroused serious arguments on certain cases [67, 68] in the past. The critical difficulty emerges in the special requirement of the computational domain, which must contain a region with a typical dimension larger than that of the flow region by about a characteristic wavelength of the radiated sound [69].

1.2.6 Euler Equations

In comparison with Navier-Stokes equations the Euler equations possess remarkable superiority on computing cost, and are superior to linearised governing equations due to the presence of the nonlinear effect.

There has been some applications of Euler equations to computing sound generation when the viscosity plays a negligible role, e.g. the gust-cascade/airfoil interaction problem. Lockard [70] studied the interaction of a vortical gust with a finite thickness airfoil, and demonstrated the influence of viscous effects via implementing Euler and Navier-Stokes equations respectively. In addition, the Kirchhoff method was employed to obtain the far-field sound. Nallasamy et al. [71] focused on the study of the linear/nonlinear acoustic response of the gust-cascade problem using this method.

1.2.7 Linearised Euler Equations with Source

The use of linearised governing equations is justified when the hydrodynamic/acoustic systems can be considered linear, namely the hydrodynamic field is assumed to be independent of the acoustic excitation. Linearised perturbation equations can represent all basic dynamics of perturbations, i.e. the acoustic wave, vorticity wave and entropy wave, but the computational cost is significantly reduced. Generally the flow variables

are decomposed as the time-mean part and the perturbed part, following the form of Equation 1.7.

$$F(\boldsymbol{x},t) = \bar{F}(\boldsymbol{x}) + F'(\boldsymbol{x},t). \tag{1.7}$$

The mean flow is obtained by a steady viscous aerodynamic simulation and is then subtracted from the original nonlinear governing equations. The resulting linearised equations govern the small-amplitude perturbations. Starting from the Euler equations, the linearised Euler equations can be deduced. By introducing the isentropic assumption ($\partial\bar{s}/\partial t = 0$) the first-order equations for the perturbations can take the form as follows

$$\frac{\partial \rho'}{\partial t} + \nabla \cdot \left(\bar{\boldsymbol{u}}\rho' + \bar{\rho}\boldsymbol{u}'\right) = 0, \tag{1.8a}$$

$$\bar{\rho}\left(\frac{\partial}{\partial t} + \bar{\boldsymbol{u}} \cdot \nabla\right)\boldsymbol{u}' + \bar{\rho}\left(\boldsymbol{u}' \cdot \nabla\right)\bar{\boldsymbol{u}} + \rho'\left(\bar{\boldsymbol{u}} \cdot \nabla\right)\bar{\boldsymbol{u}} + \nabla p' = 0, \tag{1.8b}$$

$$\left(\frac{\partial}{\partial t} + \bar{\boldsymbol{u}} \cdot \nabla\right)s' + \boldsymbol{u}' \cdot \nabla\bar{s} = 0, \tag{1.8c}$$

while

$$s' = \frac{C_v}{\bar{p}}\left(p' - \bar{c}^2\rho'\right). \tag{1.9}$$

Considering a perfect gas, as $\bar{c}^2 = \gamma\bar{p}/\bar{\rho}$ and $\gamma = C_p/C_v$, Equation 1.8c and Equation 1.9 can be merged as

$$\left(\frac{\partial}{\partial t} + \bar{\boldsymbol{u}} \cdot \nabla\right)p' + \boldsymbol{u}' \cdot \nabla\bar{p} + \gamma p'\nabla \cdot \bar{\boldsymbol{u}} + \gamma\bar{p}\nabla \cdot \boldsymbol{u}' = 0. \tag{1.10}$$

If further assuming that the mean flow is homentropic ($\nabla\bar{s} = 0$) and absolutely isentropic ($s' \equiv 0$), the pressure and density perturbations are related by

$$p' = \bar{c}^2\rho'. \tag{1.11}$$

Eventually, when holding the irrotational base-flow hypothesis, the linearised equations can be reduced to the form of a wave equation.

LEE describes both sound generation and sound propagation. The majority of applications of LEE in aeroacoustics is in the simulation of sound propagation in flows wherein the viscothermal effect can be safely ignored. By incorporating various source schemes, LEE directly resolves the acoustic refraction and scattering effects. LEE can also be used to investigate sound generation with a vorticity wave as the source.

Although LEE solves a higher level of physical realism than wave equations, its solution might fail in the presence of shear layers. The spatially growing instability wave may be triggered by a range of periodical excitation [72] and develops unlimitedly, consequently overwhelming the actual acoustic field. In fact, the same fundamental

problem occurred in the use of Lilley's acoustic analogy [30, 73–75], which attempted to account for the propagation effects in the wave operator.

A solution is to filter out the growing instability waves, namely implementing LEE in the frequency domain via a direct solver. It is worth mentioning that APE method completely excludes the vortical part of the variables, which will be discussed later. The frequency-domain LEE method transfers the governing equations by a Fourier transform, and this actually implies the assumptions of a time-harmonic source and response, therefore the unstable time-asymptotic response is eliminated. The resulting equations become time-independent as well as single-frequency. The frequency-domain methodology has been exploited by Ehlers [76] and Verdon [77] in the subject of unsteady aerodynamic analysis. Subsequently this method was applied to computing aeroacoustic responses of axial-flow turbo-machinery blading by Montgomery and Verdon [78]. Later, Verdon [79] and Envia [80] used this method to study the rotor-stator interaction tone noise. Agarwal and Morris [8], as well as Özyörük et al. [9–11] performed the frequency-domain method on generic problems of sound propagation with an impressive computational efficiency.

Alternatively, the time-domain LEE can be modified to overcome the instability issue. The LDE method developed by Zhang and Chen [6] attempts to eliminate the solenoidal component of momentum equations. The terms removed by this class of method in fact affect the far-field sound pressure level and sound directivity [81] by an unjustified way. The method developed by Bailly and Juvé [82] introduces nonphysical nonlinear terms into LEE to dampen the instability waves. Another approach generally used is the so-called gradient term suppression (GTS) method by which the terms containing derivatives of the mean velocity are removed from momentum equations to some degrees, this was demonstrated by Bogey et al. [83] and Zhang et al. [42]. Bogey et al. [83] suggested the mean shear $\partial\bar{u}_1/\partial x_2$ leads to the growing instability waves, and all the terms containing the derivatives of the mean velocity are dropped from the momentum equations. The momentum equations in the two-dimensional conservative form for the GTS method adopted by Bogey et al. [83] can be reformulated as Equation 1.12, and the deducing processes are given in Appendix A.

$$\bar{\rho}\frac{\partial u_1'}{\partial t} + \bar{\rho}\bar{u}_1\frac{\partial u_1'}{\partial x_1} + \bar{\rho}\bar{u}_2\frac{\partial u_1'}{\partial x_2} + \frac{\partial p'}{\partial x_1} = 0, \tag{1.12a}$$

$$\bar{\rho}\frac{\partial u_2'}{\partial t} + \bar{\rho}\bar{u}_1\frac{\partial u_2'}{\partial x_1} + \bar{\rho}\bar{u}_2\frac{\partial u_2'}{\partial x_2} + \frac{\partial p'}{\partial x_2} = 0, \tag{1.12b}$$

Nevertheless, due to the main factor of the instability issues is related to the mean flow gradient, some researches [84, 85] use the GTS method which only discards the gradient terms, therefore the original momentum equations for the LEE method are modified to

a relative small degree, as shown in Equation 1.13.

$$\bar{\rho}\frac{\partial u_1'}{\partial t} + \bar{\rho}\bar{u}_1\frac{\partial u_1'}{\partial x_1} + \bar{\rho}\bar{u}_2\frac{\partial u_1'}{\partial x_2} + \frac{\partial p'}{\partial x_1} + \bar{\rho}u_1'\frac{\partial \bar{u}_1}{\partial x_1} + \rho'\bar{u}_1\frac{\partial \bar{u}_1}{\partial x_1} = 0, \tag{1.13a}$$

$$\bar{\rho}\frac{\partial u_2'}{\partial t} + \bar{\rho}\bar{u}_1\frac{\partial u_2'}{\partial x_1} + \bar{\rho}\bar{u}_2\frac{\partial u_2'}{\partial x_2} + \frac{\partial p'}{\partial x_2} + \bar{\rho}u_2'\frac{\partial \bar{u}_2}{\partial x_2} + \rho'\bar{u}_2\frac{\partial \bar{u}_2}{\partial x_2} = 0, \tag{1.13b}$$

where the terms related to $\partial\bar{u}_i/\partial x_i$ are conserved. The GTS method in this form is employed in this thesis.

Additionally, a variant named two-and-a-half dimensional LEE has been proposed by Zhang and Chen [42, 86] by assuming a homogeneous medium in the circumferential direction and an axisymmetric base flow. This method can study three-dimensional phenomenon nearly at around the cost of a two-dimensional computation.

1.2.8 Vortical/acoustic Splitting Method

On the basis of Helmholtz's theorem [87], the irrotational and solenoidal components of velocity can be split into independent parts, respectively the acoustic part (ignoring the entropy effects) and the vortical part, as follows

$$\boldsymbol{u} = -\nabla\varphi + \nabla \times \boldsymbol{A}, \tag{1.14}$$

where φ is a scalar potential, and $\boldsymbol{A}$ is a vector potential. This identity has been utilized for two kinds of purpose in the realm of aeroacoustics.

The first is to compute sound generation by using the linearised perturbation equations, especially in the presence of a dipole-type source. This method stems from the study of streaming motions with small disturbances, in general called the gust-cascade/airfoils interaction problem. Based on the rapid distortion approximation [88, 89], the linearised Euler equations can be decomposed through Equation 1.14, then can be employed to solve unsteady disturbances. Often the vortical part is computed analytically, while the acoustic part is obtained by solving a Poisson's equation. Hunt [90] first used the vortical/acoustic decomposition to generalize the theory of incompressible flows around bluff bodies, where a vector (two-dimensional) Poisson's equation needed to be solved. Goldstein [73] introduced this method to compute the sound generated by a cascade, where the linearised acoustic-vorticity equations were used. Later, a unified approach was proposed by Goldstein [91], by which the entropic disturbance can be considered. A scalar Poisson's equation needs to be solved with regard to incompressible cases. Furthermore, given the considerable loss of accuracy, modifications and extensions have been carried out to improve the prediction of the far-field aeroacoustic response [92–96].

Going down a different route, Ewert et al. [5], by using the Helmholtz's theorem, developed the APE method to address the instability issue. The key process is the so-called source filtering, by which all excitations of Kelvin-Helmholtz instability can be eliminated. Furthermore, by decomposing the perturbed velocity into the acoustic mode

and the vorticity mode, the original APE formulation can be obtained, where all terms of acoustic particle velocity are held in the left-hand side of the equations, to govern sound propagation, while the vorticity disturbances are contained in the source terms. As the vortex sound source can be readily computed by using the pressure fluctuation of the unsteady incompressible flow, a variant named APE-2 was developed to tackle the case of low Mach number isentropic flow. Here, the total pressure perturbation is corrected by the terms of hydrodynamic pressure fluctuation (coming from the unsteady incompressible flow). As only a scalar Poisson's equation needs to be solved, APE-2 becomes much more practical than the original APE, which includes a vector Poissons equation. Later, versions called APE-3 and APE-4 were also developed to avoid solving the Poisson's equation. There are some problems associated with the APE method. Firstly, due to the necessity of solving Poisson's equations, the computational cost increases in the use of APE-1 and APE-2. Moreover, the wave operator employed by the APE method is essentially identical to the one derived by Pierce [97], which is only valid when the hydrodynamic field is slowly varying relative to an acoustic wavelength [8, 97]. Therefore this method limits its application to relatively high frequencies. Also, the acoustic-vorticity coupling can not be resolved by the APE method.

1.2.9 Linearised Navier-Stokes Equations

Generally, using the decomposition Equation 1.7 the Navier-Stokes equations linearised about the mean flow retain the molecular viscosity. In terms of acoustic problems, considering viscosity is not necessary for free field propagation over short distances, however, in internal flows the regions containing strong shears can exist, in which viscosity plays an important role in damping acoustic waves. Furthermore, some researches have shown that the LNS approach is superior to inviscid methods when the coupling of acoustic and hydrodynamic waves is significant [98–101].

As a linear model, LNS equations are useful in investigating basic properties of a nonlinear system. There has been solid evidences that a linear mechanism plays a fundamental role in the dynamics of transition and the dynamics of the near wall layer in fully turbulent boundary layers [102–104], therefore LNS equations can be used to solve these problems with accuracy. A general method based on LNS equations [105] is presented to calculate the response of a bounded flow to stochastic forcing. In the problem of turbulence suppression in channel flow, the LNS method has shown superiorities for designing the linear feedback controllers to reduce the skin-friction drag [103, 106]. Furthermore, LNS equations are performed to study the turbulent skin-friction reduction using the streamwise-travelling waves of spanwise velocity [104] which has become a promising method to reduce the drag in a wall-bounded turbulent flow [107]. The majority of the previous numerical studies on this topic have been implemented using DNS, therefore the studies have been restricted to relatively low Reynolds numbers due to the computational limitations. The LNS approach provides a practical way to study the high

Reynolds number flow. This study shows a correlation between the skin-friction reduction demonstrated in DNS studies and the percentage change in streak amplification obtained by the LNS approach.

In the field of CAA, linearised Navier-Stokes equations including only the molecular viscosity have been firstly performed in the problem of sound propagation and scattering in flow duct systems, and implemented in frequency domain [108, 109]. This LNS method is used to simulate the scattering of sound waves in a sudden area expansion [98], where the flow-acoustic interaction is considerable and the unstable hydrodynamic modes may be excited by incident acoustic waves. The scattering matrix and the acoustic end correction for this case are obtained. Compared with analytical model, this method shows its advantages at the frequencies when the coupling between acoustic and hydrodynamic waves is strong. At these frequencies, $St \approx 1$, the time scales of the acoustic and the vorticity waves are of same order, strong interactions can occur and leads to a significant drop of the end correction. This LNS method is also employed to predict the whistling of an orifice plate in a flow duct system [99]. Whistling induced by flow-acoustic coupling can degrade the performance of mufflers and can give rise to risk for such as an engine exhaust system. Although whistling is a non-linear phenomena, the LNS method shows its ability to determine if a flow duct system goes to whistle or not. Also, to accurately predict the whistling potentiality [110] the acoustic boundary layer (ABL) is resolved. Furthermore, this approach is implemented to determine the acoustic performance of liner attached at the end of duct [111]. The results obtained by this method show good agreement with those of the linear semi-empirical model, while give some discrepancies to the experimental results. In addition, the time-domain LNS method is used to analyse the rotor-stator interaction tone noise [112, 113], namely the gust response problem. In comparison with the method based on linearised Euler equations, the LNS based approach improves the whole prediction process by removing inconsistent and ambiguous procedural elements based on inviscid methodology. Moreover, the frequency-domain LNS approach [100, 101] is revised to include the turbulence information. Different from the traditional double decomposition as shown in Equation 1.7, the triple decomposition [114] is used to split variables, therefore the turbulence information can be taken into account. This LNS method is used to study the linear interaction of the acoustic and hydrodynamic fields in a two-dimensional T-junction, where the complicated flow results in strong turbulence and the considerable coupling to the acoustic waves. The LNS method including turbulence effect strongly improves the solved scattering matrix which is used to predict the ability of a two-dimensional T-junction system to resonances or not.

1.3 Fluid Dynamic Instability

Many current acoustic propagation models experience the instability issues as mentioned previously [82, 83]. This issue actually relates to the mechanism of transition from laminar to turbulent flow. Although most acoustic propagation problems of practical

interest involve turbulent flows, the turbulence information is often discarded when introducing the mean values of the base flow into the linearised perturbation equations. Therefore, the mean flow often becomes actual laminar parallel flows in the absence of turbulence. This approach has advantage especially when the acoustic damping effects of viscosity and turbulence are not of interest. However, the absence of turbulence information gives rise to the classic flow dynamic stability problems that is concerned in the study of transition to turbulence.

Transition from laminar to turbulent flow is induced by fluid dynamic instabilities, and depends on the Reynolds number as well as the size and type of the disturbances. The main excitation sources are usually acoustic waves, vorticity waves and wall vibrations. Linear hydrodynamic stability theory is used to determine the behaviour of disturbances. When a disturbance has a positive growth rate the laminar base flow is unstable. Linear stability analysis is generally based on the linearised Navier-Stokes equations. If assuming a two-dimensional parallel base flow, the LNS equations can be simplified as the so-called Orr-Sommerfeld equation. The stability analysis therefore becomes the problem of eigenvalue analysis to find the unstable perturbation. Ignoring the viscous terms in the Orr-Sommerfeld equation the Rayleigh equation is obtained to investigate the inviscid stability problem. When the flow is non-parallel or/and three-dimensional, for example there are curved boundary layers or velocity gradients in the streamwise direction, the Orr-Sommerfeld equation is not applicable and the PSE method has been used for such problems [57, 58, 115]. Although classic linear stability theory seems to be an efficient and effective tool to determine the evolution of disturbances in a laminar flow, its predictions fail to match most experiments [102, 116, 117] for the flows driven by shear forces, such as Poiseuille flow with a parabolic velocity profile and Couette flow with a linear velocity profile. For example, Couette flow is stable for all Reynolds numbers based on the prediction using the classic linear theory, namely no exponentially unstable perturbations can be found. However, in fact transition is identified for Reynolds number as low as $Re \approx 350$ [102]. This situation can be explained by the transient growth due to algebraic instability [116, 117], which can be studied using the non-modal stability theory [118] instead of the classic hydrodynamic stability theory based on modal (eigenvalue) analysis.

Fluid dynamic instabilities can be classified according to their properties in spatial evolution. If the disturbance grows and moves away downstream, the instability is defined convective; whereas the instability is absolute if the disturbance grows and eventually diffuses over the whole flow field. Also, the instabilities are classified according to associated physical mechanisms. The Tollmien-Schlichting wave [116] is a main mechanism of viscous boundary layer transition, and is initiated generally due to the interaction of disturbances (such as acoustic wave and vorticity wave) with leading edge roughness. The Rayleigh-Taylor instability [119] is buoyancy-driven and generally occurs in fluid flows that contain species of different densities in the presence of gravity and/or other accelerations. The Richtmyer-Meshkov instability [120] occurs due to the

interaction between the shock wave and the interface separating two different fluids. The Görtler instability [121] is induced by surface curvature, and has been considered in the quiet hypersonic wind tunnel design[122]. Considering acoustic propagation problems, shear layers are generally present in most practical flows, such as the engine jet flow and the flow around a wing with deployed high-lift devices in the airframe noise problem, as well as the separated flows at area expansions and orifices in the duct acoustic problem. When these sheared flows are employed as uniform parallel flows into a linear acoustic propagation model and are perturbed by acoustic waves, the Kelvin-Helmholtz instability may be originated.

Infinitely thin shear layers are always unstable to disturbances [123]. According to the quantitative analysis [124], given a long wave disturbance ($k \to 0$), a shear layer is unstable when a threshold of velocity difference is reached and the stability is independent of surface tension. Considering a short wave disturbance ($k \to \infty$), due to the stabilization effect of surface tension a shear layer is stable if the velocity difference is smaller than a threshold; while a shear layer will be unstable for any velocity difference if ignoring surface tension. As the threshold of velocity difference depends on the wave number of disturbance, a shear layer of finite thickness is only unstable over a limited range of frequency. The Kelvin-Helmholtz instability grows exponentially in magnitude and convected by the mean flow, eventually suppressed by viscous and non-linear effects. However, in an inviscid simulation, the instability will grow unlimitedly and eventually corrupt the solution.

In an acoustic propagation simulation, the resulting extensive vorticity product due to Kelvin-Helmholtz instability mechanism poses a challenge to obtain reasonable acoustic solutions. To overcome this issue, some methods based on LEE have been proposed as reviewed in Section 1.2.7 and Section 1.2.8. These methods deal with this issue mainly in some manners to manipulate the vorticity component. Next, the physical effect that vorticity imposes on sound propagation will be reviewed.

1.4 Viscosity and Vorticity Effects on Sound Propagation

Up to this point, the methodology of linearised perturbation equations has shown its advantages in terms of the aeroacoustic application. Meanwhile the instability issue has been discussed. To obtain a complete understanding of the related physical mechanism and further to find a solution to the current issues, firstly it is worth giving a review of the viscosity and vorticity effects on sound propagation.

The sound wave is dissipated by the viscothermal effect. Kirchhoff [125] developed a general model including this effect for sound propagation in cylindrical tubes. Afterwards, Zwikker and Kosten [126] obtained a simplified version of Kirchhoff's equation for circular geometries, which was later justified by Tijdeman [127] et al.. Thereafter, Peat [128] and Ih et al. [129], investigated steady laminar mean flow by assuming a parabolic velocity distribution and disregarding the influence of radial velocity components. On the basis of the same assumptions, Astley and Cummings [130] proposed a

finite element method solving linearised perturbation equations that can deal with non-circular geometries. Subsequently, the studies focusing on the effect of the radial velocity term [131, 132], as well as the effects of pressure and temperature gradients [133–135] have been carries out. Recently, Kierkegaard et al. [98, 99, 108] proposed a linearised Navier-Stokes equations method to solve internal aeroacoustics in the frequency domain. In principle, the laminar viscosity effect can be resolved by this approach with regard to arbitrary geometries and complicated flows. In sum, the attenuation of sound by the viscothermal effect can be neglected when dealing with free-field propagation over short distances, but is significant in the field of internal flows due to the presence of viscous and thermal boundary layers.

Another mechanism that contributes to the attenuation of sound is the vorticity effect [136]. At first, sound waves can be scattered by turbulence, which results in an attenuation of sound [137, 138]. This process does not involve any energy transfer between the acoustic wave and the turbulence. More important, sound is dissipated due to its energy transferring into the kinetic energy of vortical motion. As is well known, this kind of dissipation can be significantly induced either by acoustic waves at high amplitude encountering geometric discontinuities, or by acoustic waves traversing a field of turbulence [139–141]. Also, the presence of a mean flow can improve the dissipation caused by geometric discontinuities [142]. This is because the vorticity produced by acoustic waves at an edge or corner is shed and convected downstream by the mean flow into regions where the interaction between the vorticity and the acoustic field is weak. Eventually the kinetic energy of the vortices is damped into heat by viscous and thermal conduction [141]. Otherwise, a substantial amount of the kinetic energy of the vortices could be transferred back into acoustic energy if the vortices encounter obstacles.

To study this kind of acoustic-vorticity coupling, Howe [141, 143] has proposed what can be regarded as the most complete analytical model in terms of circular ducts. Howe [141] classified the problem into three types, under the limit of small characteristic Mach number, where the efficiency of sound absorption depends on the relationship between the dimensions of the vorticity and the sound, namely the time and length scales. (1) Firstly, when the acoustic wave encounters structural discontinuities, a vortical flow is generated. This phenomenon can be enhanced either by a mean flow [142, 144] or by a sound wave at high amplitude [139]. Also, the effect is inhibited with higher frequencies of incident waves [145]. In this situation, the vorticity initiated by the sound has the time scale in the same order to that of acoustic wave. In principle, the formula proposed by Howe in this case is valid at arbitrary subsonic, uniform mean flows, only if the thin airfoil theory [146] is applicable. (2) Secondly, we have the absorption of sound by mean-flow turbulence. In a low Mach number flow, when the acoustic wavelength is much greater than the length scale of the turbulence, the energy transfer from the acoustic waves to the vortical motion becomes considerable. An extension of Lighthill's acoustic analogy has been developed to examine this phenomenon. (3) The last situation is the interaction of sound with turbulent wall boundary layers. The attenuation of sound is

significantly increased due to the presence of an ABL [147], since this layer imposes great gradients of acoustic particle velocity and then enhances the viscothermal and turbulent effects, namely the viscous and turbulent stresses are strengthened at this layer. The thickness of the ABL depends on the frequency of the incident sound wave. Specifically, at a high frequency when the ABL is entirely immersed into the viscous sublayer, the viscothermal effect dominates the dissipation of sound; in the opposite situation, at a low frequency when this layer extends into the turbulent flow to a great extent, the acoustic damping resulted by turbulence is primary.

At the same time, Cummings [139, 148] proposed a time-domain solution that is used to solve cases associated with structural discontinuities, such as orifice plates and perforated plates in a tube. Further extensions of Howe's model have been developed by Dokumaci [149] and Knutsson [150, 151] to include the influence of the mean velocity profile. Moreover, DNS and LES methods [145, 152, 153] have been employed in the study of vortex shedding induced by sound, but restricted to mechanism investigation due to high costs. Also, experimental tools have been employed to study the acoustic damping by turbulence. Ronneberger and Ahrens [154, 155] developed a series of experiments to examine the wall impedance imposed by the sound wave. Some subsequent experiments have been implemented with the emphasises on extending the examined range of the frequency and amplitude of incident sound waves, as well as on considering more complicated mean flows, for example the study by Peters [156]. Allam and Åbom [157] carried out experiments that first completely validated the theory of Munt [158] and Howe's model [143]. Dokumaci's model [159] was also validated by Allam's experiments with regard to higher frequencies. Additionally, extensive experiments have been carried out for practical applications, such as the design of duct liners in aircraft [160], and the design of a silencer with superimposed flows.

1.5 Sound Propagation in non-uniform Flow: Issues and Solutions

So far, two subjects have been discussed in terms of linear aeroacoustic modellings, namely simulating the sound propagation in shear flows and resolving the acoustic-vorticity coupling.

The instability wave arises in shear layers by acoustic excitations. According to the linear stability theory, in a laminar flow the instability wave grows exponentially when the incident sound wave is of a limited range of frequency. In a turbulent shear flow, viscous and turbulent effects prevent this growth of instabilities. However, by using the LEE method, the viscosity and turbulence are eliminated due to the inviscid assumption, hence the instability can grow unlimitedly. To address this issue, either the instability wave can be excluded or the cause of the instability can be eliminated, for example the APE method for the former and the GTS method for the latter. However, this kind of method generally has a disadvantage that cannot resolve the acoustic-vorticity coupling.

Alternatively, the viscosity and turbulence effects can be reintroduced to suppress the unlimitedly growing instability. This is what herein is proposed.

From another point of view, the instability wave triggered by sound physically absorbs the energy from acoustic waves. As a consequence the sound can be dissipated. This phenomenon is of fundamental importance for fluid dynamics, as well as having practical implications, especially in the realm of duct acoustics. To evaluate this effect, the analytical solutions and the wave equations method can be used, but they only tackle very simple configurations and mean-flow profiles. A novel means based on DNC coupled with analytical post-processing has shown some potential, this is called the CFD-SI method [161–164]. Nevertheless, this method has a considerable computational cost.

With regard to the issues from the two subjects, herein a time-domain linearised Navier-Stokes equations method including turbulence information is proposed. In this method, the turbulent effect is introduced to suppress the instability waves. Therefore this method intends to simulate the sound propagation in arbitrary turbulent flows. Also using this method the acoustic-vorticity coupling can be resolved in a linear manner, thus some problems that have strong relationships with this coupling, such as the dissipation of sound by turbulence and the aeroacoustic property of a T-junction, can be properly solved.

1.6 Structure of Thesis

A code based on the SotonCAA program [165] is developed to implement the LNS method. The main objectives of this thesis are to validate the LNS method and form some guidances on its use through some basic applications.

Firstly in Chapter 2, the computational methodology of this approach to solving sound propagation is given and the linearised Navier-Stokes equations including viscosity and turbulence is derived. The concepts of the perturbation Reynolds stress (PRS) and the ABL are interpreted. Secondly, in Chapter 3, the stability of the LNS method against the cases of turbulent shear layers is validated. The effect that the turbulence stabilises flows is revealed via a turbulent linear stability analysis. Also, the gird convergence study in respect of the mean-flow simulation and the sound propagation problem is carried out and eventually provides the grid guidance for such problems. In this chapter, the LNS method is conducted for a benchmark case and a realistic application, where the use of turbulent models is demonstrated. In addition to the stability study, the turbulent effect on sound propagation is investigated in respect of the near-field and far-field results. Subsequently in Chapter 4, the problem of acoustic damping due to turbulence are investigated by the LNS method. Firstly, the grid convergence study is performed to provide the grid guidance for the acoustic damping problem. Further, the two-dimensional benchmark cases are performed to validate the accuracy of the LNS method dealing with the acoustic damping in turbulent duct flows. Eventually, the attenuation of sound waves at high-order duct modes are evaluated. In Chapter 5, the LNS method is used to investigate the effect of the boundary layer on external noise

radiation. The effect raises concerns in two aspects, namely the engine noise impact on the fuselage at cruise conditions and the far-field noise distribution at take-off/landing conditions. Three simplified models are employed to investigate the boundary layer effects with regard to the two problems. Finally, a summary about the PhD work and the recommendations for the future work are given in Chapter 6.

Chapter 2

Computational Methodology

All motions of idea fluids assumed as continuum are governed by the Navier-Stokes equations. To solve the aerodynamic noise, the hydrodynamic field and acoustic field can simultaneously be simulated, although at a very high cost of computation. Instead, linearising these equations deliveries a more efficient solution when the nonlinear process is not of interest. Compared with the wave equation method and the analytical solutions, the linearised governing equations solve a higher level of physical realism by involving the non-uniformity of the hydrodynamic field. Therefore the refraction and scattering of acoustic waves are solved, as well as the coupling of the acoustic mode, vorticity mode and entropy mode, which can all be resolved in a linear manner. Nevertheless, this coupling can provoke the instability issue for inviscid solutions, for example the LEE method. At this point, a linearised Navier-Stokes equations methodology involving the modelling of turbulence has been proposed.

2.1 Navier-Stokes Equations

The instantaneous compressible Navier-Stokes equations in conservation form can be written in Einstein notation as [166, 167]

$$\frac{\partial \rho}{\partial t} + \frac{\partial (\rho u_i)}{\partial x_i} = 0, \tag{2.1a}$$

$$\frac{\partial (\rho u_i)}{\partial t} + \frac{\partial (\rho u_j u_i)}{\partial x_j} = f_i - \frac{\partial p}{\partial x_i} + \frac{\partial \tau_{ij}}{\partial x_j}, \tag{2.1b}$$

$$\frac{\partial}{\partial t}\left[\rho(e + \frac{1}{2}u_i u_i)\right] + \frac{\partial}{\partial x_j}\left[\rho u_j (h + \frac{1}{2}u_i u_i)\right] = -\frac{\partial q_j}{\partial x_j} + \frac{\partial (u_i \tau_{ij})}{\partial x_j} + f_i u_i, \tag{2.1c}$$

where the heat-flux vector, q_j, is usually obtained from Fourier's law as

$$q_j = -\kappa \frac{\partial T}{\partial x_j}, \tag{2.2}$$

where κ is thermal conductivity. The viscous stress tensor, τ_{ij}, involves the second viscosity and the molecular viscosity, and is expressed as

$$\tau_{ij} = 2\mu s_{ij}, \tag{2.3}$$

so that the strain-rate tensor is given as

$$s_{ij} = \frac{1}{2}\left(\frac{\partial u_i}{\partial x_j} + \frac{\partial u_j}{\partial x_i} - \frac{2}{3}\frac{\partial u_k}{\partial x_k}\delta_{ij}\right). \tag{2.4}$$

Note that for isotropic fluids $s_{ij} = s_{ji}$, so that $\tau_{ij} = \tau_{ji}$ (not standing for some anisotropic liquids).

2.2 Variable Decomposition and Approximations

Equation 2.1 governs the motion of a Newtonian fluid, including the motion of acoustic waves, vorticity waves and entropy waves. As reviewed in Chapter 1, linear models have advantage of computational efforts in simulating acoustic propagation. Conventionally, upon an inviscid assumption, the governing equations can be linearised by splitting variables as shown in Equation 1.7. However, this approach does not take the turbulence into account, a main interest of this study is the interaction between the turbulent fluctuation and the acoustic perturbations, therefore the triple decomposition proposed by Reynolds and Hussain [114] is employed as follows

$$F(\mathbf{x}, t) = \bar{F}(\mathbf{x}) + \tilde{F}(\mathbf{x}, t) + \acute{F}(\mathbf{x}, t), \tag{2.5}$$

where $\bar{F}$ corresponds to the time-mean part, $\tilde{F}$ denotes the organised disturbance, and $\acute{F}$ indicates the random turbulent contribution. Also, the time average and the phase average are defined as, respectively

$$\overline{F}(\mathbf{x}, t) = \lim_{T\to\infty} \frac{1}{T}\int_t^{t+T} F(\mathbf{x}, \tau)\mathrm{d}\tau, \tag{2.6}$$

$$\langle F(\mathbf{x}, t)\rangle = \lim_{N\to\infty} \frac{1}{N}\sum_{n=0}^{N} F\left(\mathbf{x}, t + \frac{n}{f}\right). \tag{2.7}$$

Notice that the time average and the phase average are used here as conceptual tools for the equation derivations. The basic properties of the two operators are

$$\begin{gathered} \overline{\tilde{F}} = 0, \qquad \overline{\acute{F}} = 0, \qquad \left\langle \acute{F} \right\rangle = 0, \\ \overline{\bar{F}G} = \bar{F}\bar{G}, \qquad \left\langle \bar{F}G \right\rangle = \bar{F}\left\langle G \right\rangle, \qquad \left\langle \tilde{F}G \right\rangle = \tilde{F}\left\langle G \right\rangle, \\ \overline{\langle F \rangle} = \bar{F}, \qquad \left\langle \bar{F} \right\rangle = \bar{F}, \qquad \overline{\tilde{F}\acute{G}} = \overline{\left\langle \tilde{F}\acute{G} \right\rangle} = 0. \end{gathered} \tag{2.8}$$

Now the main objective is to yield two sets of equations that govern the base flow and the coherent perturbations, separately. As the time-mean and random components

of the equations are assumed to be frozen from the organised motion, they can be solved independently. The time-mean part comes from the time-averaged results of a solution. The random turbulent component can be obtained from an unsteady solution, or can be reconstructed stochastically, such as using the method of stochastic noise generation and radiation [168]. Currently, the effect of random motions on organised waves is ignored, although this effect needs to be considered in some cases. For example in the boundary layer of the fuselage, the sound waves are scattered due to the turbulent fluctuations and then the acoustic field is changed including a strong shift of the frequency range to higher frequencies[169]. Also, when carrying out the acoustic measurement in an open test section environment of the wind tunnel, the result has to be corrected considering the acoustic scattering due to the turbulence in the open jet which results in spectral broadening or the so-called "haystacking"[170]. This phenomenon means that part of acoustic energy of a tonal source is scattered to other frequencies thereby leading to a broadband hump around the main spectral peak and a reduced peak level.

Up to this point, the deviation of equations is still quite complicated due to the compressibility of flows if directly using the triple decomposition 2.5 for the linearisation. In terms of the continuity equation 2.1a, applying the triple decomposition and time-average operator, yields

$$\frac{\partial \bar{\rho}}{\partial t} + \frac{\partial}{\partial x_i}\left(\bar{\rho}\bar{u}_i + \overline{\tilde{\rho}\tilde{u}_i} + \overline{\acute{\rho}\acute{u}_i}\right) = 0, \tag{2.9}$$

where $\overline{\acute{\rho}\acute{u}_i}$ represents the compressibility effect on the turbulence, and an approximations for the correlation between $\acute{\rho}$ and $\acute{u}_i$ is needed to achieve closure for the equation. Moreover, triple correlations involving $\acute{\rho}$, $\acute{u}_i$ and $\acute{u}_j$ appear for the momentum equations. Generally, the effect of density fluctuations on the turbulence can be neglected for wall bounded flows at subsonic speeds according to Morkovin's hypothesis [166, 171], therefore the computation for such compressible flows can only take the non-uniform mean density into account. However, regarding sheared flows or flows with significant heat transfer for example, the turbulent density fluctuations generally become considerable relative to the mean density. In these cases, the extra correlations between the turbulent density fluctuation and the turbulent velocity fluctuation will markedly increase the complexity of establishing the closure approximations. Conventionally, this problem can be simplified by performing the Favre averaging [172] with a renewed double decomposition.

We herein extend the Favre averaging methodology for the triple decomposition to simplify the processes of establishing the appropriate forms of the time-averaged equations and the linearised equations. At first, instead of the density-weighted time average used in Favre averaging, a density-weighted phase average is applied to the

velocity,

$$\langle u_i \rangle_\rho = \frac{1}{\langle \rho \rangle} \lim_{N \to \infty} \frac{1}{N} \sum_{n=0}^{N} \rho \left(\mathbf{x}, t + \frac{n}{f} \right) u_i \left(\mathbf{x}, t + \frac{n}{f} \right), \tag{2.10}$$

thus we can give

$$\langle u_i \rangle_\rho = \frac{\langle \rho u_i \rangle}{\langle \rho \rangle}. \tag{2.11}$$

Now the velocity is decomposed into the density-weighted phase-averaged part, $\langle u_i \rangle_\rho$, and a fluctuation part, u_i'', therefore

$$u_i = \langle u_i \rangle_\rho + u_i''. \tag{2.12}$$

Furthermore, we assume that the density fluctuation on the turbulence has no effects on the organized perturbation of velocity and only influences the time-mean part, therefore we can give a renewed triple decomposition for the velocity

$$u_i = \bar{u}_i^\rho + \tilde{u}_i + u_i'', \tag{2.13}$$

where $\bar{u}_i^\rho$ is the mass-averaged velocity, and u_i'' denotes the fluctuating velocity relative to the density-weighted phase-averaged part. Also, the original triple decompositions for density and pressure are

$$\rho = \bar{\rho} + \tilde{\rho} + \acute{\rho}, \tag{2.14}$$

$$p = \bar{p} + \tilde{p} + \acute{p}. \tag{2.15}$$

Although the effect of turbulent density fluctuation on the coherent perturbation of velocity has barely been studied so far, we herein focus on other parts and therefore ignore this effects. Also, recall that we have already ignored the effect of random motions on organised waves. Now we have

$$\langle \rho u_i \rangle = \langle \rho \rangle \langle u_i \rangle_\rho + \left\langle \rho u_i'' \right\rangle, \tag{2.16}$$

and taking with Equation 2.11, we can give

$$\left\langle \rho u_i'' \right\rangle = 0, \tag{2.17}$$

then

$$\overline{\rho u_i''} = 0. \tag{2.18}$$

Eventually, the continuity equation 2.1a can be rewritten as

$$\frac{\partial \bar{\rho}}{\partial t} + \frac{\partial}{\partial x_i}\left(\bar{\rho}\bar{u}_i^{\rho} + \overline{\tilde{\rho}\tilde{u}_i}\right) = 0. \tag{2.19}$$

This is a significant simplification for finally solving the equations and actually the momentum per unit volume, ρu_i, has herein been treated as a dependent variable rather than the velocity.

Moreover, under the linear approximation the disturbance wave is assumed to have a small enough magnitude, therefore the second and higher order terms in relation to perturbations, such as $\overline{\tilde{\rho}\tilde{u}_i}$, can be dropped. Furthermore, the mean flow is assumed to be frozen, thus the time-mean parts of variables are time independent, so that $\partial \bar{F}(\mathbf{x})/\partial t = 0$. Also, considering the current applications, the isentropic relation between density and pressure is used so that Equation 2.1c is decoupled and the relationship between the density and the pressure in Equation 1.11 is applied. Meanwhile, the external force density f_i is ignored.

Finally we can decompose the governing Equations 2.1a and 2.1b with Equations 2.13 to 2.15 and obtain

$$\frac{\partial}{\partial t}\left(\bar{\rho} + \tilde{\rho} + \acute{\rho}\right) + \frac{\partial}{\partial x_i}\left[\left(\bar{\rho} + \tilde{\rho} + \acute{\rho}\right)\left(\bar{u}_i^{\rho} + \tilde{u}_i\right) + \rho u_i^{''}\right] = 0, \tag{2.20a}$$

$$\begin{aligned} &\frac{\partial}{\partial t}\left[\left(\bar{\rho} + \tilde{\rho} + \acute{\rho}\right)\left(\bar{u}_i^{\rho} + \tilde{u}_i\right) + \rho u_i^{''}\right] \\ &+\frac{\partial}{\partial x_j}\Big[\left(\bar{\rho} + \tilde{\rho} + \acute{\rho}\right)\left(\bar{u}_i^{\rho} + \tilde{u}_i\right)\left(\bar{u}_j^{\rho} + \tilde{u}_j\right) + \rho u_i^{''} u_j^{''} \\ &+\rho u_j^{''}\left(\bar{u}_i^{\rho} + \tilde{u}_i\right) + \rho u_i^{''}\left(\bar{u}_j^{\rho} + \tilde{u}_j\right)\Big] \\ &= -\frac{\partial}{\partial x_i}\left(\bar{p} + \tilde{p} + \acute{p}\right) + \frac{\partial}{\partial x_j}\left(\bar{\tau}_{ij} + \tilde{\tau}_{ij} + \acute{\tau}_{ij}\right). \end{aligned} \tag{2.20b}$$

2.3 Mean Flow Equations

Taking time averages of Equations 2.20a and 2.20b, gives the time-averaged equations

$$\frac{\partial}{\partial x_i}\left(\bar{\rho}\bar{u}_i^{\rho}\right) = 0, \tag{2.21a}$$

$$\frac{\partial}{\partial x_j}\left(\bar{\rho}\bar{u}_i^{\rho}\bar{u}_j^{\rho}\right) = -\frac{\partial \bar{p}}{\partial x_i} + \frac{\partial \bar{\tau}_{ij}}{\partial x_j} - \frac{\partial}{\partial x_j}\overline{\rho u_i^{''} u_j^{''}}. \tag{2.21b}$$

The deducing processes are detailed in Appendix B. This set of equations is mostly similar to the Favre averaged mean conservation equations [166]. Nevertheless, $\bar{u}_i^{\rho}$ is different from the relevant one obtained through the Favre averaging. The density-weighted time mean part of velocity is defined as

$$\bar{u}_i^{Favre} = \frac{1}{\bar{\rho}} \lim_{T\to\infty} \frac{1}{T} \int_t^{t+T} \rho(\mathbf{x}, \tau) u_i(\mathbf{x}, \tau) \mathrm{d}\tau, \tag{2.22}$$

thus we can give

$$\bar{u}_i^{Favre} = \frac{\overline{\rho u_i}}{\bar{\rho}}. \tag{2.23}$$

This procedure is referred as Favre averaging. Now applying time averaging to Equation 2.11 yields

$$\overline{\bar{u}_i^{\rho} + \tilde{u}} = \overline{\frac{1}{\bar{\rho} + \tilde{\rho}} \langle \rho u_i \rangle}, \tag{2.24}$$

and finally gives

$$\bar{u}_i^{\rho} = \frac{\overline{\rho u_i}}{\bar{\rho}} - \overline{\frac{\tilde{\rho}}{\bar{\rho}^2} \langle \rho u_i \rangle}, \tag{2.25}$$

showing that there is a difference between $\bar{u}_i^{\rho}$ and $\bar{u}_i^{Favre}$. The extra component for $\bar{u}_i^{\rho}$ represents the effect of organized waves to the mean flow. When holding the linear assumption, we have $\tilde{\rho}/\bar{\rho} \ll 1$, therefore the extra term can be ignored and this indicates that the mean flow is stationary from the perturbations.

Eventually, the time-mean parts of all variables can be obtained by solving the Favre averaged mean conservation equations. Also, when the density variation in the turbulent motion is assumed negligible and even the flow is incompressible, the mean flow equations can be obtained via the conventional Reynolds averaging procedures. Considering the effect of compressibility induced by the fluctuating density on the turbulence, extra attentions are needed for the turbulence modelling and additional closure approximations may be necessary to close the system of equations defining the model. Nevertheless, no extra efforts are needed in the acoustic propagation modelling with respect to the compressibility of base flows, as the mean flow can be obtained through the CFD simulation with no considerations of the sound wave.

2.4 Perturbation Equations: Linearised Navier-Stokes Equations for Organised Motion

At first, applying the operator of the phase average, the random components are excluded from Equation 2.20, and the resulting phase-averaged equations are yielded as

$$\frac{\partial \tilde{\rho}}{\partial t} + \frac{\partial}{\partial x_i} \left(\bar{\rho} \bar{u}_i^{\rho} + \bar{\rho} \tilde{u}_i + \tilde{\rho} \bar{u}_i^{\rho} \right) = 0, \tag{2.26a}$$

$$\begin{aligned} &\frac{\partial}{\partial t} \left(\tilde{\rho} \bar{u}_i^{\rho} + \bar{\rho} \tilde{u}_i \right) + \frac{\partial}{\partial x_j} \left(\bar{\rho} \bar{u}_i^{\rho} \bar{u}_j^{\rho} + \bar{\rho} \bar{u}_i^{\rho} \tilde{u}_j + \bar{\rho} \tilde{u}_i \bar{u}_j^{\rho} + \tilde{\rho} \bar{u}_i^{\rho} \bar{u}_j^{\rho} \right) \\ &\quad = -\frac{\partial}{\partial x_i} \left(\bar{p} + \tilde{p} \right) + \frac{\partial}{\partial x_j} \left(\bar{\tau}_{ij} + \tilde{\tau}_{ij} \right) - \frac{\partial}{\partial x_j} \left\langle \rho u_i'' u_j'' \right\rangle. \end{aligned} \tag{2.26b}$$

Subsequently, subtracting the time-averaged Equation 2.21 from the phase-averaged Equation 2.26, gives the dynamic equations of the organised wave disturbance for a

turbulent flow.

$$\frac{\partial \tilde{\rho}}{\partial t} + \tilde{u}_i \frac{\partial \bar{\rho}}{\partial x_i} + \tilde{\rho} \frac{\partial \bar{u}_i^{\rho}}{\partial x_i} + \bar{u}_i^{\rho} \frac{\partial \tilde{\rho}}{\partial x_i} + \bar{\rho} \frac{\partial \tilde{u}_i}{\partial x_i} = 0, \tag{2.27a}$$

$$\begin{aligned} &\bar{\rho} \frac{\partial \tilde{u}_i}{\partial t} + \bar{\rho} \bar{u}_j^{\rho} \frac{\partial \tilde{u}_i}{\partial x_j} + \bar{\rho} \tilde{u}_j \frac{\partial \bar{u}_i^{\rho}}{\partial x_j} + \tilde{\rho} \bar{u}_j^{\rho} \frac{\partial \bar{u}_i^{\rho}}{\partial x_j} \\ &= -\frac{\partial \tilde{p}}{\partial x_i} + \frac{\partial \tilde{\tau}_{ij}}{\partial x_j} - \frac{\partial}{\partial x_j} \left(\left\langle \rho u_i'' u_j'' \right\rangle - \overline{\rho u_i'' u_j''} \right), \end{aligned} \tag{2.27b}$$

together with

$$\tilde{p} = c_0^2 \tilde{\rho}. \tag{2.28}$$

$\tilde{\tau}_{ij}$ describes the molecular diffusion due to perturbation velocity and is given as

$$\tilde{\tau}_{ij} = \mu \left(\frac{\partial \tilde{u}_i}{\partial x_j} + \frac{\partial \tilde{u}_j}{\partial x_i} - \frac{2}{3} \frac{\partial \tilde{u}_k}{\partial x_k} \delta_{ij} \right). \tag{2.29}$$

The stress imposed by turbulence on organised motion

$$\tilde{\Gamma}_{ij} = -\left(\left\langle \rho u_i'' u_j'' \right\rangle - \overline{\rho u_i'' u_j''} \right), \tag{2.30}$$

is named the perturbation Reynolds stress (PRS), which is the difference between the phase and time averages of the Reynolds stress of the background turbulence. $\tilde{\Gamma}_{ij}$ represents the oscillation of the background Reynolds stress induced by the organized motion [114]. The PRS tensor poses the closure problem in the linearised governing equations.

2.5 Perturbation Reynolds Stress

Generally, Reynolds stress appearing in the mean flow Equation 2.21 is modelled on the basis of the Boussinesq hypothesis in which the stress is assumed to be proportional to the mean strain rate $\bar{s}$, then

$$-\overline{\rho u_i'' u_j''} = 2\mu_t \bar{s}_{ij}, \tag{2.31}$$

where μ_t is the turbulent viscosity (also called eddy viscosity) which is postulated in analogy with the molecular viscosity, whereby the effect of turbulent transport is described by an enhanced effective value of viscosity. Eventually, the turbulent viscosity itself has to be modelled to complete the closure. Here, the perturbation Reynolds stress is modelled by extending this concept. Firstly, the stress tensor is described as

$$\Gamma_{ij} = -\rho u_i'' u_j'' = 2\mu_t s_{ij}, \tag{2.32}$$

then the oscillation of the stress can be given by subtracting its mean component from its phase-averaged product

$$\begin{aligned}\tilde{\Gamma}_{ij} &= \langle 2\mu_t s_{ij}\rangle - \overline{2\mu_t s_{ij}} \\ &= 2\left(\bar{\mu}_t\tilde{s}_{ij} + \tilde{\mu}_t\bar{s}_{ij} + \tilde{\mu}_t\tilde{s}_{ij} + \langle\acute{\mu}_t\acute{s}_{ij}\rangle - \overline{\acute{\mu}_t\acute{s}_{ij}} - \overline{\tilde{\mu}_t\tilde{s}_{ij}} - \overline{\acute{\mu}_t\tilde{s}_{ij}}\right),\end{aligned} \tag{2.33}$$

where $\bar{\mu}_t$ describes the time-mean effects induced by the turbulence transport. $\tilde{\mu}_t$ represents the oscillation of the eddy viscosity due to the organised disturbance. $\acute{\mu}_t$ can be regarded as the fluctuating eddy viscosity owing to the fluctuating vorticity. If neglecting the perturbed eddy viscosity, namely assuming that the turbulent energy and time scale remain unchanged in the presence of the disturbance wave, the model reduces to a quasi-steady one, also called quasi-static or the Newtonian eddy model. Equation 2.33 therefore reduces to that proposed by Reynolds and Hussain [114], as given in Equation 2.34

$$\tilde{\Gamma}_{ij} = 2\bar{\mu}_t\tilde{s}_{ij}. \tag{2.34}$$

This identity implies that the turbulent kinetic energy is not modulated by the wave motion, whereas Howe [141] proposed a quasi-steady model

$$\tilde{\Gamma}_{ij} = 4\bar{\mu}_t\tilde{s}_{ij}. \tag{2.35}$$

This model actually takes the term of $2\tilde{\mu}_t\bar{s}_{ij}$ into account, however regards it as $2\bar{\mu}_t\tilde{s}_{ij}$.

A basic model for PRS can be obtained using the Prandtl's mixing length hypothesis. In a simple shear flow where $\partial\bar{u}_1/\partial x_2$ dominates, the phase and time averages of Reynolds stress can be written as

$$-\left\langle\rho u_i'' u_j''\right\rangle = \rho l_m^2\left[\frac{\partial\left(\bar{u}_1+\tilde{u}_1\right)}{\partial x_2}\right]^2, \tag{2.36}$$

$$-\overline{\rho u_i'' u_j''} = \rho l_m^2\left|\frac{\partial\bar{u}_1}{\partial x_2}\right|\frac{\partial\bar{u}_1}{\partial x_2}, \tag{2.37}$$

where l_m is the mixing length, which is assumed to be independent of sound waves. Subtracting Equation 2.36 from Equation 2.37 gives

$$\begin{aligned}\tilde{\Gamma}_{ij} &= -\left(\left\langle\rho u_i'' u_j''\right\rangle - \overline{\rho u_i'' u_j''}\right) \\ &= \rho l_m^2\left|\frac{\partial\bar{u}_1}{\partial x_2}\right|\frac{\partial\tilde{u}_1}{\partial x_2} + \rho l_m^2\left|\frac{\partial\tilde{u}_1}{\partial x_2}\right|\frac{\partial\bar{u}_1}{\partial x_2} \\ &= \bar{\mu}_t\frac{\partial\tilde{u}_1}{\partial x_2} + \tilde{\mu}_t\frac{\partial\bar{u}_1}{\partial x_2},\end{aligned} \tag{2.38}$$

where

$$\bar{\mu}_t = \rho l_m^2\left|\frac{\partial\bar{u}_1}{\partial x_2}\right|, \tag{2.39}$$

is the traditional eddy viscosity for the turbulent flow, and $\tilde{\mu}_t$ represents the change of eddy viscosity due to coherent waves. Similarly as Howe proposed, we can assume that $\bar{\mu}_t \frac{\partial \tilde{u}_1}{\partial x_2}$ and $\tilde{\mu}_t \frac{\partial \bar{u}_1}{\partial x_2}$ are equivalent, therefore

$$\tilde{\Gamma}_{ij} = 2\bar{\mu}_t \frac{\partial \tilde{u}_1}{\partial x_2}. \tag{2.40}$$

The value of the equivalent eddy viscosity in this model is twice as much as that in the traditional Prandtl's mixing length model. This implies that the turbulent kinetic energy is adjusted by the wave motion. Now the model is determined by the mixing length l_m. Prandtl postulated that l_m is space dependent, specifically is proportional to the distance from the surface for flows near solid boundaries. Furthermore, the mixing length depends on the nature of the flow, thus is different for each flow. For example, l_m is proportinal to the half-width of the shear layer, and is defined for each flow with a different coefficient of proportionality, as follows

$$\begin{aligned} l_m &= 0.09\delta, && \text{for plane jet,} \\ l_m &= 0.075\delta, && \text{for circular jet,} \\ l_m &= 0.071\delta, && \text{for mixing layer.} \end{aligned} \tag{2.41}$$

Considering general flows, the PRS term can be solved using Equation 2.35 or Equation 2.34, where the mean part of turbulent viscosity $\bar{\mu}_t$ is obtained with accuracy through a mean-flow simulation based on, generally a one or two-equations model. However, at sufficiently low frequencies the non-equilibrium effect imposed on the turbulence by the sound wave becomes significant, and this effect can lead to a considerable local minimum of the attenuation of sound by turbulence [156]. To maintain the linear approximation, generally the non-equilibrium effect is modelled in the acoustic propagation simulation, rather than in the mean-flow computation. Peters et al. [156] proposed that the turbulent memory effect is responsible for this local minimum and extended the rigid plate model developed by Ronneberger and Ahrens [154] to include this memory effect. Later, Howe [143] proposed a more complete model which introduces the memory effect into the turbulent viscosity by extending Prandtl's linear approximation, therefore the turbulent kinematic viscosity ν_t is expressed as

$$\nu_t = \begin{cases} 0, & x_2 < \delta_v(\omega) \\ \kappa u_\tau \left[x_2 - \delta_v(\omega) \right], & x_2 > \delta_v(\omega), \end{cases} \tag{2.42}$$

where κ is the von Karman constant. The effective thickness of viscous sublayer $\delta_v(\omega)$ is determined by

$$\frac{\delta_v u_\tau}{\nu} = 6.5 \left[1 + \frac{\sigma \left(\omega/\omega_* \right)^3}{1 + \left(\omega/\omega_* \right)^3} \right], \quad \omega_* \nu / u_\tau^2 \approx 0.01, \quad \omega > 0, \tag{2.43}$$

where σ is a constant and controls the acoustic damping at high frequencies, and equals

1.7 to obtain the best correspondence with experiment. ω_* is a critical frequency, and we can define $t_* = 1/\omega_*$ as the turbulent memory time scale which is on the order of

$$t_* \approx 100\nu/u_\tau^2, \tag{2.44}$$

as originally suggested by Ronneberger [173], and later used by Howe, as well as Knutsson and Åbom [143, 151]. Equation 2.42 indicates that the turbulent viscosity is ignorable within the effective viscous sublayer. Based on this model, Howe derived an analytical solution for the attenuation of sound for the low Mach number turbulent flow in pipes and successfully predicted the transition of attenuation. However, Equation 2.42 is still a quasi-static model, as there is no phase lag between the shear wave strain rate and the PRS included in this model to enable non-equilibrium. Recently, Weng et al. [12] developed a phase-dependent non-equilibrium model by directly modifying the equilibrium closure in Equation 2.35. In this model the PRS is defined as

$$\tilde{\Gamma}_{ij} = 2\nu_A \tilde{s}_{ij} \tag{2.45}$$

by introducing the turbulent viscosity including oscillations

$$\nu_A = \frac{2\nu_T}{1 + i\omega t_*}. \tag{2.46}$$

ν_A is different from the traditional turbulent viscosity as it is complex and depends on the frequency of the sound wave. Here the memory time scale t_* has the order identical to that in Equation 2.44.

In other situations, when both the turbulent viscosity and the strain-rate tensor are small enough to be neglected, the PRS can be solved by a quasi-laminar model, eventually the model can reduce to the linearised Euler equations by ignoring the molecular viscosity.

At present in order to simulate the turbulence effect, the quasi-steady models Equation 2.35 of Howe [141] have been employed. The turbulent viscosity can be computed by built-in algebraic models, or solved from CFD simulation. The solving approach depends on the application, primarily it is a matter of the near-wall treatments. When aiming to obtain the dissipation of sound in the ABL, the near-wall region has to be resolved all the way down to the wall, therefore a near-wall model is necessary. On the other hand, in a high-Reynolds-number flow the wall functions can be used to save computational cost, consequently the viscosity-affected wall region is not resolved. All in all, the mean turbulent viscosity, as well as the acoustic-vorticity interaction depending on it, rely on the proper implementation of a turbulent model.

2.6 Acoustic Boundary Layer

Considering that the acoustic oscillation parallels to the surface of an impermeable rigid wall, at the surface the particle velocity is zero and the temperature is constant, whereas,

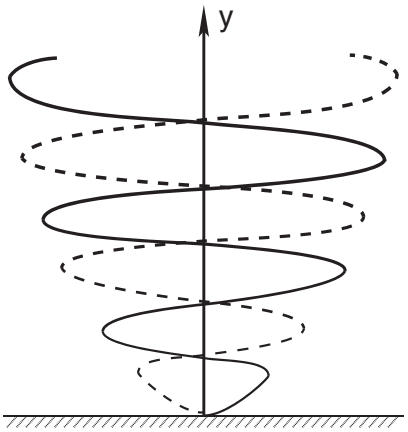

FIGURE 2.1: Schematic of the ABL showing the particle velocity at two instants.

far from the surface all the flow properties oscillate sinusoidally. The value of the particle velocity varies from zero at the surface to the sinusoidal values far from the surface thereby imposing a no-slip condition at the wall boundary, consequently the so-called ABL is formed. The ABL plays an important role in defining the characteristics of sound waves propagation in ducts, where the viscosity together with thermal conductivity and the turbulence coupled with the strong shear stress induce the considerable attenuation of the sound wave.

In terms of the viscosity effects, there are three approaches to carry out the analysis via the linearised perturbation equations [174]. Firstly, the viscosity effects are ignored in both the mean flow and the perturbation equations. In a duct case, this generally implies that the mean flow is uniform and parallels to the axis of the duct. Secondly, the viscosity effects are considered in the mean flow equations but ignored in the perturbation equations. This approach is generally used for the most external acoustic propagation problems. Thirdly, the viscosity effects are included in both the mean flow and the perturbation equations. Furthermore, in terms of the third approach, there are two kinds of cases for different purposes. One aims to obtain the acoustic damping associated with the viscosity and turbulence effects in the wall boundary layer, therefore the ABL needs to be resolved. The another kind of case takes no count of the near wall region, and may focus on the viscosity and turbulence effects during the acoustic-vorticity interaction in shear layers.

The thickness of the ABL plays an important role in determining the characteristics of the sound wave in wall boundary layers, and it is defined as [175]

$$\delta_A = \sqrt{\frac{2\nu}{\omega}}, \tag{2.47}$$

and the viscous sublayer thickness of a turbulent pipe flow can approximately be expressed as

$$\delta_v \approx \frac{10\nu}{u_\tau}, \tag{2.48}$$

where the wall-friction velocity u_τ is calculated by

$$u_\tau = \sqrt{\tau_w/\bar{\rho}}, \tag{2.49}$$

in which τ_w is the wall shear stress and $\bar{\rho}$ is the time-mean density. When the ABL is immersed in the viscous sublayer, the damping of sound waves is only induced by the molecular viscosity. On the other hand, when the ABL is thicker than the viscous sublayer, the damping of sound waves is induced by the turbulent stresses and the viscosity. In the log-law region of a turbulent boundary, the turbulent viscosity increases approximately linearly with the distance from the wall. Subsequently this can lead to significant dissipation of acoustic energy. The normalised thickness of the acoustic boundary is thus introduced to represent the relationship between the ABL and the viscous sublayer, as

$$\delta_A^+ = \sqrt{\frac{2\nu}{\omega}}\frac{u_\tau}{\nu}. \tag{2.50}$$

To resolve the ABL the mesh resolution has to be fine enough within this layer, the grid convergence analysis related to the CAA grid will be conducted in Chapter 4. Moreover, the no-slip wall boundary condition is necessary rather than the slip wall boundary condition that is generally employed when there is no intention of resolving the wall boundary layer.

2.7 Sound Sources

The point source is modelled using Gaussian function to form a bell-shaped pressure distribution and the pressure varies with the period of the sound wave. The function is implemented in Equation 2.27a with the form

$$\tilde{p} = \hat{p}sin(\omega t)exp\left[-\frac{(x-c_x)^2+(y-c_y)^2+(z-c_z)^2}{b^2}\right], \tag{2.51}$$

where $\hat{p}$ is the amplitude of acoustic pressure, (c_x, c_y, c_z) is the coordinates of acoustic source, and ω is the frequency of the acoustic source. The parameter b is related to the width of the bell shape. This function constructs a pressure distribution over a limited region with periodic variations which models a point source.

In terms of duct acoustic problems, the sound source is constructed for axisymmetric duct problems and two-dimensional problems [42, 176]. Corresponding to a duct mode (m, n), where m and n are respectively the azimuthal and radial modes, the incident

acoustic wave is specified as

$$\begin{aligned}
\tilde{\rho}\left(x,r,\theta,t\right) &= a\left[J_m\left(k_r r\right)+c_1 Y_m\left(k_r r\right)\right] cos\left(kt-k_a x-m\theta\right),\\
\tilde{u}\left(x,r,\theta,t\right) &= \frac{k_a}{k-k_a M_j}\tilde{p},\\
\tilde{v}\left(x,r,\theta,t\right) &= -\frac{a}{k-k_a M_j}\frac{d\left[J_m\left(k_r r\right)+c_1 Y_m\left(k_r r\right)\right]}{dr} sin\left(kt-k_a x-m\theta\right),\\
\tilde{w}\left(x,r,\theta,t\right) &= -\frac{am}{r\left(k-k_a M_j\right)}\left[J_m\left(k_r r\right)+c_1 Y_m\left(k_r r\right)\right] cos\left(kt-k_a x-m\theta\right),\\
\tilde{p}\left(x,r,\theta,t\right) &= a\left[J_m\left(k_r r\right)+c_1 Y_m\left(k_r r\right)\right] cos\left(kt-k_a x-m\theta\right),
\end{aligned} \tag{2.52}$$

where M_j is dimensionless velocity inside the duct and is calculated via the velocity at the middle point of the duct inlet; J_m and Y_m is the m^{th}-order Bessel function of the first kind and the second kind, respectively. The non-dimensional modal amplitude a is normally fixed at 10^{-4} to ensure small relative changes in fluctuating density (as requested for linear acoustic assumption). The radial wave number k_r is decided by turning points of the Bessel functions. The axial wave number k_a is calculated from

$$k_a = \frac{k}{\chi^2}\left(-M_j \pm \sqrt{1-\xi^2}\right), \tag{2.53}$$

where

$$\chi = \sqrt{1-M_j^2}, \qquad \xi = \frac{k_r \chi}{k}. \tag{2.54}$$

ξ is cut-on ratio. A duct mode will propagate downstream if and only if $\xi < 1$. The constant c_1 meets the following relations

$$c_1 = -\frac{\frac{d}{dr}\left[J_m\left(r_{outer}k_r\right)\right]}{\frac{d}{dr}\left[Y_m\left(r_{outer}k_r\right)\right]}, \qquad c_1 = -\frac{\frac{d}{dr}\left[J_m\left(r_{inner}k_r\right)\right]}{\frac{d}{dr}\left[Y_m\left(r_{inner}k_r\right)\right]}, \tag{2.55}$$

where y_{outer} and y_{inner} are the height of the inlet duct inner wall and the inner hub radius at the inlet.

2.8 Boundary Conditions

Along with Equation 2.27, in general four types of boundary conditions are employed in the present work, namely, the slip and no-slip wall boundary conditions, the non-reflecting boundary condition, and the symmetric boundary condition.

2.8.1 Wall Boundary Conditions

When aiming to compute the dissipation of sound due to viscosity and turbulence in the near-wall region, the no-slip wall condition created by the interaction of a rigid wall with the acoustic waves is used and implemented as

$$\tilde{\boldsymbol{u}} = \boldsymbol{0}, \qquad \boldsymbol{n}\cdot\nabla\tilde{\boldsymbol{\rho}} = 0, \qquad \boldsymbol{n}\cdot\nabla\tilde{\boldsymbol{p}} = 0, \tag{2.56}$$

where $\boldsymbol{n}$ is a unit vector normal to the wall. Otherwise, if the behaviours of the acoustic waves in near-wall region is not of interest, the slip rigid wall boundary condition should be used and is performed as [177]

$$\tilde{\boldsymbol{u}} \cdot \boldsymbol{n} = 0, \qquad \boldsymbol{n} \cdot \nabla \tilde{\boldsymbol{\rho}} = 0, \qquad \boldsymbol{n} \cdot \nabla \tilde{\boldsymbol{p}} = 0. \tag{2.57}$$

The slip wall boundary condition has an advantage of computational cost, since the ABL does not need to be resolved by the computational mesh. In general, the thickness of the ABL has a much smaller order in comparison with the acoustic wavelength. Therefore resolving the ABL leads to a quite small grid interval in CAA grids, consequently the time step size has to be greatly reduced in order to maintain the Courant-Friedrichs-Lewy (CFL) condition.

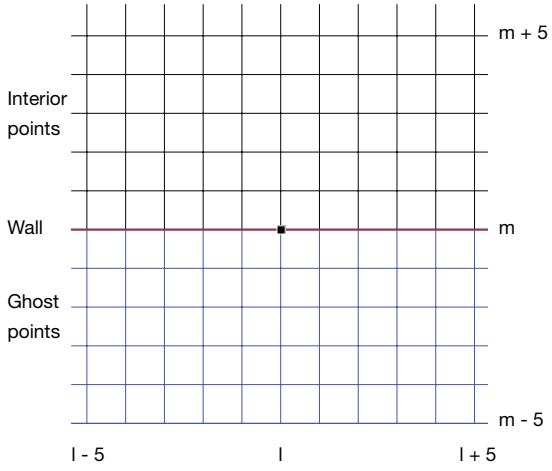

FIGURE 2.2: Eleven-point central stencil for boundary points on the wall. The interior points are located in the physical domain while the ghost points are outside the physical wall.

If solving Equation 2.27 with high-order schemes, the order of the resulting difference equations is higher than that of the original partial differential equations. Hence the wall boundary conditions proposed in Equation 2.56 and Equation 2.57 are inadequate to confine a unique solution. Tam and Dong [178] proposed the imposition of extraneous conditions by introducing extra ghost points. The minimum number of ghost points must be the same as the number of extraneous boundary conditions. In terms of the slip boundary condition, at least one ghost point per boundary point on the wall is needed to specify a boundary condition of perturbation pressure. With regard to the no-slip boundary condition, a corresponding minimum of two ghost points is necessary to further appoint the shear stress value. In the current study, five ghost points per point on the wall are used to enable an eleven-point central compact scheme [179] as shown in Figure 2.2, where l and m are the indices of the mesh points. The resulting

slip and no-slip wall boundary conditions are respectively embodied as

$$\begin{gathered}\tilde{\boldsymbol{u}}_{l,m}\cdot\boldsymbol{n}=0,\qquad \tilde{\rho}_{l,m}=\tilde{\rho}_{l,m+1},\qquad \tilde{p}_{l,m}=\tilde{p}_{l,m+1},\\ \tilde{\boldsymbol{u}}_{l,m-i}\cdot\boldsymbol{n}=-\tilde{\boldsymbol{u}}_{l,m+i}\cdot\boldsymbol{n},\qquad \tilde{\boldsymbol{u}}_{l,m-i}\cdot\boldsymbol{b}=\tilde{\boldsymbol{u}}_{l,m+i}\cdot\boldsymbol{b},\\ \tilde{\rho}_{l,m-i}=\tilde{\rho}_{l,m+i},\qquad \tilde{p}_{l,m-i}=\tilde{p}_{l,m+i},\end{gathered}\tag{2.58}$$

and

$$\begin{gathered}\tilde{\boldsymbol{u}}_{l,m}=\boldsymbol{0},\qquad \tilde{\rho}_{l,m}=\tilde{\rho}_{l,m+1},\qquad \tilde{p}_{l,m}=\tilde{p}_{l,m+1},\\ \tilde{\boldsymbol{u}}_{l,m-i}\cdot\boldsymbol{n}=-\tilde{\boldsymbol{u}}_{l,m+i}\cdot\boldsymbol{n},\qquad \tilde{\boldsymbol{u}}_{l,m-i}\cdot\boldsymbol{b}=-\tilde{\boldsymbol{u}}_{l,m+i}\cdot\boldsymbol{b},\\ \tilde{\rho}_{l,m-i}=\tilde{\rho}_{l,m+i},\qquad \tilde{p}_{l,m-i}=\tilde{p}_{l,m+i}.\end{gathered}\tag{2.59}$$

where $\boldsymbol{b}$ is a unit vector parallel to the walls, and i is a series of numbers from 1 to 5.

2.8.2 Non-Reflecting Boundary Condition

In terms of a flow-field simulation, spurious reflections produced at computational domain boundaries may be ignorable considering the hydrodynamic order amplitudes of interest, however, such reflections may be significant relative to the acoustic quantities and as a result may corrupt the acoustic-field simulation. Therefore, non-reflecting boundary conditions are used to emulate the free acoustic field for a confined computational domain.

Various non-reflecting boundary conditions have been developed to minimize spurious reflections for the computational domain, mainly including the characteristic method [180, 181], the far-field asymptotic solution [182], the buffer zone techniques [183], and the perfectly matched layer method [184]. Generally, the buffer zone techniques employ an extra domain within which the solution is damped using grid stretching [185], numerical damping or by accelerating the base flow to supersonic speeds at the end of the buffer zone [186]. Here, the buffer zone technique based upon an explicitly numerical damping is employed [187]. Within the extra buffer zone of set length L, the amplitude of the outgoing wave is damped to a specified target value by a damping function, $\sigma(x')$.

$$\mathbf{U}^{n+1}=\overline{\mathbf{U}^{n+1}}-\sigma(x')\left(\overline{\mathbf{U}^{n+1}}-\mathbf{U}_{target}\right),\tag{2.60}$$

where $\overline{\mathbf{U}^{n+1}}$ is the solution vector computed after each time step, x' is the distance from initial boundary of the buffer zone. The damping coefficient, σ, varies smoothly according to the function

$$\sigma(x')=\sigma_{max}\left|1-\frac{L-x'}{L}\right|^{\beta},\tag{2.61}$$

where σ_{max} and β are constant coefficients to determine the shape of the damping function. Therefore, the damping function equals zero at the initial boundary which allows outgoing waves to smoothly enter the buffer zones, whereas at the end of the

buffer zones the damping function is set to the maximal value, σ_{max}. The target solution $\mathbf{U}_{target}$ is set as zero to diminish outgoing perturbation waves.

Furthermore, If the target solution $\mathbf{U}_{target}$ is specified as a certain value, such as listed in Equation 2.52, the buffer-zone boundary condition actually specifies incident acoustic waves.

2.8.3 Symmetry Boundary Condition

When the expected patterns of the flow and acoustic fields have mirror symmetry, the symmetry boundary condition can be employed to reduce the computational cost. On the symmetry boundary, the velocity components normal to the boundary are set as zero. To solve the normal derivatives near the boundary, the mirrored variable quantities on the opposite side of the boundary are set through five ghost points. The operation is similar to that used in creating the slip wall boundary condition. Also, the symmetry boundary condition is used at the centre line as the axis boundary condition when solving an axisymmetric acoustic field.

2.9 Numerical Method

This set of linearised Navier-Stokes equations is numerically solved on the basis of the SotonCAA suite of programs [6]. The current solver has been programmed with Fortran language and has been parallelized using Message Passing Interface (MPI) libraries. In addition, the code has been migrated to the Intel Xeon Phi co-processor.

2.9.1 Spatial Discretisation

In terms of the spatial discretization, a finite difference discretization approach is used to compute the first-order spatial derivatives of the governing equations. The second-order spatial derivatives in Equation 2.27 are evaluated via repeating the finite difference for the discretization results of the first-order spatial derivatives. A curvilinear coordinate system is used to maintain the accuracy for complex geometries. To accurately resolve acoustic waves propagation over a larger distances, a high-order spatial discretization scheme is necessary if considering feasible scale of grid resources [182]. Specifically, a sixth-order prefactored compact finite-difference scheme developed by Hixon [188] is performed to evaluate first-order spatial derivatives within the interior regions of a grid block. The scheme can be expressed as

$$
\begin{aligned}
D_i &= \frac{1}{2}\left(D_-^F + D_i^B\right), \\
\alpha_F D_{i+1}^F + \beta_F D_i^F + \gamma_F D_{i-1}^F &= \frac{1}{\Delta x}\left(a_F f_{i+1} + b_F f_i + c_F f_{i-1}\right), \\
\alpha_B D_{i+1}^B + \beta_B D_i^B + \gamma_B D_{i-1}^B &= \frac{1}{\Delta x}\left(a_B f_{i+1} + b_B f_i + c_B f_{i-1}\right),
\end{aligned}
\tag{2.62}
$$

where D denotes the first-order spatial derivative, f is scalar function, i denotes a point of grid, and the superscripts F and B represent the forward and backward operators, respectively. The stencil coefficients, $(\alpha, \beta, \gamma, a, b, c)$, are constant. At boundaries, explicit boundary stencils are used to compute the first-order spatial derivatives. At the interface between two blocks, a symmetric stencil is used with the data from the adjoining blocks, as follows

$$D_i^F = \frac{1}{\Delta x} \sum_{j=-5}^{j+5} b_i f_{i+j}, \qquad D_i^B = \frac{1}{\Delta x} \sum_{j=-5}^{j+5} -b_i f_{i+j}. \tag{2.63}$$

In terms of exterior boundaries of the computational domain, including the buffer zone inflow and outflow conditions, a one-sided stencil is used as follows

$$\begin{aligned} D_{i=1}^F &= \frac{1}{\Delta x} \sum_{j=1}^{7} -e_j f_{i+j-1}, \qquad D_{i=1}^B = \frac{1}{\Delta x} \sum_{j=1}^{7} s_j f_{i+j-1}, \\ D_{i=N}^F &= \frac{1}{\Delta x} \sum_{j=N-6}^{N} -s_{N+1-j} f_{i+j-N}, \qquad D_{i=N}^B = \frac{1}{\Delta x} \sum_{j=N-6}^{N} e_{N+1-j} f_{i+j-N}, \end{aligned} \tag{2.64}$$

where b, e and s represents constant coefficients. At wall boundaries, a biased stencil employing a single ghost point can be used [187], however, due to the numerical stability issue, the symmetric stencil explicit scheme incorporating five ghost points is actually performed at the wall boundary and the symmetry boundary.

2.9.2 Temporal Integration

In terms of the temporal integration, multi-stage Runge-Kutta schemes have been generally applied in CFD schemes due to their low storage requirements in comparison with the multi-step type. Considering the requirements of spatial and temporal accuracy for CAA applications, the temporal integration needs to be improved. An explicit p-stage Runge-Kutta scheme [189] can be represented as

$$\begin{aligned} U^{n+1} &= U^n + K_p, \\ K_l &= \Delta t F\left(U^n + \beta_l K_{l-1}\right), \qquad l = 1, 2, ..., p. \end{aligned} \tag{2.65}$$

Through a wave number analysis, Hu et al. [189] give an accuracy criteria to determine if a Runge-Kutta scheme is time accurate, which is

$$ck_* \Delta t \leq L, \tag{2.66}$$

where k_* is the numerical wave number and L is the accuracy limit. With regard to the four and six-stage Runge-Kutta scheme, the value of L is 0.67 and 1.28, respectively, after optimising can be improved to 0.85 and 1.75, respectively [189]. In this work, to make a compromise between the computational cost and the accuracy, an optimised

four/six stage alternating Runge-Kutta scheme [187] is employed with an accuracy limit $ck_*\Delta t \leq 1.64$, where the conventional four-stage and an optimised six-stage scheme are used on alternating time steps.

2.9.3 Spatial Filtering

Due to the limited spatial resolution for a finite difference scheme, the waves of high enough frequencies will not be resolved with fidelity by the computational mesh, however, such waves emerge in numerical procedures [182]. For CAA applications there is little inherent numerical damping owing to the use of high-order, low-dissipation numerical schemes, therefore the non-physical, very high frequency waves cannot be suppressed and may corrupt the simulations. Consequently, an artificial numerical filtering [190] is usually necessary for removing the spurious waves, by which the damping process is only applied to the waves with certain wave numbers. Generally, an n^{th}-order filter can be written as

$$\alpha_f \hat{f}_{i-1} + \hat{f}_i + \alpha_f \hat{f}_{i+1} = \frac{1}{2} \sum_{n=0}^{N} a_n \left(f_{i+n} + f_{i-n} \right), \tag{2.67}$$

where $\hat{f}_i$ denotes the filtered variable and f_i is the original solution variable. When α is non-zero, the filtered variable also depends on the neighbouring variables and the filter scheme is termed implicit. Alternatively, the scheme is explicit when α equals zero. The explicit filter is considered more computationally efficient [191]. A 10^{th}-order explicit filter [191] is here adopted.

2.10 Grid Convergence Study

The accuracy of a numerical solution depends on the spatial and temporal resolutions, the numerical discretization schemes, the boundary conditions, the numerical models and so on. Generally, the spatial discretization error can be reduced by refining grid, thus the accuracy of the numerical result approaching an asymptotic numerical value is improved. This process involves the grid convergence study which is employed here to evaluate the discretization error due to computational grids, therefore the final grids can be assured of the results with acceptable accuracies.

Traditional grid convergence analysis starts by assuming a relation between the exact solution and the numerical solution. The exact solution can be estimated by Richardson extrapolation method [192] which is used to calculate a higher-order estimate of the flow fields from a series of lower-order discrete values. The order of convergence can be obtained by plotting the discretization error as a function of the grid discretization parameter, generally in $log - log$ space.

Alternatively, the grid convergence index (GCI) suggested by Roache [193, 194] can be used to evaluate the spatial convergence. The GCI is based on the estimated fractional error derived from the theory of generalized Richardson extrapolation. The GCI provides a uniform measure of grid convergence, and indicates an error band on how far the

solution is away from the asymptotic numerical value. It indicates how much the solution could be improved with a further refined grid. Generally, the grid convergence study is carried out over two or three sets of grids, and the solutions are denoted as f_3, f_2 and f_1, respectively for the coarse, medium and fine grids. The GCI for the fine grid is defined as [195]

$$GCI_{21} = \frac{F_s e_a^{21}}{r^o - 1}, \tag{2.68}$$

where F_s is a factor of safety. $F_s = 3.0$ is recommended for comparisons of two grids and $F_s = 1.25$ is for comparisons over three or more grids. For the medium grid, GCI is defined as

$$GCI_{32} = \frac{F_s e_a^{32}}{r^o - 1}, \tag{2.69}$$

and for the coarse grid, the GCI can be calculated by

$$GCI_{23} = \frac{F_s e_a^{32} r^o}{r^o - 1}, \tag{2.70}$$

The approximate relative error e_a^{21} is defined as

$$e_a^{21} = \left| \frac{f_2 - f_1}{f_1} \right|. \tag{2.71}$$

The grid refinement ratio r is generally a constant and should be greater than 1.3 [195] based on experiences to obtain good results using the GCI. r can be computed using

$$r^{21} = h_2/h_1, \tag{2.72}$$

where h is the grid spacing parameter. Alternatively, an effective r can be calculated as

$$r_{effective}^{21} = \left(N_1/N_2\right)^{(1/D)}, \tag{2.73}$$

where N is the total number of grid points and D is the dimension of the flow domain. The order of convergence o is defined as

$$o = ln \left| \frac{f_3 - f_2}{f_2 - f_1} \right| / ln\left(r\right). \tag{2.74}$$

The generalized Richardson extrapolation can be expressed as

$$f_{ext} = \frac{r^o f_1 - f_2}{r^o - 1}. \tag{2.75}$$

The extrapolated relative error for f_1 is defined as

$$e_{ext}^1 = \left| \frac{f_{ext} - f_1}{f_{ext}} \right|. \tag{2.76}$$

The extrapolated relative error for f_2 is defined as

$$e_{ext}^2 = \left| \frac{f_{ext} - f_2}{f_{ext}} \right|. \tag{2.77}$$

Also, the convergence ratio R is used to determine the convergence conditions of a system and defined as

$$R = \frac{f_2 - f_1}{f_3 - f_2}. \tag{2.78}$$

The possible convergence conditions are

1. Monotonic convergence if $0 < R < 1$;
2. Oscillatory convergence if $R < 0$;
3. Divergence if $R > 1$.

Also, we can check the solutions are in the asymptotic range of convergence by

$$A = GCI_{32} / \left(r^o GCI_{21}\right) \cong 1. \tag{2.79}$$

The procedures for the grid convergence study can comply with the following steps [195].

1. Determine the grid spacing parameter h and the grid refinement ratio r with Equation 2.72;
2. Run simulations over different sets of grids to obtain the variable values of interest;
3. Calculate the order of convergence o with Equation 2.74;
4. Calculate the extrapolated values f_{ext} with Equation 2.75;
5. Calculate the relative errors e_a and e_{ext}, as well as the GCI, in order to report the accuracy of solutions and the numerical uncertainty for the corresponding grid.

2.11 Acoustic Far Field

Up to now, the flow field is solved using the mean flow equation, and the acoustic field based on the flow field is simulated using the perturbation equations. In some case, we are also interested in the acoustic far field which is here solved using the Ffowcs Williams-Hawkings (FW-H) equation. As reviewed in Section 1.2.2, the FW-H equation is a generalized acoustic analogy method, which can deal with arbitrary motions of rigid surfaces and the permeable surfaces. Using the double-decomposition in Equation 1.7, the FW-H equation [33, 38, 196] can be written as

$$\begin{aligned} \frac{1}{c^2}\frac{\partial^2 p'}{\partial t^2} - \nabla^2 p' = & \frac{\partial^2}{\partial x_i \partial x_j}\left[T_{ij} H(f)\right] \\ & - \frac{\partial}{\partial x_j}\left\{\left[P_{ij} n_j + \rho u_i \left(u_n - v_n\right)\right] \delta(f)\right\} \\ & + \frac{\partial}{\partial t}\left\{\left[\rho_0 v_n + \rho \left(u_n - v_n\right)\right] \delta(f)\right\}, \end{aligned} \tag{2.80}$$

where u_i is the fluid velocity component in the x_i direction, u_n is the fluid velocity component normal to the surface $f = 0$, v_i is the surface velocity components in the x_i direction, v_n is the surface velocity components normal to the surface, $\delta(f)$ is the Dirac delta function, and $H(f)$ is the Heaviside function. $f = 0$ represents a mathematical surface used to define the confine of a source region in an unbounded space, whereby the generalized function theory and the free-space Green's function can be readily implemented. The surface $f = 0$ can be impermeable (i.e. body surface) or permeable. n_i is the unit normal vector pointing toward the exterior region ($f > 0$). T_{ij} is the Lighthill stress tensor and defined as

$$T_{ij} = \rho u_i u_j + P_{ij} - c^2 \rho' \delta_{ij}. \tag{2.81}$$

P_{ij} is the compressive stress tensor and can be given by

$$P_{ij} = p' \delta_{ij} - \tau_{ij}. \tag{2.82}$$

Equation 2.80 is solved using the free-space Green's function by assuming a free-space flow and absence of obstacles between the sound sources and the receivers. As expressed in Equation 2.83, the solution to Equation 2.80 contains surface integrals and volume integrals. The surface integrals represent the monopole and dipole sources, as well as include partial contributions from quadruple sources, whereas the volume integrals represent quadrupole sources in the region outside the source surface. When the flow is at low Mach number and the main source regions are enclosed by the source surface, the contribution of the volume integrals become small and can be ignored.

$$\begin{aligned} p'(\mathbf{x}, t) = & \frac{1}{4\pi} \frac{\partial^2}{\partial x_i \partial x_j} \int_V \left[\frac{T_{ij}}{r\,(1 - M_r)} \right]_\tau dV \\ & - \frac{\partial}{\partial x_i} \int_S \left[\frac{L_i}{r\,(1 - M_r)} \right]_\tau dS \\ & - \frac{\partial}{\partial t} \int_S \left[\frac{Q}{r\,(1 - M_r)} \right]_\tau dS, \end{aligned} \tag{2.83}$$

where

$$\begin{aligned} Q &= \rho_0 U_i n_i, \\ L_i &= P_{ij} n_j + \rho u_i \left(u_n - v_n \right), \end{aligned} \tag{2.84}$$

with

$$U_i = \left[v_i + \frac{\rho}{\rho_0} \left(u_i - v_i \right) \right]. \tag{2.85}$$

The distance between an observer and the body is defined as $r = |x - y|$, where x is the observer point and y is the body location. The square brackets in Equation 2.83 denote that the kernels of the integrals are computed at the retarded time, τ, where $\tau = t - r/c$. The subscript r denotes the unit vector in the radiation direction. $\mathbf{M}$ is a local Mach number vector, where $M_r = M_i \cdot r_i / r$.

When the integration surface coincides with an impenetrable wall, the two surface integrals in Equation 2.83 are generally referred to as the loading and thickness noise terms, respectively, according to their physical meanings. Thus, we have loading noise term

$$\begin{aligned} 4\pi p'_L(\mathbf{x},t) = & \frac{1}{c}\int_{f=0}\left[\frac{\dot{L}_r}{r\left(1-M_r\right)^2}\right]dS \\ & + \int_{f=0}\left[\frac{L_r - L_M}{r^2\left(1-M_r\right)^2}\right]dS \\ & + \frac{1}{c}\int_{f=0}\left\{\frac{L_r\left[r\dot{M}_r + c\left(M_r - M^2\right)\right]}{r^2\left(1-M_r\right)^3}\right\}dS, \end{aligned} \tag{2.86}$$

and thickness noise term

$$\begin{aligned} 4\pi p'_T(\mathbf{x},t) = & \int_{f=0}\left[\frac{\rho_0\left(\dot{U}_n + U_{\dot{n}}\right)}{r\left(1-M_r\right)^2}\right]dS \\ & + \int_{f=0}\left\{\frac{\rho_0 U_n\left[r\dot{M}_r + c\left(M_r - M^2\right)\right]}{r^2\left(1-M_r\right)^3}\right\}dS, \end{aligned} \tag{2.87}$$

where $L_r = L_i \cdot r_i/r$ and $L_M = L_i \cdot M_i$.

Note that when the source surface $f = 0$ is permeable and placed at a certain distance off the body surface, the integral solutions given by Equations 2.86 and 2.87 also include the contributions from the quadrupole sources within the source region. In this case, the mesh resolution needs to be fine enough to resolve both the flow structure and the acoustic waves inside the confined source region.

Chapter 3

Stable Simulation of Sound in Shear Flow

According to the linear theory of hydrodynamic stability, in a laminar shear layer the instability waves are triggered by disturbances. If the growth rate of instability waves is positive, the flow system is unstable and transitioned. This could happen at a limited range of oscillation frequencies in terms of a connectively unstable system. When using a "two-step"approach to solve the sound propagation in a turbulent flow, usually, the mean flow taken into the perturbation simulation ignores the turbulence information, thus actually presents laminar parallel velocity profiles in the absence of turbulence. Considering the mean flow with such simplified velocity profiles or with actual laminar shear layers, the instability waves cannot be properly modelled via an inviscid solution, such as the LEE method. The resulting instability waves could grow infinitely rather than exhibit the growth and the decay due to jet spreading. Therefore the inviscid approach is inherently unsuitable for such problems.

In this chapter, the stability of turbulent shear layers is studied through the proposed LNS methodology, thereafter the LNS method is employed to simulate sound waves propagating in turbulent shear flows. An algebraic turbulent model is employed in a benchmark case, and then a realistic case is carried out by incorporating a CFD-based mean flow.

3.1 Linear Stability Analysis in Turbulent Flow

A hydrodynamic stability analysis is employed to investigate the evolution of disturbances to the underlying mean flow especially including the turbulence information. Primarily, the hydrodynamic stability analysis is used to studying the laminar-turbulent transition. In general the analysis is based on a set of laminar disturbance equations where the perturbations are of "normal mode"form. In terms of a turbulent flow, the turbulence may introduce significant viscous effects and then results in the reduction of the effective Reynolds number, therefore the stability analysis needs to take the turbulent effects into account. Considering the following sound propagation problems, some

simplified turbulent jet profiles are used to evaluate the stability of the proposed equations. Although the turbulence information is mostly simplified the stability analysis tends to give an insight of the effects of the turbulence stabilising the flows.

3.1.1 Governing Equations

To simplify, the density is assumed constant, thus only the velocity and pressure components can be taken as initial disturbances. Considering the acoustic magnitudes are usually quite small, this simplification is reasonable. Consequently Equation 2.27 reduces to

$$\frac{\partial \tilde{u}_i}{\partial x_i} = 0, \tag{3.1a}$$

$$\frac{\partial \tilde{u}_i}{\partial t} + \bar{u}_j \frac{\partial \tilde{u}_i}{\partial x_j} + \tilde{u}_j \frac{\partial \bar{u}_i}{\partial x_j} = -\frac{1}{\bar{\rho}} \frac{\partial \tilde{p}_i}{\partial x_i} + \frac{1}{\bar{\rho}} \frac{\partial \tilde{\tau}_{ij}}{\partial x_j}, \tag{3.1b}$$

where $\tilde{\tau}_{ij} = 2\mu_e \tilde{s}_{ij}$. μ_e represents the effective viscosity including the molecular viscosity and the turbulent viscosity, which is assumed constant. Since the components of the perturbation viscous stress tensor can now be written as

$$\frac{\partial}{\partial x_j}\left(\frac{\partial \tilde{u}_i}{\partial x_j} + \frac{\partial \tilde{u}_j}{\partial x_i} - \frac{2}{3}\frac{\partial \tilde{u}_k}{\partial x_k}\delta_{ij}\right) = \frac{\partial^2 \tilde{u}_i}{\partial x_j \partial x_j} = \nabla^2 \tilde{u}_i, \tag{3.2}$$

the conservations of mass and momentum reduce to

$$\frac{\partial \tilde{u}_i}{\partial x_i} = 0, \tag{3.3a}$$

$$\frac{\partial \tilde{u}_i}{\partial t} + \bar{u}_j \frac{\partial \tilde{u}_i}{\partial x_j} + \tilde{u}_j \frac{\partial \bar{u}_i}{\partial x_j} = -\frac{1}{\bar{\rho}} \frac{\partial \tilde{p}_i}{\partial x_i} + \nu_e \nabla^2 \tilde{u}_i, \tag{3.3b}$$

where $\nu_e = \mu_e/\rho$ is the effective kinematic viscosity.

By introducing the scales and non-dimensional variables, as listed in Equation 3.4, Equation 3.3 is rewritten in a non-dimensional form as Equation 3.5.

$$\begin{gathered} x_i^* = \frac{x_i}{L}, \qquad t^* = \frac{tU}{L}, \qquad u_i^* = \frac{u_i}{U}, \qquad p^* = \frac{p}{P}, \\ \frac{\partial}{\partial x_i} = \frac{1}{L}\frac{\partial}{\partial x_i^*}, \qquad \frac{\partial}{\partial t} = \frac{U}{L}\frac{\partial}{\partial t^*}, \end{gathered} \tag{3.4}$$

$$\frac{U}{L}\frac{\partial \tilde{u}_i^*}{\partial x_i^*} = 0, \tag{3.5a}$$

$$\frac{U^2}{L}\frac{\partial \tilde{u}_i^*}{\partial t^*} + \frac{U^2}{L}\bar{u}_j^* \frac{\partial \tilde{u}_i^*}{\partial x_j^*} + \frac{U^2}{L}\tilde{u}_j^* \frac{\partial \bar{u}_i^*}{\partial x_j^*} = -\frac{P}{\bar{\rho}L}\frac{\partial \tilde{p}_i^*}{\partial x_i^*} + \frac{\nu_e U}{L^2}\nabla^{*2}\tilde{u}_i^*, \tag{3.5b}$$

where * denotes the non-dimensional variable. Now dropping * as a sign of the non-dimensional variable, finds

$$\frac{\partial \tilde{u}_i}{\partial x_i} = 0, \tag{3.6a}$$

$$\frac{\partial \tilde{u}_i}{\partial t} + \bar{u}_j \frac{\partial \tilde{u}_i}{\partial x_j} + \tilde{u}_j \frac{\partial \bar{u}_i}{\partial x_j} = -\frac{P}{\bar{\rho} U^2} \frac{\partial \tilde{p}_i}{\partial x_i} + \frac{\nu_e}{UL} \nabla^2 \tilde{u}_i. \tag{3.6b}$$

Defining the effective Reynolds number attributed to the molecular and turbulent viscosity as

$$Re = \frac{UL}{\nu_e}. \tag{3.7}$$

Also, the pressure scale is defined as

$$P = \bar{\rho} U^2. \tag{3.8}$$

Finally, the governing equations in the non-dimensional form are given as

$$\frac{\partial \tilde{u}_i}{\partial x_i} = 0, \tag{3.9a}$$

$$\frac{\partial \tilde{u}_i}{\partial t} + \bar{u}_j \frac{\partial \tilde{u}_i}{\partial x_j} + \tilde{u}_j \frac{\partial \bar{u}_i}{\partial x_j} = -\frac{\partial \tilde{p}_i}{\partial x_i} + \frac{1}{Re} \nabla^2 \tilde{u}_i, \tag{3.9b}$$

Equation 3.9 takes the normal forms of the incompressible linearised perturbation equations, however, the effective Reynolds number Re herein is fundamentally different from the normal Reynolds number which depends on only the molecular viscosity. In a turbulent flow, the effective Reynolds number contributed from the turbulence is generally several orders of magnitude greater than that owing to the molecular viscosity. Therefore Equation 3.9 would behave in fundamental respects quite differently from the normal one.

3.1.2 Methodology of Stability Analysis

To yield the equations for stability analysis, the normal mode forms of the disturbances are introduced as

$$\{\tilde{u}, \tilde{v}, \tilde{w}, \tilde{p}\} = \{\hat{u}(y), \hat{v}(y), \hat{w}(y), \hat{p}(y)\} \, e^{i(\alpha x + \beta z - \omega t)}. \tag{3.10}$$

The spatial stability analysis is here of main interest, in which the disturbance is applied in time and the evolution of the disturbance is observed in space. In general, (ω, β) are given as real numbers, and the streamwise wavenumber α is allowed to be complex. The minus imaginary part, $-\alpha_i$ represents the spatial growth rate of disturbances. If the growth rate is positive, the flow system is unstable. Otherwise, using real (α, β) and allowing the complex frequency ω, a temporal stability analysis is performed. Further, assuming that both (α, ω) are complex, an absolute stability analysis is carried out.

Here we consider a uni-directional base flow

$$\bar{\mathbf{u}} = \begin{pmatrix} \bar{u}(y) \\ 0 \\ 0 \end{pmatrix}. \tag{3.11}$$

Substituting Equation 3.10 into Equation 3.9 obtains the equations in two-dimensions

$$0 = \Bigg[-\omega \underbrace{\begin{pmatrix} -i & 0 & 0 \\ 0 & -i & 0 \\ 0 & 0 & 0 \end{pmatrix}}_{E} + \overbrace{\underbrace{\begin{pmatrix} \frac{1}{Re}\frac{\partial^2}{\partial y^2} & -\frac{\partial \bar{u}}{\partial y} & 0 \\ 0 & \frac{1}{Re}\frac{\partial^2}{\partial y^2} - \frac{\partial}{\partial y} & \\ 0 & \frac{\partial}{\partial y} & 0 \end{pmatrix}}_{A_{00}} + \alpha \underbrace{\begin{pmatrix} -i\bar{u} & 0 & -i \\ 0 & -i\bar{u} & 0 \\ i & 0 & 0 \end{pmatrix}}_{A_1} + \alpha^2 \underbrace{\begin{pmatrix} -\frac{1}{Re} & 0 & 0 \\ 0 & -\frac{1}{Re} & 0 \\ 0 & 0 & 0 \end{pmatrix}}_{A_2}}^{\mathrm{A}} \Bigg] \underbrace{\begin{pmatrix} \hat{u} \\ \hat{v} \\ \hat{p} \end{pmatrix}}_{\hat{q}}. \tag{3.12}$$

If α is given, ω is the eigenvalue of a generalized eigenvalue problem

$$\omega E \hat{q} = A \hat{q}, \tag{3.13}$$

while if ω is given, then α is the eigenvalue of a polynomial eigenvalue problem

$$0 = \left(A_0 + \alpha A_1 + \alpha^2 A_2 \right) \hat{q}, \tag{3.14}$$

where $A_0 = -\omega E + A_{00}$.

Generally there are three methods to solve the problem: the shooting method, the finite difference method and the collocation method. Here the Chebychev collocation method is implemented in Matlab, and the program is implemented on the basis of Hoepffner's source code [197]. In respect to a spatial stability analysis, the direct solution of Equation 3.14 can be expensive, as the eigenvalue α occurs to the second power in parts of the equations. The solution is to transform the polynomial eigenvalue problem into a generalised one by adding additional unknowns, $\hat{h} = \alpha \hat{q}$.

$$0 = \underbrace{\begin{pmatrix} A_0 & 0 \\ 0 & 1 \end{pmatrix}}_{B_0} \begin{pmatrix} \hat{q} \\ \hat{h} \end{pmatrix} + \alpha \underbrace{\begin{pmatrix} A_1 & A_2 \\ -1 & 0 \end{pmatrix}}_{B_1} \begin{pmatrix} \hat{q} \\ \hat{h} \end{pmatrix} \tag{3.15}$$

3.1.3 Turbulent Stability Analysis

There are two types of velocity profiles adopted to show the impacts of turbulence on the jet instability, referring to the studies given by Morris [198] and Michalke [199].

Profile 1: the initial mixing region

$$\bar{u}(y) = \frac{1}{2} \left\{ 1 + tanh \left[\frac{1}{4\theta} \left(\frac{1}{y} - y \right) \right] \right\}. \tag{3.16}$$

Profile 2: the fully developed jet

$$\bar{u}(y) = \left(1 + y^2\right)^{-2}. \tag{3.17}$$

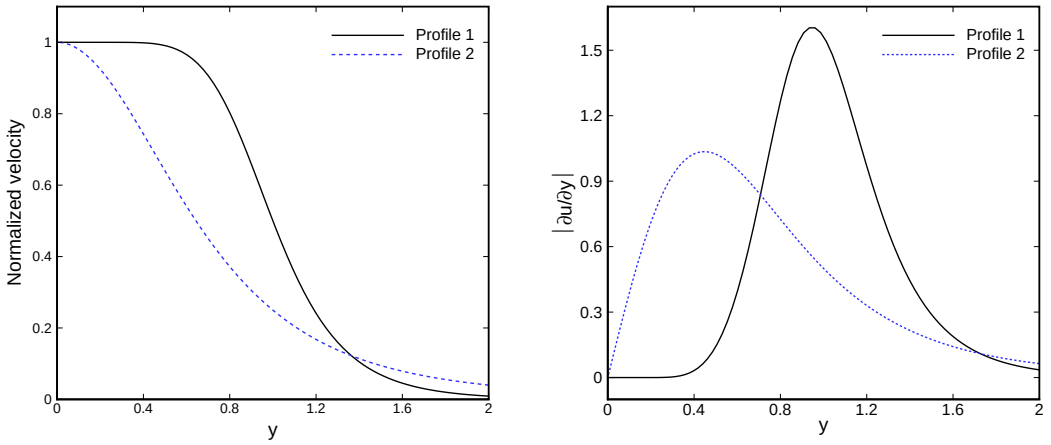

FIGURE 3.1: Jet velocity profiles and their vorticity distributions.

Profile 1 describes a parallel shear layer with a hyperbolic-tangent velocity profile. The momentum thickness of the shear layer, θ used here is equal to 0.16. Profile 2 represents the fully developed jet downstream of the potential core.

In a laminar stability analysis, the Reynolds number in Equation 3.9 depends on the velocity difference and length scale. Here the reference length is set as 1 m. In a turbulent flow, however, the effective Reynolds number can decrease significantly due to the viscous effects induced by the turbulence. To decide the effective Reynolds number, the basic model based on the mixing length hypothesis is employed. The model gives the kinematic turbulent viscosity

$$\nu_t = l_m^2 \left| \frac{\partial \bar{u}}{\partial y} \right|, \tag{3.18}$$

where $l_m = a\delta$ is the mixing length, $a = 0.071$ is the closure coefficient for the mixing layer, and δ is the thickness of the mixing layer. Figure 3.1 gives the distributions of the vorticity magnitude. Based on the biggest values of turbulent viscosity, the effective Reynolds numbers are calculated to be approximately 57 and 51 for Profile 1 and 2, respectively. Notice that the laminar viscosity effect is ignored in comparison to the turbulence effects.

Now using the Chebychev collocation method, the least stable eigenvalues can be found at an effective Reynolds number and a frequency. Subsequently the relationships between the growth rate and the frequency, as well as between the growth rate and the Reynolds number, can be constructed using the collocation method with an iterative process. Figure 3.2 and Figure 3.3 show the spatial growth rate $(-\alpha_i)$ as a function

of the real frequency at given Reynolds numbers, and its dependence on the effective Reynolds number.

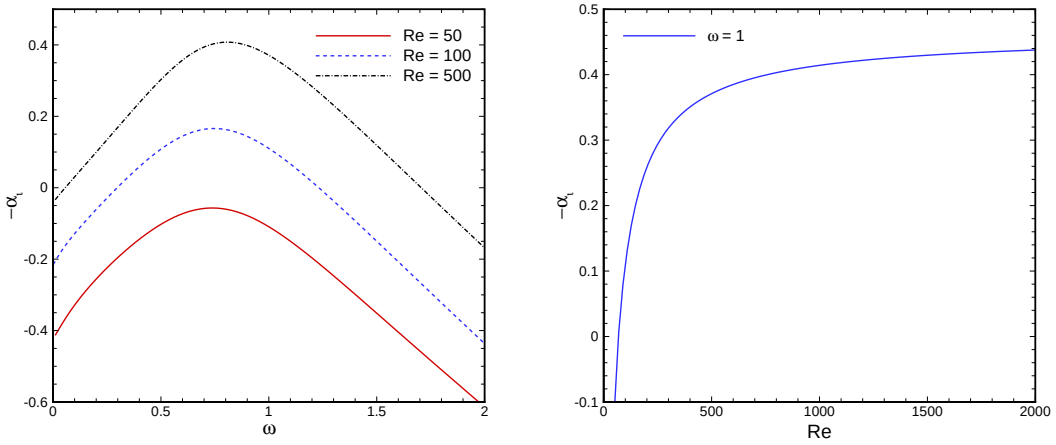

FIGURE 3.2: Spatial growth rate as a function of the real frequency and the effective Reynolds number for mean velocity Profile 1.

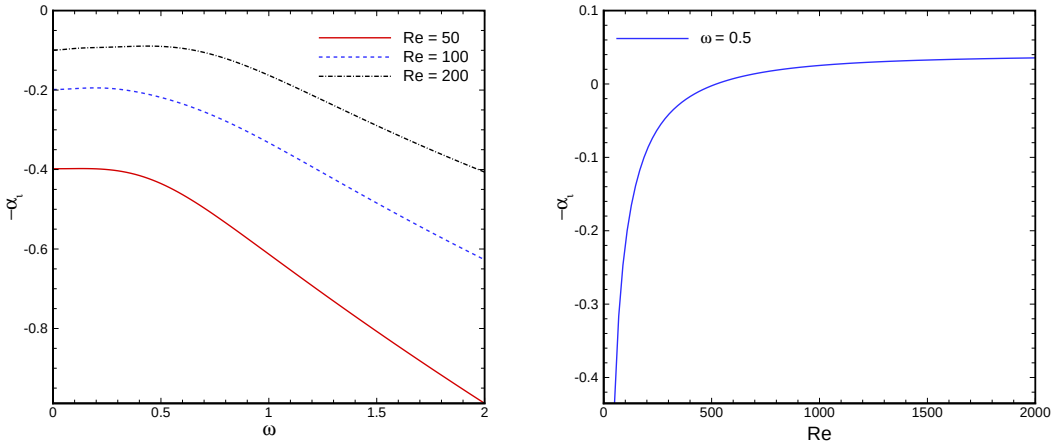

FIGURE 3.3: Spatial growth rate as a function of real frequency and Reynolds number for mean velocity Profile 2.

The figures show the stability of the flows, where the effective Reynolds number depends on turbulence viscosity. Firstly, the profile of the fully developed jet behaves more stable than that of the initial mixing region. Furthermore, it is observed that the increase in Reynolds numbers corresponds to the higher amplification rate. The flow is drastically stabilised in the region of low Reynolds numbers, whereas at high Reynolds numbers the viscous effects can be ignored in consideration of the almost constant growth rate. Also notice that as the Reynolds number is increased, the frequency corresponding to the maximum growth rate is higher.

Note that the influence of the ν_t gradient is not considered here, but has elsewhere been examined in terms of a turbulent swirling flow [200]. At present, the linear stability

analysis shows that turbulence helps significantly stabilising flows. Although the turbulent viscosity cannot be rigorously fixed on the basis of the prescribed velocity profiles and algebraic turbulent models, this approach can shed some light on the stability of turbulent flows, especially in consideration of the LNS method applied to the turbulent mean flow.

3.2 Noise Radiation from a Semi-Infinite Duct

The well-know theory of Munt [158, 201] on the basis of a thin-shear-layer model is used to model the ducted fan noise radiation. The Munt theory employs a semi-infinite circular duct to emulate the fan exhaust and uses an infinite or finite straight duct to model the engine after-body. To obtain a unique solution, Munt's model introduces a full Kutta condition to the lip of the pipe. This Kutta condition in fact implies that the acoustic energy can be transferred into kinetic energy of vortical motion [157]. Munt's theory models the interactions of sound with a subsonic jet, and can consider the instability waves triggered by the incident acoustic disturbance. Therefore, in addition to the far-field directivity, this theory can also predict the sound pressure reflection coefficient at an open end, as well as the low frequency sound absorption. Munt's theory has good agreement with the experimental data [144, 157].

In this section, the Munt type models are employed to validate the stability of the proposed LNS method by incorporating an infinitely thin shear layer. Also, the acoustic far-field directivity predicted by the LNS method, the GTS approaches, the LEE method and the Munt solutions are compared at two realistic flight conditions.

3.2.1 Problem Setup

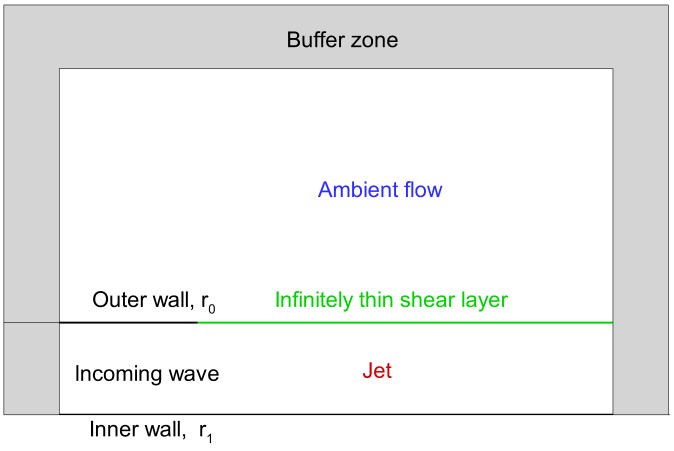

FIGURE 3.4: Schematic of the problem setup for the Munt type model.

As shown in Figure 3.4, given that only the plane wave is considered here, both the mean flow and the acoustic field are assumed axisymmetric without the swirl component,

thus the problem can be simplified as a two-dimensional one. As the wall boundary layer is not taken into account in this problem, the slip wall boundary condition is employed at walls. The buffer zones are placed around the outer boundaries of the domain, and the symmetry boundary condition is used at the centre axis. At the beginning of the duct the plane waves are initiated. As will be shown later in Section 3.3.2, the gird with $PPW = 7$ can give results at an acceptable accuracy, therefore the acoustic fields are solved using a grid with at least $PPW = 7$ up to 2600 Hz.

Geometry / Condition	r_1, m	r_0, m	M_{jet}	$\bar{\rho}$, kg/m^3	Frequency, Hz
Circular duct	0	1	0.5	1.225	400 to 2600
Annular duct / Static approach	0.947	1.212	0.447	1.177	866
Annular duct / Static cutback	0.947	1.212	0.737	1.163	1430

TABLE 3.1: Geometries and operating conditions for the Munt type models. Ambient conditions: $\rho_\infty = 1.225$ kg/m^3, $T_\infty = 288$ K, $M_\infty = 0$

.

Case	Solver	Mean flow
Analytical	GXMunt	–
GTS-thin SL	SotonCAA-GTS, time-domain	Infinitely thin shear layer
GTS-realistic SL	SotonCAA-GTS, time-domain	CFD-solved
LNS-thin SL	LNS, time-domain	Infinitely thin shear layer
LNS-realistic SL	LNS, time-domain	CFD-solved
F-LEE	FLESTURN, frequency-domain	Analytical description
F-GTS	FLESTURN, frequency-domain	Analytical description

TABLE 3.2: Cases for studying the acoustic far-field directivity.

As listed in Table 3.1, three conditions are performed. The circular duct case without centre body is employed to validate the stability. An infinitely thin shear layer is configured in this case, therefore simulations of the time-domain LEE method can be easily corrupted at various frequencies. Nevertheless, the acoustic-vorticity interaction in this thin shear layer could be modelled by the LNS method with a proper turbulence model. A long-running test is performed with a multi-frequency acoustic input to examine the stability. The acoustic frequencies range from 400 Hz to 2600 Hz with a sample interval of 200 Hz. Later, a semi-infinite annular duct with infinite centre body is used to study the acoustic far-field directivity. The geometries and the operating conditions approximate to those for a modern high bypass engine [85].

In terms of the acoustic far-field directivity, various approaches based on various flow conditions are carried out, as summarised in Table 3.2. The far-field observers are located 46 m away from the centre point. The analytical solutions are obtained using the "GXMunt "solver which is developed by Gabard and Astley [202]. The time-domain GTS method is based on the SotonCAA suite of programs [6], where only the gradient terms are dismissed from the momentum equations as given in Equation 1.13.

The results of the frequency-domain LEE and GTS method denoted as "F-LEE "and "F-GTS "are cited from Tester et al. [85], which are solved with "FLESTURN "[203] on the basis of analytically described jet profiles. The thin shear layer cases are also performed in the two realistic conditions to evaluate the differences between the results by employing realistic jet profiles and by using an infinitely thin shear layer.

3.2.2 Eddy Viscosity

To govern the acoustic-vorticity interaction in the infinitely thin shear layer, the methodology of the subgrid scale (SGS) eddy viscosity model is introduced here, starting with somewhat of an intuition. In the model of Munt's theory, an infinitely thin vortex sheet in the vicinity of the pipe lip is demonstrated, however, in numerical practice the thickness of this shear layer is not infinitesimal but depends on the grid size. As is well known, the SGS model is used to parameterize the effects of subgrid-scale motions on the resolved field. If assuming that the vortical motion in Munt's case is confined in subgrid dimensions, the situation would be essentially akin to that when implementing LES, thus the SGS model approach could be reasonably employed in the simulation of this case. Based on this idea, the most commonly used model for the SGS stress, namely the Smagorinsky model [204, 205], is herein extended for the organised motion as

$$\tilde{\tau}_{ij}^{SGS} = 4\bar{\mu}_t^{SGS}\tilde{s}_{ij}, \tag{3.19}$$

$$\bar{\mu}_t^{SGS} = \bar{\rho}\left(C_s^2\Delta_x\Delta_y\right)\sqrt{2\bar{s}_{ij}\bar{s}_{ij}}, \tag{3.20}$$

where Δ_x and Δ_y are the grid spatial dimensions, and C_s is the Smagorinsky coefficient. Lilly [206] derived the value of C_s as approximately $0.16-0.20$ dependent on particular applications, and $C_s = 0.2$ is adopted here.

3.2.3 Validation of Stability

Figure 3.5 displays the instantaneous pressure perturbations simulated by the LNS and the GTS methods with a multi-frequency acoustic source. As is shown, the sound fields are solved properly by both the two method, and there are rarely differences between the two solved pressure fields. Figure 3.6 gives the time traces of pressure at the monitor point (3.6, 1.0) which is located in the thin shear layer. The oscillations for a physical time equal to 0.35 s show steady amplitudes and thus the simulations are considered stable. As is already known, the GTS method is stable to deal with this problem. Also, the LNS method coupled with the SGS model shows its stability in the presence of such an infinitely thin shear layer. Moreover, the amplitude of the pressure perturbations obtained by the LNS method is equal to about 31 Pa, and it is greater than that solved by the GTS method which is equal to about 27.5 Pa.

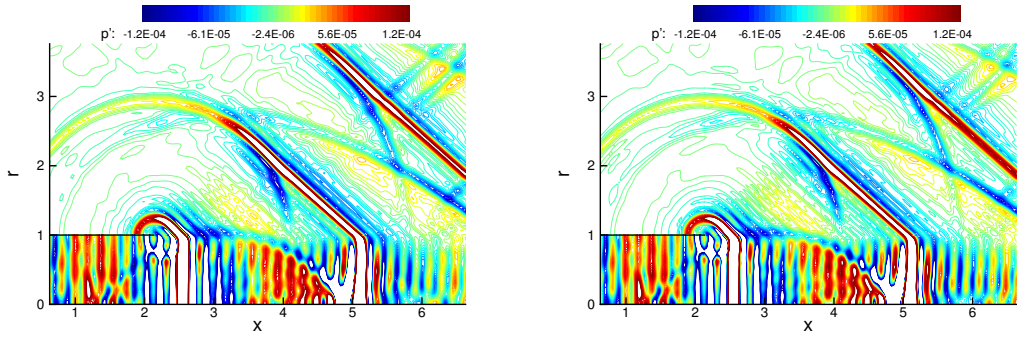

(a) LNS (b) GTS

FIGURE 3.5: Instantaneous pressure perturbation solved with a multi-frequency source.

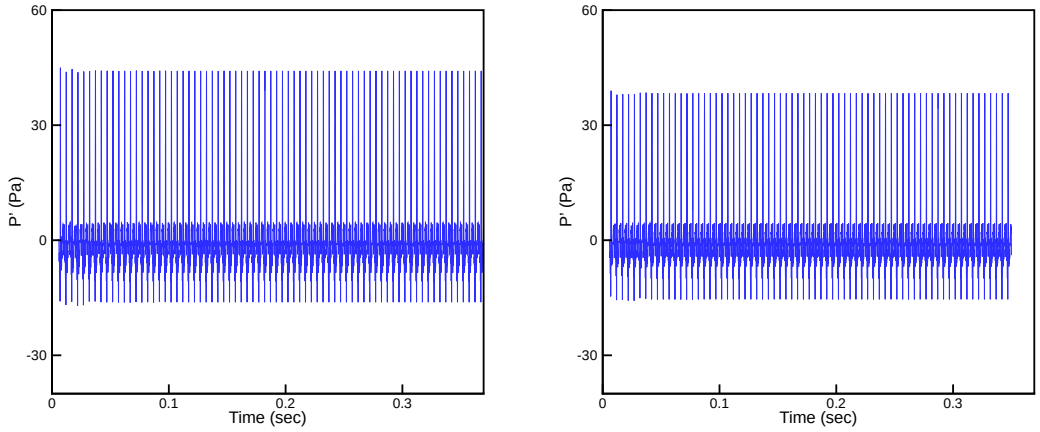

(a) LNS (b) GTS

FIGURE 3.6: Time histories of perturbation pressure at monitor point (3.6, 1.0).

3.2.4 Comparison of Far-field Directivity

At first, Figure 3.8 compares the far-field results solved with the infinitely thin shear layer and the CFD-solved mean flow. The use of realistic jet profiles leads to reductions of the main lobe widths at the low angle range, especially in the static approach condition. Also, the use of realistic jet profiles results in reductions of the main peak magnitudes which are approximately 1.2 dB for LNS and 0 dB for GTS at the static approach condition, as well as 1.5 dB for LNS and 1.9 dB for GTS at the static cutback condition. Furthermore, at the static cutback condition, the realistic shear layer leads to shifts of the main peak angle for about $-2.5°$ for LNS and $-2.6°$ for GTS; at the static approach condition, the results for GTS also show about $-2.0°$ shift of the main peak angles.

Figure 3.9 shows the results solved with more realistic jet profiles. Firstly, in terms of the main lobe widths, at the static approach condition both the analytical described and the CFD-solved jet profiles lead to narrower widths at the low angle range in comparison with the analytical solutions, whereas at the static cutback condition the influence on

the the main lobe widths is weak. Secondly, in terms of the main peak magnitudes the results of "F-LEE "are most close to the analytical solutions although there are differences of about 0.6 dB and 1.9 dB for the static approach and cutback conditions respectively. Meanwhile, the results of "F-GTS "give the differences from the analytical solutions for about 2.6 dB and 4.4 dB. Also, the results of "LNS-realistic SL "show the differences from the analytical solutions for about 1.1 dB and 3.0 dB respectively. Furthermore, the analytically described jet profiles result in lesser shifts of the peak angle rather than those for the CFD-solved mean flow.

In conclusion, firstly in terms of the predicted peak magnitudes the LEE approach gives the best agreement with the analytical solutions, then for the LNS method and last for the GTS method. The turbulence information included in the LNS formulations demonstrates lesser effects than the ignored gradient terms in the GTS formulations in this case. Moreover, the mean flows obtained by different approaches lead to differences of the peak magnitudes and the peak angles. Nevertheless, all the numerical solutions have reasonable agreements with the Munt solutions.

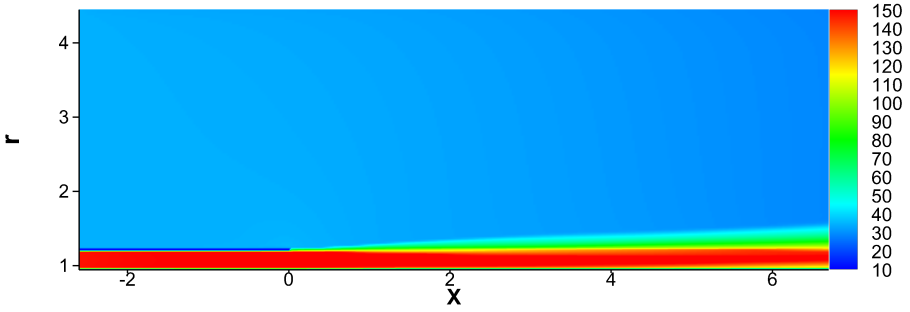

(a) Static approach

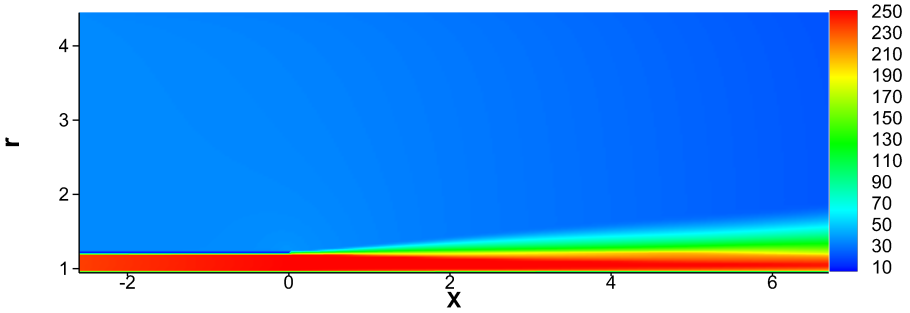

(b) Static cutback

FIGURE 3.7: Mean flows for the semi-infinite annular duct geometry.

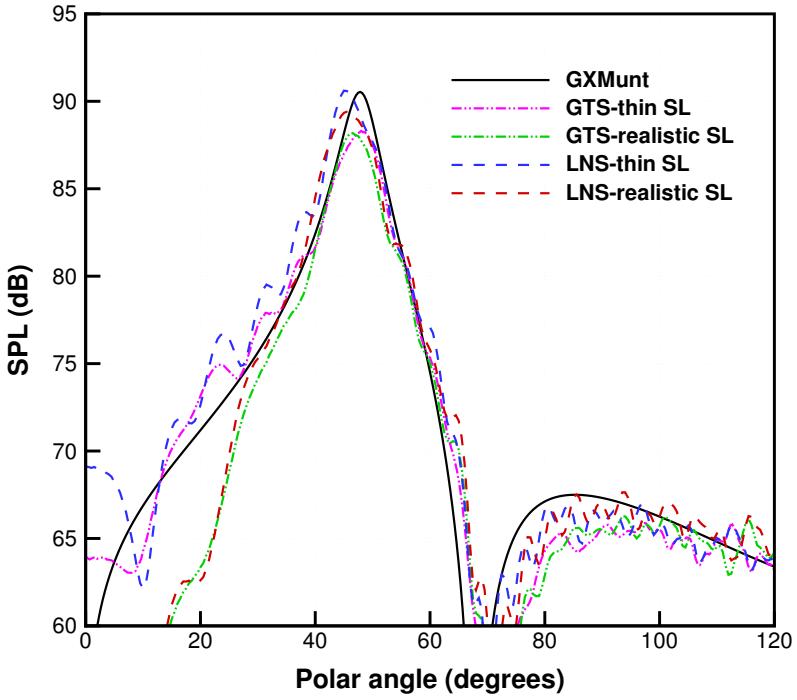

(a) Static approach

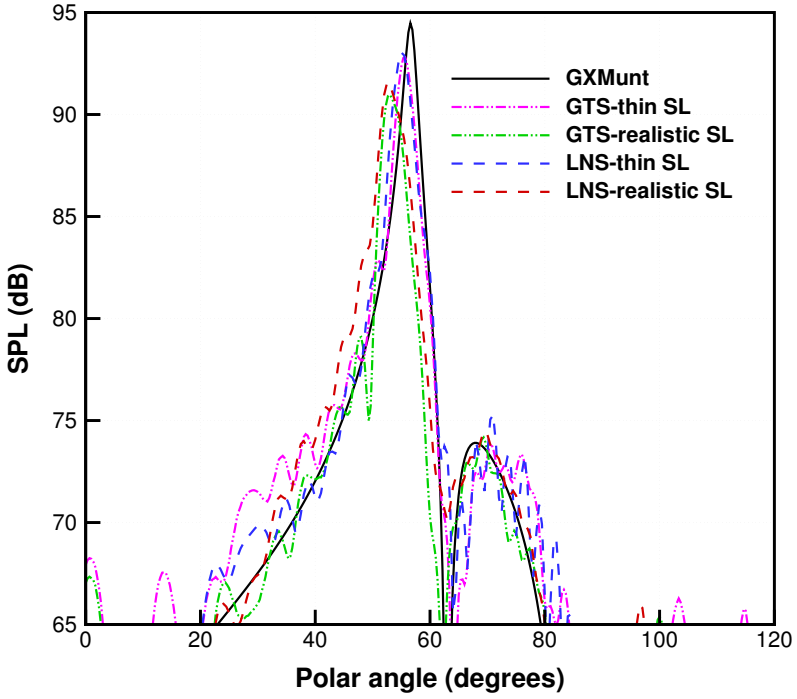

(b) Static cutback

FIGURE 3.8: Comparison of far-field directivity with regards to the infinitely thin shear layer.

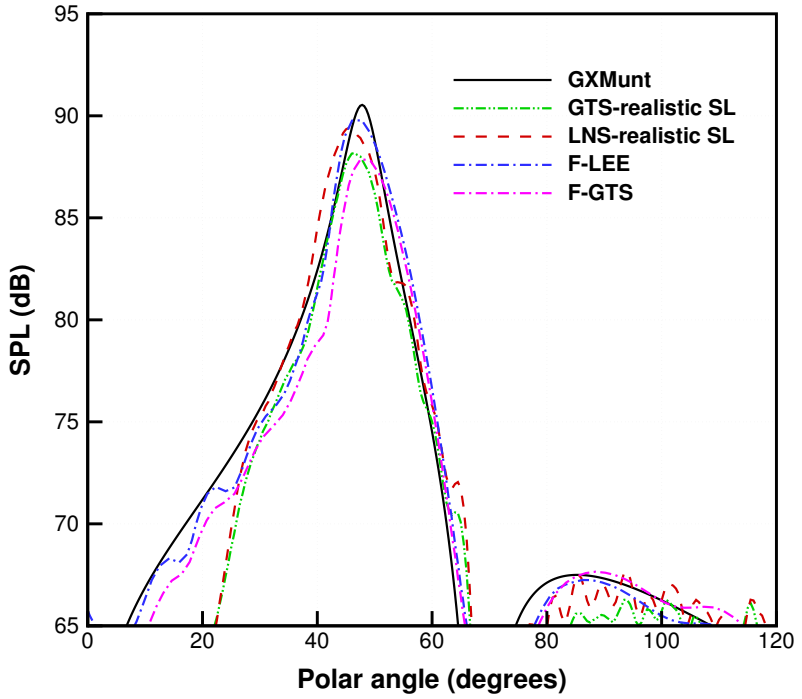

(a) Static approach

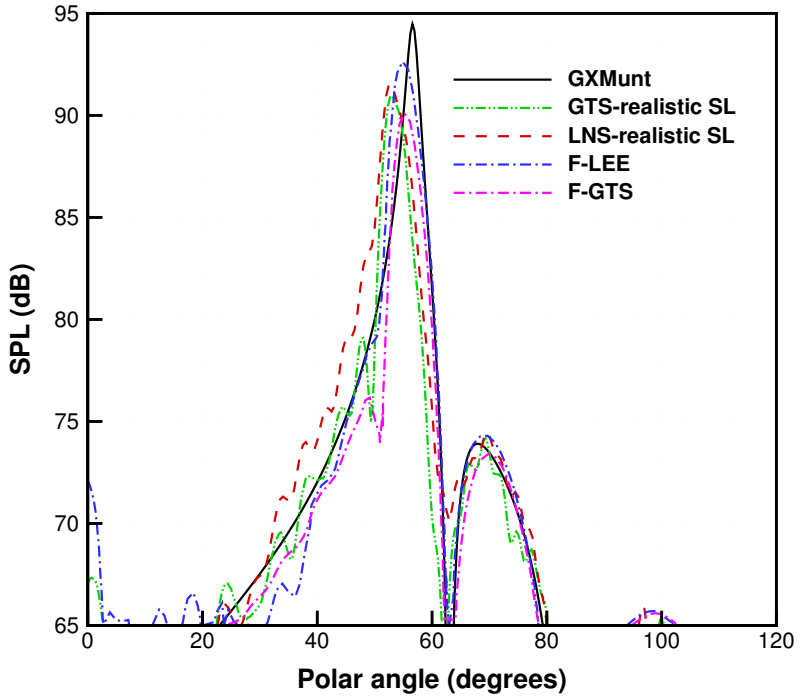

(b) Static cutback

FIGURE 3.9: Comparison of far-field directivity with regards to realistic jet profiles.

3.3 Noise Radiation from a Generic Engine Bypass Duct

Engine tone noise is one of main concerns for the aircraft noise problem. A fully numerical solution of the noise generation and propagation for the engine is still a costly and time-consuming process. However, in the duct downstream of the rotor-stator region of an aero-engine, where the nonlinear effect of noise generation is minimal, the propagation of the resultant tone noise can be studied using linearised equations at an acceptable cost. The acoustic source, described by the frequency and duct mode, can be found by an analytical solution. Nevertheless, the hydrodynamic instability contained in the jet may result in unstable solutions in the simulations of LEE, thereby corrupting the desired acoustic solutions. This concern is the main topic of this chapter.

In this section, a two-dimensional case of turbofan aft noise radiation is employed. Primarily, the instability issue is examined with regard to the proposed approach, as well as the LEE and GTS methods. Furthermore, the influence of PRS terms on sound propagation is evaluated in terms of the near-field and far-field sound distributions. Moreover, the vortex shedding triggered by sound waves is investigated, then the frequency dependence of the acoustic-vorticity interaction is identified.

3.3.1 Problem Setup

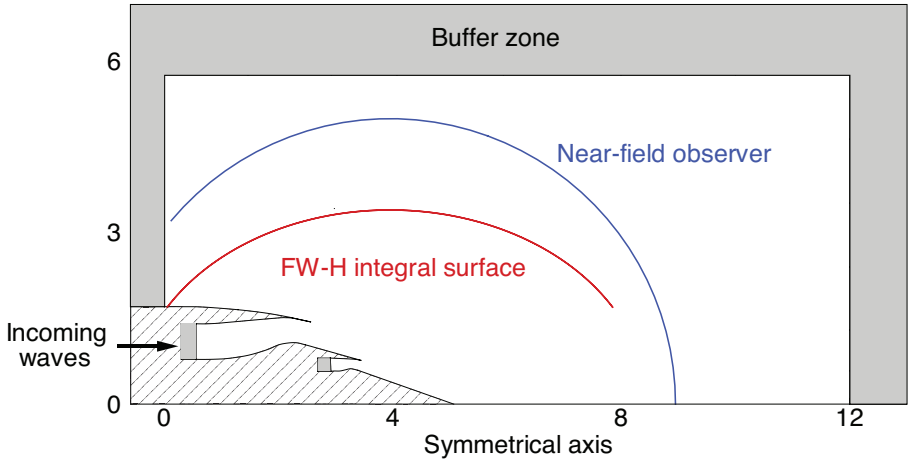

FIGURE 3.10: Schematic of the problem setup including aircraft engine primary and secondary exhausts.

The take-off condition is a typical situation that the engine noise plays a dominant role in the overall noise for a turbofan aircraft [207]. In terms of a simplified model of a generic engine exhaust system without splitter, the flow field can be assumed axisymmetric without swirl component [208]. Furthermore, if only considering the first order azimuthal mode, namely $m = 0$, the acoustic field can also be considered axisymmetric. Therefore, the problem can be simplified as a two-dimensional one. Figure 3.10 displays the half model of a generic engine exhaust system. The outer and inner radii of the

bypass duct are 1.4 m and 0.8 m, respectively. For the core exhaust the outer and inner radii are 0.8 m and 0.57 m, respectively. The flow characteristics at take-off condition for this generic engine [208] are listed in Table 3.3.

	Mach no.	Static pressure, Pa	Temperature, K	Sound speed, m/s
Upstream of the primary exhaust	0.262	114096	783.05	560.99
Upstream of the secondary exhaust	0.449	123013	334.68	359.59
Free stream	0.26	97890	296.27	345.04

TABLE 3.3: Flow parameters for the take-off condition of a generic turbofan engine.

The problem of aft fan noise radiation is simulated using LEE, LNS and GTS methods, and the resulting acoustic characteristics are evaluated by the pressure levels at near-field observers and the far-field acoustic directivity. The near-field observers are along the circle from 0° to 140° with the centre point at (3.95, 0) and with the radius of 5 m. The far-field sound directivity is calculated by incorporating the FW-H solver. The FW-H integral surface is part of an ellipse, for which the major and minor semi-axes are 4.5 m and 3.4 m respectively, the centre point is located at (3.95, 0). The far-field observers are located at 100 m away from the centre point.

The acoustic source is initiated at the bypass duct inlet with an equal sound power assumption. To examine the stability, a multi-frequency acoustic source is employed and the simulation is carried out for quite a long physical time as a long-running test. The acoustic frequencies range from 400 Hz to 2600 Hz with a sample interval of 200 Hz. The physical time of the simulation is 0.6 s. Three discrete frequencies, 1000 Hz, 1500 Hz, and 2000 Hz, are employed to investigate the influence of PRS terms and the acoustic-induced vortices, whereby the frequency dependence of these effects can be observed. Furthermore, The physical time of these simulations is equal to 0.03 s, whereby the LEE method is expected to yield relatively weak instability waves once the sound waves have arrived at the outer boundary. To investigate the vortex shedding, the LNS method is employed. As the vortex shedding frequency is derived by a fast Fourier transform (FFT), in order to provide sufficient samples in time series the simulations are implemented for a physical time of 0.3 s. In all cases, the duct mode $(0, 1)$ is used.

3.3.2 Influence of Computational Setup

As this problem focuses on the free-space acoustic radiation, there is no need to resolve the viscous sublayer and the ABL. Therefore, the RANS approach coupled with the $\kappa-\epsilon$ model can be used at a relatively low computational cost. Specifically, the realisable $\kappa - \epsilon$ model is employed, as it provides improved predictions for the spreading rate of both planar and round jets, also shows superior ability to capture the mean flow of the complex structure. The standard wall function is adopted to model the viscosity-affected

region in the wall boundary layer. As the log-law region is maintained for $y^+ > 30$ to 60 and the wall function ceases to be valid in the viscous sublayer, the y^+ value is desired to be about 30. y^+ is a non-dimensional wall distance for a wall bounded flow and is defined as

$$y^+ = u_\tau \Delta s / \nu, \tag{3.21}$$

where Δs is the wall-adjacent cell height. Based on the predefined y^+ value, Δs can be estimated for grid generation. The flow is simulated with a density-based steady solver using Fluent. Uniform mass flux is initiated from the bypass duct and the core exhaust using the mass flow inlet boundary condition. The outer boundaries of the computational domain are set as the pressure far-field boundary condition. The axis boundary condition is set at the centreline of the axisymmetric geometry. The flow variables are solved with second-order schemes. When the mean flow is solved, the mean field values are interpolated from the CFD grids to the CAA grids.

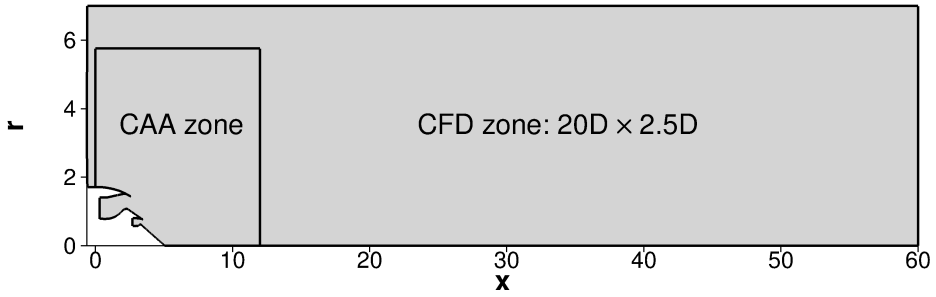

FIGURE 3.11: Schematic of the CFD and CAA computational domains.

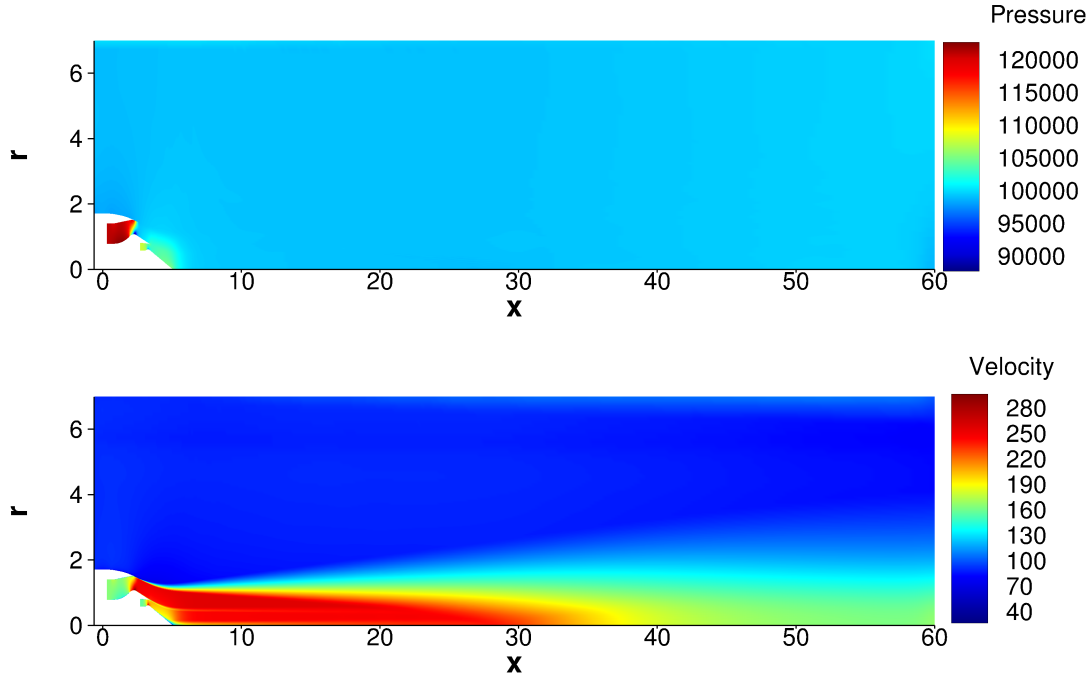

FIGURE 3.12: Mean flow components.

Figure 3.10 shows the CAA computational domain. The buffer zones are placed around the outer boundaries of the domain and at the beginning of the core exhaust nozzle. The bypass duct inlet is used to input the modal acoustic waves. As the main concern is here to investigate the acoustic-vorticity interaction in the shear layers, therefore the ABL at walls is ignored using the slip wall boundary condition. Also, the turbulent viscosity in the ambient is removed. Figure 3.11 displays the CFD computational domain. To ensure the engine exhaust flow is fully developed, the CFD computational domain is expanded to about 20 times the engine diameter in the streamwise direction and about $2.5D$ in the radial direction. Figure 3.12 gives the pressure and velocity distributions, and there are no reflections of mean flow components observed at the downstream boundary.

Next, the influence of spatial resolutions on the flow field and the acoustic field are investigated by performing the grid convergence study.

3.3.2.1 Grid Convergence Study of Mean Flow Simulation

The CFD gird is refined by a factor of $\sqrt{2}$ in all directions simultaneously. Table 3.4 gives the parameters of grids at three sizes. As the wall-adjacent cell height is determined once the y^+ values meet the requirement, the aspect ratios are improved by refining the grid.

Mesh	Total cells	Aspect ratio maximum
Fine	$214,444$	122
Medium	$108,676$	170
Coarse	$54,619$	270

TABLE 3.4: Grid parameters for the grid convergence study of CFD simulations.

Figure 3.13 shows the y^+ values for the three sets of grids. All the y^+ values meet the requirement for the wall function and are mostly close to 30 which is the desirable value.

Point	o	R	A	u_{ext}, m/s	e^1_{ext}	e^2_{ext}	GCI_{32}	GCI_{21}
$(16.52, 1.24)$	2.58	-0.41	1.0037	155.988	0.25%	0.62%	0.78%	0.32%
$(16.52, 0.68)$	5.21	0.16	1.0032	251.652	0.06%	0.39%	0.49%	0.08%

TABLE 3.5: Calculations of discretization error for axial velocities.

Referring to the study to quantify numerical error for a laminar round jet simulation [209], the axial velocities at points $(16.52, 1.24)$ and $(16.52, 0.68)$ downstream the bypass duct and the core exhaust, respectively, are used to calculate the GCI. Table 3.5 summarises the order of accuracy for the axial velocity from the simulation results on the three grids. All the results are obtained after a statistically steady flow was obtained. The theoretical order of convergence is $o = \sqrt{2}$, while the calculated o are 2.58

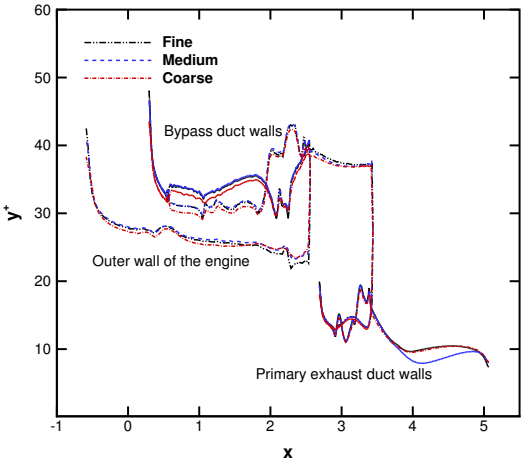

FIGURE 3.13: y^+ values at the walls.

and 5.21, respectively. The convergence ratios R are -0.41 and 0.16 which indicate an oscillatory convergence and a monotonic convergence, respectively. For both points, the reduction of GCI values for the successive grid refinement is observed. $GCI_{21} < GCI_{32}$ indicates that the grid dependency of the numerical simulation is reduced. Furthermore, the values of the ratio A according to Equation 2.79 are equal to 1.0037 and 1.0032, respectively. Both are approximately 1, which indicates that the solutions are well within the asymptotic range of convergence. In conclusion from Table 3.5, the extrapolation values of the axial velocity for the two points are 155.988 m/s with an error band of 0.32% and 251.652 m/s with an error band of 0.08%, respectively. Both the error bands are small enough.

Moreover, the spatial discretization error is evaluated for the field contained in the CAA computational domain. However, due to the sensitivity of GCI, it is hard to obtain a reasonable evaluation for the whole field at once. Therefore, the error band is represented by the approximate relative error e_a^{21}, as shown in Figure 3.14. Uncertainty due to spatial discretization error represented by e_a^{21} is less than or equal to 0.5% in most of the area and increases in the the mixing layer.

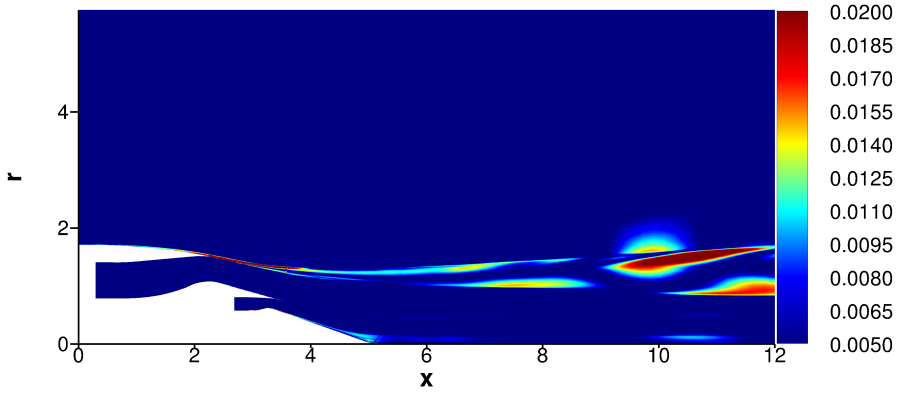

FIGURE 3.14: Approximate relative error e_a^{21} calculated for the axial velocity.

3.3.2.2 Grid Convergence Study of Perturbation Simulation

The CAA gird is refined by a factor of $\sqrt{2}$ in all directions simultaneously, whereby the approximate PPW are equal to 7, 10 and 15 in terms of the sound waves at 2000 Hz for the three sets of grids, respectively. Table 3.6 gives the parameters of grids. The grid convergence is also compared between the LNS and the LEE methods.

Mesh	PPW	Total cells
Fine	15	114, 848
Medium	10	232, 788
Coarse	7	464, 139

TABLE 3.6: Grid parameters for the grid convergence study of CAA simulations.

	o	R	A	SPL_{ext}, dB	e^1_{ext}	e^2_{ext}	e^3_{ext}	GCI_{23}	GCI_{32}	GCI_{21}
60°										
LEE	2.57	0.41	1.0079	88.82	0.54%	1.33%	3.24%	4.10%	1.68%	0.68%
LNS	2.36	0.44	1.0082	88.16	0.64%	1.45%	3.29%	4.18%	1.84%	0.80%
90°										
LEE	8.50	0.05	1.0007	71.32	0.004%	0.08%	1.50%	1.87%	0.10%	0.01%
LNS	6.09	−0.12	0.9984	71.03	0.02%	0.18%	1.11%	1.83%	0.22%	0.03%

TABLE 3.7: Calculations of discretization error for the SPL.

The SPL values at two points are used to calculate the GCI. The coordinates for the two points are $(6.45, 4.33)$ and $(3.95, 5.00)$, located at the 60° and 90° angles of the near-field observation circle, respectively. Also, the approximate relative error e^{21}_a at the whole field is calculated. All the results are obtained once the sound waves have arrived at the outer boundary.

Table 3.7 summarises the calculations of discretization errors at the two points and for the LEE and LNS methods, respectively. Firstly, the values of the convergence ratio R demonstrates that all the solutions at the two points reach oscillatory or monotonic convergence. Also, all the values of A are approximately 1, which indicates that all the solutions are well within the asymptotic range of convergence. Furthermore, for both the two points, $GCI_{21} < GCI_{32} < GCI_{23}$, which proves that the successive gird refinement reduces the grid dependency of the numerical simulation. Furthermore, all the values of GCI_{32} and GCI_{21} are small, which indicates that the fine and medium grids give sufficiently small spatial discretization error. Also, the convergence indexes for the coarse gird GCI_{23} and the extrapolation relative errors e^3_{ext} are relatively small, which indicates, to some extent, the coarse grid with $PPW = 7$ could give acceptable discretization error levels.

Figure 3.15 gives the approximate relative error e^{21}_a at the whole CAA computational field. Large errors in Figure 3.15(a) are found downstream the jet and in the vicinity of

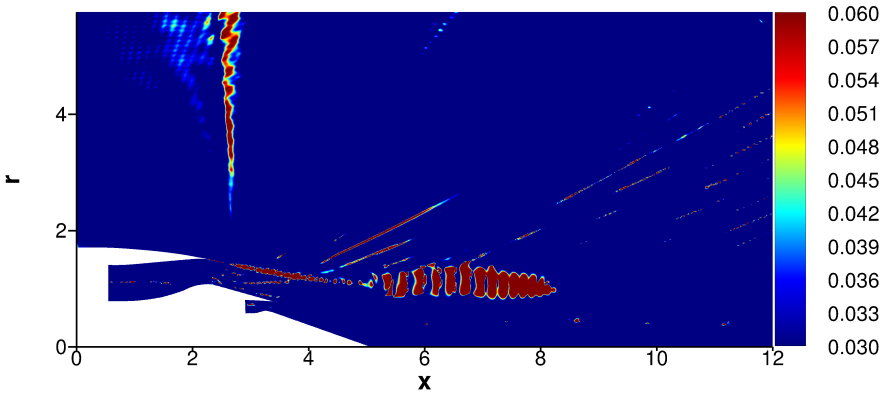

(a) LEE

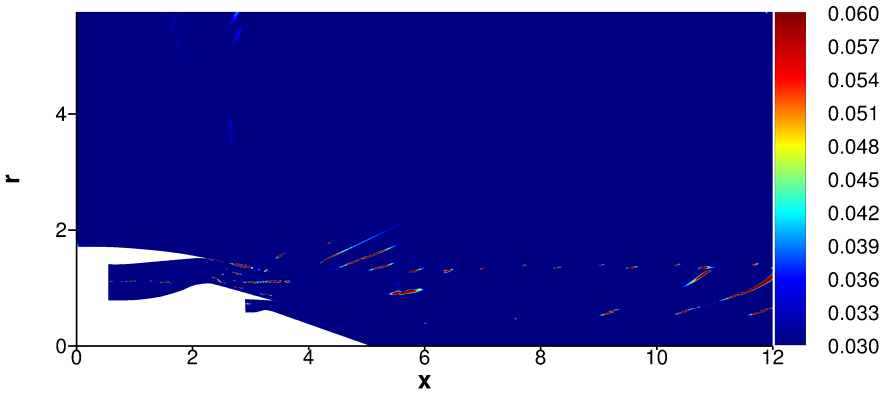

(b) LNS

FIGURE 3.15: Relative error e_a^{21} calculated for the SPL.

the outer lip of the bypass duct. In these regions, the instability waves are quite strong. As shown in Figure 3.17, the resolved instability waves in the downstream jet area induce outstanding SPL distributions. As the refined grid gives stronger instability waves, the resulting SPL becomes higher as compared in Figure 3.17(a) and Figure 3.17(b). Therefore, we may assume that, the LEE method can hardly give a grid-independent solution with regards to such problems. Moreover, Figure 3.15(a) shows relatively large errors along the radial direction around 90° angle. This could be also induced due to the instability wave. The instability wave in the vicinity of the outer lip of the bypass duct influences the sound wave radiation from the duct, however, as shown in Figure 3.17 such instability wave is strengthened due to the grid refinement, therefore its effect on the sound radiation adjusts correspondingly. Furthermore, Figure 3.15(a) shows obvious errors along the path of the sound waves propagation, which could be explained by the refractions to different degrees. As the produce of instability waves is dependent on the grid spatial resolution, the resulting refraction effect varies and leads to differences in directivity of the sound waves propagation. In contrast, the solution solved by LNS shown in Figure 3.18 rarely gives differences due to grid refinements. Figure 3.15(b) shows no relatively distinct errors along the radial direction at 90° angle, as well as

there are no apparent directivity differences. In the mixing layer, relatively large errors appear but are rare. From the whole field of view, the uncertainty represented by e_a^{21} is less than or equal to 3% in most of the area for both the LEE and LNS approaches. In addition, the relative error e_a^{31} is calculated for the coarse gird, as shown in Figure 3.16. Apparently, the accuracy of the upstream result degrades for both the LNS and LEE solvers. Except for this region, the relative error rarely shows obvious increase at most of the area in which the uncertainty is less than or equal to 5%. In conclusion, the fine and medium grids give sufficiently small error bands in most of the computational zones, and the coarse gird delivers higher error levels which could be acceptable in some cases.

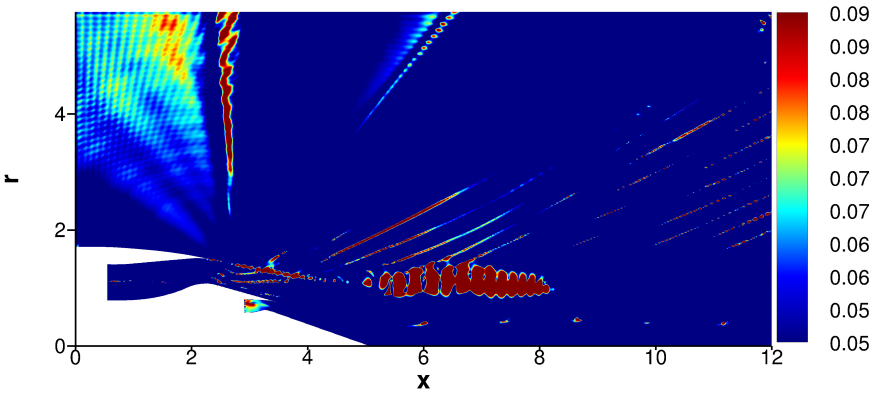

(a) LEE

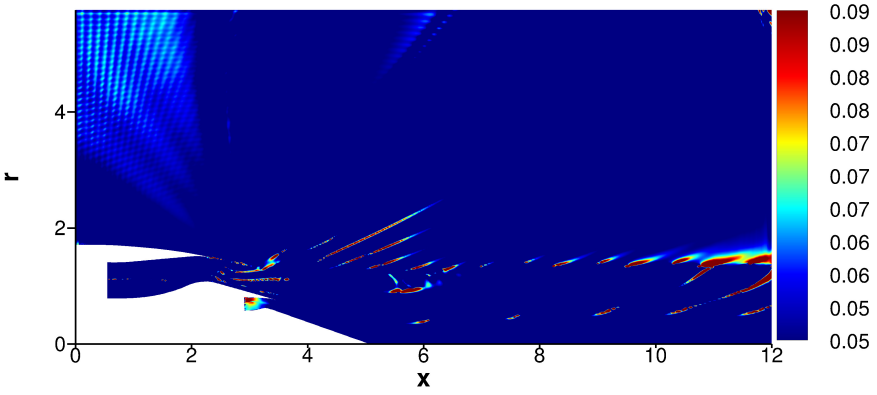

(b) LNS

FIGURE 3.16: Relative error e_a^{31} calculated for the SPL.

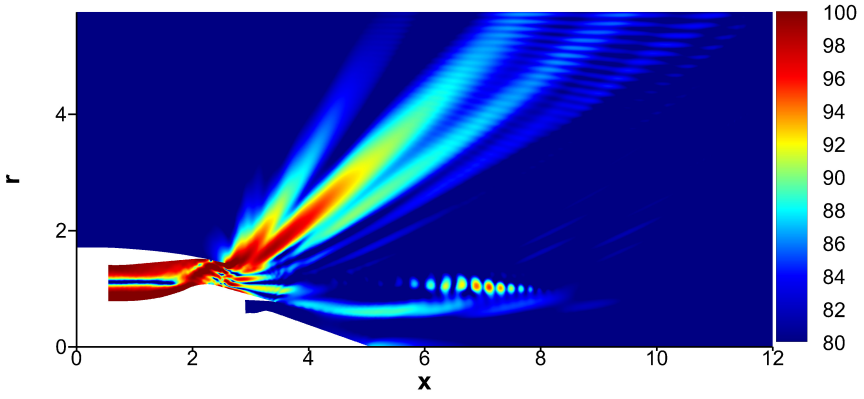

(a) Medium mesh

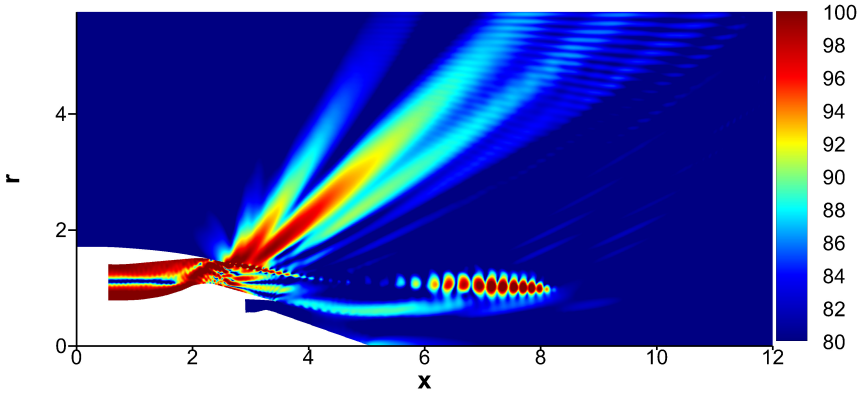

(b) Fine mesh

FIGURE 3.17: SPL solved by LEE with different grids.

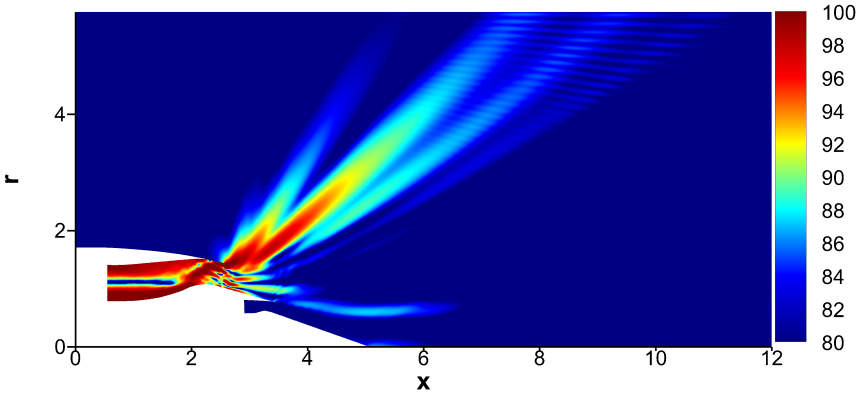

(a) Medium mesh

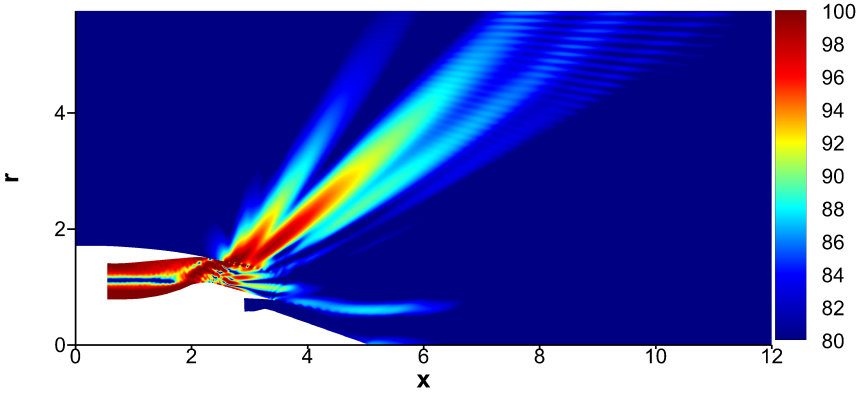

(b) Fine mesh

FIGURE 3.18: SPL solved by LNS with different grids.

3.3.2.3 Conclusions for Grid Convergence Study

In terms of the mean-flow simulation, the fine grid as listed in Table 3.4 gives sufficiently small approximate relative errors in most of the computational area. The gird convergence study at points shows the fine mesh gives grid convergent results with sufficiently small error bands. Therefore, the mean flow is solved by the fine gird.

In consideration of the perturbation simulation, the fine and medium grids as shown in Table 3.6 give sufficiently small approximate relative errors in most of the computational domain, and the GCI results show the fine and medium meshes deliver grid convergent solutions with sufficiently small error bands. The coarse grid leads to relatively extensive regions with relatively large errors, but might provide acceptable error bands at most of the domain of interest. Eventually, the grid used here to perform the simulations gives at least $PPW = 10$ up to 2200 Hz.

Additionally, the grid convergence study shows the results solved by LEE is influenced by the instability waves to a large degree, and therefore no grid convergent results could be provided especially in the mixing layer.

3.3.3 Mean Flow Results

Figure 3.19 displays the non-dimensional mean-flow components. The reference values of length, density and sound speed are 1 m, 1.28 kg/m^3 and 359.59 m/s respectively. As shown, the flow contains strong velocity shear layers especially between the ambient and the jet. Also, density gradients are present between the jets of the primary and the secondary exhausts due to the temperature difference. The turbulent viscosity grows with the jet spreading.

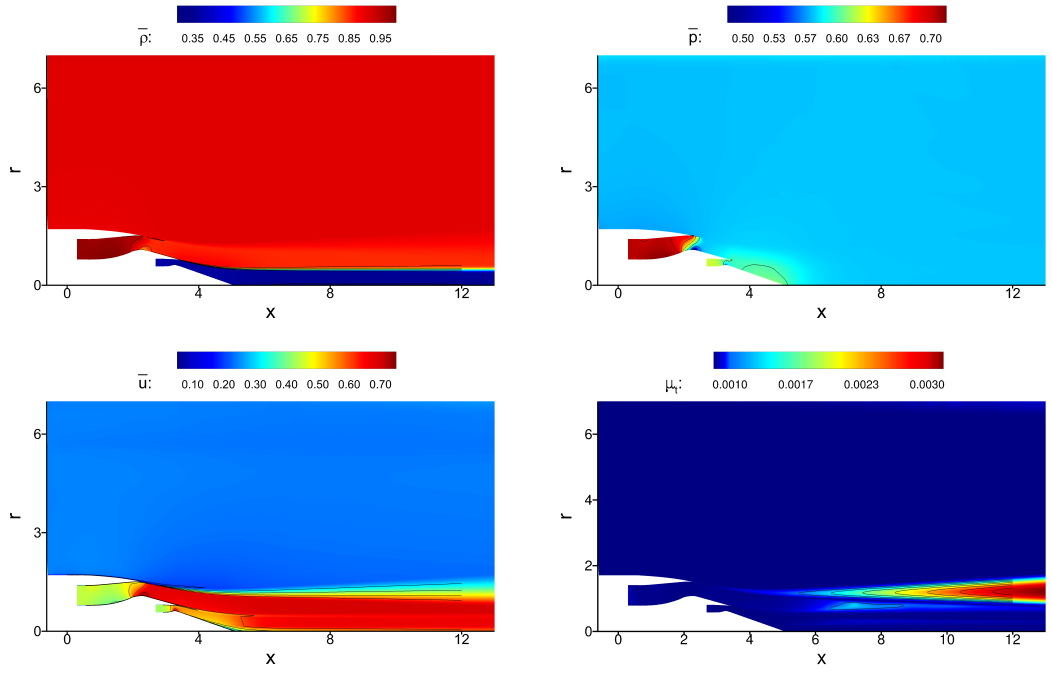

FIGURE 3.19: Non-dimensional mean flow components.

3.3.4 Instability Issue

Firstly, the instability waves appearing in a form of vortex sheets do not necessarily lead to an unstable flow system, only when the resulting instability waves and the flow have the special nature as described in Section 1.3. If an unstable system is formed, although the spatial instability is initiated by weak periodic forcing, it develops with an exponential growth rate as shown in Figure 3.20 for the results obtained by LEE. Subsequently, the acoustic field can rapidly be polluted due to the exponentially growing instabilities. Figure 3.20 gives the time histories of the perturbation pressure at the points A (4.02, 3.51) and B (5.57, 1.30). Point A is relatively far away from the jet, where the pressure perturbation may avoid the direct influence of the vorticity. Point B is located in the shear layer between the ambient and the jet, and thus can record the information of the vorticity convected downstream. In terms of LEE, at point B the oscillation jumps early due to the instant reaction of instability waves, whereas at point A the prominent growth is first observed at near 0.1 s when the additional sound initiated by the resulting vortices arrives at the monitor point. Meanwhile, the oscillations given by LNS and GTS are stable in the presence of steady amplitudes.

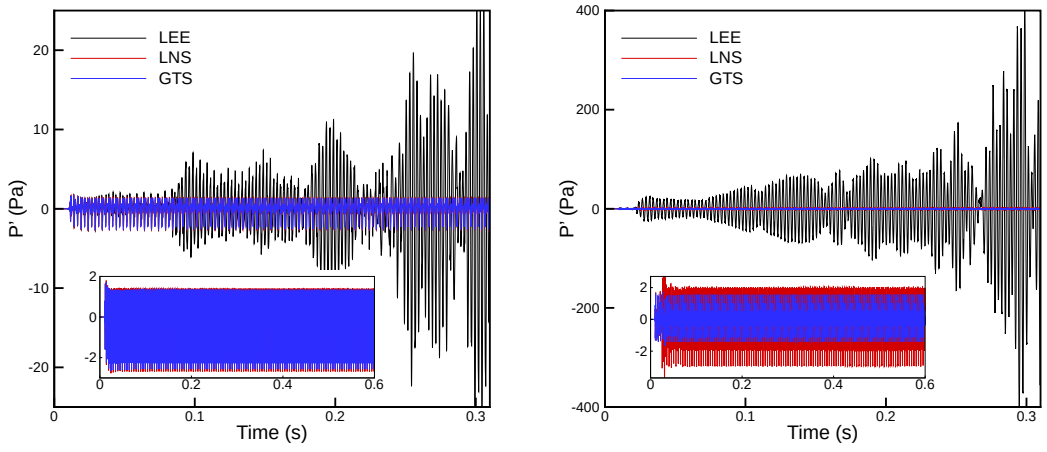

(a) Point A, (4.02, 3.51)

(b) Point B, (5.57, 1.30)

FIGURE 3.20: Time histories of perturbation pressure at monitor points.

Further, Figure 3.21 shows that the pressure field solved by LEE is thoroughly overwhelmed by the unrealistic pressure perturbations. Two sheets of vortices appear downstream the exhaust nozzles. The above one is clearly growing and spreading along the shear layer, while the below one is developing along the layer between the jets of the primary and the secondary exhausts where presents considerable density gradients. Whereas, as shown in Figure 3.22 and Figure 3.23, the LNS and GTS methods properly solve the pressure field in different manners. The simulations by LNS also demonstrate the two sheets of vortices, however, the above vortex sheet is quickly suppressed in the downstream region where presents strong turbulent viscosity, while the below vortex sheet is steadily convected away by the main stream and is maintained almost at

a steady strength. Meanwhile, the GTS method obtains almost "clean" acoustic fields where the vorticity is rarely initiated and shed by the mean flow.

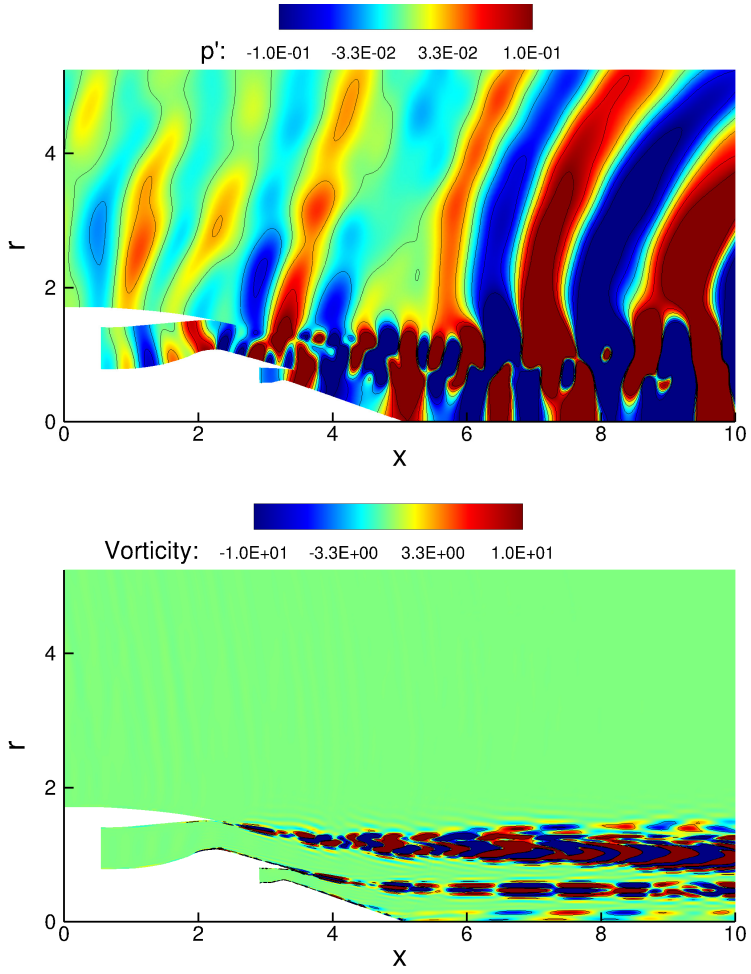

FIGURE 3.21: Instantaneous perturbation fields simulated by LEE with a multi-frequency source.

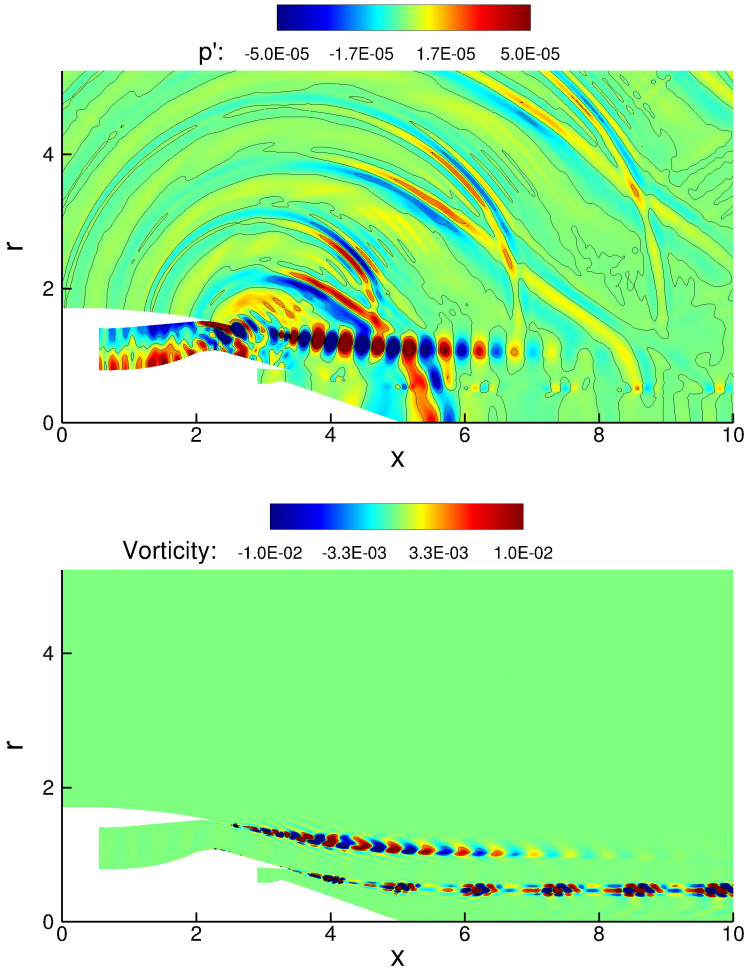

FIGURE 3.22: Instantaneous perturbation fields simulated by LNS with a multi-frequency source.

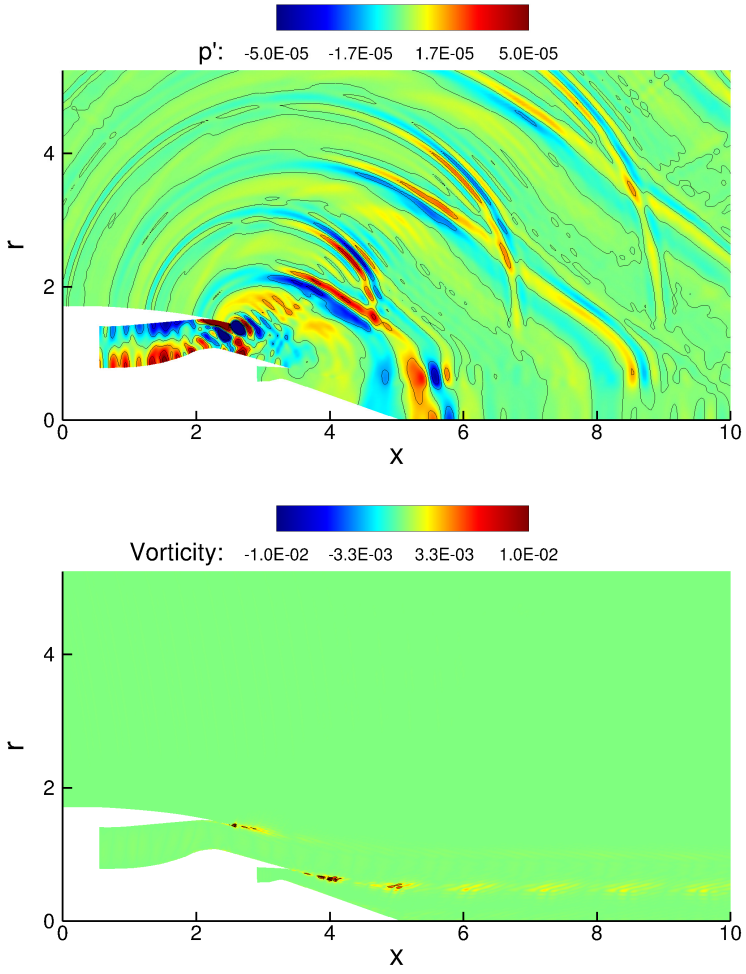

FIGURE 3.23: Instantaneous perturbation fields simulated by GTS with a multi-frequency source.

3.3.5 Vortex Shedding Induced by Sound

As is well-known, the vorticity is initiated by the interactions of sound waves with geometrical discontinuities and shear layers. It is then rolled up with a characteristic frequency. Subsequently the shed vortices are convected downstream and eventually mixed out due to viscous effects. At this point, the vortex shedding induced by sound waves is surveyed on the basis of the reasonable governing physics of the LNS method on this subject.

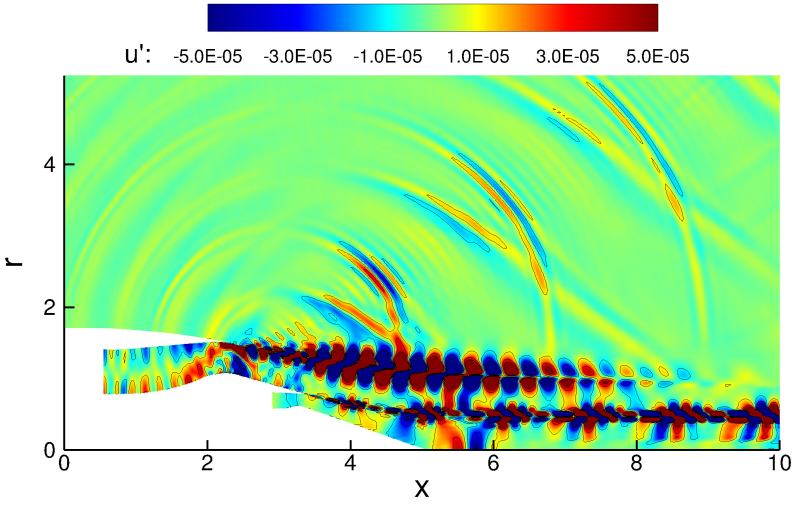

FIGURE 3.24: Instantaneous velocity perturbation simulated by LNS with a multi-frequency source.

Figure 3.24 clearly demonstrates two vortex sheets in the presence of a multi-frequency acoustic source. Here, the acoustic energy is transformed into the hydrodynamic energy of vortices from the shear layers and duct lips. To record the information of the vortices, two monitor points, namely B (5.57, 1.30) and C (8.00, 0.48), are respectively placed far downstream from the primary and secondary exhaust nozzles and located in the vortex sheets. To calculate the vortex shedding frequency, the FFT should be applied to the time history of the fluctuating velocity. Nevertheless, considering that the acoustic field is dominant here and the vorticity information may therefore be overwhelmed, the vorticity component rather than the velocity component is used with the intention of excluding the acoustic signal, as according to Helmholtzs theorem the irrotational acoustic component and the solenoidal vortical components of the velocity are independent of one another.

Figure 3.25 demonstrates the time traces of vorticity at the monitor points, where intermittent packets of fluctuations can be identified from the sustained perturbations. Furthermore, by the means of FFT, two types of bands can be found in the vorticity spectra, for instance as displayed in Figure 3.26 for point C. One owns a sharp peak associated with the vortex shedding frequency which is identical to that of the acoustic wave. The other presents a relatively broad peak, corresponding to the shear-layer frequency [210]. The broadband peak is a consequence of the convectively unstable

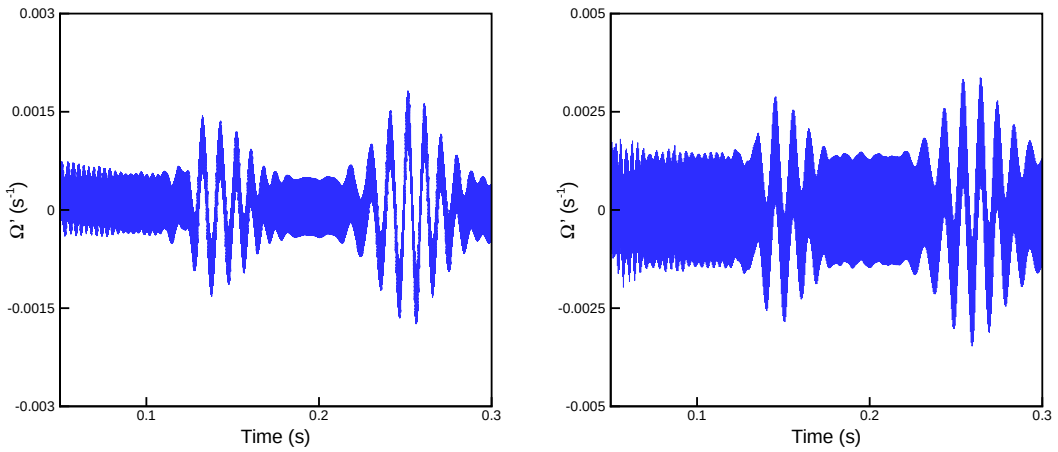

(a) Point B, (5.57, 1.30)

(b) Point C, (8.00, 0.48)

FIGURE 3.25: Time histories of fluctuating vorticity at monitor points solved by LNS at 2000 Hz.

nature of shear layer instability [210]. As demonstrated in Figure 3.26, although the sharp peak is moving with the frequency of the acoustic waves, the broadband peak stays at around 100 Hz. The invariability of the shear-layer frequency can also be validated from the vorticity spectra with the multi-frequency acoustic source. The most unstable frequency of the broadband peak scales with the surrounding velocity and with the momentum thickness of the shear layer [210]. Furthermore, the intermittency of the shear layer fluctuations is thought to be attributable to the random streamwise motion of the transition point [210]. Moreover, given the spectra with the multi-frequency source, the sharp peaks decrease in magnitude with higher acoustic frequencies. This coincides with evidence reported in the literature, namely, that this acoustic-structure interaction is diminished with increasing frequencies.

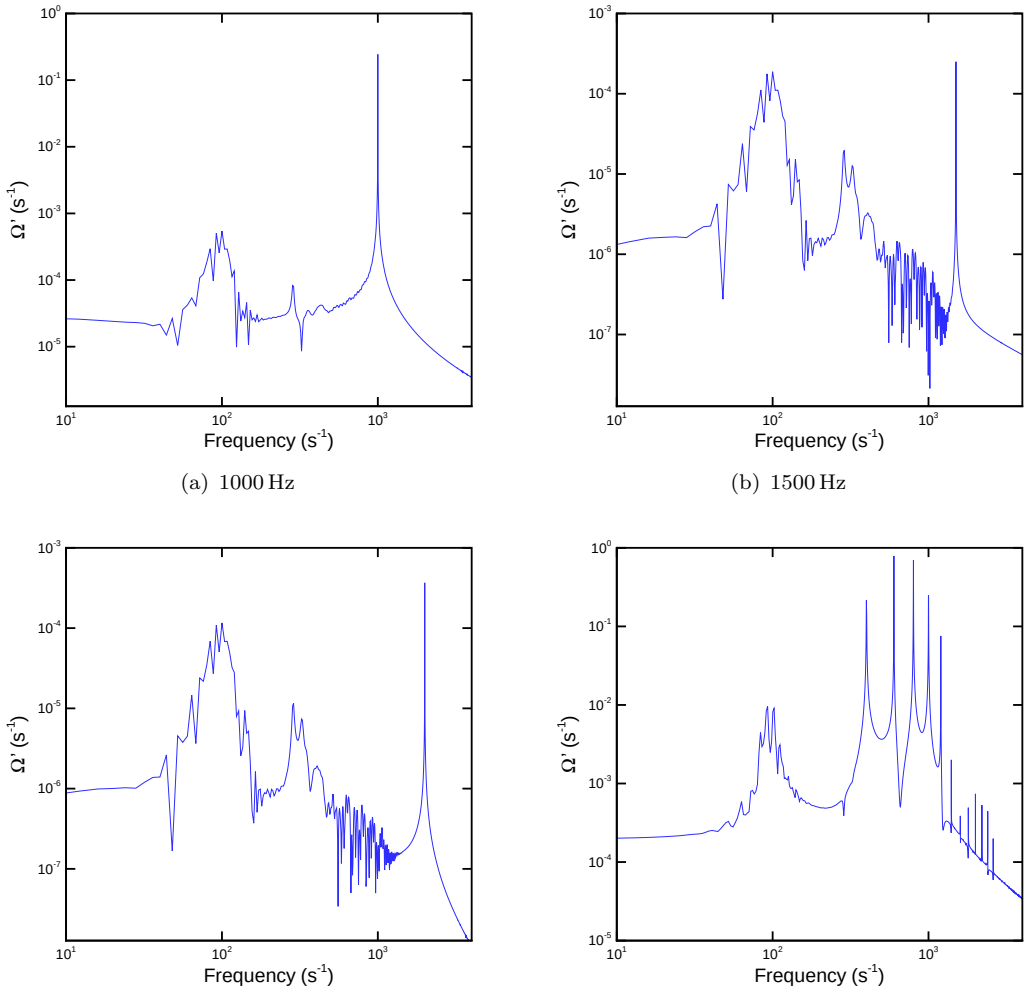

(a) 1000 Hz

(b) 1500 Hz

(c) 2000 Hz

(d) Broadband source

FIGURE 3.26: Spectra of fluctuating vorticity at point C (8.00, 0.48).

3.3.6 Effects of Perturbation Reynolds Stress

First of all, in a physical sense, the sound can be amplified or attenuated when it encounters shear layers and geometrical discontinuities. The vortex shedding process extracts energy from both the sound wave and the hydrodynamic field, while the shed vortices arouse sound. The net result depends on a balance between the global energy production and the global energy dissipation. Under this process, the LNS method introduces PRS terms to suppress the instability waves while resulting in attenuation of sound. The damping is, however, mostly case-dependent. With regard to the current jet case, the effect is assessed with the intention of comparing it with the inviscid methods rather than as an experimental methodology.

The effect is evaluated in consideration of two aspects, namely the near-field fluctuating pressure level and the far-field sound pressure level. Note that actually the near-field results include the acoustic and vorticity compositions. Figure 3.27 shows that the pressure fields solved by LEE are maintained at a reasonable state with the affection of the instability waves which result in the outstanding pressure distributions in the downstream region, and the extra pressure distributions are strengthened at the lower frequency. Meanwhile, at the lower frequency the pressure field solved by LNS, as shown in Figure 3.28(a), presents the instability waves in the vicinities of the duct lips which are either convected downstream at a steady strength or suppressed quickly. At the higher frequency as given in Figure 3.28(b), there are even no noticeable instability waves. In terms of the GTS method, as shown in Figure 3.29, "pure" acoustic fields are obtained without any outstanding pressure distributions.

3.3.6.1 Near-field Fluctuating Pressure Level

Figure 3.30 demonstrates the perturbation pressure levels at the near-field observation line and their differences. Apparently, the results obtained by LEE, LNS and GTS give disparities in the region of 0°-30° angles. In this region the differences between the results obtained by LEE and LNS are enlarged at higher frequencies as a consequence of the stronger turbulence damping, and the maximal differences represented by "LNS-LEE" are equal to about −9 dB, −18 dB and −21 dB, respectively at 1000 Hz, 1500 Hz and 2000 Hz. Corresponding to this angle range, the mean-flow field contains strong shear layers and great turbulent viscosity, whereby the perturbation field solved by LEE contains strong products of the instability waves while the perturbation field solved by LNS imposes considerable turbulent effects on the acoustic field. Consequently, significant differences appear between the pressure levels obtained by LEE and LNS. Also, the phase change of the sound waves induced by the instability waves which is found in Section 3.3.2.2 could partly contribute to the disparity. In comparison between results obtained by LEE and GTS, the maximal differences represented by "GTS-LEE" are equal to about −6 dB and −12 dB, respectively at 1500 Hz and 2000 Hz; at 1000 Hz, the differences in the range of 0°-30° angles present relatively great values equal to about −9 dB and 7 dB. The differences denoted as "GTS-LEE" are also relatively large and

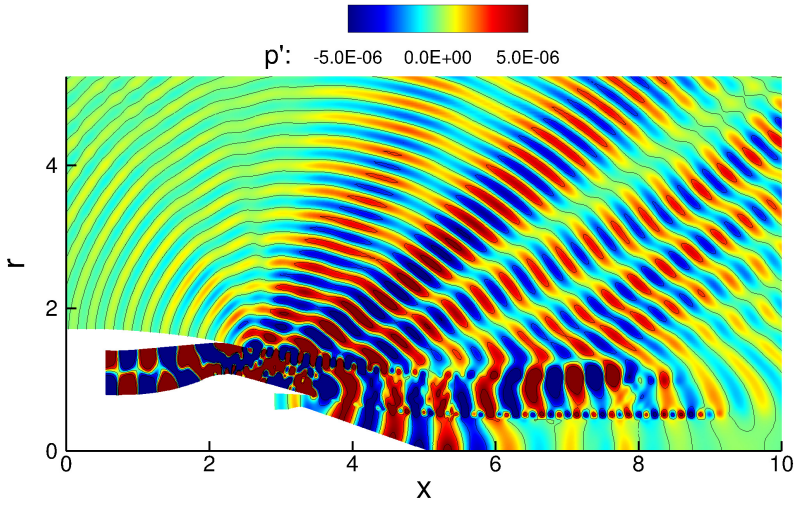

(a) 1000 Hz

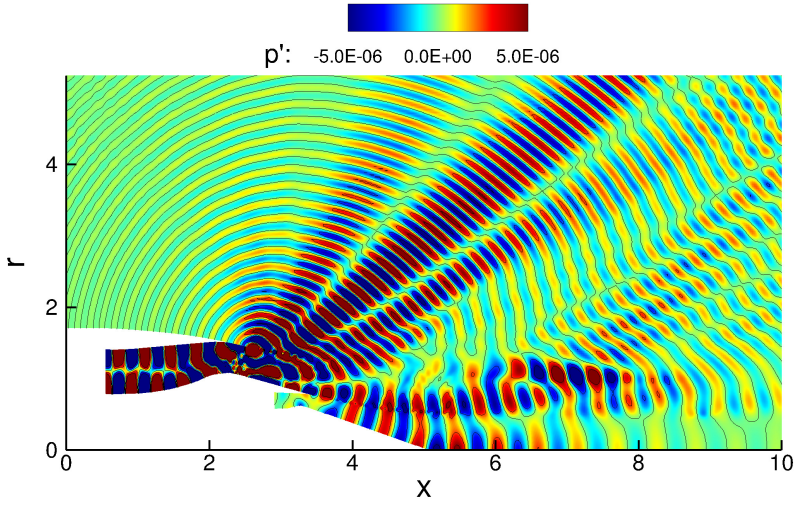

(b) 1500 Hz

FIGURE 3.27: Instantaneous pressure perturbation computed by LEE at discrete frequencies.

could be attributed to the influence of instability waves. In the range of 0°-30° angles, the GTS method do not produce instability waves while the LEE method results in considerable vorticity waves.

In the rest regions, the differences between the results obtained by LEE and LNS are small. The pressure levels solved by GTS show apparent disturbances around those of LEE, and a maximum of the differences equal to about −9 dB emerges at around 101° angle for 1000 Hz. It is also observed that the results of GTS demonstrate greater differences at the lower frequencies. This is probably due to the lack of vortex sheets in the GTS results. In contrast, both the LEE and LNS method obtain the vortex sheets which are strengthened at lower frequencies.

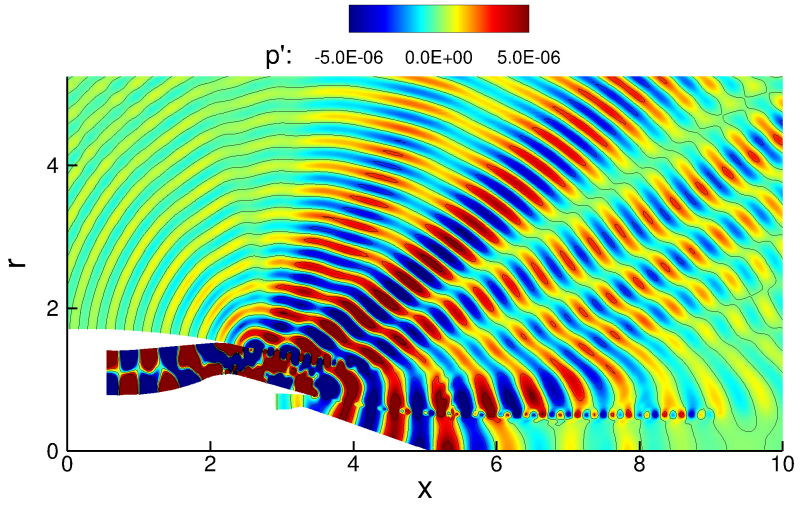

(a) 1000 Hz

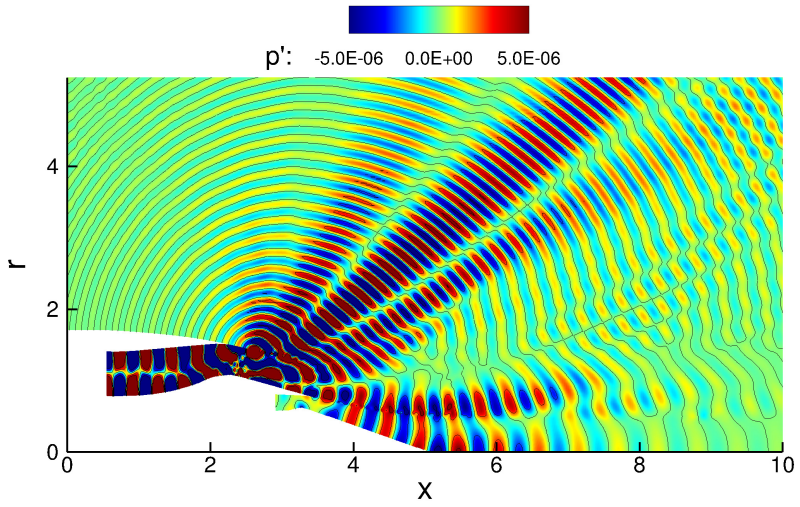

(b) 1500 Hz

FIGURE 3.28: Instantaneous pressure perturbation computed by LNS at discrete frequencies.

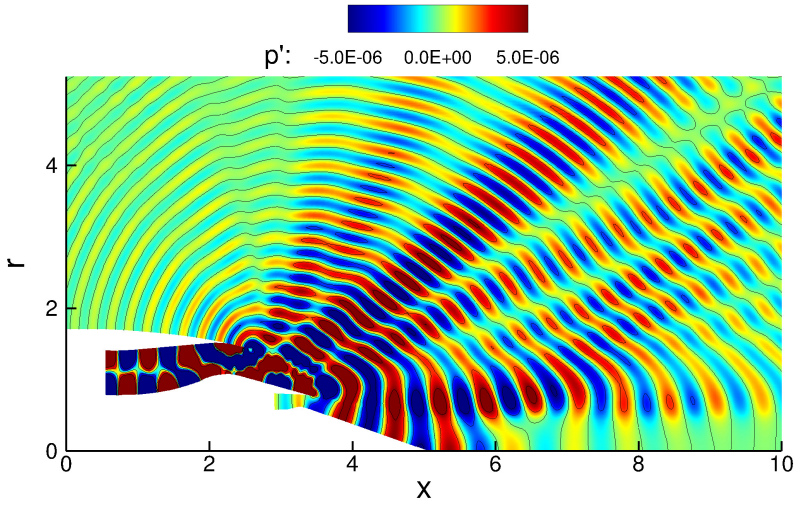

(a) 1000 Hz

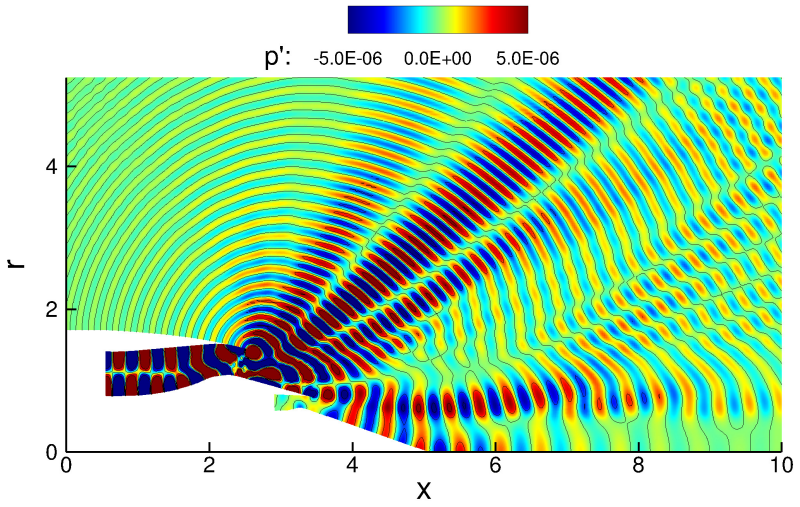

(b) 1500 Hz

FIGURE 3.29: Instantaneous pressure perturbation computed by GTS at discrete frequencies.

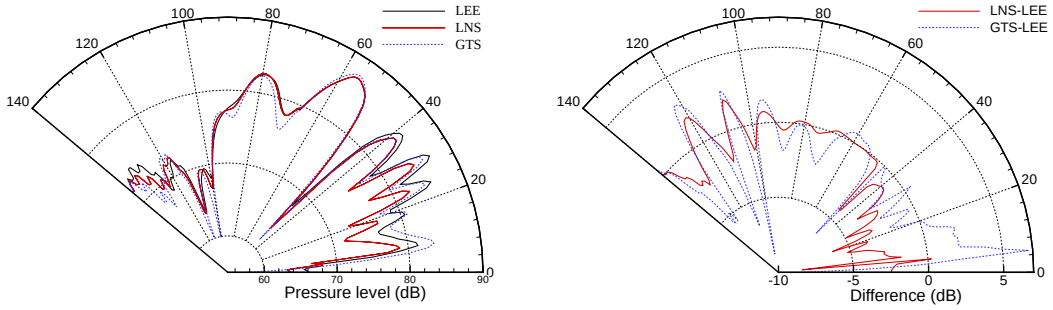

1000 Hz

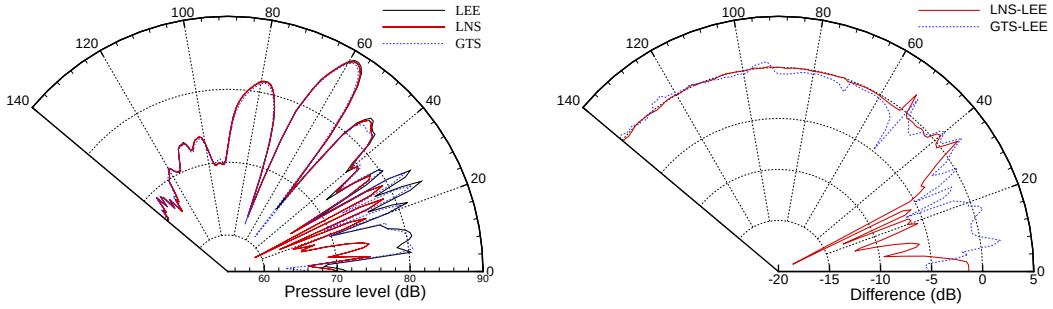

1500 Hz

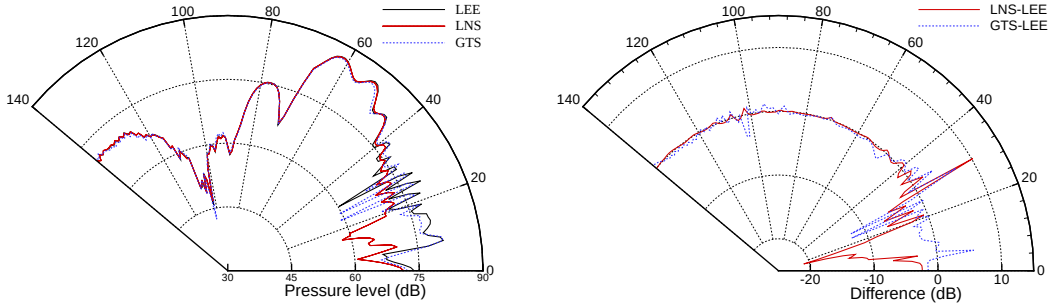

2000 Hz

FIGURE 3.30: Comparison of near-field fluctuating pressure levels and the differences.

3.3.6.2 Far-field Sound Pressure Level

As is already demonstrated, the results obtained by LEE in the jet areas are time-asymptotic and dependent on the spatial resolution. Also, the flow field in the jet areas is not uniform. In consideration of these situations, the jet areas are excluded from the FW-H integration regions. Figure 3.31 gives the far-field acoustic directivity calculated by including the jet areas into the FW-H integration. In terms of the LNS and GTS approaches, the results induced by the jet areas rarely show distinctions. Nevertheless, relatively large differences appear at 110° angle for both the LNS and GTS results, and the absolute values are about 3 dB and 8 dB for the LNS and GTS results respectively. However, such large differences emerge only at 110° angle, thus the characteristics of the far-field directivity are barely altered. In terms of the LEE method, the influence of the jet areas becomes considerable due to strong instability waves. As displayed, including the jet areas results in significantly higher levels in general in the range of 65°-80° angles, also obvious distinctions emerge in the range of 80°-120° angles. Moreover, at 110° angle a large difference comes into view as those shown in the LNS and GTS results. In conclusion, the jet area is necessarily removed from the far-field acoustic directivity calculation to obtain reasonable results for the LEE method.

Figure 3.32 shows good agreement in terms of the far-field directivity, and the consistency is improved at higher frequencies. At 2000 Hz, relative to the LEE results, the absolute differences are lesser than 2.5 dB and 1.7 dB, respectively for LNS and GTS. At 1500 Hz, the absolute differences for LNS are within 3.5 dB; for GTS, the absolute differences are lesser than 4 dB in general except for the extraordinary maximum equal to almost 10 dB at 75° angle. At 1000 Hz, the differences become more significant in an extensive range of 75°-95° angles, and the maximal absolute differences are equal to about 10 dB and 13 dB respectively for LNS and GTS. Also, it is observed that for all the frequencies the SPL differences become most serious in the range of 75°-95° angles. In this region, as already discussed in Section 3.3.2.2 the instability wave plays an important role to influence the sound propagation, while the products of instability waves obtained by the three methods show obvious distinctions. Nevertheless, it is clear that the outstanding differences of near-field pressure levels between LNS and LEE results do not lead to corresponding distinctions for the far-field SPL, and the GTS results actually present more serious differences in the far-field directivity relative to the LEE results. Notice that even if the jet areas are included in the FW-H integral, as shown in Figure 3.31, the differences between the LNS and GTS results would rarely be changed. It is therefore concluded that the PRS terms barely impact the far-field sound directivity, although the perturbations in the jets are significantly modulated by the turbulent effects.

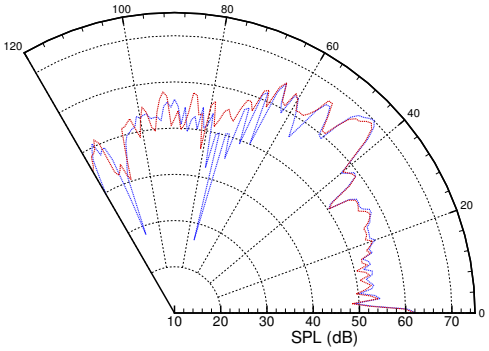

(a) LEE

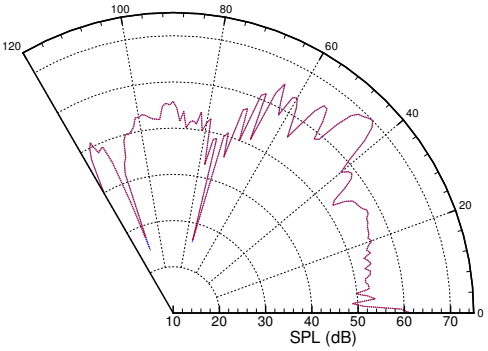

(b) LNS

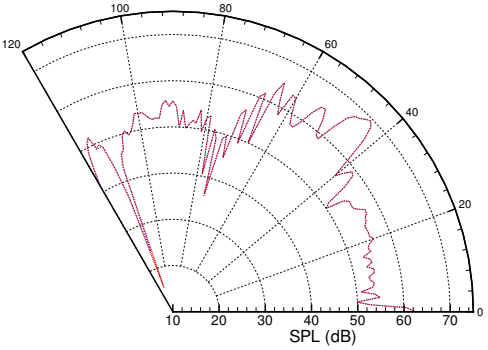

(c) GTS

FIGURE 3.31: Comparison of far-field directivity at 1500 Hz. (- - -) including the area of jets in the FW-H integration regions ; (- - -) not including this area.

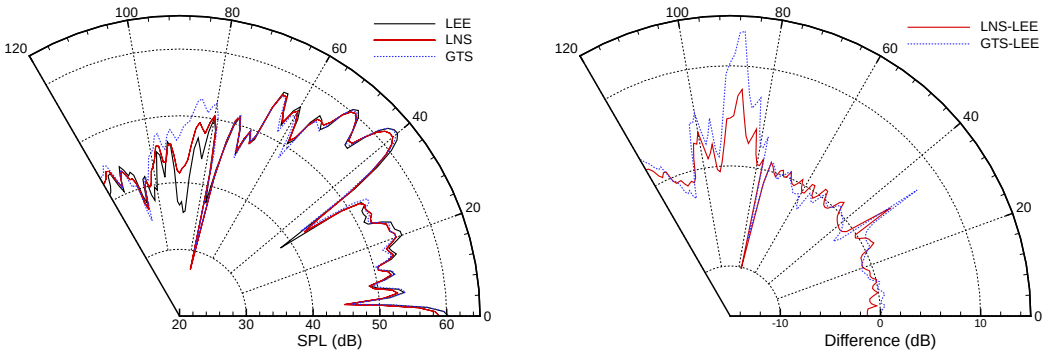

1000 Hz

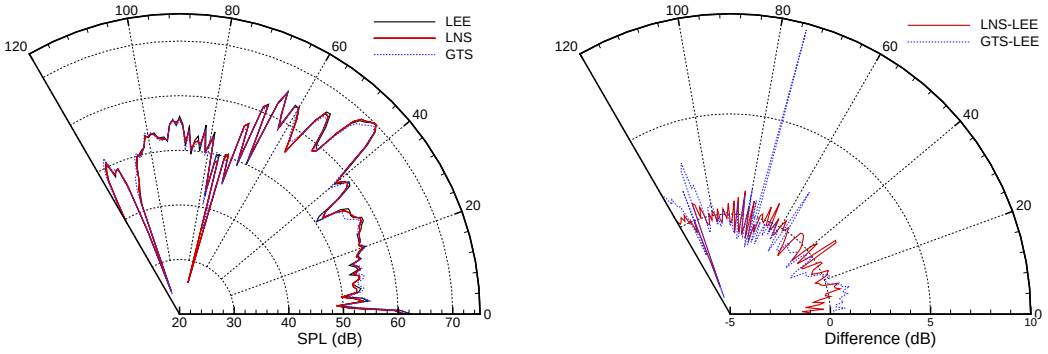

1500 Hz

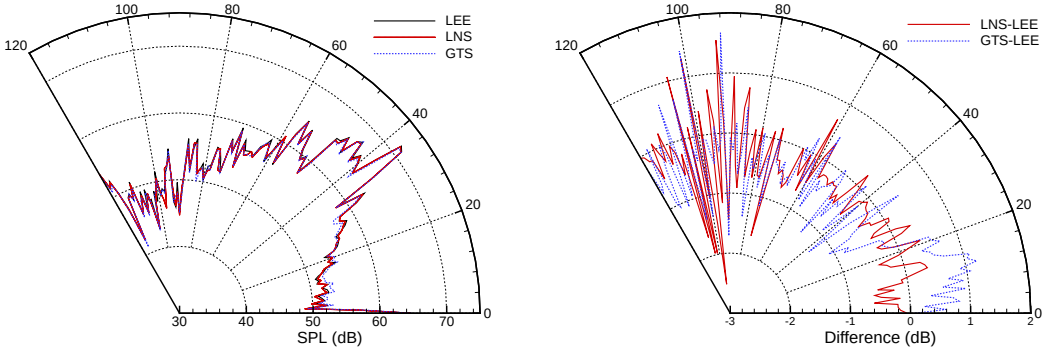

2000 Hz

FIGURE 3.32: Comparison of far-field sound pressure levels and the differences.

3.4 Summary

In this chapter, linear stability analysis has been performed with regard to turbulent shear flows. The analysis demonstrates that the growth rate of instabilities is dramatically reduced due to the low effective Reynolds number. Therefore the proposed LNS approach can stably simulate the sound propagation in turbulent shear flows by incorporating a proper turbulent model.

Furthermore, the grid convergence study is carried out with regard to the sound propagation problem. The conclusion shows that the grid with $PPW = 10$ can give a satisfactory simulation accuracy and certainty, while the grid with $PPW = 7$ can also give the error band to an acceptable degree at most of the domain of interest. Moreover, the grid convergence study shows the numerical accuracy obviously degrades when the angle of the sound radiation from the duct is beyond 90°, especially for the LEE method. This could be related to another conclusion, namely the LEE results are greatly dependent on the spatial resolution especially in the mixing layer, and the fine gird gives stronger products of the instability waves in comparison to the coarser girds. In sum, the simulations based on the LEE method show the temporal instability and the grid-dependent solutions when an unstable system takes place.

This method has subsequently been implemented against the well-known Munt solutions. An algebraic eddy viscosity model is employed to validate the stability of the proposed LNS method, and stable simulations are obtained. Considering the far-field sound directivity, the results predicted by the time-domain LNS and GTS methods, as well as by the frequency-domain LEE and GTS methods are compared with the Munt solutions. The LNS method shows better agreements with the analytical solutions than the GTS method especially in terms of the main peak magnitudes. All the numerical solutions have reasonable agreements with the Munt solutions.

Further, the problem of a realistic turbofan aft noise radiation has been studied. Firstly, the LNS method presents stable simulations while obtains the instability waves at a relatively steady status, whilst the products of the instability waves are over-predicted by the LEE method and are excluded from the the GTS method. Moreover, benefiting from this feature of the LNS approach, the vortex shedding induced due to the sound waves at sharp edges can be investigated in such a linear manner. Subsequently, the vortex shedding frequencies in line with the sound frequencies have been found, as well as the shear layer frequency has been identified. Last but certainly not least, the effect of PRS terms on sound propagation has been evaluated. At first, the near-field pressure solved by LNS is significantly dampened in the shear layer due to strong turbulence viscosity, and the differences between the results obtained by LNS and LEE are enlarged when the frequency increases therefore this implies stronger damping due to turbulence at higher frequencies. Also, in the mixing layer region the GTS results show relatively obvious distinctions in comparison with the LEE results. Nevertheless, at the rest regions, the differences among the near-field pressure level results obtained by the three methods are moderate in general, but the consistency between the GTS

and LEE results obviously becomes worse at lower frequencies. Eventually, the results of the far-field directivity demonstrate good agreement, and the consistency is improved at higher frequencies probably due to the weaker products of the instability waves for LNS and LEE. In conclusion, the differences in the near-field pressure levels do not necessarily lead to the corresponding alterations in the far-field acoustic distributions. More precisely, when the frequency is higher, the turbulent damping in the mixing layer becomes stronger for LNS, and this therefore results in the increasing differences of the near-field pressure levels in this region; whereas, the products of the instability waves become weaker at higher frequency for LNS and LEE, and thus the far-field acoustic distributions predicted by the three method give better consistency with each other.

Chapter 4

Attenuation of Sound by Turbulence in Duct

As reviewed, sound waves can be attenuated due to scattering and damping by turbulence. The dissipation of sound can be significantly enhanced in the presence of wall boundary layers. In laminar internal flows, the damping is mainly attributed to viscothermal effects and mean-flow convection. In turbulent flows, the dissipation of sound is induced by turbulent mixing if the ABL is thicker than the viscous sublayer [154]. The damping by turbulence becomes considerable in a narrow duct at sufficiently low frequencies (namely small Helmholtz numbers). In such a case, the ABL is largely immersed into turbulent flows and it accounts for a considerable portion of the duct cross-section.

In this chapter, the LNS method is employed to evaluate the attenuation of sound in a fully developed turbulent pipe flow. Such cases have already been carried out using various turbulent models and solution methods [12, 143, 149, 154]. The current method is proposed due to several advantages. For instance, it can easily take account of complex geometries and mean flow profiles. Furthermore, multi-frequency signals and broadband sources can be directly simulated by the proposed method. After a brief introduction to the mechanisms of acoustic damping in a duct, the LNS method is firstly verified with a plane wave problem, then the attenuation of sound at high-order spinning modes is studied.

4.1 Mechanisms of Acoustic Damping in Duct

The sound waves can be attenuated by various mechanisms as listed below. Theoretically, the LNS method can simulate all the effects although the thermal effect is currently not involved. The turbulent absorption due to the acoustic-vorticity interaction has been reviewed in Section 1.4, the other effects will be briefly introduced in this section.

- Viscous and thermal effects;
- Mean flow convection;

- Mean flow refraction;
- Turbulent absorption (vorticity effect);
- Moderate Compressibility Effect.

4.1.1 Viscothermal Effects

Considering the sound propagation in a duct containing quiescent fluid, the viscothermal effect due to the ABL is a main attribution to the attenuation of sound. The acoustic boundary layer contains a viscous layer and a thermal layer, in which, respectively, the viscous and the thermal effect are important.

As shown in Equation 2.29, the molecular diffusion is related to two parts of the perturbation velocity, namely the irrotational components $\partial\tilde{u}_i/\partial x_i$ and the solenoidal components $\partial\tilde{u}_i/\partial x_j$. The former results in considerable acoustic damping only at high frequencies or for long distance propagation [211]. The latter is negligible in free space propagation within a uniform flow, however, becomes significant in the wall boundary layer. Therefore, the perturbation vorticity is the main cause for the viscous loss of the sound wave propagating in duct.

In air the thickness of the viscous and the thermal boundary layers is close [212], thus the acoustic boundary layer is generally defined as shown in Equation 2.47. The molecular and the thermal diffusions of the sound wave propagating in the boundary layer are also related to the ratio between the ABL thickness and the duct radius. This ratio indicates the proportion of the energy distributed in the ABL compared to the total amount of energy in the pipe cross-section.

4.1.2 Mean Flow Convection and Refraction Effects

In the perturbation equations 2.27, the terms $\bar{u}_i^\rho\partial/\partial x_i$ describe the convection effect, and the terms $\tilde{u}_j\partial\bar{u}_i^\rho/\partial x_j$ give the refraction effect. Some simplified models, such as the GTS method, discard the refraction terms using an assumption of uniform flows, therefore only the convection effects can be considered. Based on such simplification, the plane wave propagating in an inviscid and adiabatic fluid can be described by [212]

$$K_\pm(M) = \frac{k_\pm}{k_0} = \frac{\pm 1}{1 \pm M}, \tag{4.1}$$

where $K_\pm$ is the dimensionless wavenumber. Equation 4.1 indicates that the convection effect increases the phase speed of the downstream propagating wave, while decreases the phase speed of the upstream propagating wave. Taking bulk viscosity into account, $K_\pm$ can be given as [212]

$$K_\pm(sh, M) = \frac{\pm K_0}{1 \pm M}, \tag{4.2}$$

where K_0 is the dimensionless wavenumber in quiescent viscous fluid and sh is the shear wavenumber. Equation 4.2 indicates that, in comparison with the upstream propagating wave, the downstream wave is dissipated to a lower degree.

The refraction effect, however, influences the sound attenuation in an opposite way. In a realistic pipe flow, the mean flow demonstrates a strong shear near the wall where the viscothermal effects are important, and the resulting modification of the phase velocity of the sound wave is non-uniform. Therefore when the sound waves propagate through wall boundary layer, the downstream waves would be refracted toward the wall while the upstream waves would be refracted towards the pipe centre. As a result, compared to the upstream waves, more acoustic energy of the downstream waves would be captured into the boundary layer where the viscothermal effects are significant, thus the downstream waves would suffer more damping.

In sum, the convection effect tends to make the attenuation coefficients smaller and bigger than those in a quiescent fluid for the downstream and upstream waves, respectively; while the refraction effect results in the opposite outcomes. At small Helmholtz numbers, the convection effect dominates, whereas when the Helmholtz numbers is lager than a critical number the refraction effect overwhelms the convection effect.

4.1.3 Moderate Compressibility Effect

When the flow velocity becomes comparable to the speed of sound, typically reaching 0.3 Mach number and above, the compressibility effect becomes more prominent. Firstly, the sound speed is in relation to the fluid compressibility. Furthermore, when the compressibility effect becomes considerable the distribution of the mean-flow velocity along the streamwise direction could show significant non-uniformity, in such a case the terms $\partial \bar{u}_i^{\rho}/\partial x_i$ give considerable impact on sound propagation.

4.2 Problem Description

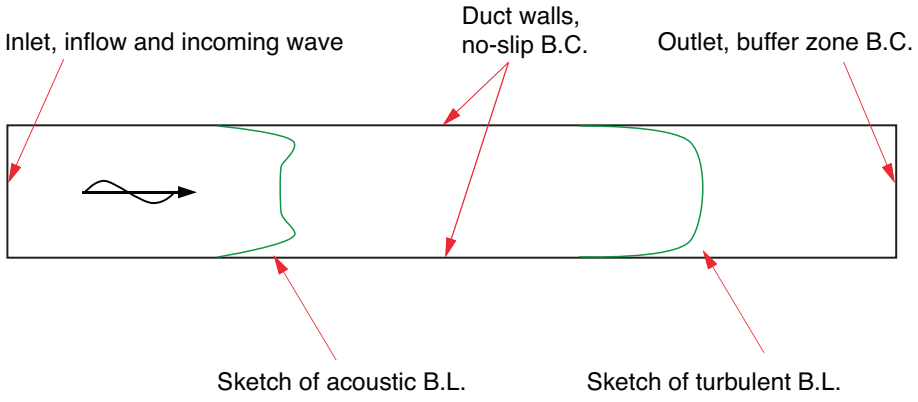

FIGURE 4.1: Schematic of the pipe system.

Figure 4.1 shows typical profile of the ABL which demonstrates significant velocity gradients near the walls. The turbulent absorption effect on sound becomes considerable when there is a sufficiently small Helmholtz number by which the ABL overwhelms the viscous sublayer of the turbulent boundary layer. Table 4.1 summaries the main

parameters used in the literature. The settings with $f = 250\,\text{Hz}$ used by Allm and Åbom [157] are adopted in the plane wave problem, as well as used for the study of the influence of computational setup. The corresponding Helmholtz number (kR) and Stokes number ($R\sqrt{\omega/\nu}$) are 0.080 and 179, respectively. The Reynolds number ranges from 7700 to 172000 based on the pipe diameter. In terms of the high-order mode problem, the Helmholtz number is raised to 7.2076 with diameter 0.75 m and frequency 1050 Hz which will be discussed in Section 4.5.1.

	Diameter, m	Frequency, Hz	Helmholtz no.	Mach no.
Ref. [154]	0.020	630	0.115	$0.01 - 0.33$
Ref. [154]	0.020	3350	0.614	$0.01 - 0.30$
Ref. [156]	0.030	88	0.024	$0.018 - 0.10$
Ref. [157]	0.035	100	0.032	$0.01 - 0.22$
Ref. [157]	0.035	250	0.080	$0.01 - 0.22$

TABLE 4.1: Main settings for measurements of the acoustic damping in the pipe flows.

Considering the plane wave problem, the acoustic damping is evaluated using the non-dimensional attenuation coefficients against the non-dimensional thickness of the ABL, namely δ_A^+. In terms of the high-order mode problem, to compare the attenuation of sound at various modes the dimensional attenuation is used, namely ΔSPL which indicates how much SPL in dB is reduced in one meter. δ_A^+ is calculated by Equation 2.50, and the wall-friction velocity is obtained from mean flow simulations and calculated by Equation 2.49. Then the attenuation coefficient a is computed as follows. Firstly, the propagating waves are assumed in the form

$$p = \hat{p} e^{-ax} e^{i(\omega t - kx)}. \tag{4.3}$$

The amplitude of p is

$$|p| = |\hat{p}|\, e^{-ax}, \tag{4.4}$$

which gives

$$ln(|p|) = -ax + ln(|\hat{p}|). \tag{4.5}$$

Therefore the procedure of obtaining a is to

1. get amplitudes of p from perturbation simulations, where the root mean square (RMS) pressure is computed over a period of the sound wave;

2. plot $ln(|p|)$ against x, and obtain the slope of the curve by linear curve-fitting, i.e. $y = ax + b$;

3. obtain $a = -a$.

The resulting a is then normalised by the attenuation coefficient in a quiescent fluid, namely a_0, which can be computed by Kirchhoff theory following the formulation [151]

$$a_0 = \frac{\omega}{c}\left[\frac{1}{\sqrt{2}S}\left(1+\frac{\gamma-1}{\xi}\right)+\frac{1}{S^2}\left(1+\frac{\gamma-1}{\xi}-\frac{\gamma}{2}\frac{\gamma-1}{\xi^2}\right)\right], \tag{4.6}$$

where S is the Stokes number, and ξ is the Prandtl number. This formulation includes the effect of viscosity as well as heat conduction, the latter is not considered in the current simulations. In this study a_0 is obtained by a perturbation simulation using quiescent fluid.

4.3 Influence of Computational Setup

According to the literature review, neither the acoustic dissipation nor the ABL has been studied using a time-domain linearised governing equations method, therefore it is necessary to carry out studies to find out the suitable computational setups for this problem. The plane wave problem with the settings as described in last section is used to perform this study. For the plane wave, namely the $(0,0)$ mode wave, the amplitude of the acoustic pressure is uniformly distributed over the pipe cross section, therefore the computational domain is simplified as a two-dimensional duct.

The CAA simulation is based on the given flow field in which the wall shear stress and turbulent viscosity along with the pressure, density and velocity fields are desired for the CAA simulation. To obtain the base flow, the shear-stress transport (SST) $\kappa-\omega$ model is employed as the viscosity-affected region needs to be resolved. The SST $\kappa-\omega$ [213] is a two-equation eddy viscosity model, which modifies the turbulent viscosity formulation to include the transport effects of the principal turbulent shear stress. The SST model uses a $\kappa-\omega$ formulation in the inner region of the boundary layer and switches to a $\kappa-\varepsilon$ model in the outer part of the boundary layer, therefore it can have the advantage over the two standard models.

The structure mesh is performed over the two-dimensional domain. As the viscous sublayer is modelled, the wall-adjacent cells must have a wall distance on the order of $y^+ = 1$. The flow is simulated with a pressure-based steady solver using Fluent. A uniform inflow velocity is set at the pipe inlet using the velocity inlet boundary condition. The turbulence intensity and length scale are used to specify the turbulence input parameters. For a fully developed pipe flow, they are estimated from the following formula

$$I = 0.16Re^{-1/8}, \qquad l = 0.07D. \tag{4.7}$$

The pipe outlet is set as the outflow boundary conditions. The flow variables are solved with second-order schemes. Once the flow is solved, the mean field value is interpolated from the CFD grids to the CAA grids.

As shown in Figure 4.2, the wave propagation region is along the axis from $x = 0$ to $x = 5.1$ which is equal to almost 3λ and 3.75λ, respectively for $Ma = 0.22$ and 0. In

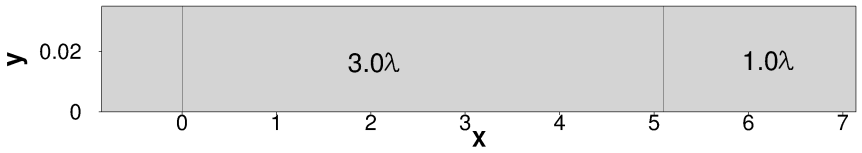

FIGURE 4.2: Sketch of the CAA simulation domain. The parameters are calculated when $Ma = 0.22$.

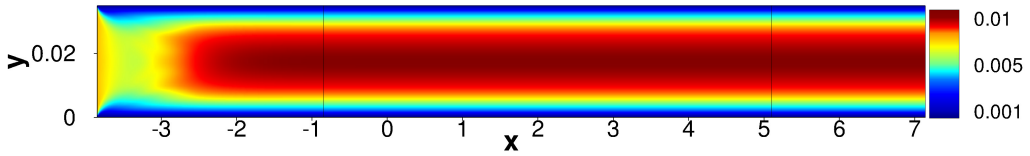

FIGURE 4.3: Distribution of the turbulent viscosity in the CFD simulation domain when $Ma = 0.22$.

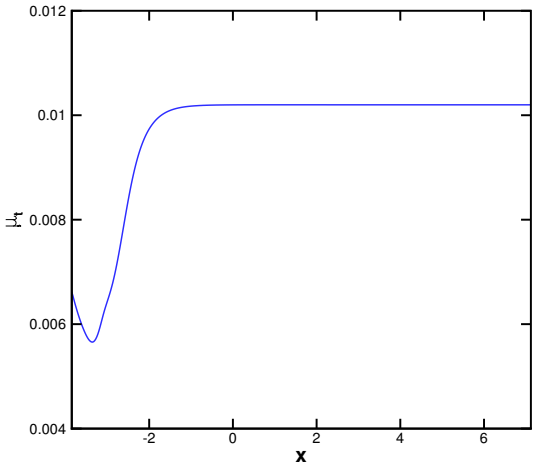

FIGURE 4.4: Turbulent viscosity along the x-axis of the CFD simulation domain when $Ma = 0.22$.

this domain the sound wave behaviour is approximated to that in a pipe with infinite length. The input zone has the length identical to that of the adjacent grid block in the main region, therefore the grid spacing for the two blocks are also identical to ensure a good grid transition for the computational sake. The buffer zone is employed at the end of pipe and has stretched grid to enforce the damping. The length of the buffer zone shown in Figure 4.2 is 1.0λ, which however will be investigated in next sections. The CFD simulation region is shown in Figure 4.3, which is extended upstream to $x = -3.85$ to guarantee that the turbulent flows used for the CAA simulations are fully developed. As shown in Figure 4.3, the turbulent viscosity reaches a steady distribution in the CAA simulation range. Also as shown in Figure 4.4, the turbulent viscosity along the x-axis is changing until almost at $x = -1$ and finally reaches the steady value of $\mu_t \cong 0.0102$.

Next, the effects of the spatial resolution on the flow fields and the final acoustic fields are investigated by carrying out the grid convergence study. In addition, the accuracy of the acoustic field results is influenced by boundary conditions and the resolving degrees

to the wall boundary layers, which is also investigated in this section. Furthermore, some primary acoustic results obtained with different models for the perturbation simulation is demonstrated in Section 4.4.3.

4.3.1 Grid Convergence Study of Mean Flow Simulation

The flow field at $Ma = 0.22$ is used to carry out the grid convergence study, as the demands on the grid are most rigorous at this condition especially considering the requirement of y^+ on the order of 1. The grid generation for other flow conditions can then refer to the conclusions of grid convergence study at this condition. As shown in Figure 4.5, the y^+ value meets the requirement to resolve the viscosity-affected layer and reaches a steady state over the wall regions of interest, and the maximum is equal to 1.3. Subsequently, the grid along radial direction is refined in the region away from the first layer. In the axial direction, as the flow field is required for CAA simulations, the grid spacing along the x-axis is constant to ensure a good streamwise resolution. The grid is refined with a ratio of $\sqrt{2}$ in the axial and radial directions. As the height of the first mesh cell off the wall is unchanged with refined grids, the corresponding maximal aspect ratio is reduced. The parameters of three sets of grids are demonstrated in Table 4.2.

Case no.	Grid	Aspect ratio maximum	Length ratio maximum
1	170×2190	700	1.07
2	120×1546	1000	1.11
3	85×1091	1400	1.17

TABLE 4.2: Grid parameters for the grid convergence study of CFD simulations.

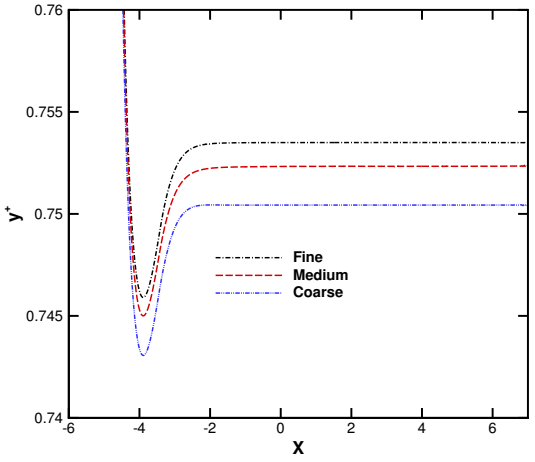

FIGURE 4.5: y^+ value through a spline processing along the walls of the CFD simulation domain.

The wall shear stress important to the final acoustic results is used to calculate the GCI. An average is calculated by the values from $x = 0$ to 6, where the wall shear stress has steady magnitudes, as shown in Figure 4.6. Table 4.3 summarises the order of

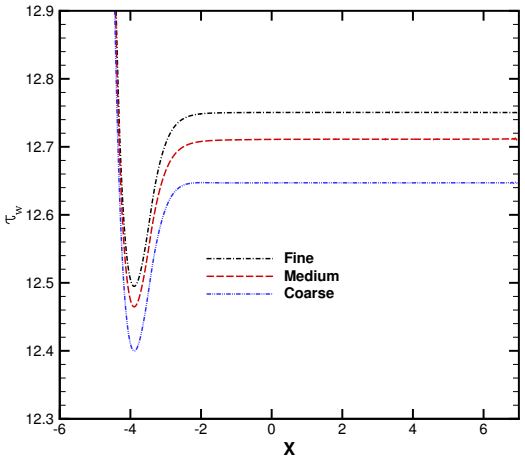

FIGURE 4.6: Wall shear stress value through a spline processing along the walls of the CFD simulation domain.

accuracy for the mean wall shear stress from the simulation results on the three grids. All the results are obtained once a statistically steady flow was observed. The theoretical order of convergence is $o = \sqrt{2}$, while the calculated one is $o = 1.375$. This different could be induced due to turbulence modelling, non-linearities in the solution, grid stretching and so on. The convergence ratio is $R = 0.62$, which indicates a monotonic convergence. A reduction of GCI value for the successive grid refinement is observed. $GCI_{21} < GCI_{32}$ indicates that the grid dependency of the numerical simulation is reduced. Also, the ratio calculating from Equation 2.79 is equal to 1.003 which is approximately 1, thus the solutions are well within the asymptotic range of convergence. We can conclude from the study that the wall shear stress is estimated to be $\tau_w = 12.815$ with an error band of 0.63%. As the solution obtained from the medium grid has a relatively low extrapolated relative error of 0.81%, and the GCI_{32} indicates a relatively low error band of 1.03%, the grid no. 2 is actually employed to solve the flow fields at all flow conditions.

o	R	A	$\tau_{w(ext)}$, $\mathrm{kg \cdot m^{-1} \cdot s^{-2}}$	e^1_{ext}	e^2_{ext}	GCI_{32}	GCI_{21}
1.375	0.62	1.003	12.815	0.51%	0.81%	1.03%	0.63%

TABLE 4.3: Calculations of discretization error for the wall shear stress.

4.3.2 Influence of Computational Setting for Perturbation Simulation

The sound propagation is simulated on the basis of corresponding mean flows. So far the quasi-steady turbulent models have been employed to solve the time-dependent perturbation field. The RMS pressure field is desired and computed over the last period of the sound wave. The solution accuracy is influenced by the spatial resolution, temporal resolution and boundary conditions and so on. As the ABL is resolved spatially, the time step has to be small enough to maintain a reasonable CFL number, whereby the

corresponding temporal resolution will be sufficient to resolve the sound waves. Eventually, the accuracy of the resulting RMS pressure is mainly influenced by the following factors.

1. Streamwise resolution. Considering that the thickness of the ABL is generally less than the wavelength of sound wave by orders, resolving the ABL in the near-wall region will usually result in an extremely fine resolution in the radial direction of the narrow pipe. Therefore the spatial resolution is investigated here mainly focusing on the axial direction.

2. Resolution in the ABL. The interaction of sound waves in the ABL with the molecular viscosity and turbulence plays an dominant role in the overall damping of sound in the pipe flow. The effect of the interaction varies depending on the distribution of turbulence boundary layers which is determined by the flow conditions.

3. Buffer zones. Although the buffer zone technique is used to emulate the free acoustic radiation, irregular acoustic distributions are produced due to buffer zones and can affect a limited computational region. To obtain reasonable results over a specified computational domain, the influence due to buffer zone should be taken care of.

Additionally, the effect of the ABL is evaluated when this layer is thinner than the viscous sublayer. Various resolving degrees to the wall boundary layers are compared in terms of the resulting acoustic field.

4.3.2.1 Streamwise resolution

The flow condition when $Ma = 0$ is employed to study the effect of streamwise resolutions. Initially, the $PPW = 7$ at the stationary condition is used according to the general CAA simulation guide [182] and the study in Section 3.3.2. The grid is then refined in the x-axis by a factor of $\sqrt{2}$. The ABL is resolved with 15 points. The buffer zone has a width of about 1.5λ. The running time is set as 5 times periods of the sound wave to ensure the simulation reaches a relatively stable state. Table 4.4 summarises the computational settings for investigating the effect of streamwise resolutions.

Case no.	Mach no.	Streamwise PPW	Resolution of ABL	Buffer zone width
1.1	0	7	15	1.5λ
1.2	0	10	15	1.5λ
1.3	0	15	15	1.5λ
1.4	0	20	15	1.5λ
1.5	0	30	15	1.5λ

TABLE 4.4: Computational settings for the study of the effect of streamwise resolutions.

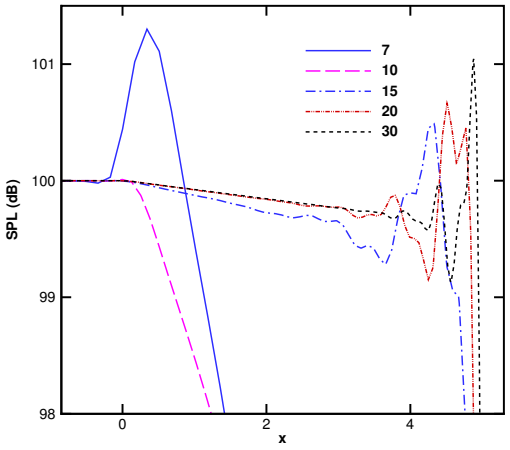

(a) SPL

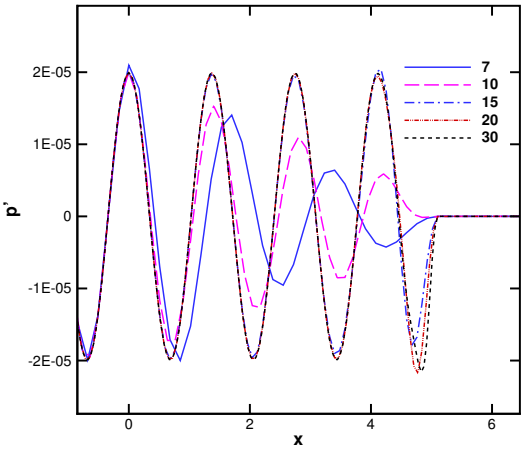

(b) Pressure

FIGURE 4.7: SPL and instantaneous pressure distributions along the x-axis obtained with various streamwise resolutions.

Figure 4.7 gives the SPL and instantaneous pressure distributions along the x-axis obtained with various streamwise resolutions. We can observe significant dissipations when $PPW = 7$ and 10. Also, obvious dispersion errors increasing downstream can be found in the instantaneous pressure distribution for $PPW = 7$ and 10. Additionally, we can observe that the regions influenced by the buffer zone is narrowed by increasing streamwise resolutions.

The effect of streamwise resolutions is evaluated by a grid convergence analysis for the $PPW = 15$, 20 and 30. The target variable is ΔSPL which is calculated using the values from $x = 0$ to $x = 2.0$, where the magnitudes of SPL are relatively stable. Table 4.5 summarises the order of accuracy for ΔSPL and SPL from the simulation results on the finest three grids. The calculated orders of convergence are $o = 7.67$. The convergence ratio is $R = 0.07$ which indicates a monotonic convergence. The reduction from GCI_{32} to GCI_{21} are relatively high, which implies that the grid independent solutions are nearly

achieved. Furthermore, the ratios calculating from Equation 2.79 are equal to 0.958 which is approximately 1, thus the solutions are well within the asymptotic range of convergence. The solution obtained from the medium grid has an extrapolated relative error of 4.76%, and the GCI_{32} indicates an error band of 5.68% for the medium grid. Also notice that the discretization error here is calculated via the SPL difference. In terms of the directly solved variable, namely the SPL, the extrapolated relative error of 0.00549% and the GCI_{32} of 0.00686% are both relatively low. Considering for the acoustic damping calculations, the medium grid gives a reasonable level of discretization error at an acceptable computational cost.

	o	R	A	$()_{ext}$, dB	e^1_{ext}	e^2_{ext}	GCI_{32}	GCI_{21}
ΔSPL	7.67	0.07	0.958	0.077	0.33%	4.76%	5.68%	0.42%
SPL	7.67	0.07	1.00005	99.885	0.00039%	0.00549%	0.00686%	0.00048%

TABLE 4.5: Calculations of discretization error for ΔSPL and SPL obtained with various streamwise resolutions.

4.3.2.2 Resolution in the acoustic boundary layer

Two flow conditions, namely $Ma = 0$ and $Ma = 0.22$, are used to validate the resolution in the ABL. When $Ma = 0$, the acoustic damping is weak and induced only by the molecular viscosity. When $Ma = 0.22$, the acoustic damping will be strongly influenced by the wall boundary layer. The initial resolution is set with 10 points in the ABL, then mesh under the ABL is refined by a factor of $\sqrt{2}$. The streamwise PPW is greater than 20. The buffer zone has a width of 2.14 m. The running time is also set as 5 times periods. Table 4.6 summarises the corresponding computational settings. Notice that the ABL is equally divided by points, thus the nearest wall distances are reduced with increasing resolutions. As a result, the effects of resolutions in the ABL here actually also includes the effect induced by different heights of wall-adjacent cells.

Case no.	Mach no.	Streamwise PPW	Resolution of ABL	Δs
2.1	0 and 0.22	> 20	10	1.5×10^{-5}
2.2	0 and 0.22	> 20	15	1.0×10^{-5}
1.4	0 and 0.22	> 20	20	7.0×10^{-6}

TABLE 4.6: Computational settings for the study of the effect of resolutions in the ABL.

Figure 4.8 and Figure 4.9 show the SPL and instantaneous pressure distributions along the x-axis obtained with various resolutions in the ABL, when $Ma = 0$ and 0.22, respectively. In the stable ranges of SPL distributions, the differences among the results obtained by various resolutions in the ABL are quite small, although enlarged a little when $Ma = 0.22$. Furthermore, Figure 4.10 demonstrates the instantaneous velocity profiles at cross section $x = 2$. The profiles of ABLs resolved with the three resolutions coincides well.

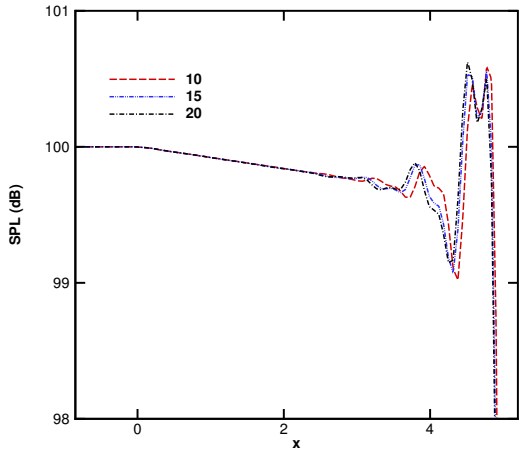

(a) SPL

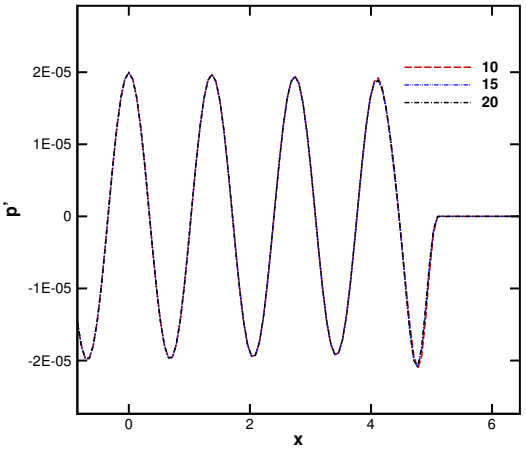

(b) Pressure

FIGURE 4.8: SPL and instantaneous pressure distributions along the x-axis obtained with different resolutions in the ABL when $Ma = 0$.

The grid convergence analysis is employed to investigate the effect of resolutions in the ABL, where we uses the grid parameters in the ABL to set this analysis, therefore the gird refinement ratio is considered equal to $\sqrt{2}$. Also, ΔSPL is calculated using the value from $x = 0$ to $x = 2.0$. Table 4.7 summarises the calculations of discretization errors for ΔSPL. The calculated orders of convergence are $o = 1.74$ and 3.40, respectively. The convergence ratios are $R = -0.55$ and -0.31, respectively for $Ma = 0$ and 0.22, therefore both the two groups of simulations have oscillatory convergence. The ratios A are equal to 0.994 and 1.022, respectively for $Ma = 0$ and 0.22, which are both approximately 1, thus the solutions are well within the asymptotic range of convergence. The discretization errors for $Ma = 0$ are smaller than those for $Ma = 0.22$. GCI_{21} for both flow conditions are small. The error band GCI_{32} for $Ma = 0.22$ is equal to 3.96% which can be acceptable for the subsequent acoustic damping calculations. GCI_{32} should

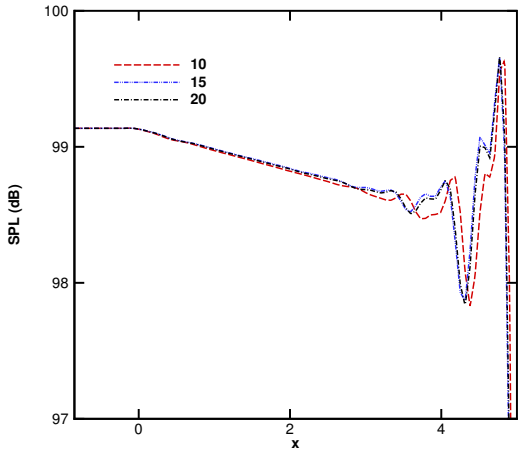

(a) SPL

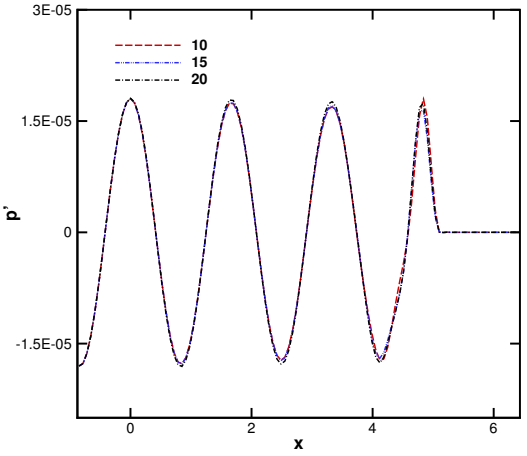

(b) Pressure

FIGURE 4.9: SPL and instantaneous pressure distributions along the x-axis obtained with different resolutions in the ABL when $Ma = 0.22$.

	o	R	A	ΔSPL_{ext}, dB	e^1_{ext}	e^2_{ext}	GCI_{32}	GCI_{21}
$Ma = 0$	1.74	-0.55	0.994	0.080	0.76%	1.39%	1.71%	0.94%
$Ma = 0.22$	3.40	-0.31	1.022	0.153	0.94%	3.07%	3.96%	1.19%

TABLE 4.7: Calculations of discretization errors for ΔSPL obtained with various resolutions in the ABL.

range from 1.71% to 3.96% when the flow velocity varies from $Ma = 0$ to 0.22, therefore the medium resolution in the ABL is fine enough for the computation.

4.3.2.3 Influence of the buffer zone

The purpose of this chapter is to calculate the acoustic damping in pipe flows, thus we need to obtain the stable RMS pressure distribution over a reasonable distance. This objective, however, is influenced by the buffer zone from two aspects. Firstly, as shown in

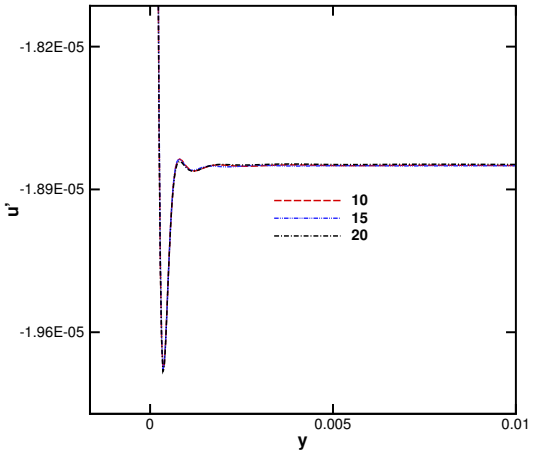

(a) $Ma = 0$

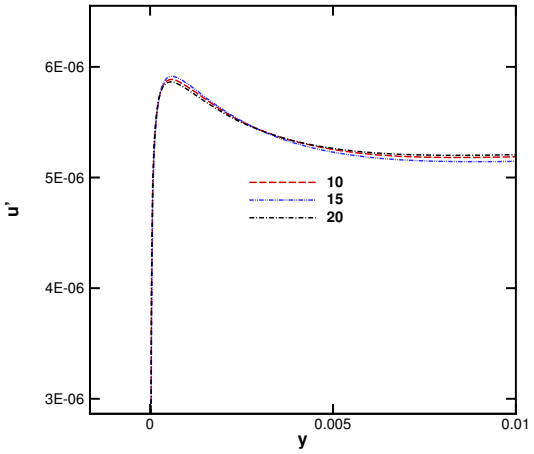

(b) $Ma = 0.22$

FIGURE 4.10: Instantaneous velocity profiles at cross section $x = 2$ when $Ma = 0$ and 0.22.

the SPL distributions such as in Figure 4.7, the region near the buffer zone demonstrates significant fluctuations of the SPL value, which can not be used to calculate the acoustic damping. To minimise the range of this region, the influences of buffer zone widths is investigated. The widths of the buffer zones are set as 0.5λ, 1λ and 1.5λ. The grid is stretched with an initial spacing identical to that of the adjacent grid block. As the amount of grid points of the buffer zone keeps unchanged, the grid stretching is reinforced along with the increasing widths. Secondly, at the interface between the buffer zone and the main computational zone, a reflection wave may be initiated. Although this potential reflection wave can be avoided by performing the simulations over a short physical time, its effect is evaluated. The performed physical time is set as 8 times periods of the sound wave, by which the reflected wave can almost propagate upstream to the inlet. In addition, the ABL is resolved with 15 points and the streamwise resolution is set with 20 points. Also, there is no flow employed in this study. The corresponding computational

settings are summarised in Table 4.8, where the physical time is measured by the period of the sound wave.

Case no.	Streamwise PPW	Resolution of ABL	Buffer zone width	Physical time
3.1	20	15	0.5λ	8
3.2	20	15	1.0λ	8
3.3	20	15	1.5λ	8
1.4	20	15	1.5λ	5

TABLE 4.8: Computational settings for the study of the effect of buffer zone widths.

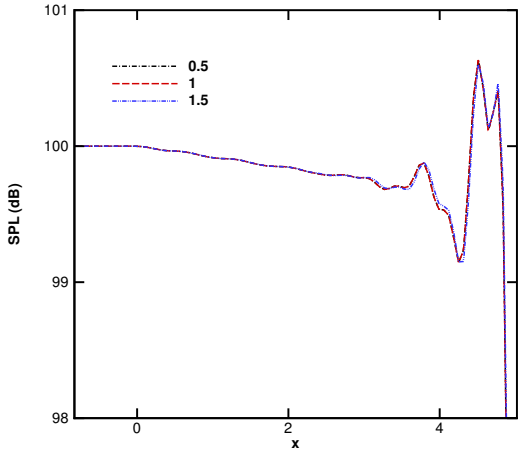

(a) SPL

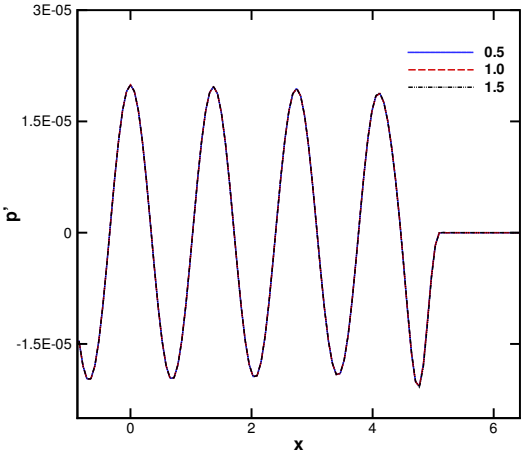

(b) Pressure

FIGURE 4.11: SPL and instantaneous pressure distributions along the x-axis obtained with various widths of the buffer zone.

As shown in Figure 4.11, the distributions of SPL and instantaneous pressure obtained with various buffer zone widths agree well, and little differences can be identified. Therefore the widths of the buffer zones and the resulting grid stretching should not

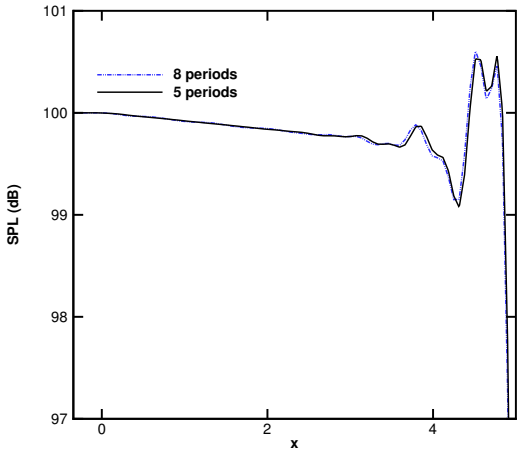

(a) Normal view

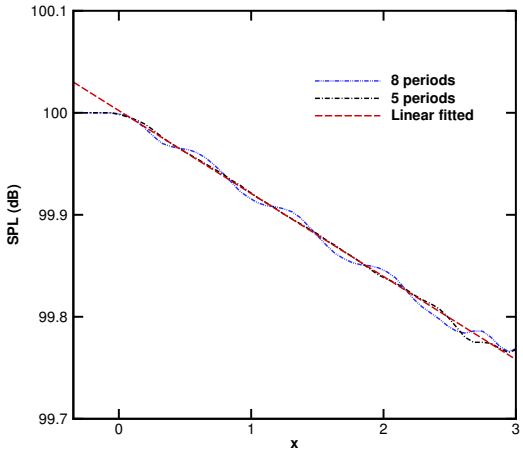

(b) Enlarged view

FIGURE 4.12: SPL distributions along the x-axis obtained with different performed physical time.

be regarded as the main reasons for the irregular distributions. In Figure 4.7, we can observe that the regions demonstrating irregular SPL distributions are narrowed along with increasing grid resolutions. Therefore the width of the region infected by the buffer zone is strongly in relation to the grid resolution.

Figure 4.12 shows the SPL distributions along the x-axis obtained with different performed physical time. Firstly, from an overall scope of view, Figure 4.12(a) shows that the two SPL distributions agree well, especially the region influenced by the buffer zone does not expand with time. Furthermore, as shown in Figure 4.12(b), the enlarged figure shows that there are oscillations of the SPL distribution along the x-axis for the longer performed physical time. This implies that a reflection wave is overlapped with the main wave. However, the reflection wave is relatively small in magnitude and the resulting SPL distribution is oscillated around a base line which is formed by a shorter performed physical time. In conclusion that, the reflection wave barely changes the

characteristics of the sound wave decay. Specifically, for the simulation with a longer physical time, the slope of the SPL decay can be obtained by a linear fitting as given in Figure 4.12(b), which gives a line that coincides well with the base line.

4.3.2.4 Thin acoustic boundary layer

When the ABL is thinner than the viscous sublayer, the acoustic damping in wall boundary layer is weak and mainly induced by the molecular viscosity rather than turbulence. The investigation about the effects of resolving degrees of wall boundary layer is carried out to evaluate the necessary of grid resolved computations at this situation. Four resolving degrees of wall boundary layers are performed with a flow velocity of $Ma = 0.03$. Firstly, the boundary layer is not resolved with a slip-wall boundary condition, however, the molecular viscosity and turbulence is reserved. The first layer of grid has a wall distance equal to the thickness of viscous sublayer, namely $\Delta s = 2.65 \times 10^{-4}$ according to Equation 2.48. Secondly, the boundary layer is resolved with no-slip wall boundary condition to the viscous sublayer, namely $\Delta s = 2.65 \times 10^{-4}$. Thirdly, the boundary layer is resolved to the ABL, namely $\Delta s = 1.39 \times 10^{-4}$ according to Equation 2.47. At last, the ABL is resolved with 15 points, namely $\Delta s = 1.0 \times 10^{-5}$. In addition, the streamwise resolution is set with 20 points and the buffer zone has a width of about 1.5λ.

Case no.	Mach no.	Streamwise PPW	Resolving degree	Δs, m
4.1	0.03	20	Not resolved	2.65×10^{-4}
4.2	0.03	20	To viscous sublayer	2.65×10^{-4}
4.3	0.03	20	To ABL	1.39×10^{-4}
4.4	0.03	20	Resolved ABL	1.0×10^{-5}

TABLE 4.9: Computational settings for evaluating the effects of the resolving degrees of wall boundary layers on acoustic damping.

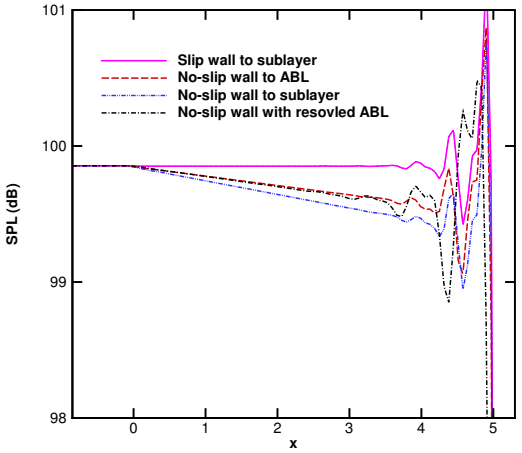

FIGURE 4.13: SPL distributions along the x-axis obtained with various resolving degrees of wall boundary layers.

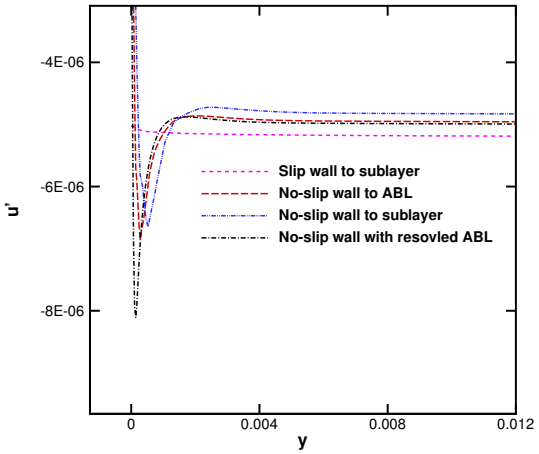

FIGURE 4.14: Instantaneous velocity profiles at cross section $x = 1$ when $Ma = 0.03$.

As shown in Figure 4.13, the result obtained with no resolved boundary layer shows barely SPL decay. In comparison with the results obtained with resolved boundary layers, we can conclude that the boundary layer plays a key role in acoustic damping. Furthermore, we can observe that the acoustic attenuation is over-predicted by resolving the boundary layer to the viscous sublayer, while the SPL decay obtained by resolving the ABL matches well with that solved by a grid which has the nearest wall distance equal to the thickness of the ABL. Moreover, Figure 4.14 demonstrates the velocity profiles at cross section $x = 1$ and clearly shows the resolving degrees of wall boundary layers. Firstly, the velocity at the wall is non-zero using a slip-wall boundary condition, thus there is no boundary layer formed at this condition. Otherwise, if resolving the wall boundary layer the velocity varies from zero at the wall to the value at the flat region and a trough is demonstrated. The trough shown in the resolved ABL line is deepest and narrowest, while the troughs for the other situations show similar depths and the result obtained with the resolving degree to the sublayer shows thickest boundary layer.

4.3.3 Conclusions for Computational Setup

In conclusion, in terms of the mean-flow simulations, the y^+ value should be on or under the order $y^+ = 1$. A medium grid shown in Table 4.2 can be used for all the flow conditions.

In terms of the perturbation simulations, the streamwise resolution should be set as $\geqslant 20$ PPW. If using an identical grid for all flow conditions, the actual resolution is refined along with increasing flow velocities due to Doppler effect. The ABL can be well resolved using 15 points. The width of the buffer zone has weak influence, which together with the sufficient gird resolution gives an acceptable influence on the SPL distribution. Also, the effects of wall boundary layers are evaluated when the ABL is thinner than the viscous sublayer. The results show that the ABL is important for the acoustic damping at this situation.

4.4 Plane Wave Problem

4.4.1 Setup

The physical configuration of the plane wave problem has been set in Section 4.2, and the corresponding CFD and CAA computational domains has been defined in Section 4.3. According to the conclusion for computational setup, the CFD simulations employ the medium grid as given in Table 4.2. The CAA gird uses a streamwise resolution of 20 PPW based on a quiescent fluid. The ABL is resolved with 15 points and the resulting height of wall-adjacent cell is equal to almost 1.0×10^{-6}.

Streamwise PPW	Resolution of ABL	Δs, m	Buffer zone width
20	15	1.0×10^{-6}	1.5λ

TABLE 4.10: Grid parameters for CAA simulations. The parameters are calculated when $Ma = 0$.

4.4.2 Simulation Results

Totally eleven flow conditions are simulated over $Ma = 0 - 0.22$. Table 4.11 gives some mean values and the resulting normalised ABL thickness. These values are calculated according to mean-flow results in the fully developed flow region. The calculated values of δ_A^+ meet well with the experimental data [157] in which δ_A^+ ranges from 1.97 to 30.67. Figure 4.15 shows the mean flow components at $M = 0.22$.

Mach no.	0.01	0.03	0.05	0.07	0.09	0.11	0.13	0.15	0.18	0.20	0.22
Re no., $\times 10^3$	7.7	24	40	57	73	90	106	123	139	156	172
y^+	0.05	0.13	0.21	0.28	0.36	0.42	0.49	0.56	0.62	0.69	0.75
u_τ	0.22	0.57	0.90	1.22	1.54	1.83	2.12	2.41	2.70	2.98	3.26
δ_A^+	1.98	5.24	8.27	11.2	14.2	16.8	19.5	22.1	24.8	27.4	30.0

TABLE 4.11: Mean-flow values obtained at different Mach numbers.

The sound propagation downstream and upstream is simulated, and for each case there are twelve flow conditions. Figure 4.16 shows the instantaneous pressure and velocity perturbations, where the ABL is visible in the velocity contour.

4.4.3 Results and Analysis for Attenuation of Sound

The relationship of the attenuation coefficient against δ_A^+ is yielded. The experimental data from Allam and Åbom [157], as well as the computational results obtained by Howe's analytical model [143] and by the non-equilibrium model of Weng et al. [12] are compared. Comparison is also performed with the wave equations method which employs the quasi-steady models suggested by Reynolds [114] and by Howe [214] and is implemented by Weng.

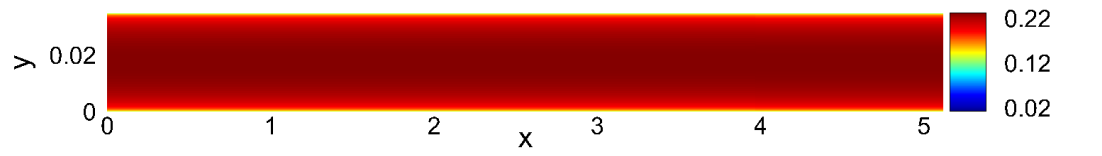

(a) $\bar{u}$

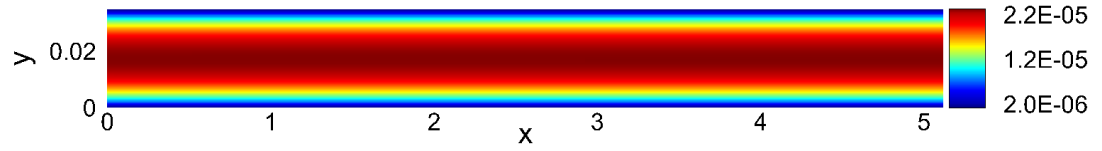

(b) μ_t

FIGURE 4.15: Non-dimensional mean flow components at $M = 0.22$.

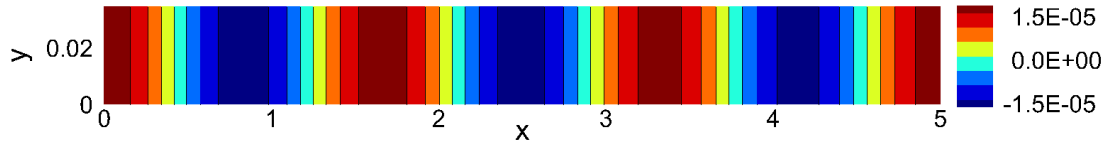

(a) p'

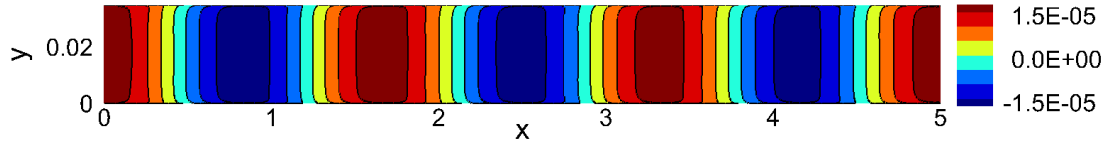

(b) u'

FIGURE 4.16: Instantaneous perturbation fields at $M = 0.22$.

Figure 4.17 demonstrates the profiles of the instantaneous perturbation velocity and mean velocity at the same cross-section. Where $u^* = |u/u_{max}|$, represents the velocity ratio of the local value to the maximum. As shown, at higher Mach numbers, the ABL falls into the log-law region of the turbulent boundary layer to a large degree. In the logarithmic region, namely the fully turbulent region, the eddy viscosity increases approximately linear with the distance from the wall thereby resulting in significant damping of sound. Also, the phase-dependent profiles of the ABL are observed using the time-dependent simulation, as shown in the velocity perturbation contour in Figure 4.16.

Figure 4.18 plots the normalised attenuation coefficient against the non-dimensional thickness of the ABL. Firstly, the results solved by LNS show reasonable agreements with those obtained by wave equation with the corresponding turbulent models, and the normalised attenuation coefficients are slightly greater at large δ_A^+ values The results from Howe (1995) and Weng et al. (2013) show good agreement with the experimental data by Allam et al., especially for the transition of attenuation at almost $5 < \delta_A^+ < 19$ where a local minimum of the attenuation is observed. Peters et al. [156] attributed this

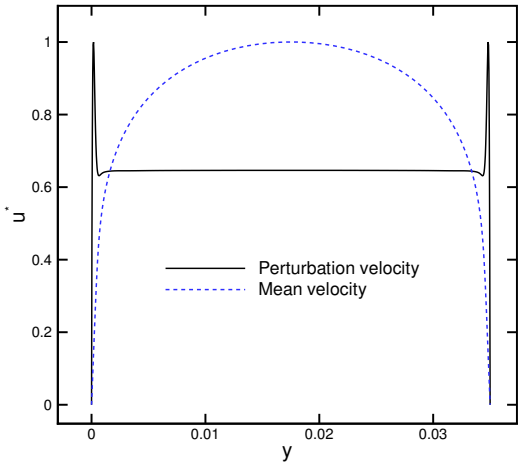

(a) $M = 0.01$

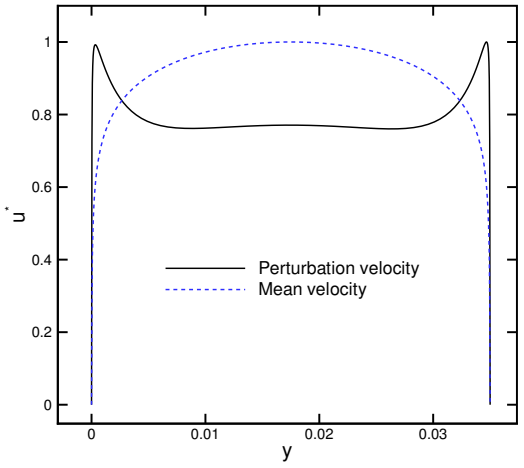

(b) $M = 0.22$

FIGURE 4.17: Relationship between the acoustic and turbulent boundary layers.

transition to the influence of the turbulent memory effect and extended Ronneberger and Ahrens' rigid plate model [154] by including this memory effect. Later, Howe [143] proposed an analytical model by extending Prandtl's linear approximation, the memory effect is introduced into the eddy viscosity. Moreover, Weng et al. [12] developed a phase-dependent model of eddy viscosity further by including the non-equilibrium effect. The other models, however, do not take the turbulent memory effect and the non-equilibrium effect into account, therefore the transition of attenuation cannot be resolved.

Figure 4.18 also shows that the Reynolds's quasi-steady model underestimates the attenuation beyond the transition region, whereas the Howe's quasi-steady model can provide more reasonable results with increasing δ_A^+. As indicated in Equation 2.33, the Reynolds's model is derived by vanishing the term $\tilde{\mu}_t$, which implies that the turbulent kinetic energy is not modulated by the wave motion.

In addition, we can observe that more attenuation is conduced when sound wave propagates upstream. According to Section 4.1.2, we can conclude that the convection

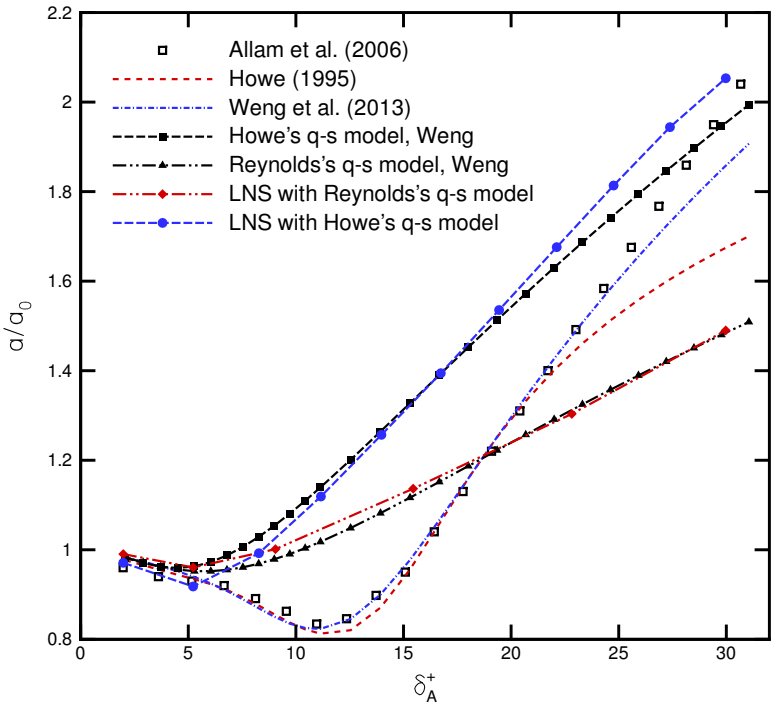

(a) Downstream

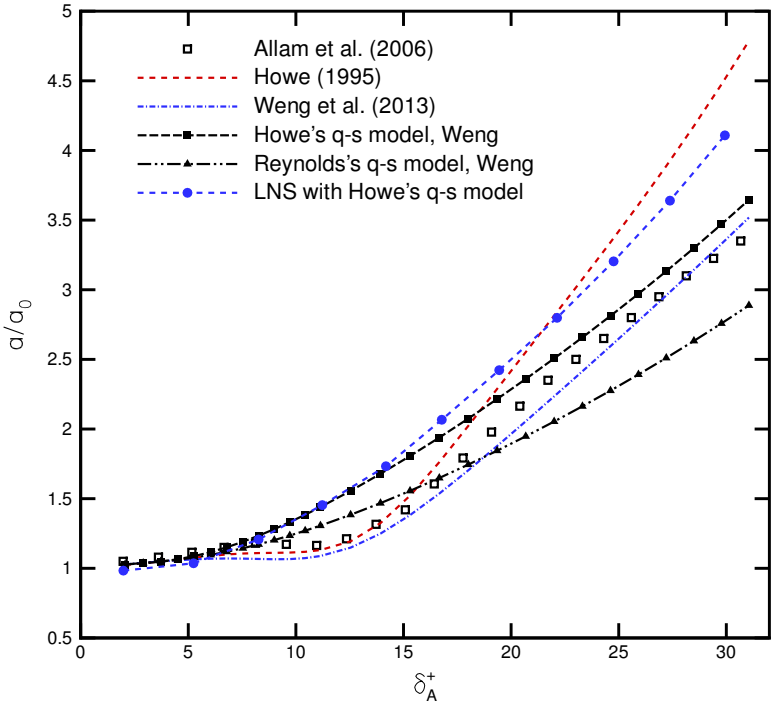

(b) Upstream

FIGURE 4.18: Relationship between acoustic damping and δ_A^+.

effect dominates the mean-flow effects.

4.5 High-order Modes

In the previous section, the attenuation of sound by turbulence has been studied for the plane wave problem where the Helmholtz number is lower than the first cut-on frequency, thus the higher order acoustic modes are cut-off. For some applications, the sound propagation at high-order modes needs to be precisely characterized, for instance when applying the N-port method [215] to determine the aeroacoustic characteristics in a duct system. Also, when designing the noise suppressor for aero-engine inlet and exhaust ducts, neither axisymmetric sound propagation theory nor flow duct empericism can predict the actual extensive attenuation which is suggested in relation to the spinning mode character of sound [216]. The spinning duct modes are produced by rotor-stator interaction and by inlet distortion-rotor interaction.

This section aims to investigate the character of acoustic damping induced by turbulence depending on high-order spinning modes, which is still a less-explored subject.

4.5.1 Problem Setup

With regards to acoustic waves in a circular duct, the derivative of the Bessel function has an infinite number of zeros as defined in Equation 4.8.

$$\left.\frac{dJ_m(k_r r)}{dr}\right|_{r=R} = J'_m(\eta_{mn}) = 0, \quad m = 0, 1, \cdots. \tag{4.8}$$

Some of these roots η_{mn} are listed in Table 4.12. The cut-off frequency for a mode is determined using Equation 4.9.

$$f = \frac{\eta_{mn} c}{2\pi R}\sqrt{1 - M^2}. \tag{4.9}$$

If the acoustic frequency is above that given by Equation 4.9 the corresponding mode can propagate. Otherwise, the mode declines exponentially if it is driven below the cut-off frequency. To enable a series of high-order acoustic modes, the duct diameter

n \ m	0	1	2	3
0	0	1.8412	3.0542	4.2012
1	3.8317	5.3314	6.7061	8.0152
2	7.0156	8.5263	9.9695	11.3459
3	10.1735	11.7060	13.1704	14.5859

TABLE 4.12: Some roots of Equation 4.9.

and the acoustic frequency are set to obtain a relatively high Helmholtz number, as shown in Table 4.13. Given that the Helmholtz number is equal to 7.2076 with a sound speed of 343.2378 m/s, the duct modes $(0, 0)$, $(0, 1)$ and $(0, 2)$, as well as $(1, 0)$, $(2, 0)$ and $(3, 0)$ are expected to be able to propagate and are performed in this study of acoustic damping by turbulence at high-order modes.

Diameter, m	Frequency, Hz	Mach no.	ABL thickness, m	Helmholtz no.
0.75	1050	$0.01 - 0.22$	6.74×10^{-5}	7.2076

TABLE 4.13: Main settings for researches of the acoustic damping at high-order modes.

The attenuation of sound waves is calculated using the method described in Section 4.2.

4.5.2 Computational Setup

The geometry of the circular duct is a clean axisymmetric pipe. Also, the mean flow is considered to be axisymmetric without swirl component. Therefore, the computational domain can be reduced from a realistic three-dimensional circular duct, whereby the computational efforts can be significantly decreased. Due to the azimuthal periodicity of the acoustic problem, the CAA computational domain can be reduced to $2\pi/m$ in circumferential direction, where $m > 0$ is the azimuthal mode, for example as shown in Figure 4.19. A periodic boundary condition was applied at the boundaries in the circumferential direction. The mean flow is simulated using a two-dimensional domain, subsequently is extended into the $2\pi/m$ domain for CAA simulations. In terms of the $(0, 0)$ mode, a two-dimensional domain is employed, and a $2\pi/3$ domain is used to perform the $(0, 1)$ and $(0, 2)$ modes.

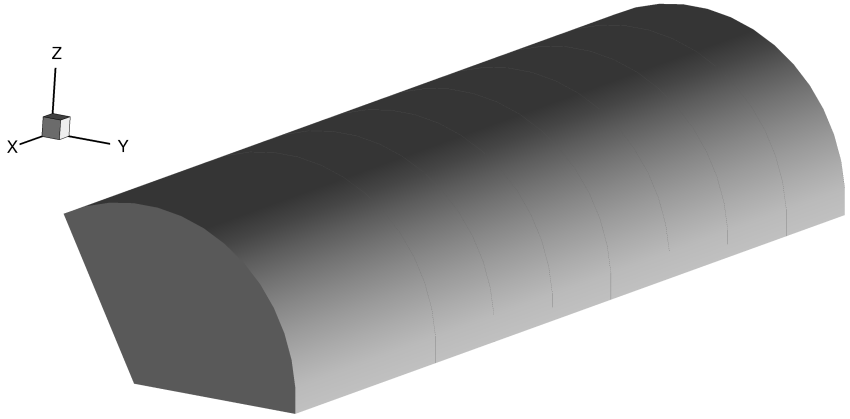

FIGURE 4.19: Sketch of the CAA simulation domain for mode $(3, 0)$.

As shown in Figure 4.20, the CAA simulation domain contains a wave propagation region which has the length equal to almost 3.75 wavelengths of the sound wave when $Ma = 0.22$. The input zone and the buffer zone are set similarly as those used in Section 4.3. The CFD computational domain is half of the duct with an axisymmetric condition at the lower boundary, as shown in Figure 4.21, which is extended to $x = -4.25$ to make sure that the turbulent flows employed in the CAA simulations are fully developed. As shown in Figure 4.22 and Figure 4.23, when $Ma = 0.22$, the wall shear stress along the wall and the turbulent viscosity along the x-axis demonstrate steady distributions within the CAA simulation domain.

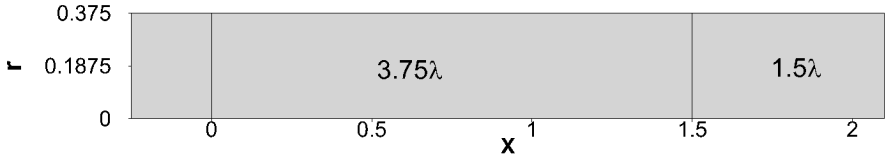

FIGURE 4.20: Sketch of the CAA simulation domain. The parameters are calculated when $Ma = 0.22$.

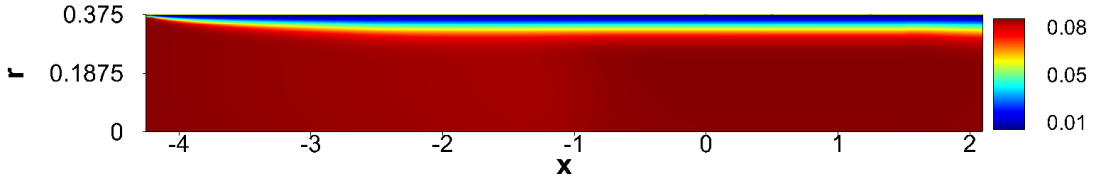

FIGURE 4.21: Distribution of the turbulent viscosity in the CFD simulation domain when $Ma = 0.22$.

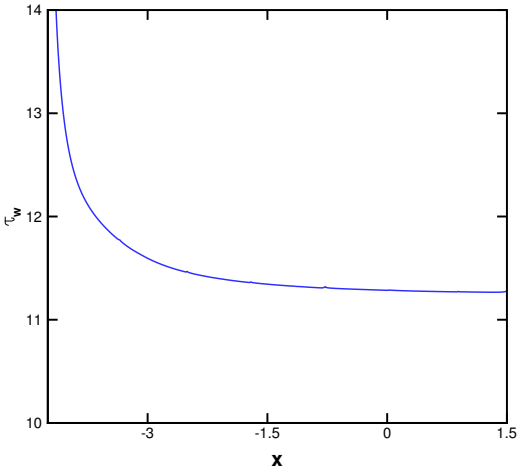

FIGURE 4.22: Wall shear stress value through a spline processing along the walls of the CFD simulation domain.

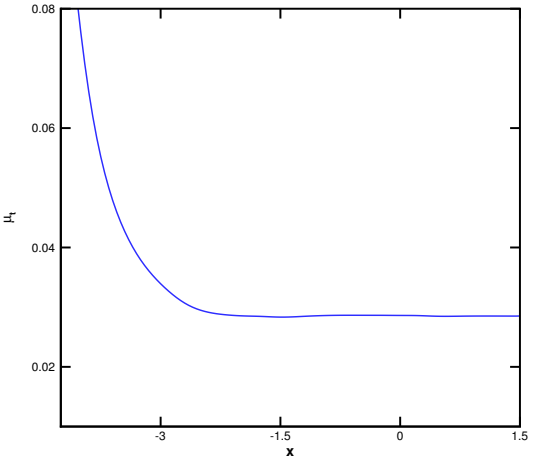

FIGURE 4.23: Turbulent viscosity along the x-axis of the CFD simulation domain.

To obtain grid convergent results and relatively small errors, the CFD and CAA grid is set according to the study for computational setup in Section 4.3. The mean-flow simulations employ a refined grid with settings as demonstrated in Table 4.14. The $\Delta s = 7.0 \times 10^{-6}$m ensures that the y^+ value is on or under the order $y^+ = 1$ for all flow conditions.

Grid	Aspect ratio maximum	Length ratio maximum	Δs, m
150×2400	360	1.06	7.0×10^{-6}

TABLE 4.14: Grid parameters for CFD simulations.

In terms of the perturbation simulations, the streamwise resolution is set as almost 20 PPW when $Ma = 0$, whereby the refined resolutions are applied to other flow conditions. Compromising with the computational cost, the ABL is resolved using 10 points and the corresponding height of wall-adjacent cell is equal to almost 7.0×10^{-6}. According to Section 4.3.2.2, the extrapolated relative errors e^3_{ext} for the coarse gird are 0.24% and 3.85%, respectively for $Ma = 0$ and 0.22. The width of the buffer zone is equal to or greater than 1.5λ according to the flow velocities.

Streamwise PPW	Resolution of ABL	Δs, m	Buffer zone width
20	10	7.0×10^{-6}	$\geq 1.5\lambda$

TABLE 4.15: Grid parameters for CAA simulations.

4.5.3 Simulation Results

In total, seven flow conditions are simulated over $Ma = 0 - 0.22$. According to mean-flow results in the fully developed flow region, some mean values and δ^+_A are calculated and given in Table 4.16.

Mach no.	0.03	0.06	0.09	0.12	0.15	0.19	0.22
Re no., $\times 10^5$	5.27	10.5	15.8	21.1	26.3	31.6	36.9
y^+	0.15	0.27	0.39	0.50	0.61	0.72	0.82
u_τ	0.64	1.17	1.68	2.17	2.64	3.11	3.57
δ^+_A	2.86	5.24	7.52	9.71	11.84	13.93	15.99

TABLE 4.16: Mean-flow values obtained at various Mach numbers.

For CAA simulations, as described, there are total 6 modes selected and for each mode there are 8 cases performed with various flow velocities. To identify the influence of turbulence on the acoustic damping, each case is performed using the LEE and LNS methods, respectively. The LEE method uses the slip-wall boundary condition and leads to an inviscid approach, whereas the LNS method uses the no-slip wall boundary condition to resolve the ABL based on a turbulent flow. The following results shown in Figure 4.24 and Figure 4.25 are obtained using the simulation data when $Ma = 0$.

Copying the computational results of a $2\pi/m$ domain to a whole duct field, Figure 4.24 shows the perturbation pressure distributions at multiple cross-sections along the x-axis, and the spinning mode sound propagation can be identified. Also, we can notice that Figure 4.24(b) shows a significant decrease of the perturbation pressure for the mode $(0, 2)$. Figure 4.25 demonstrates the corresponding SPL distributions at an axial section. Apparent gaps can be found at the interfaces of the radial modes, as show in Figure 4.25(b) and 4.25(c). Also, as shown in Figure 4.25(a), 4.25(d),4.25(e) and 4.25(f), as the azimuthal mode increases the SPL near the central axis drops. We may assume that when the azimuthal mode increases the acoustic energy concentrates towards the wall and lesser pressure oscillations occur near the central axis, hence the acoustic damping due to the ABL would become stronger.

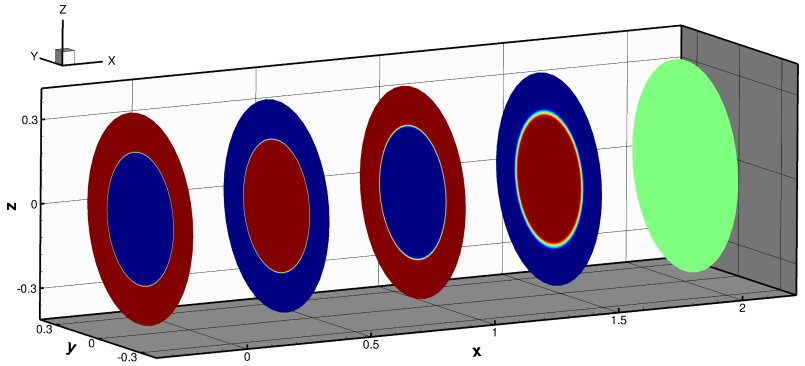

(a) $(0, 1)$

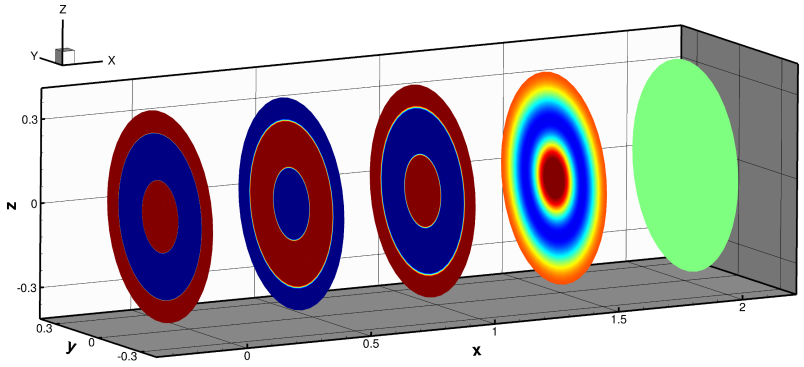

(b) $(0, 2)$

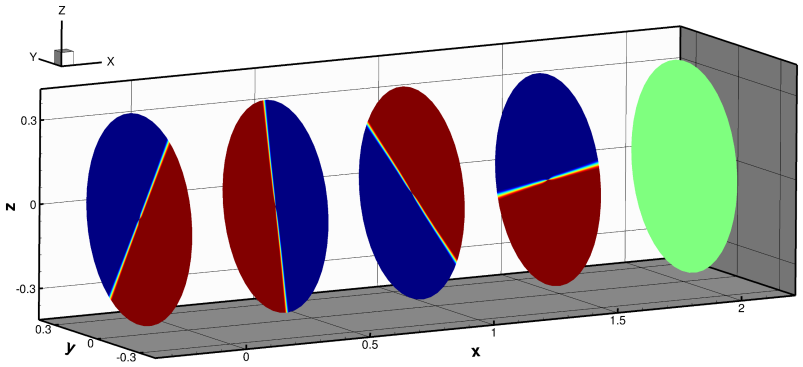

(c) $(1, 0)$

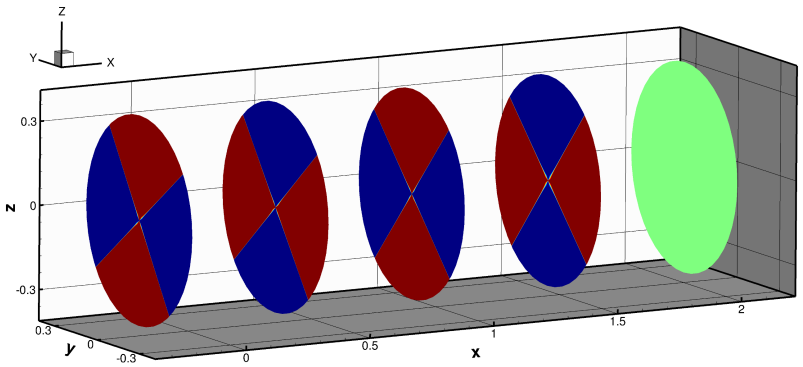

(d) $(2, 0)$

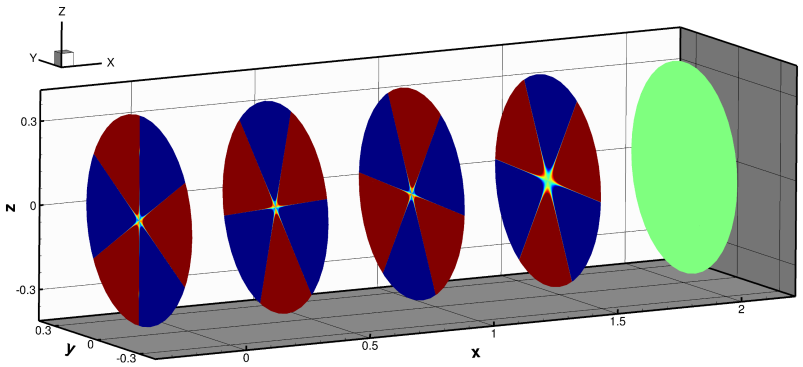

(e) $(3, 0)$

FIGURE 4.24: Perturbation pressure distribution along the x-axis for each mode.

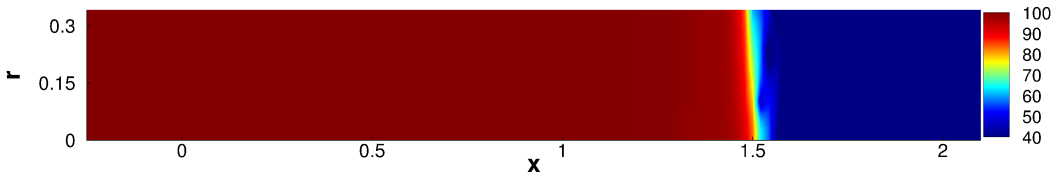

(a) $(0, 0)$

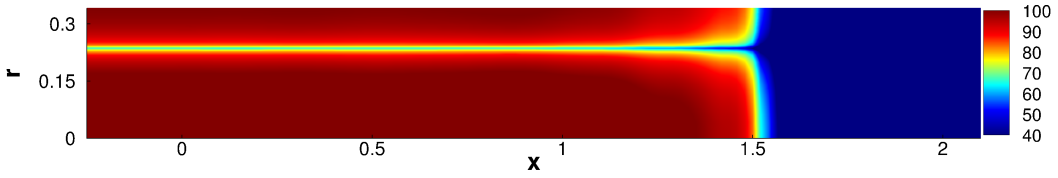

(b) $(0, 1)$

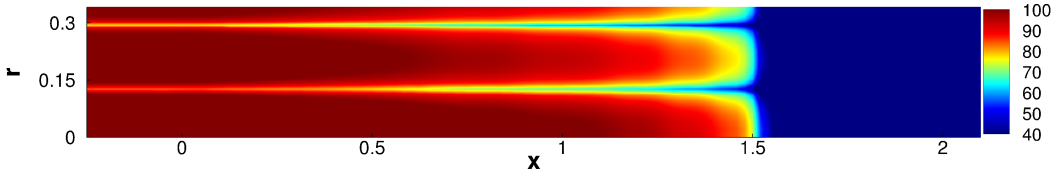

(c) $(0, 2)$

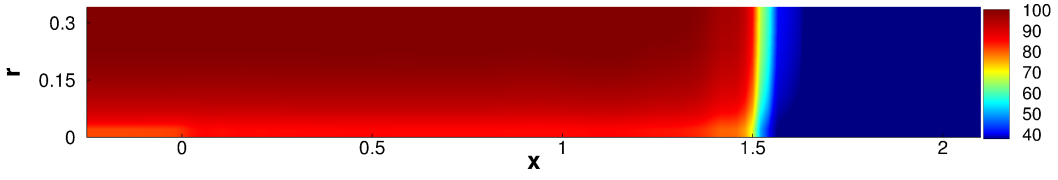

(d) $(1, 0)$

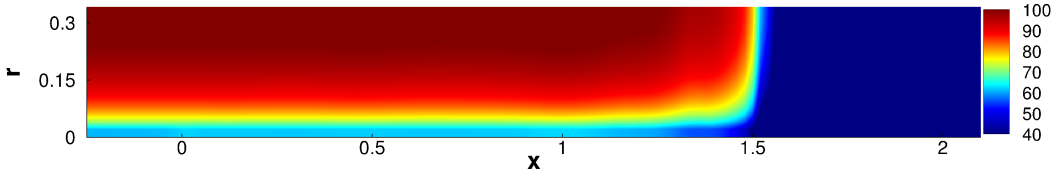

(e) $(2, 0)$

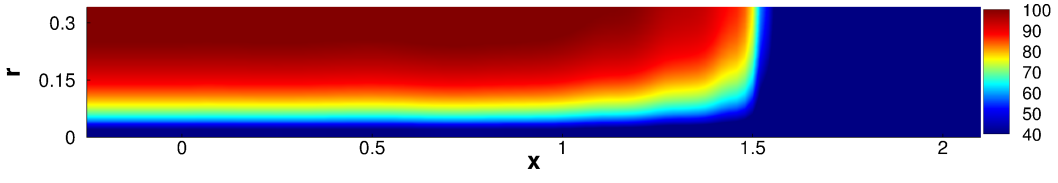

(f) $(3, 0)$

FIGURE 4.25: SPL distribution on an axial section along the x-axis for each mode.

4.5.4 Results and Analysis for Attenuation of Sound

Firstly, the attenuation coefficients at mode $(0, 0)$ for 250 Hz and 1050 Hz are compared as shown in Figure 4.26. The attenuation coefficient obtained for 1050 Hz is much higher than that given for 250 Hz, a greater growth rate of the attenuation coefficient is also observed for the higher frequency.

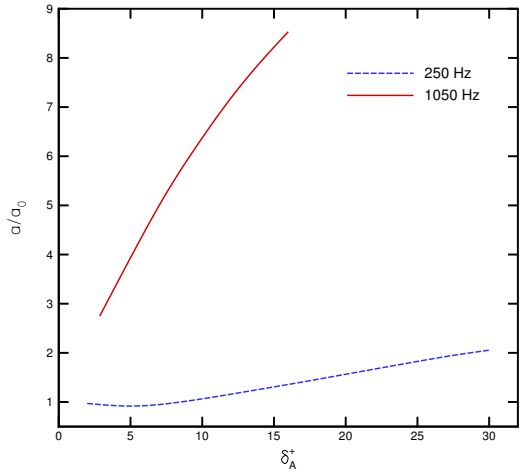

FIGURE 4.26: Attenuation coefficients of the acoustic wave at mode $(0, 0)$ for 250 Hz and 1050 Hz.

Next, to evaluate the attenuation of sound at the high-order modes, ΔSPL is calculated along a streamwise line at $y = 0.35$. Here the streamwise attenuation ratio of sound is assumed identical at any radial location. The performed cases are classified into two group, respectively for the radial modes as shown in Figure 4.28 and for the azimuthal modes as shown in Figure 4.29.

Figure 4.27(a) shows the attenuation of sound when the viscous and turbulent effects are not taken into account. In terms of the group of radial modes, namely the modes $(0, 0)$, $(0, 1)$ and $(0, 2)$, ΔSPL is enhanced when the radial modes are higher. With regards to the group of azimuthal modes, namely the modes $(0, 0)$, $(1, 0)$, $(2, 0)$ and $(3, 0)$, we can find the trend that ΔSPL is improved at higher azimuthal modes, except for mode $(2, 0)$ for which ΔSPL demonstrates a decreasing tendency from the beginning. Moreover, an obvious decreasing trend of the growth rate of ΔSPL along with the increasing δ_A^+ can be found for modes $(0, 1)$, $(0, 2)$ and $(1, 0)$. This may be caused by the lengthened wavelength at higher flow velocities. As the wavelength of the sound wave is lengthened the total acoustic energy distributed over a meter is decreased, then the resulting SPL difference over a meter is reduced. In brief, the mean-flow convection effect shows its influence.

Taking into account the viscous and turbulent effects, the attenuation of sound is considerably strengthened, as shown in Figure 4.27(b). Given the negligible effect of molecular viscosity, we can conclude that the turbulent effect plays an important role in the attenuation of sound waves at high-order modes when the ABL thickness is

obviously greater than the sublayer thickness. Also, the resulting ΔSPL clearly trends higher along with the increasing δ_A^+, except for the mode $(0, 2)$. The growth of ΔSPL can be explained by the increasing turbulent viscosity and its gradient at higher flow velocities. Also, the decreasing trend of the growth rate at relatively high Mach numbers can be found for modes $(0, 1)$, $(0, 2)$ and $(1, 0)$, which is also attributed to the mean-flow convection effect. With regards to mode $(0, 2)$, as other effects rather than the viscous and turbulent effects play a dominant role in the attenuation of sound, ΔSPL begins to decrease at almost $\delta_A^+ = 5.24$. Furthermore, the assumption in Section 4.5.3 according to the SPL distribution at each azimuthal mode can be confirmed. As demonstrated, ΔSPL is approximately enhanced when the azimuthal mode is higher, although ΔSPL of mode $(2, 0)$ at high δ_A^+ values is less than that of mode $(1, 0)$.

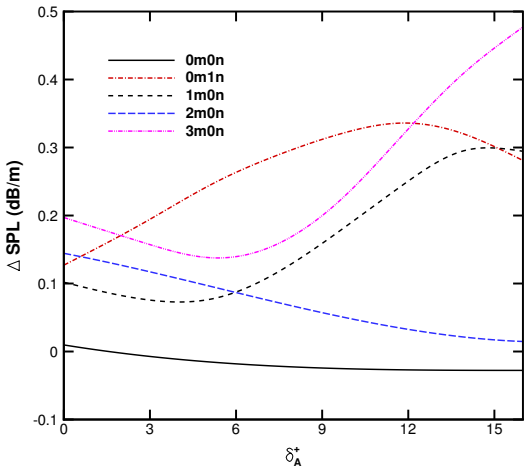

(a) No viscous and turbulent effects

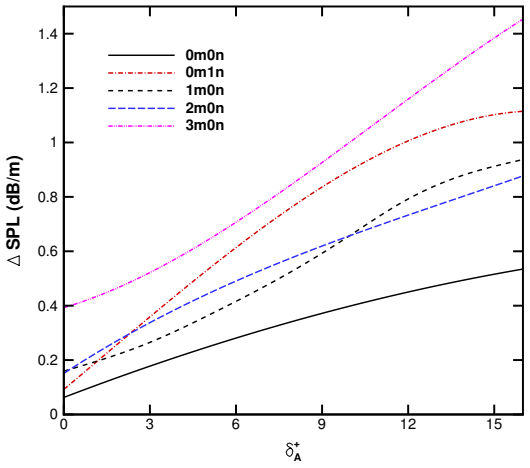

(b) Including viscous and turbulent effects

FIGURE 4.27: Acoustic damping at each mode.

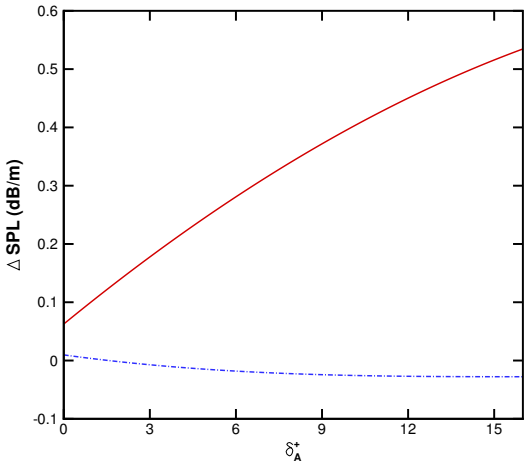

(a) $(0, 0)$

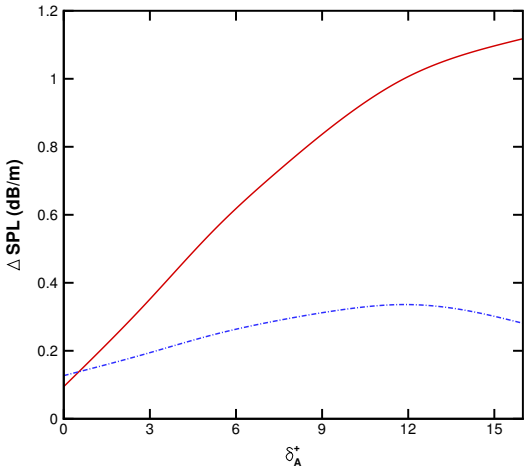

(b) $(0, 1)$

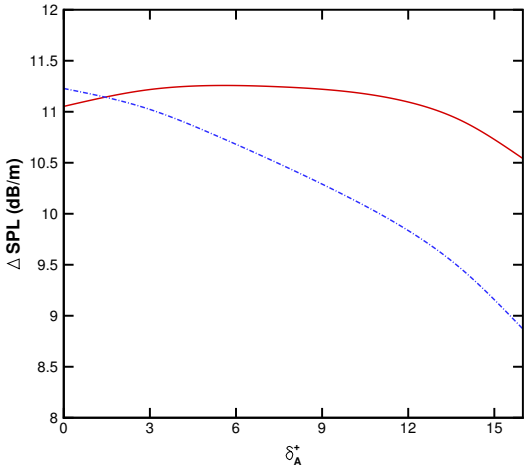

(c) $(0, 2)$

FIGURE 4.28: Acoustic damping at each radial mode. (——) including viscous and turbulent effects; (-·-·-) not including viscous and turbulent effects.

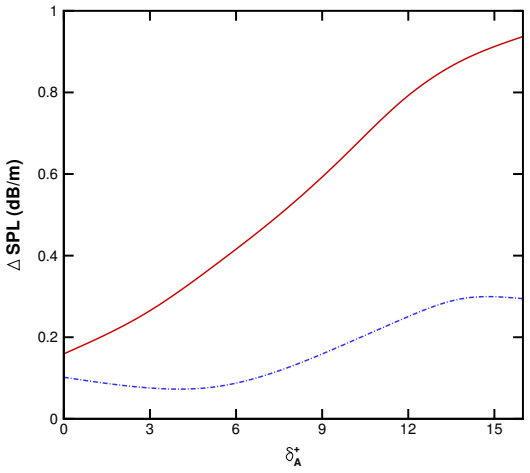

(a) $(1,0)$

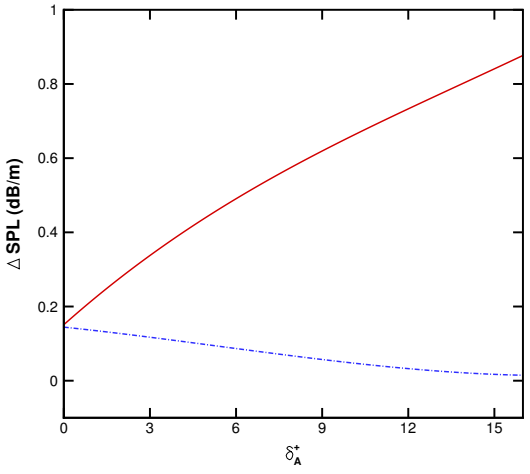

(b) $(2,0)$

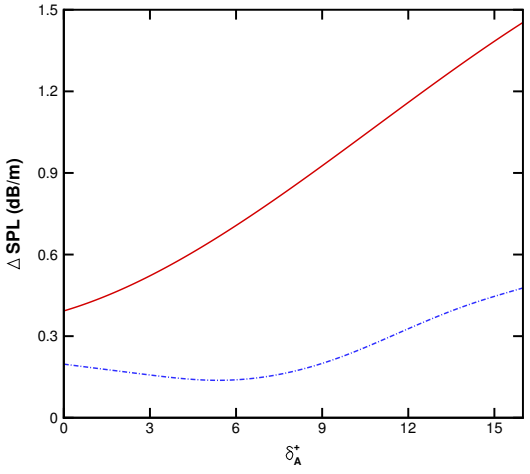

(c) $(3,0)$

FIGURE 4.29: Acoustic damping at each azimuthal mode. (——) including viscous and turbulent effects; (-·-·-) not including viscous and turbulent effects.

Chapter 5

Effects of Wall Boundary Layer on External Noise Radiation

Analytical methods can effectively calculate the engine noise scattering by a fuselage, such as the equivalent source method (ESM). However, the effect of boundary layers can not be taken into account by such tools. When the acoustic waves radiated from the engine arrive at the boundary layer, refraction due to the velocity gradients and scattering due to the turbulent fluctuations occur. The scattering effect has not been taken into account in current studies, which can be simulated by the LNS method employing, such as the random-particle-mesh method. In general, the effect of the wall boundary layer raises concerns in two aspects. The first is the far-field noise distribution at take-off/landing conditions. The main concern in this area is the community noise impact from the commercial aircraft. Current approaches to the far-field radiation of aircraft noise barely take the influence of boundary layers into account. The other area is the engine noise impact on the fuselage at cruise conditions, which results in a significant part of the cabin noise. Experiments and computations [217–219] have shown that refraction is considerable at cruise conditions.

In this chapter, the acoustic refraction induced by the boundary layer is investigated by the LNS method. The primary purpose here is to validate the usability of the LNS method in this problem. Furthermore, the surface sound pressure distributions influenced by the refraction effect are evaluated at the take-off and landing conditions, and the resulting influence on the far-field acoustic directivity is also investigated by incorporating an FW-H solver.

5.1 Problem Setup

Instead of a realistic airplane configuration, simplified models containing basic elements are employed with the intention of simulating the fundamental mechanisms. The engine noise is simplified as a monopole source, and the fuselage is emulated firstly by a flat plate, further by a cylinder. To evaluate the influence on the far-field sound directivity, a lengthened cylinder model is subsequently used. The monopole sound source is modelled

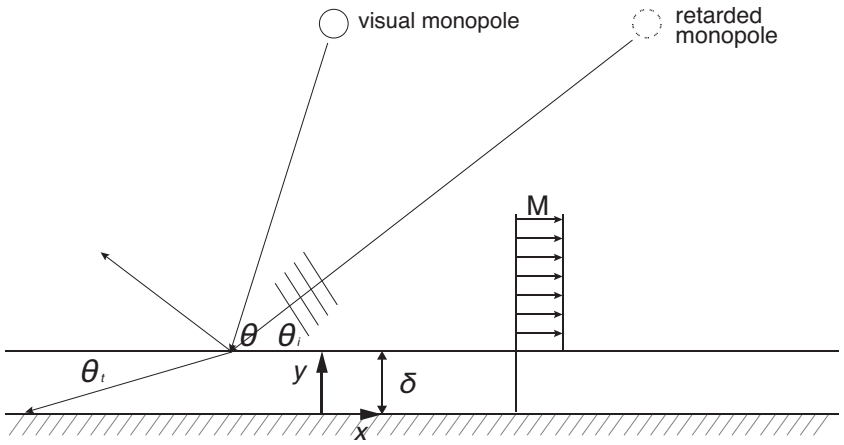

FIGURE 5.1: Sketch of the refraction of sound waves by the boundary layer.

Model	Frequency, Hz	Mach no.	Helmholtz no.
Plate	400 and 800	0.3 and 0.75	π and 2π
Cylinder	400 and 800	0.3 and 0.75	π and 2π
Lengthened cylinder	800	0.3	2π

TABLE 5.1: Settings for acoustic and flow parameters.

by the Gaussian function. Two source frequencies, 400 Hz and 800 Hz are adopted in the current simulations. The boundary layer thickness corresponds to the wavelength of a sound wave at 800 Hz, hence the Helmholtz numbers based on the boundary layer thickness are respectively about π and 2π. Two flow velocities are employed, 0.3 is a typical Mach number at the take-off condition and $Ma = 0.75$ corresponds to the cruise condition.

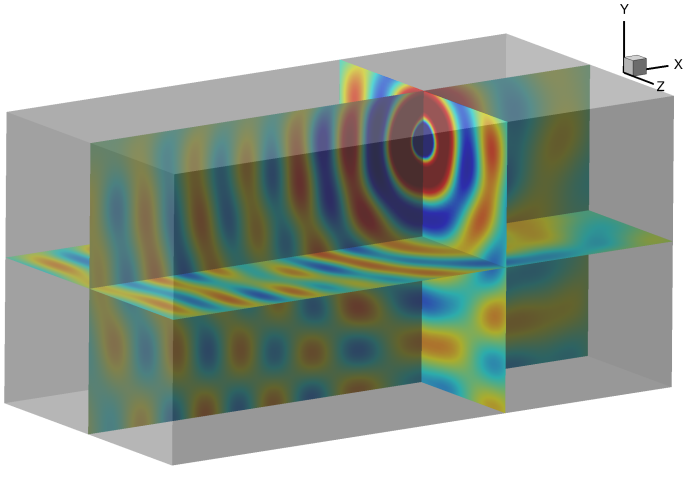

FIGURE 5.2: Sketch of the plate model.

The flat plate model is the most simple one where the sound waves are reflected by the solid plane surface and refracted due to the wall boundary layer. The dimensions of the flat plate are 3 m in the spanwise direction and 6 m in the streamwise direction, as

shown in Figure 5.2. The dimensions of the computational domain including the buffer zones are 5 m in spanwise direction, 7.7 m in streamwise direction, and 4 m in height. The width of buffer zones is at least 0.85 m which corresponds to the wavelength of the sound waves at 400 Hz.

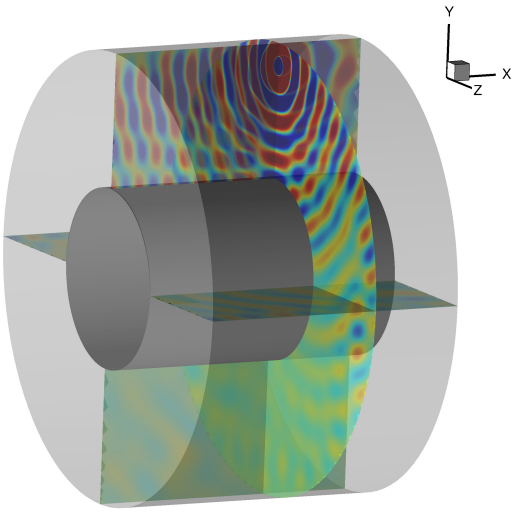

FIGURE 5.3: Sketch of the cylinder model.

The scattering of sound waves by a cylinder is more complex, as shown in Figure 5.3, where the sound waves could propagate into the boundary layer with relatively large incident angles. The dimensions of the cylinder are 4 m in diameter and 6 m in the streamwise direction. The diameter of the cylinder relates to the typical dimension of a commercial aircraft. The computational domain including the buffer zones is an annular duct of which the inner and outer diameters are 4 m and 12 m respectively, and the length is 7.7 m.

The lengthened cylinder is extended upstream for 4 m and has a total length equal to 10 m. As shown in Figure 5.4, a cylindrical surface of radius equal to 4.7 m is used for the FW-H integral. The far-field observers are located at 100 m away from the central point of the cylinder and are used to imitate the measurement of the sound radiation to the ground. For the computational domain, the inner and outer diameters are 4 m and 13.28 m respectively, and the length is 11.28 m.

The clearance between the sound source and the wall is 2.5 m, which corresponds to the typical distance from the sound source of the engine to the fuselage. And the sound source is located at $x = 4$ position in the streamwise direction.

5.2 Computational Setup

Due the symmetrical geometries of the flat plate and the cylinder models, the flow field can be simulated with a two-dimensional flat plate model at a relatively low computational cost. To show considerable refraction effect, as indicated in Section 4.1.2, the

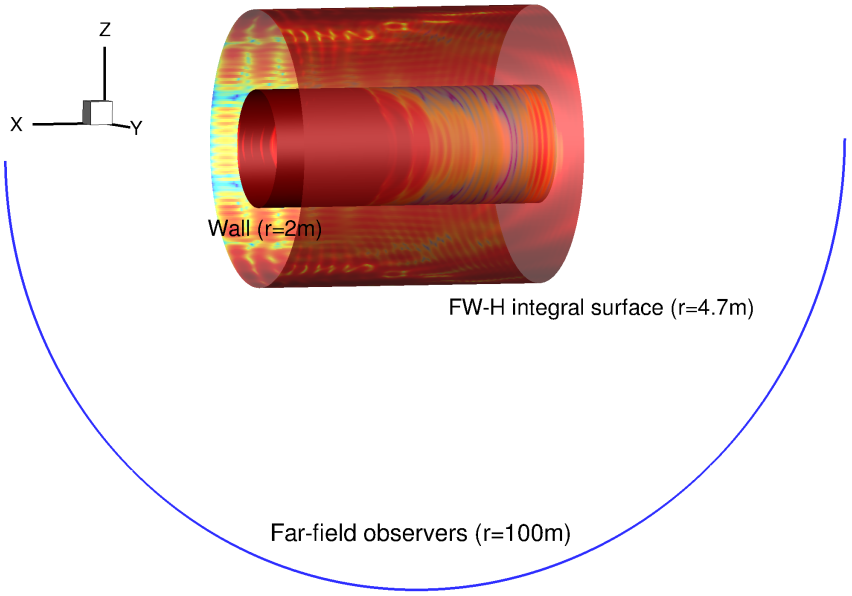

FIGURE 5.4: Sketch of the lengthened cylinder and the FW-H integral surface.

Model	Dimensions, m	Mach no.	Grid size
Plate	W:5; H: 4; L: 7.7	0.3 and 0.75	4,013,940 cells
Cylinder	D:(12-4); L: 7.7	0.3	11,659,536 cells
		0.75	19,634,832 cells
Lengthened cylinder	D:(13.28-4); L: 11.28	0.3	22,044,552 cells

TABLE 5.2: Computational domains and grid settings for CAA simulations.

Helmholtz numbers should be relatively large, which is expected here to be approximately 2π based on the wavelength at 800 Hz. Therefore the boundary layer thickness should be approximately equal to 0.425 m. Customarily, the boundary layer thickness is defined as the distance from the wall to the point where the flow velocity has reached 99% of the main stream velocity [220], namely

$$u(y) = 0.99u_0. \tag{5.1}$$

For an external flow, the turbulent boundary layers develop along the streamwise direction with an almost linear growth rate in thickness, as indicated in Equation 5.2 and 5.3. The thickness of turbulent boundary layers over a flat plate can be estimated by [220]

$$\delta \approx \frac{0.16x}{{Re_x}^{1/7}}, \tag{5.2}$$

also, can be calculated by [221]

$$\delta \approx \frac{0.38x}{{Re_x}^{1/5}}, \tag{5.3}$$

Static pressure, Pa	Density, kg/m^3	Sound speed, m/s	Kinematic viscosity, m^2/s
101325	1.220	340.29	1.4607×10^{-5}

TABLE 5.3: Fluid parameters.

where $Re_x = \rho u_0 x/\mu$ and x is the distance downstream from the start of the boundary layer. To obtain the thickness around 0.425 m, according to Equation 5.2, the flow domain should be extended downstream to 41.17 m and 47.97 m, respectively for $Ma =$ 0.3 and 0.75; while the flow domain should be correspondingly extended downstream to 58.25 m and 73.25 m according to Equation 5.3. Also, to approximate to the far-field condition the outer boundary should be placed at the height that is about ten times the boundary layer thickness. Eventually, the solved boundary layer thickness reaches 0.425 m at $x = 46.16$ when $Ma = 0.3$ and at $x = 54.45$ when $Ma = 0.75$, as shown in Figure 5.6. Therefore, the dimensions of the CFD computational domain are set as 60 m $\times$ 4 m.

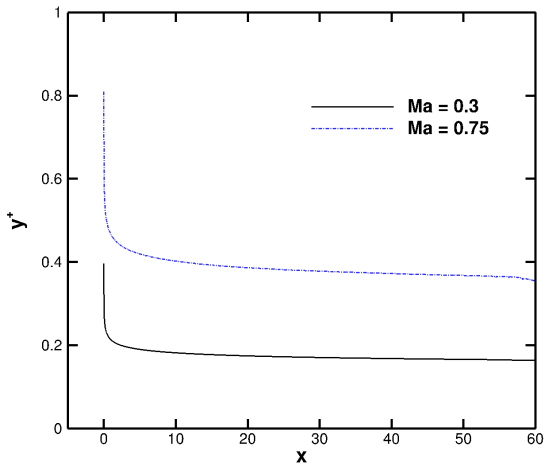

FIGURE 5.5: y^+ values at the wall.

The flow is computed using Fluent with a density-based steady solver, and the SST $\kappa - \omega$ model is employed. The mass-flow-inlet boundary condition is applied at the domain inlet, and the pressure-outlet boundary condition is used at the domain outlet. The symmetry boundary condition is employed at the outer boundary where the velocities normal to the boundary equal to zero. The flow variables are solved with second-order schemes. Due to the wall boundary layer is resolved, y^+ should be on the order of 1, and the actual maximal values of y^+ are around 0.4 and 0.8, respectively when $Ma = 0.3$ and 0.75, as shown in Figure 5.5. To simplify the computation, identical fluid parameters are used for the take-off/landing conditions and are displayed in Table 5.3.

Once the turbulent boundary layer is resolved, the mean field values at the corresponding cross-section are interpolated into the three-dimensional CAA computational domain. According to the conclusion of Section 3.3.2, the CAA grid is set with $PPW = 15$ at 400 Hz and 800 Hz, respectively. The buffer zones are placed around the

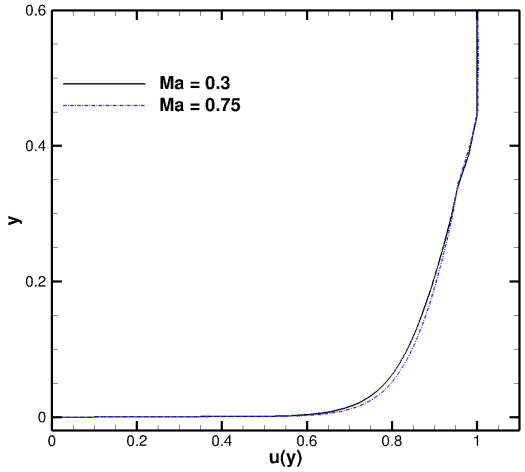

FIGURE 5.6: Normalised velocity profiles at $x = 46.16$ and $x = 54.45$, respectively for $Ma = 0.3$ and 0.75.

outer boundaries of the computational domain to emulate the free-space sound radiation. At walls, the slip boundary condition is used. As the main objective is here to investigate the mean-flow refraction effect, the molecular and turbulent viscosities are ignored. At a given Mach number and frequency, the perturbation simulation is carried out on the basis of a mean flow with/without the wall boundary layer, respectively denoted as "BL"and "no BL". The comparisons of the perturbation fields and the resulting SPL distributions are performed between the "BL"and "no BL"situations at each case.

5.3 Flat Plate

Considering the cases for $M = 0.3$, Figure 5.7 and Figure 5.8 display the instantaneous pressure perturbations on the symmetric face, while Figure 5.9 and Figure 5.10 show the SPL on the plate surface. From Figure 5.7 and Figure 5.8, we can observe that the wavelength is lengthened in the downstream region while it is shortened in the upstream domain. In addition, the interference between the directly incident waves and the wall-reflected waves can be observed. The interference also influences the SPL distribution as shown in Figure 5.9 and Figure 5.10, where obviously wavy distributions of the SPL on the plate surface are demonstrated with various wavelengths in both the spanwise and streamwise directions. Furthermore, significant drops in SPL values are found at the wavefront of the sound wave especially in the upstream region. In comparison between the "BL"and "no BL"cases, as shown for the sound waves at 800 Hz, neither the SPL distributions nor the instantaneous pressure contours demonstrates apparent differences. For 400 Hz waves, as the Helmholtz number is lesser, the differences induced by mean-flow refraction effect are more invisible. Subsequently, Figure 5.11 displays precise comparisons of the SPL on the plate surface along the streamwise symmetry line. Firstly, the phase shifts are observed for both the 400 Hz and 800 Hz cases, and the wave shapes move upstream due to the boundary layer refraction. Furthermore, the SPL values show

small differences in magnitude between the the "BL" and "no BL" cases. Also, compared with the downstream region, the upstream region gives relatively high levels in SPL magnitudes, as the acoustic energy is concentrated and diluted due to the mean-flow convection effect, respectively for the upstream and the downstream propagating waves. Also, the wavelengths of the wavy distribution of the SPL in the streamwise direction can be estimated from Figure 5.11 and are equal to about 4/5 and 1/2 of the acoustic wavelengths, respectively in the upstream and the downstream regions. Notice that the acoustic wavelengths in the upstream and the downstream regions are different due to Doppler effect.

When $M = 0.75$, the refraction effect are significantly enhanced. As shown in Figure 5.14 and Figure 5.15, the SPL distributions on the plate surface are dramatically altered in the upstream region due to the boundary layer refraction. And the alterations are improved at the higher frequency for which a "quiet" zone is displayed in the upstream region in Figure 5.15. Figure 5.12 and Figure 5.13 display the instantaneous pressure perturbations on the symmetric face. These figures clearly demonstrate the detachments of sound waves from the plate wall due to the boundary layer. The detached positions (once the SPL values are significantly less than 60 dB) are located at about $x = 2.42$ for 400 Hz and $x = 2.63$ for 800 Hz, as well as the corresponding angles between the wall and the ray formed from the source location to the detached point are respectively about 57.7° and 61.3°. Therefore, we can deduce that the lower frequency wave begins to detach at a bigger incident angle. Figure 5.16 gives the comparisons of the SPL on the plate surface along the streamwise symmetry line. In the very downstream region, the SPL distributions for the "BL" and "no BL" cases are almost identical in magnitude and in phase shape. However, the SPL magnitudes are dramatically dropped when moving upstream, namely there are rare acoustic energy propagated to the upstream plate surface due the mean-flow refraction effect.

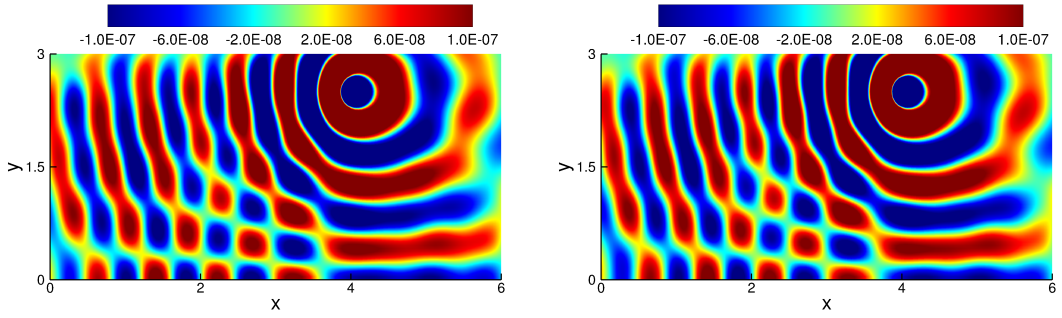

(a) No BL (b) BL

FIGURE 5.7: Instantaneous pressure perturbation on the symmetric face. $M = 0.3$, 400 Hz.

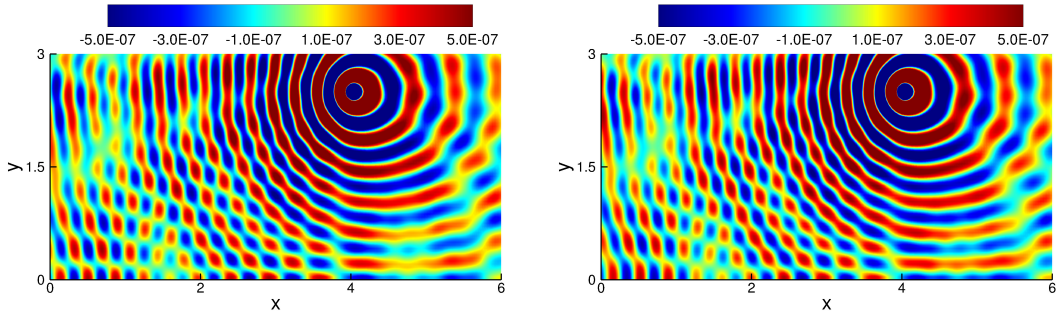

(a) No BL (b) BL

FIGURE 5.8: Instantaneous pressure perturbation on the symmetric face. $M = 0.3$, 800 Hz.

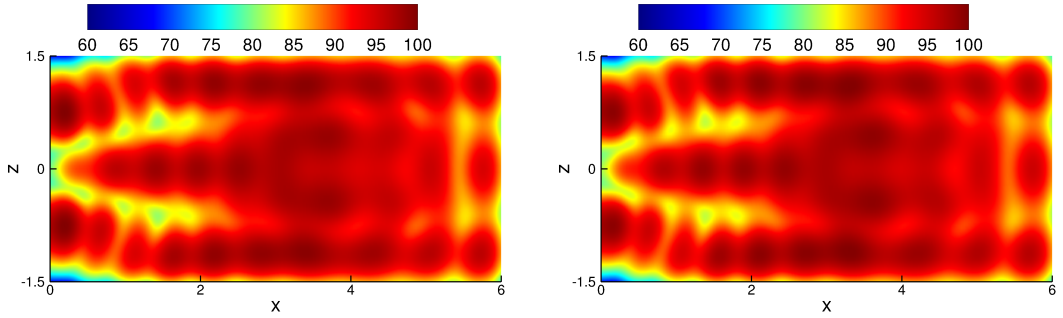

(a) No BL (b) BL

FIGURE 5.9: SPL on the plate surface. $M = 0.3$, 400 Hz.

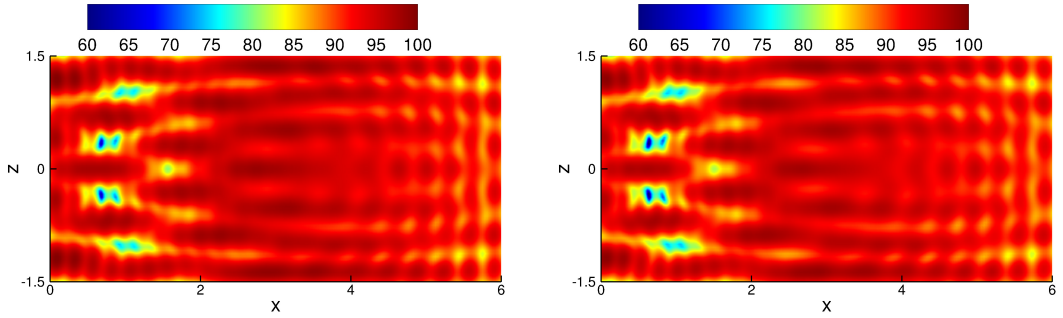

(a) No BL (b) BL

FIGURE 5.10: SPL on the plate surface. $M = 0.3$, 800 Hz.

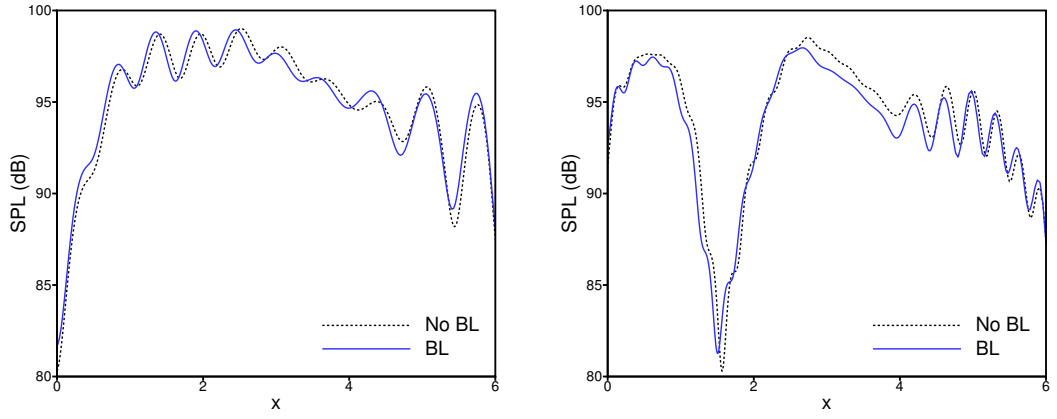

(a) 400 Hz (b) 800 Hz

FIGURE 5.11: SPL on the plate surface along the streamwise symmetry line. $M = 0.3$.

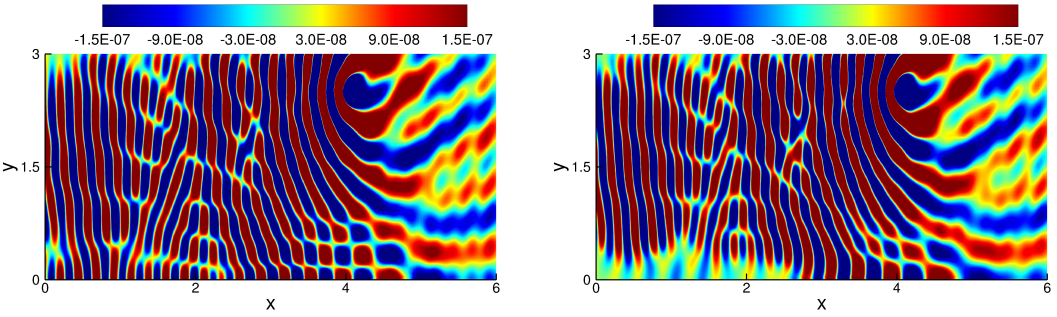

(a) No BL (b) BL

FIGURE 5.12: Instantaneous pressure perturbation on the symmetric face. $M = 0.75$, 400 Hz.

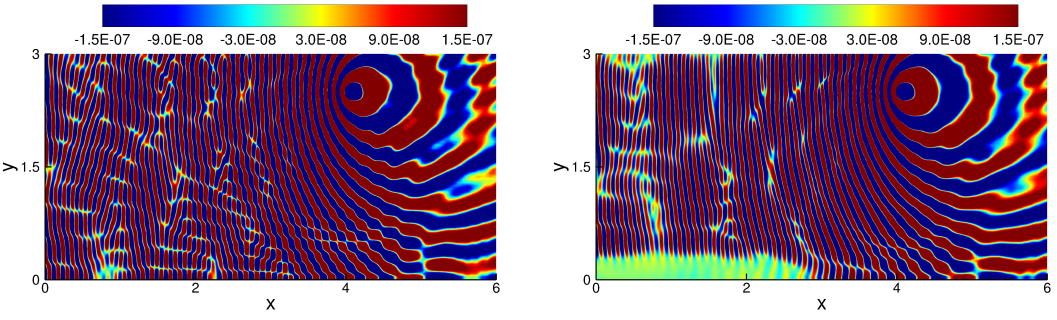

(a) No BL (b) BL

FIGURE 5.13: Instantaneous pressure perturbation on the symmetric face. M=0.75, 800 Hz.

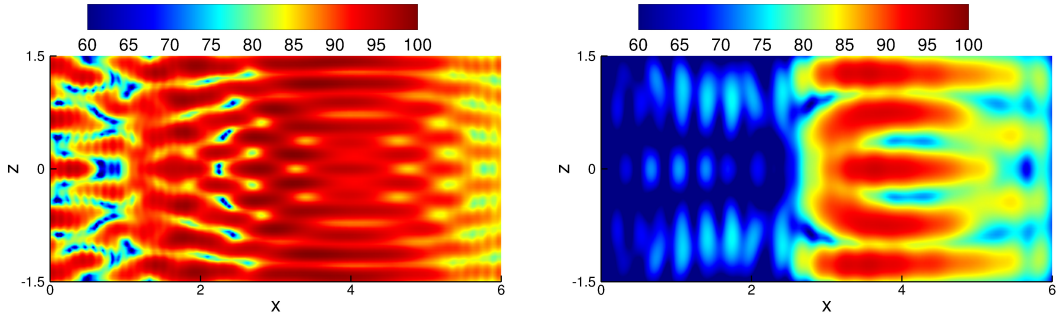

(a) No BL (b) BL

FIGURE 5.14: SPL on the plate surface. $M = 0.75$, 400 Hz.

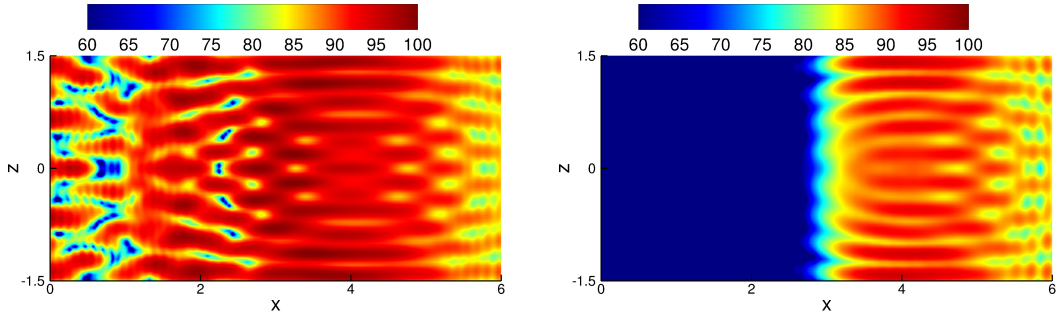

(a) No BL (b) BL

FIGURE 5.15: SPL on the plate surface. $M = 0.75$, 800 Hz.

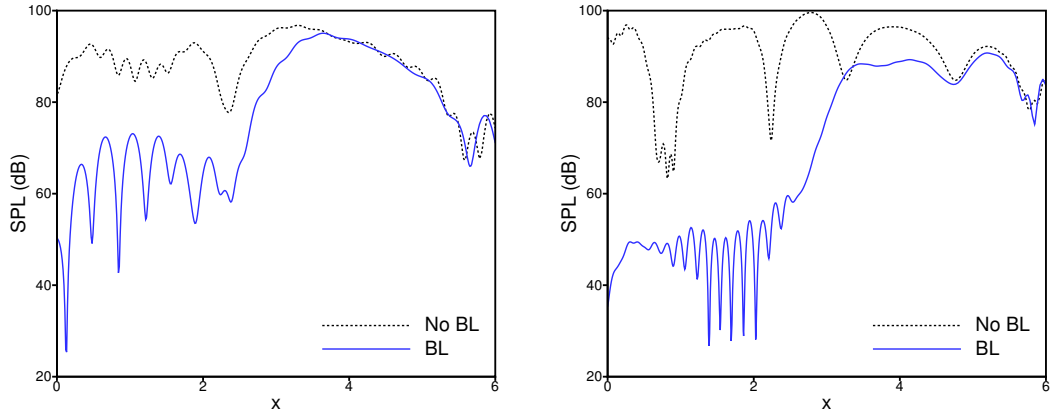

(a) 400 Hz (b) 800 Hz

FIGURE 5.16: SPL on the plate surface along the streamwise symmetry line. M=0.75.

5.4 Cylinder

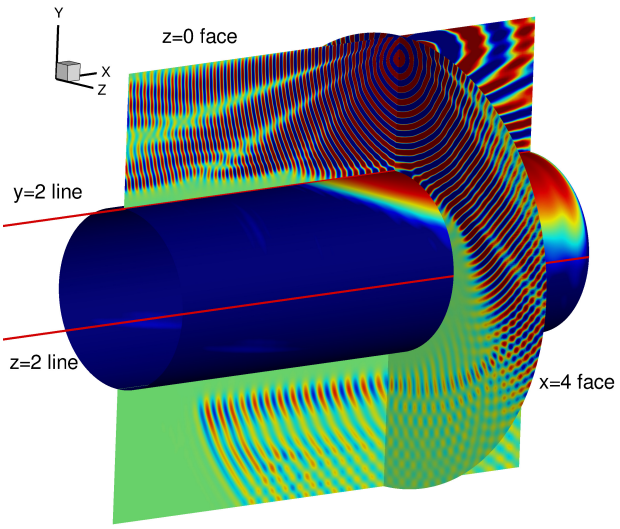

FIGURE 5.17: Sketch of the observation lines and faces for the cylinder model.

As shown in Figure 5.17, the results for the cylinder model are evaluated in the ways as follows:

- Instantaneous pressure perturbation on the $z = 0$ face (side view), which shows the behaviours of the acoustic waves along the streamwise direction;
- Instantaneous pressure perturbation on the $x = 4$ face (front view), which demonstrates the characteristics of sound propagation along a circumference at $x = 4$;
- SPL on the cylinder surface, from the top view and the side view;
- SPL on the cylinder along the streamwise direction, including the lines located on the top and the side, namely at $y = 2$ and $z = 2$;
- SPL on the cylinder along the circumferences at $x = 4$ and $x = 0.5$, respectively denoted as $r|_{x=4} = 2$ and $r|_{x=0.5} = 2$.

When $M = 0.3$, similar to the plate case, there are no considerable refraction effects. Figure 5.18 and Figure 5.19 show the sound propagation along the circumference, and there are no observable differences induced by the boundary layer for both the 400 Hz and 800 Hz cases. From the top view, as shown in Figure 5.20 and Figure 5.21, wavy distributions of the SPL on the cylinder surface are demonstrated. The wavelengths estimated from $y = 2$ lines in Figure 5.22 are also equal to about 4/5 and 1/2 of the acoustic wavelengths respectively in the upstream and the downstream regions, same as the values in the flat plate case. As also shown in Figure 5.22, the central regions instantly under the monopole source barely show differences between the "BL"and "no BL"cases. However, obvious distinctions appear in the upstream marginal regions, as

shown in Figure 5.20(b) and Figure 5.21(b). As more precisely shown in Figure 5.23 for the SPL at $r|_{x=0.5} = 2$, the sound fields show clear alterations due to the boundary layer at most regions of the circumference at $x = 0.5$. In fact, at the front of the cylinder surface instantly under the sound source, the effective incident angles of the acoustic waves into the boundary layer are much larger than those in the corresponding locations for the flat plate model, whereby the refraction effect becomes noticeable. Similarly, the distinctions emerge in the regions directly below the monopole source, namely at $r|_{x=4} = 2$, as shown in Figure 5.24, although the differences are relatively weak. Initially, if there is no mean-flow convection, on the $x = 4$ face, the acoustic waves would propagate into the boundary layers at an effective 0° incident angle. However, owing to the mean-flow convection, the location that the source is projected on the cylinder is not at $x = 4$ but moves downstream to a distance. As a consequence, above the locations at $x = 4$ the acoustic waves will not get into the boundary layer at an effective 0° incident angle, and thus the SPL distributions can be altered due to the refraction effect. As shown in Figure 5.24 at $r|_{x=4} = 2$, as the effective incident angles increase towards the marginal regions, the SPL drops to obviously lower degrees in the areas around 0° and 180°. Also, at the higher frequency the alterations of the SPL distribution appear more considerable. In terms of the side regions of the cylinder, as shown in Figure 5.25 and Figure 5.26, the effective incident angles of the acoustic waves into the boundary layer become much larger even beyond 90°, therefore the acoustic waves tend to detach from the wall and sometimes can not directly "touch"the wall surface. Figure 5.27 gives the SPL distributions on $z = 2$ lines, where the boundary layer induces an obvious decline of the SPL distributions towards the upstream direction, and the downward tendency is more significant for the 800 Hz case.

At the emulated cruise condition, namely when $Ma = 0.75$, remarkable refraction effects are generally observed. Figure 5.28 and Figure 5.29 show the detachment of the acoustic waves from the wall along the streamwise direction; meanwhile, Figure 5.30 and Figure 5.31 demonstrate the detachment from the wall along the circumference at $x = 4$. More serious detachments are found at the higher frequency for both the SPL distributions along the circumference and the streamwise direction. From the top view, as shown in Figure 5.32 and Figure 5.33, the "quiet"zones are formed due to the boundary layer refraction. As similarly done in the flat plate case, the detached positions estimated from $y = 2$ lines in Figure 5.34 are located at about $x = 2.05$ and $x = 2.70$, respectively for 400 Hz and 800 Hz cases. The corresponding angles between the wall and the ray formed from the source location to the detached point are respectively about 52.0° and 62.5°, which are close to those estimated from the flat plate case. Furthermore, Figure 5.35 gives the SPL distribution at $r|_{x=4} = 2$. As the mean-flow convection is significantly enhanced, in comparison with the corresponding values at the lower Mach number as shown in Figure 5.24, the SPL is apparently altered due to the refraction effect at the regions around 90°. Moreover, as the effective incident angles are drastically increased towards the side regions, significant reductions of the SPL induced

by the refraction effect are demonstrated as given in Figure 5.35. The detached positions ($SPL \leq 60\,\text{dB}$) are at about 24° and 156° for the 400 Hz case, while are at about 32° and 148° for the 800 Hz case. In addition, sharp drops in the SPL are observed for the "BL"case. At the lower frequency, the drops are at around 10°, 170° and 270°; meanwhile, the drops are all located at the lower cylinder surface and at around 190°, 270° and 350° for the higher frequency. For both cases, the sound waves reaching the cylinder back are significantly reduced due to the boundary layer. For the side areas, as shown in Figure 5.36 and Figure 5.37, the SPL distributions are mostly altered due to the boundary layers. $z = 2$ lines as shown in Figure 5.38 also demonstrate that the boundary layers result in relatively lower SPL values than those given by "No BL"cases, and induce the decline of the SPL towards the upstream direction.

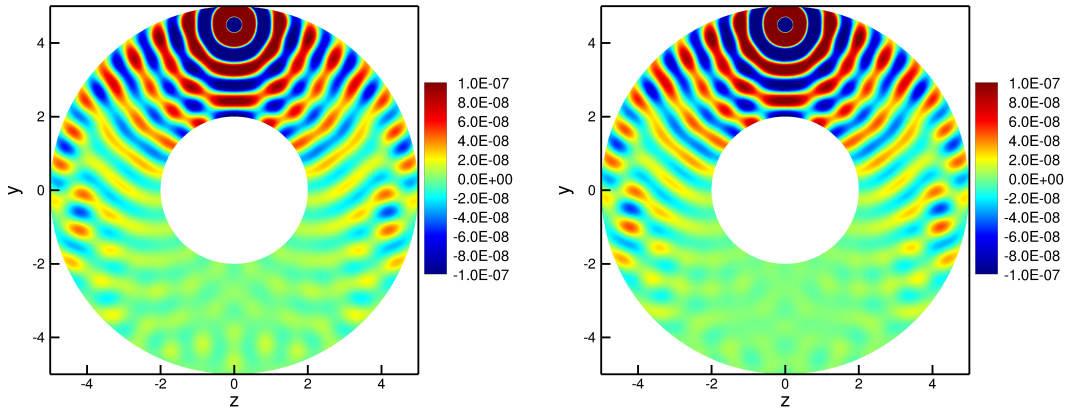

(a) No BL (b) BL

FIGURE 5.18: Pressure perturbations on the $x = 4$ face. $M = 0.3$, 400 Hz

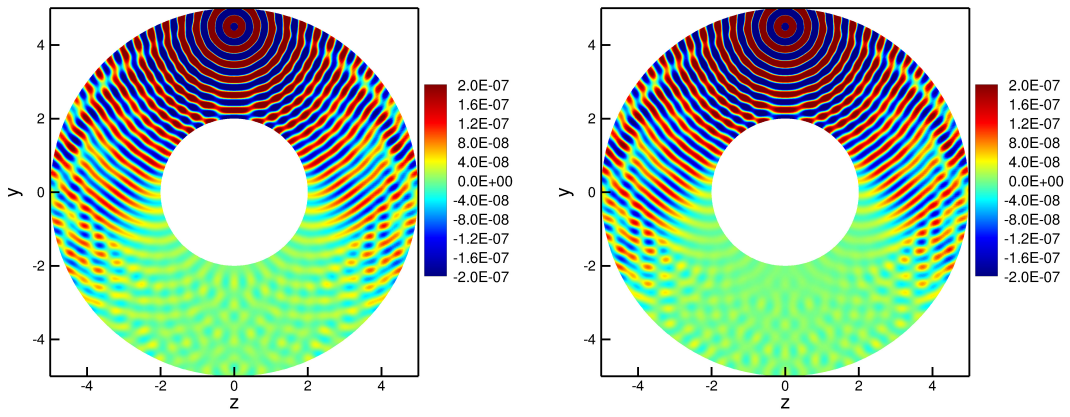

(a) No BL (b) BL

FIGURE 5.19: Pressure perturbations on the $x = 4$ face. $M = 0.3$, 800 Hz

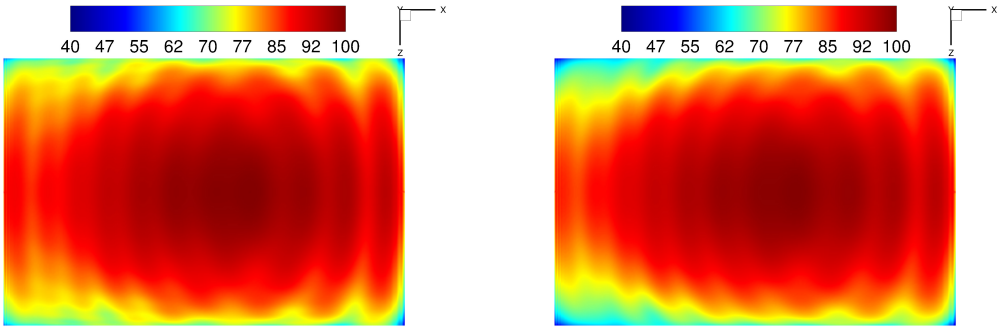

(a) No BL (b) BL

FIGURE 5.20: SPL on the cylinder surface from the top view. $M = 0.3$, 400 Hz

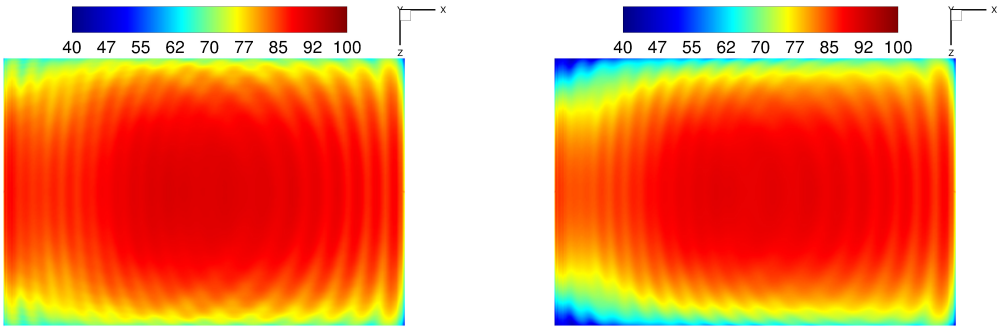

(a) No BL (b) BL

FIGURE 5.21: SPL on the cylinder surface from the top view. $M = 0.3$, 800 Hz

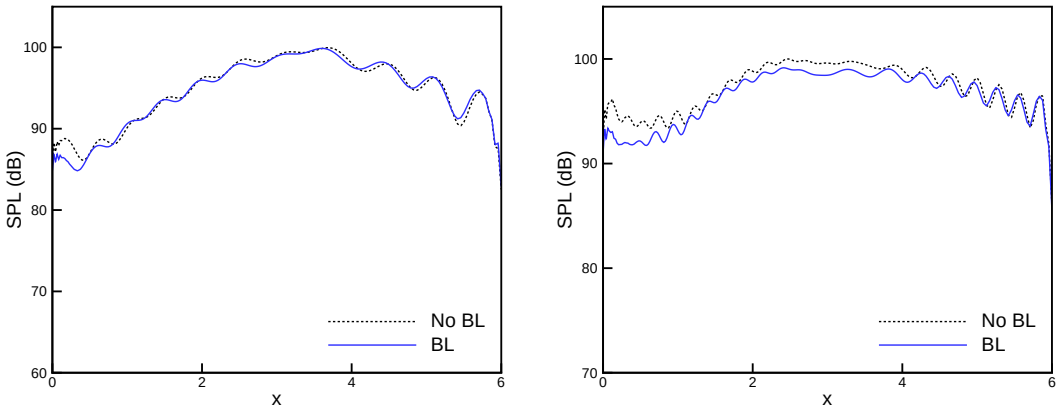

(a) 400 Hz (b) 800 Hz

FIGURE 5.22: SPL on the cylinder surface along $y = 2$ line. $M = 0.3$.

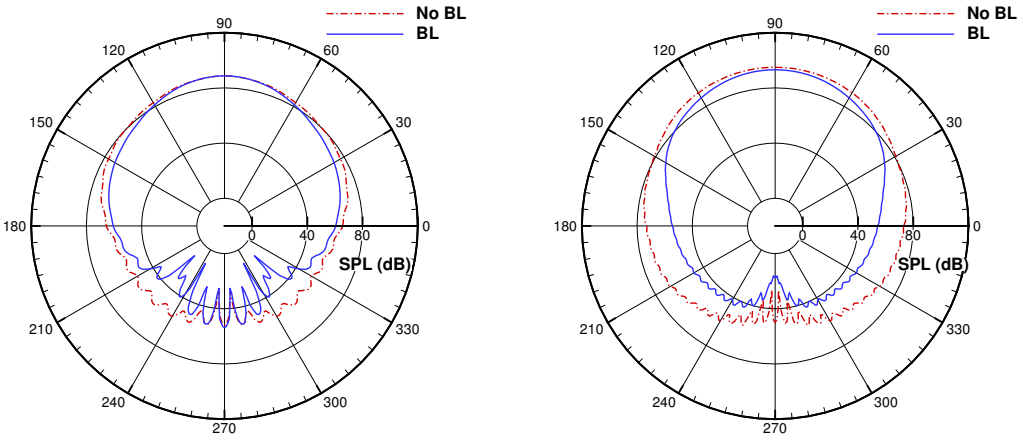

(a) 400 Hz (b) 800 Hz

FIGURE 5.23: SPL on the cylinder surface along $r|_{x=0.5} = 2$. $M = 0.3$.

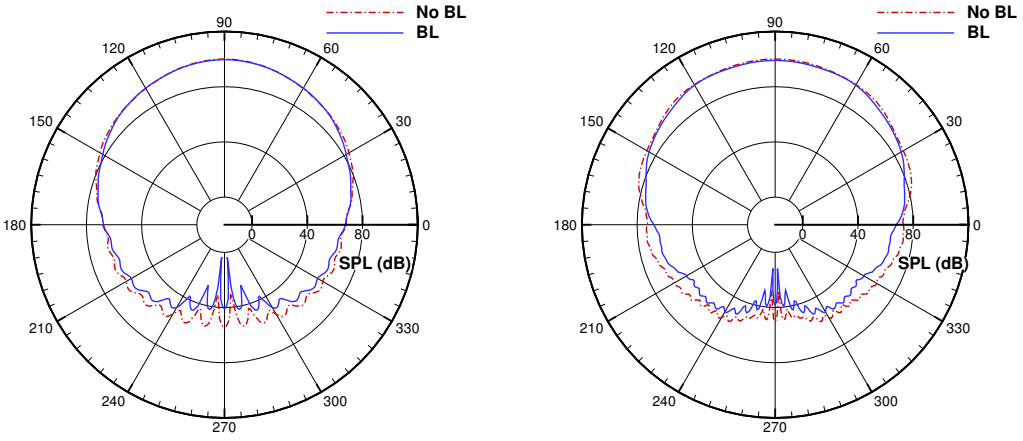

(a) 400 Hz (b) 800 Hz

FIGURE 5.24: SPL on the cylinder surface along $r|_{x=4} = 2$. $M = 0.3$.

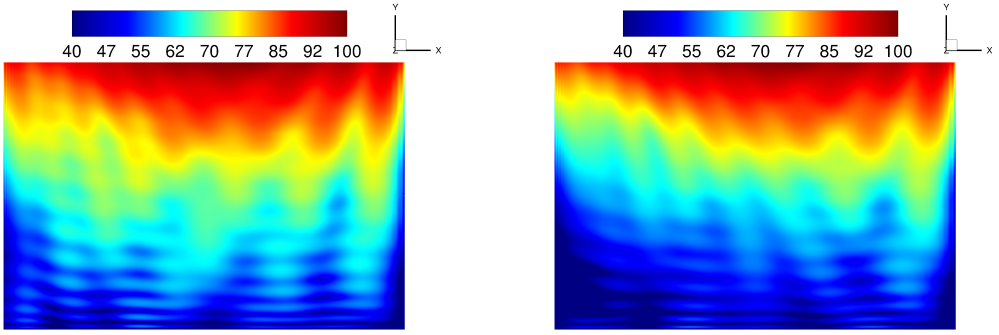

(a) No BL (b) BL

FIGURE 5.25: SPL on the cylinder surface from the side view. $M = 0.3$, 400 Hz

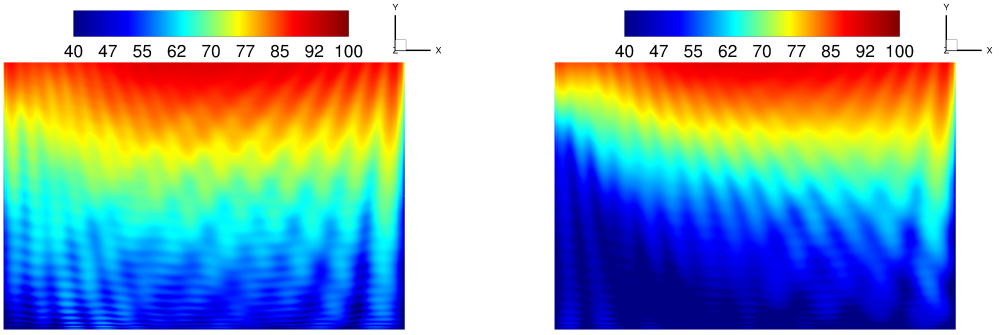

(a) No BL (b) BL

FIGURE 5.26: SPL on the cylinder surface from the side view. $M = 0.3$, 800 Hz

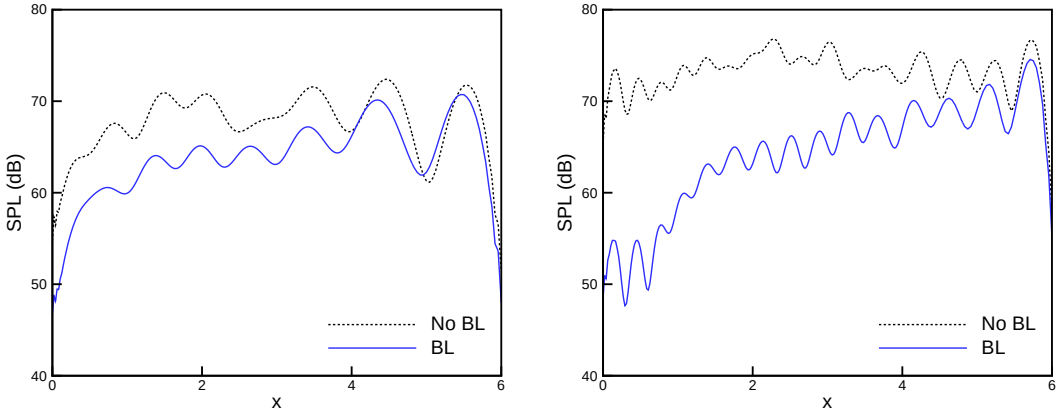

(a) 400 Hz (b) 800 Hz

FIGURE 5.27: SPL on the cylinder surface along $z = 2$ lines. $M = 0.3$.

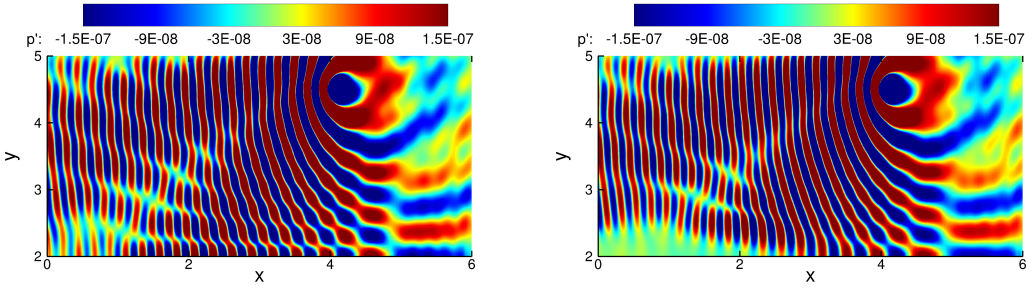

(a) No BL (b) BL

FIGURE 5.28: Pressure perturbation on the streamwise symmetry surface ($z = 0$ face). $M = 0.75$, 400 Hz

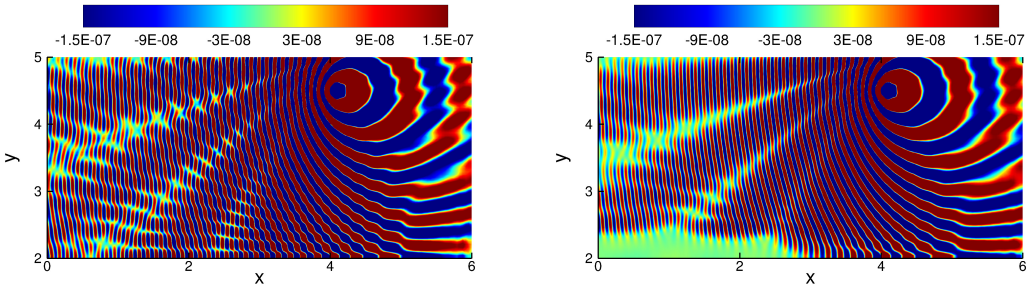

(a) No BL (b) BL

FIGURE 5.29: Pressure perturbation on the streamwise symmetry surface ($z = 0$ face). $M = 0.75$, 800 Hz

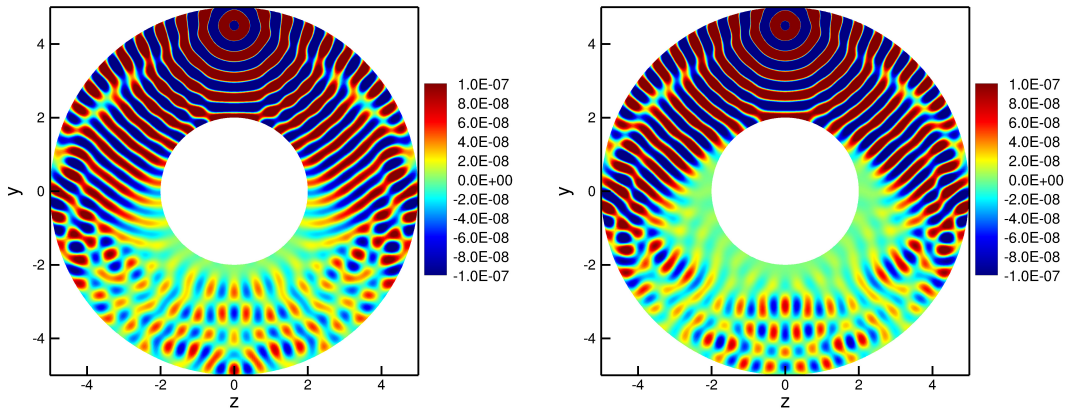

(a) No BL (b) BL

FIGURE 5.30: Pressure perturbations on the $x = 4$ face. $M = 0.75$, 400 Hz

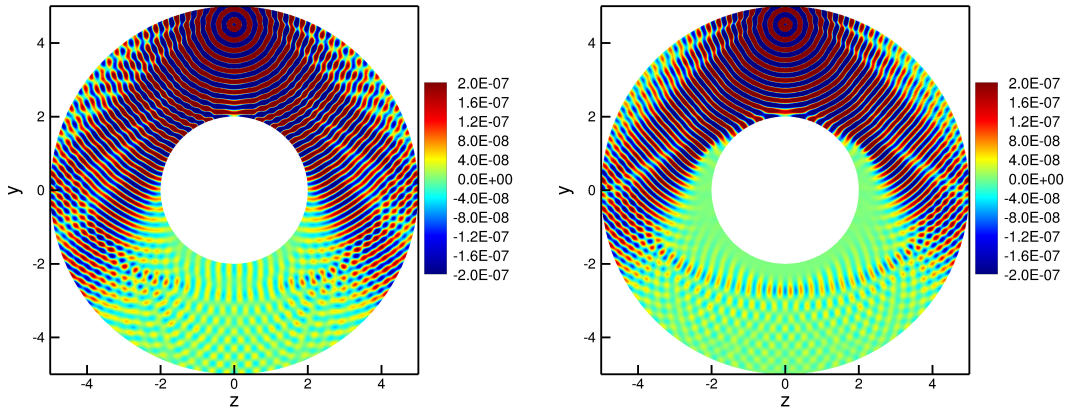

(a) No BL (b) BL

FIGURE 5.31: Pressure perturbations on the $x = 4$ face. $M = 0.75$, 800 Hz

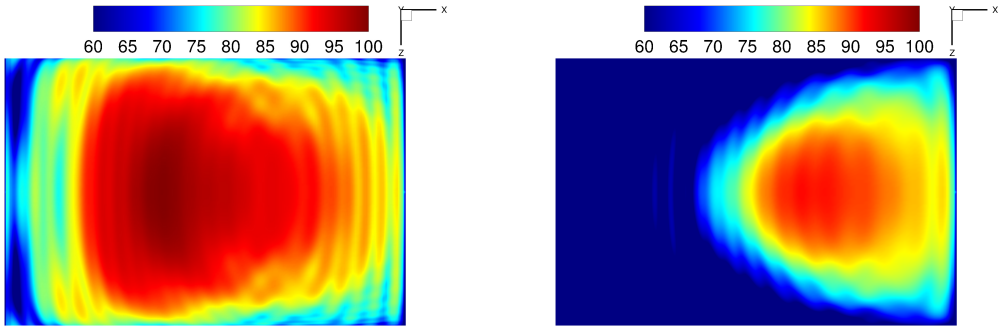

(a) No BL (b) BL

FIGURE 5.32: SPL on the cylinder surface from the top view. $M = 0.75$, 400 Hz

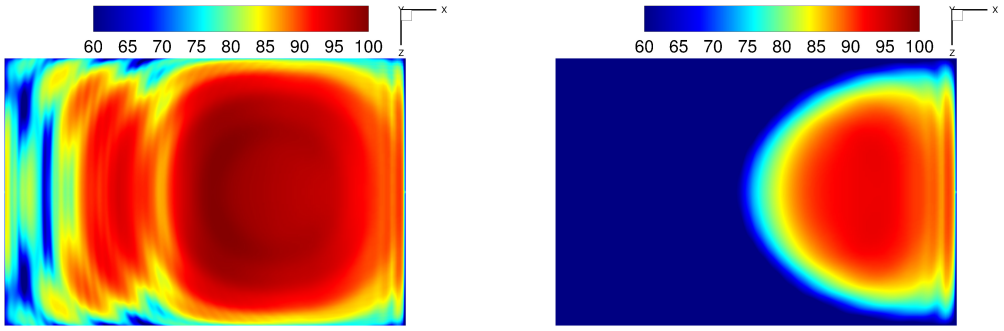

(a) No BL (b) BL

FIGURE 5.33: SPL on the cylinder surface from the top view. $M = 0.75$, 800 Hz

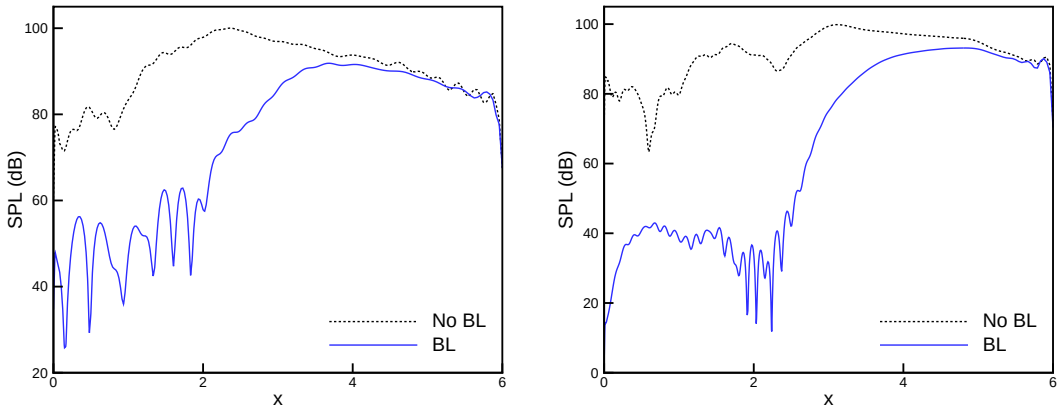

(a) 400 Hz (b) 800 Hz

FIGURE 5.34: SPL on the cylinder surface along $y = 2$ lines. $M = 0.75$.

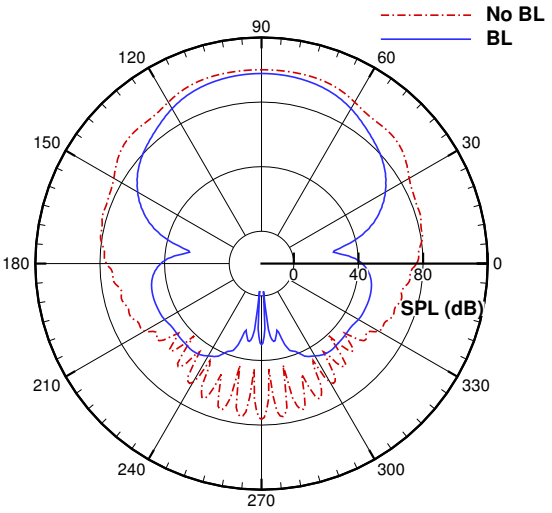

(a) 400 Hz

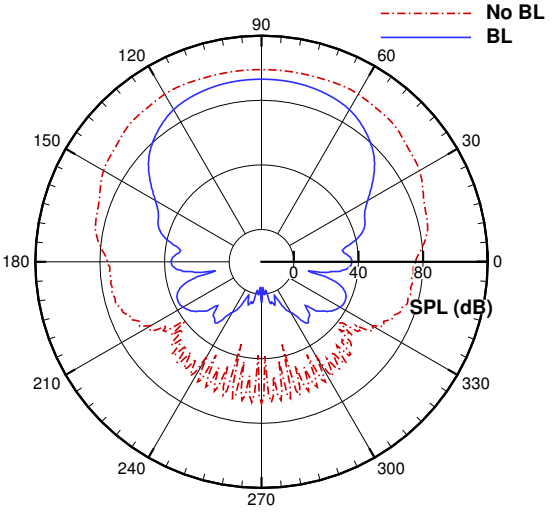

(b) 800 Hz

FIGURE 5.35: SPL on the cylinder surface along $r|_{x=4} = 2$. $M = 0.75$.

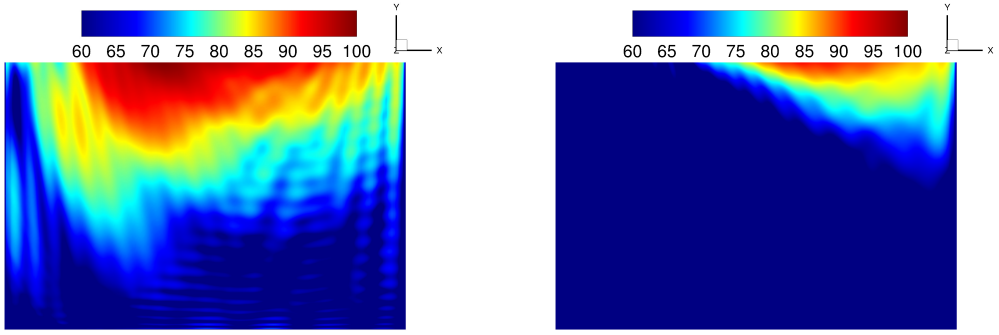

(a) No BL (b) BL

FIGURE 5.36: SPL on the cylinder surface from the side view. $M = 0.75$, 400 Hz

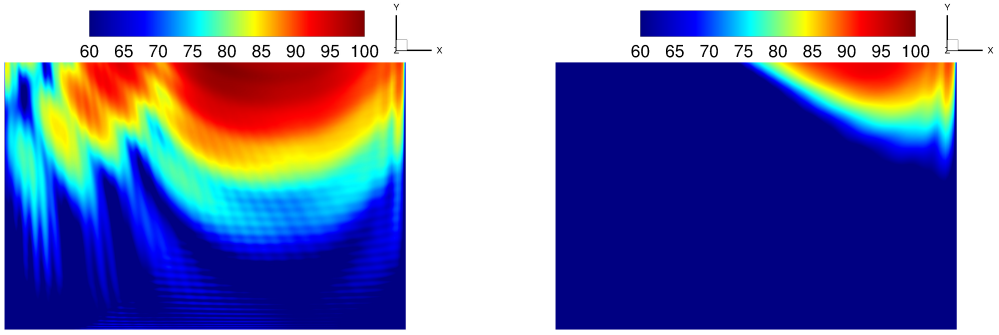

(a) No BL (b) BL

FIGURE 5.37: SPL on the cylinder surface from the side view. $M = 0.75$, 800 Hz

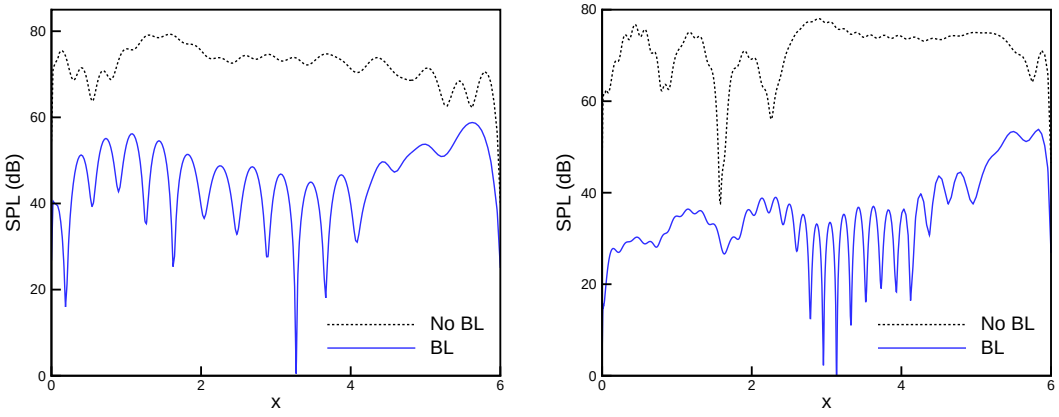

(a) 400 Hz (b) 800 Hz

FIGURE 5.38: SPL on the cylinder surface along $z = 2$ lines. $M = 0.75$.

5.5 Lengthened Cylinder

At the take-off condition the main concern is the far-field noise distribution. The results at the emulated take-off condition for the cylinder model have shown that the sound field on the cylinder surface is apparently altered due to the boundary layer, especially in the very upstream regions. However, the cylinder model is not long enough to obtain a reasonable evaluation for the far-field acoustic distribution, and the length should be extended comparable to that of a realistic aircraft. At such a length, the SPL distinctions in the very upstream regions are assumed to develop sufficiently.

Figure 5.39 and Figure 5.40 shows apparently modifications of the acoustic fields at the front of the cylinder surface due to the boundary layer, although the differences are moderate. Especially in the upstream marginal regions, the boundary layer leads to apparent reductions in SPL magnitudes although the area affected is quite limited and not developed along the upstream direction. In terms of the FW-H integral surface, no obvious differences are observed as shown in Figure 5.41 and Figure 5.42. As more precisely shown in Figure 5.43, rare differences in magnitude between the "BL"and "no BL"cases are given on $y = 4.7$ lines, but the wavy distributions show obvious phase changes; meanwhile, on $z = 4.7$ lines, the SPL magnitudes show apparent distinctions which increase towards the front of the cylinder, and the "BL"case gives higher SPL values. Figure 5.44 gives the far-field acoustic directivity, where 0° and 180° angles correspond to the downstream and upstream directions, respectively. As shown, the SPL values agree well at most of the directions which range from 0° to almost 150° angles. In the range of 150°-180° angles, the case solved with the boundary layer demonstrates much higher values and the differences reach about 6 dB at most.

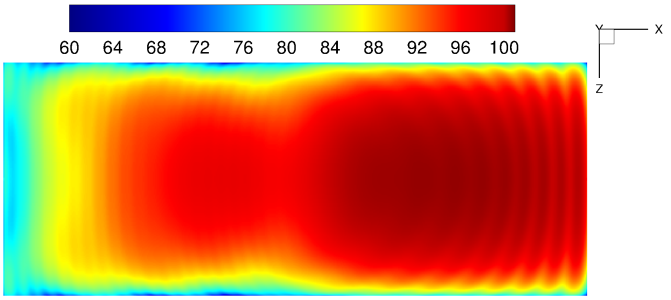

(a) No BL

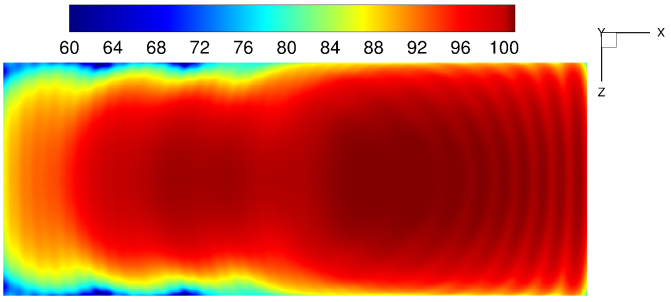

(b) BL

FIGURE 5.39: SPL on the cylinder surface from the top view.

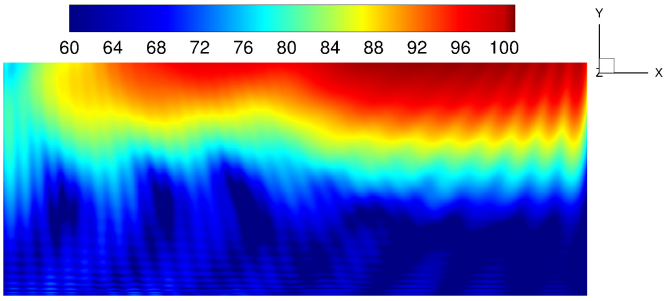

(a) No BL

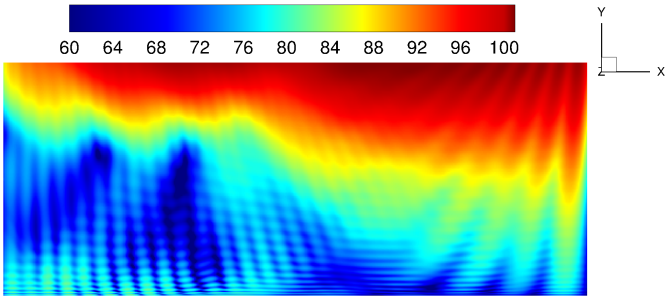

(b) BL

FIGURE 5.40: SPL on the cylinder surface from the side view.

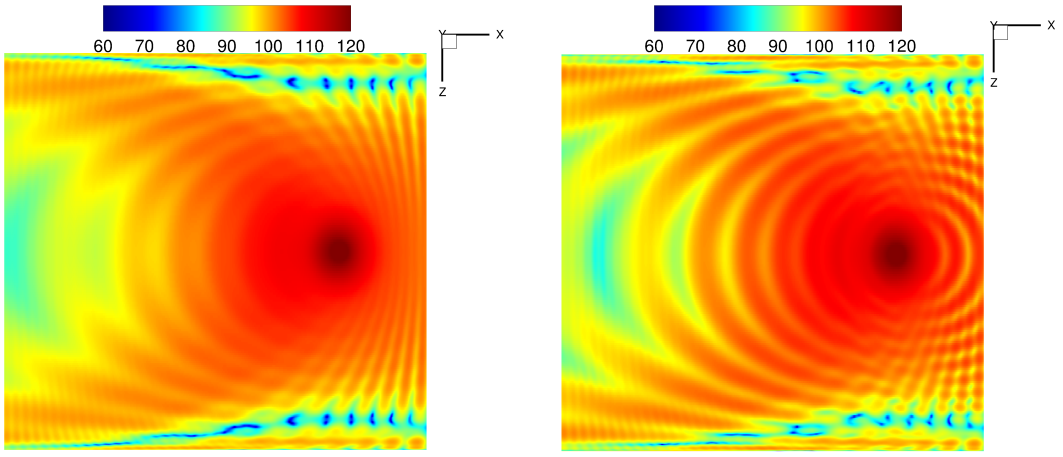

(a) No BL (b) BL

FIGURE 5.41: SPL on the cylindrical surface for FW-H integral from the top view.

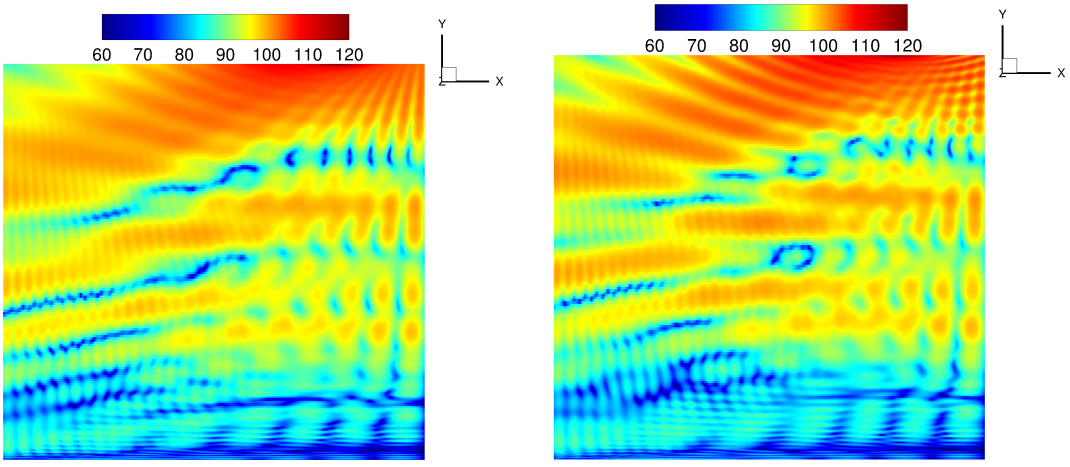

(a) No BL (b) BL

FIGURE 5.42: SPL on the cylindrical surface for FW-H integral from the side view.

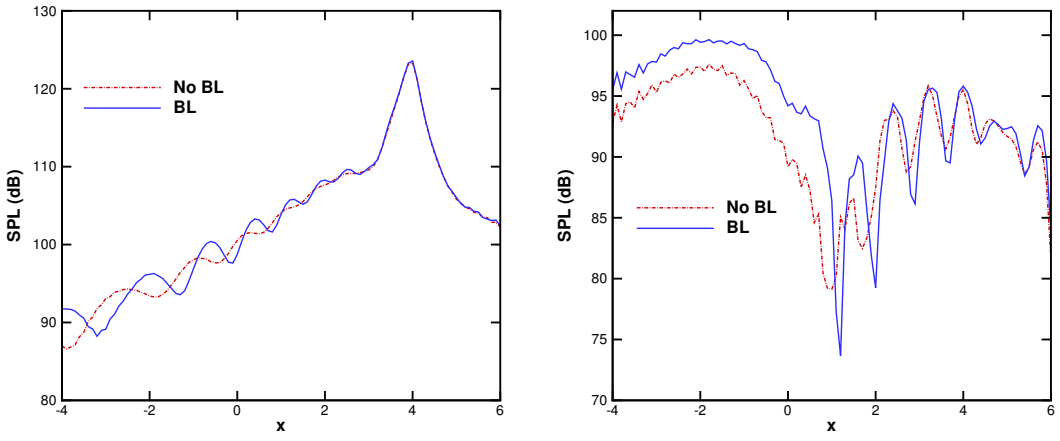

(a) $y = 4.7$ (b) $z = 4.7$

FIGURE 5.43: SPL on the FW-H integral surface along the streamwise lines.

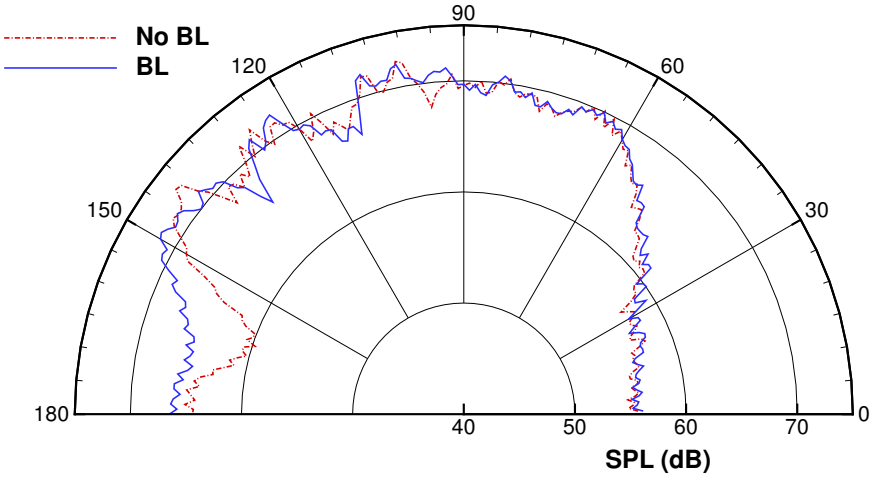

FIGURE 5.44: Far-field acoustic directivity solved by the FW-H solver.

5.6 Summary

In this chapter, the effects of the wall boundary layer to the sound wave propagation are investigated in terms of the external flow, where the mean-flow convection and refraction effects play important roles. Generally, as mentioned in Section 4.1.2, the mean-flow convection effect decreases the wavenumber of the downstream propagating waves and increases the wavenumber of the upstream propagating waves; meanwhile, due to the mean-flow refraction effect, the downstream waves are refracted toward the wall while the upstream waves are refracted away from the wall.

Through three simplified models, some similar conclusions are found in general. Firstly, significant refraction effects are found for the emulated cruise condition in the near-wall areas, and the boundary layer refraction results in a "quiet"zone in the upstream region. Secondly, the "quiet"zone is enlarged at the higher frequency, namely the refraction effect depends on the Helmholtz numbers based on the boundary layer thickness. Furthermore, as the mean-flow convection effect alters the wavenumber correspondingly, the acoustic energy distributed in one meter increases in the upstream region while decreases in the downstream region, whereby the SPL at the upstream regions near the source location is higher than that in the downstream regions if the boundary layer is not taken into account or shows refraction effects rarely. Moreover, the mean-flow convection enlarges the actual upstream region near the wall.

Also, the results obtained from the three models show apparent differences. At the emulated take-off condition, the results from the flat plate model do not show obvious refraction effects for both the lower and higher frequencies. Nevertheless, for the cylinder model, noticeable distinctions of the SPL distribution due to the boundary layer appear in the upstream marginal regions. This is induced due to the relatively large incident angles of the sound waves into the boundary layer. Therefore, the refraction effect

also largely depends on the acoustic incident angle into the boundary layer. At the emulated take-off condition, although obvious differences appear on the cylinder surface in a limited area due to boundary layer, the acoustic fields show rare alterations on the FW-H integral face. For the resulting far-field directivity, the SPL values solved with/without the boundary layer agree well at most of the directions which range from 0° to almost 150° angles. However, higher levels emerge in the directions from 150° to 180° angles when solving with the wall boundary layer, and the difference is up to about 6 dB.

Chapter 6

Conclusions and Future Work

6.1 Concluding Remarks

This work aims to develop a novel linearised numerical model to simulate the sound propagation. This work makes itself meaningful mainly from two aspects. The first is related to the instability issue for the traditional linear acoustic propagation models. Of most interest, these linear numerical models for example the LEE, are used to simulate the sound propagation in turbulent flows where the flow fields are not uniform enough to justify the use of analytical methods, such as the acoustic analogy. However, the two step approach which includes a flow solver and an acoustic solver, often discards the turbulence information when introducing the mean values of the base flow into the linearised perturbation equations. This results in the base flow owning actual laminar parallel velocity profiles in the absence of turbulence, whereby the traditional problem of the fluid dynamic instability takes place. The other aspect to make the proposed LNS approach useful is in relation to the attenuation of sound by turbulence. This problem attracts concerns especially in duct flows. Experiments, analytical models and the wave equation method have been carried out to quantify such acoustic damping. Nevertheless, the proposed LNS method makes itself superior as in theory the linearised perturbation equation can tackle arbitrary flow profiles and geometries, also the LNS method can deal with broadband acoustic waves. Intuitively, the above two problems are rarely relevant, however, they are connected by the turbulence effect in such a linearised numerical acoustic model. Precisely, the perturbation Reynolds stress plays a key role in connecting the two types of problems. As is already demonstrated, the PRS terms stabilise the initially unstable hydrodynamic-acoustic system, while they resolve the acoustic-vorticity interaction in this linear model and thus obtains quantitative results for the acoustic damping in duct flows.

The proposed LNS method is different from the traditional linearised Navier-Stokes equations by incorporating the mean turbulent information. To deduce the relevant formulas the triple decomposition are introduced, hence the flow variables are decomposed into the time-mean part, organised disturbance and the turbulent component.

This results in a practical difficulty to derive the compressible governing equations. Traditionally, the Favre averaging methodology applies the density-weighted time average to the velocity, thus the processes of establishing the compressible Reynolds-averaged Navier-Stokes equations are significantly simplified. Nevertheless, due to the triple decomposition the traditional Favre averaging methodology is not applicable. Eventually, this practical difficulty is resolved by creatively extending the Favre averaging methodology, namely introducing a density-weighted "phase"average velocity into the original triple decomposition. In this way the novel mean-flow governing equations are obtained although almost taking the forms of the Favre averaged mean conservation equations. Mainly, the density-weighted velocities averaged in "phase"and "time"are different due to an extra component which represents the effect of organized waves to the mean flow. Nevertheless, if assuming a linear relationship between the hydrodynamic field and the acoustic waves, the extra term can be ignored and this indicates that the mean flow is independent from the perturbations. Finally, the compressible linearised Navier-Stokes equations for organised motions are derived and the PRS terms play a key role. As is described, the models for the PRS terms are based on the Boussinesq hypothesis and can be classified into tree types, namely the quasi-laminar one, the quasi-steady one and the non-equilibrium model. At present the LNS method employs a quasi-steady model which can be straightforward implemented into the equations while provides mostly the mechanisms of interest.

After establishing the formulas for the LNS method, there is an immediate practical numerical problem, namely the grid guidance for the proposed numerical model. Firstly, in respect of the normal problem of the sound propagation in Chapter 3, the grid convergence study shows the grid with $PPW = 10$ can obtain the grid convergent results with satisfactory error bands in most of the computational regions, while the gird with $PPW = 7$ gives relatively large errors but could provide grid convergent results at acceptable error levels in most of the computational regions. Furthermore, from the whole computational field of view, the grid convergence study demonstrates that the solution accuracy degrades for both the LEE and LNS method when the angle of the sound radiation from the duct is greater than 90°. For the LNS results, some relatively great errors appear discretely in the vortex sheet wake which is initiated by the sound waves, while in most of the computational regions the error bands are maintained under a sufficiently small level. For the LEE results, the situations are quite different. Most distinctively, quite great relative errors emerge in the vortex sheet wake and the errors are improved by refining the grid. Probably owing to the grid-dependent results of the instability waves which impose influence on the acoustic propagation directivity, considerable errors appear along the sound radiating paths and the grid independence of results in the regions beyond the 90° radiation angle behaves worse than that for the LNS results. In short, besides the time-asymptotic feature, the grid convergence study discovers the solution solved by the LEE method is also dependent on the spatial resolution if an unstable system is present. Secondly, in terms of the problem of acoustic

damping, the grid convergence study for the SPL difference demonstrates the grid should have at least 20 points in a wavelength to gain satisfactory accuracy. In addition, the spatial resolution study in respect of the acoustic boundary layer shows the resolution set with 15 points is fine enough to resolve the ABL.

As one of the two objectives, the stability of the LNS method dealing with sound propagation in shear flows is investigated in Chapter 3. First of all, the hydrodynamic stability analysis in turbulent flows is performed in terms of two simplified jet profiles and demonstrates the fundamental mechanisms of the stability of the LNS formula. Subsequently, the stability, as well as the effect of the PRS terms on the sound propagation are evaluated by two numerical experiments. The first one which is a relatively simple case of noise radiation from a semi-infinite duct is carried out and incorporates an algebraic eddy viscosity model. The stable simulations are delivered; In terms of the acoustic far-field directivity, the turbulence information included in the LNS formulations demonstrate lesser effects than the ignored gradient terms in the GTS formulations in this case. All the numerical solutions have reasonable agreements with the Munt solutions. The second one simulates the realistic turbofan aft noise radiation. The stability as well as the vortex shedding frequency are identified at first. The features of the simulated results for the three approaches can be concluded as: the LNS method presents stable simulations while resolves the instability waves which are maintained at a relatively steady status; whilst the LEE method presents unstable simulations and the instability waves are over-predicted; finally the GTS method gives stable simulations and excludes the instability waves. Owing to these features, the differences for the near-field and far-field results can be attributed to two main factors, namely the damping effect of turbulence and the influence of the instability waves. The former leads to significant differences of near-field pressure levels in the mixing layers in comparison of the LNS results with others. As the damping effect of turbulence becomes stronger at higher frequencies, the differences of near-field pressure levels are enlarged when the frequency increases. Nevertheless, the differences in the near-field pressure levels barely lead to the corresponding alterations in the far-field acoustic distributions. For the latter factor, the instability wave results in alterations to the sound propagation, probably by refractions and reflections, and the effects are in general moderate. Since the instability waves taking the forms of vortex shedding are weaker at higher frequencies, the consistency among the results of far-field acoustic directivity is improved. Also, probably as both the LNS and LEE methods resolves the instability waves to some degrees, the corresponding consistency in far-field acoustic directivity is better than that between the LEE and GTS results.

Afterwards, the LNS method is used to resolve the attenuation of sound in turbulent pipe flows. Firstly, through a generally used plane wave case the LNS method demonstrates the satisfactory accuracy in term of the quasi-steady turbulent model. The growing trend of the normalised attenuation coefficient as a function of the non-dimensional thickness of the ABL is identified which is attributed to the turbulence effect. Also, the convection effect shows its dominant role in the mean-flow effects by

comparing the upstream and downstream results. Subsequently, the acoustic damping induced by turbulence at high-order spinning modes is investigated. It is clearly shown that the turbulence effect results in considerable damping of the sound waves at high-order duct modes, as well as the tendency of the acoustic damping growing with the increasing dimensionless ABL thickness is clearly demonstrated. Moreover, as is observed, the acoustic distributions along the duct cross-section vary at different modes. Especially, when the azimuthal modes is higher the acoustic energy concentrates towards the wall and the SPL near the central axis drops. This therefore results in an approximate relationship of the attenuation of sound increasing with the higher azimuthal modes. Besides, the mean-flow convection effect results in a decreasing trend of the growth rate at relatively high Mach numbers for modes $(0, 1)$, $(0, 2)$ and $(1, 0)$.

Finally, the effect of the wall boundary layer is studied in terms of two concerns. Three models to different degrees of simplification are employed. At the emulated cruise condition, significant refraction effects are found and improved at the higher Helmholtz number. The boundary layer refraction results in the quiet zone in the upstream region, therefore the boundary layer effect is suggested considerable for the cabin noise study in terms of the engine noise impact on the fuselage. At the emulated take-off condition, the flat plate model shows rare distinctions induced by the boundary layer, whereas the cylinder model demonstrates the alterations of the acoustic field in the very upstream regions. This is further investigated by a lengthened cylinder model, and the resulting effect on the far-field sound directivity is the main concern in this subject. Eventually, the far-field results show weak distinctions in most of the directions, nevertheless, in the range of 150°-180° angles namely in the upstream directions, the boundary layer leads to higher sound pressure levels which are higher up to about 6 dB.

In the end, the creative outcomes of the PhD work can be summarised as follows.

1. Completely compressible linearised Navier-Stokes equations including turbulence information;
2. Grid convergence study deriving the grid guidance for resolving acoustic damping;
3. Grid convergence study revealing the grid dependence of the LEE solutions;
4. Stable simulations of the sound propagation in shear flows performed by the LNS method;
5. Resolving the attenuation of sound in turbulent pipe flows by a linear acoustic propagation numerical model;
6. Resolving the damping of sound waves at high-order spinning duct modes;
7. Evaluation of the influence of wall boundary layer on the far-field acoustic directivity, in respect of an emulated model of the engine noise scattering by the fuselage at take-off condition;

6.2 Suggestions for Future Work

Firstly, to complete the formulations of the LNS method, the energy equation is necessarily deduced into the current theoretical frame, whereby the thermal effect can be considered. A situation of immediate interest is the presence of high temperature ratio and density ratio, such as the aft fan noise radiation problem. Also, in the duct acoustic problem, the viscous-thermal effect is of importance at times. To improve the current approach, a non-equilibrium model can be employed to include the non-equilibrium effects of turbulence, especially when aiming to resolve the attenuation of sound by turbulence. Also, the two-and-a-half dimensional approach is extremely useful to deal with the problems of the high-order duct mode propagation and should be developed for the LNS method.

So far, a primary work was carried out to practise the LNS method. This method has the intention to be a generalised approach in the field of linear aeroacoustics. It is expected to be applied to complex industrial cases, such as the problem of aft fan noise shielded by a wing, where serious acoustic-structure and acoustic-vorticity interactions are present. Furthermore, although it should be included for some applications the turbulence effect on the sound propagation is generally ignored for such as sound propagation along lined walls. The viscosity has already been considered in such problems [222] and shows obvious influence. The effects of turbulence especially within the boundary layer with regards to the lined wall on the sound waves could be an interesting topic for the future research.

Appendix A

Momentum Equations for the GTS method

According to [83], the original momentum equations after dropping the term $\boldsymbol{H}$ for the GTS method are given as

$$\frac{\partial\left(\bar{\rho}u_1'\right)}{\partial t}+\frac{\partial\left(\bar{u}_1\bar{\rho}u_1'+p'\right)}{\partial x_1}+\frac{\partial\left(\bar{u}_2\bar{\rho}u_1'\right)}{\partial x_2}=S_1, \tag{A.1a}$$

$$\frac{\partial\left(\bar{\rho}u_2'\right)}{\partial t}+\frac{\partial\left(\bar{u}_1\bar{\rho}u_2'\right)}{\partial x_1}+\frac{\partial\left(\bar{u}_2\bar{\rho}u_2'+p'\right)}{\partial x_2}=S_2. \tag{A.1b}$$

Ignoring the aerodynamic source terms, the equations can be rewritten as

$$\begin{aligned}&\bar{\rho}\frac{\partial u_1'}{\partial t}+\bar{\rho}\bar{u}_1\frac{\partial u_1'}{\partial x_1}+\bar{\rho}\bar{u}_2\frac{\partial u_1'}{\partial x_2}+\frac{\partial p'}{\partial x_1}\\ &+u_1'\frac{\partial\bar{\rho}}{\partial t}+\bar{\rho}u_1'\frac{\partial\bar{u}_1}{\partial x_1}+\bar{u}_1u_1'\frac{\partial\bar{\rho}}{\partial x_1}+\bar{\rho}u_1'\frac{\partial\bar{u}_2}{\partial x_2}+\bar{u}_2u_1'\frac{\partial\bar{\rho}}{\partial x_2}=0,\end{aligned} \tag{A.2a}$$

$$\begin{aligned}&\bar{\rho}\frac{\partial u_2'}{\partial t}+\bar{\rho}\bar{u}_1\frac{\partial u_2'}{\partial x_1}+\bar{\rho}\bar{u}_2\frac{\partial u_2'}{\partial x_2}+\frac{\partial p'}{\partial x_2}\\ &+u_2'\frac{\partial\bar{\rho}}{\partial t}+\bar{\rho}u_2'\frac{\partial\bar{u}_1}{\partial x_1}+\bar{u}_1u_2'\frac{\partial\bar{\rho}}{\partial x_1}+\bar{\rho}u_2'\frac{\partial\bar{u}_2}{\partial x_2}+\bar{u}_2u_2'\frac{\partial\bar{\rho}}{\partial x_2}=0.\end{aligned} \tag{A.2b}$$

And the continuity equation for the mean flow gives

$$\frac{\partial\bar{\rho}}{\partial t}+\bar{\rho}\frac{\partial\bar{u}_1}{\partial x_1}+\bar{u}_1\frac{\partial\bar{\rho}}{\partial x_1}+\bar{\rho}\frac{\partial\bar{u}_2}{\partial x_2}+\bar{u}_2\frac{\partial\bar{\rho}}{\partial x_2}=0. \tag{A.3}$$

Multiplying Equation A.3 by u_1' and u_2', respectively, then substituting the resulting equations into Equation A.2 gives

$$\bar{\rho}\frac{\partial u_1'}{\partial t}+\bar{\rho}\bar{u}_1\frac{\partial u_1'}{\partial x_1}+\bar{\rho}\bar{u}_2\frac{\partial u_1'}{\partial x_2}+\frac{\partial p'}{\partial x_1}=0, \tag{A.4a}$$

$$\bar{\rho}\frac{\partial u_2'}{\partial t}+\bar{\rho}\bar{u}_1\frac{\partial u_2'}{\partial x_1}+\bar{\rho}\bar{u}_2\frac{\partial u_2'}{\partial x_2}+\frac{\partial p'}{\partial x_2}=0, \tag{A.4b}$$

which are equivalent forms of the momentum equations for the GTS method used by Bogey et al. [83]. As shown, all the terms related to the derivatives of the mean velocity are removed from the momentum equations of the LEE method.

Alternatively, the terms related to $\partial \bar{u}_i / \partial x_i$ can be conserved to attain relative minor modifications to the momentum equations, which gives

$$\bar{\rho}\frac{\partial u_1'}{\partial t} + \bar{\rho}\bar{u}_1\frac{\partial u_1'}{\partial x_1} + \bar{\rho}\bar{u}_2\frac{\partial u_1'}{\partial x_2} + \frac{\partial p'}{\partial x_1} + \bar{\rho}u_1'\frac{\partial \bar{u}_1}{\partial x_1} + \rho'\bar{u}_1\frac{\partial \bar{u}_1}{\partial x_1} = 0, \tag{A.5a}$$

$$\bar{\rho}\frac{\partial u_2'}{\partial t} + \bar{\rho}\bar{u}_1\frac{\partial u_2'}{\partial x_1} + \bar{\rho}\bar{u}_2\frac{\partial u_2'}{\partial x_2} + \frac{\partial p'}{\partial x_2} + \bar{\rho}u_2'\frac{\partial \bar{u}_2}{\partial x_2} + \rho'\bar{u}_2\frac{\partial \bar{u}_2}{\partial x_2} = 0. \tag{A.5b}$$

The GTS method in this form is employed by Zhang et al. [84] and Tester et al. [85], as well as in this thesis.

Appendix B

Governing equations for the proposed LNS method

Expanding Equation 2.20 yields

$$\frac{\partial \bar{\rho}}{\partial t}+\frac{\partial \tilde{\rho}}{\partial t}+\frac{\partial \acute{\rho}}{\partial t}+\frac{\partial}{\partial x_i}\left(\bar{\rho}\bar{u}_i^{\rho}\right)+\frac{\partial}{\partial x_i}\left(\bar{\rho}\tilde{u}_i\right)+\frac{\partial}{\partial x_i}\left(\tilde{\rho}\bar{u}_i^{\rho}\right)+\frac{\partial}{\partial x_i}\left(\tilde{\rho}\tilde{u}_i\right)+\frac{\partial}{\partial x_i}\left(\acute{\rho}\bar{u}_i^{\rho}\right)+\frac{\partial}{\partial x_i}\left(\acute{\rho}\tilde{u}_i\right)+\frac{\partial}{\partial x_i}\left(\rho u_i^{''}\right)=0, \tag{B.1a}$$

$$\begin{aligned}&\frac{\partial}{\partial t}\left(\bar{\rho}\bar{u}_i^{\rho}\right)+\frac{\partial}{\partial t}\left(\bar{\rho}\tilde{u}_i\right)+\frac{\partial}{\partial t}\left(\tilde{\rho}\bar{u}_i^{\rho}\right)+\frac{\partial}{\partial t}\left(\tilde{\rho}\tilde{u}_i\right)+\frac{\partial}{\partial t}\left(\acute{\rho}\bar{u}_i^{\rho}\right)+\frac{\partial}{\partial t}\left(\acute{\rho}\tilde{u}_i\right)+\frac{\partial}{\partial t}\left(\rho u_i^{''}\right)\\&+\frac{\partial}{\partial x_j}\left(\bar{\rho}\bar{u}_i^{\rho}\bar{u}_j^{\rho}\right)+\frac{\partial}{\partial x_j}\left(\bar{\rho}\bar{u}_i^{\rho}\tilde{u}_j\right)+\frac{\partial}{\partial x_j}\left(\bar{\rho}\tilde{u}_i\bar{u}_j^{\rho}\right)+\frac{\partial}{\partial x_j}\left(\bar{\rho}\tilde{u}_i\tilde{u}_j\right)\\&+\frac{\partial}{\partial x_j}\left(\tilde{\rho}\bar{u}_i^{\rho}\bar{u}_j^{\rho}\right)+\frac{\partial}{\partial x_j}\left(\tilde{\rho}\bar{u}_i^{\rho}\tilde{u}_j\right)+\frac{\partial}{\partial x_j}\left(\tilde{\rho}\tilde{u}_i\bar{u}_j^{\rho}\right)+\frac{\partial}{\partial x_j}\left(\tilde{\rho}\tilde{u}_i\tilde{u}_j\right)\\&+\frac{\partial}{\partial x_j}\left(\acute{\rho}\bar{u}_i^{\rho}\bar{u}_j^{\rho}\right)+\frac{\partial}{\partial x_j}\left(\acute{\rho}\bar{u}_i^{\rho}\tilde{u}_j\right)+\frac{\partial}{\partial x_j}\left(\acute{\rho}\tilde{u}_i\bar{u}_j^{\rho}\right)+\frac{\partial}{\partial x_j}\left(\acute{\rho}\tilde{u}_i\tilde{u}_j\right)\\&+\frac{\partial}{\partial x_j}\left(\rho u_i^{''}u_j^{''}\right)+\frac{\partial}{\partial x_j}\left(\rho u_j^{''}\bar{u}_i^{\rho}\right)+\frac{\partial}{\partial x_j}\left(\rho u_j^{''}\tilde{u}_i\right)+\frac{\partial}{\partial x_j}\left(\rho u_i^{''}\bar{u}_j^{\rho}\right)+\frac{\partial}{\partial x_j}\left(\rho u_i^{''}\tilde{u}_j\right)\\&=-\frac{\partial \bar{p}}{\partial x_i}-\frac{\partial \tilde{p}}{\partial x_i}-\frac{\partial \acute{p}}{\partial x_i}+\frac{\partial \bar{\tau}_{ij}}{\partial x_j}+\frac{\partial \tilde{\tau}_{ij}}{\partial x_j}+\frac{\partial \acute{\tau}_{ij}}{\partial x_j}.\end{aligned} \tag{B.1b}$$

Taking time averages of the above equations and using the relations in Equation 2.8 and Equation 2.18, give

$$\frac{\partial \bar{\rho}}{\partial t}+\frac{\partial}{\partial x_i}\left(\bar{\rho}\bar{u}_i^{\rho}\right)+\frac{\partial}{\partial x_i}\overline{\tilde{\rho}\tilde{u}_i}=0, \tag{B.2a}$$

$$\begin{aligned}&\frac{\partial}{\partial t}\left(\bar{\rho}\bar{u}_i^{\rho}\right)+\frac{\partial}{\partial x_j}\left(\bar{\rho}\bar{u}_i^{\rho}\bar{u}_j^{\rho}\right)+\frac{\partial}{\partial t}\overline{\tilde{\rho}\tilde{u}_i}+\frac{\partial}{\partial x_j}\overline{\bar{\rho}\tilde{u}_i\tilde{u}_j}+\frac{\partial}{\partial x_j}\overline{\tilde{\rho}\bar{u}_i^{\rho}\tilde{u}_j}+\frac{\partial}{\partial x_j}\overline{\tilde{\rho}\tilde{u}_i\bar{u}_j^{\rho}}+\frac{\partial}{\partial x_j}\overline{\tilde{\rho}\tilde{u}_i\tilde{u}_j}\\&=-\frac{\partial \bar{p}}{\partial x_i}+\frac{\partial \bar{\tau}_{ij}}{\partial x_j}-\frac{\partial}{\partial x_j}\overline{\rho u_i^{''}u_j^{''}}.\end{aligned} \tag{B.2b}$$

Furthermore, dropping the time derivatives of the time-mean parts and the second and higher order terms in relation to perturbations, yields the governing equations for the mean flow

$$\frac{\partial}{\partial x_i}\left(\bar{\rho}\bar{u}_i^{\rho}\right) = 0, \tag{B.3a}$$

$$\frac{\partial}{\partial x_j}\left(\bar{\rho}\bar{u}_i^{\rho}\bar{u}_j^{\rho}\right) = -\frac{\partial \bar{p}}{\partial x_i} + \frac{\partial \bar{\tau}_{ij}}{\partial x_j} - \frac{\partial}{\partial x_j}\overline{\rho u_i'' u_j''}. \tag{B.3b}$$

Applying the operator of the phase average to Equation B.1, as well as using the relations in Equation 2.8 and Equation 2.17, give

$$\frac{\partial \bar{\rho}}{\partial t} + \frac{\partial \tilde{\rho}}{\partial t} + \frac{\partial}{\partial x_i}\left(\bar{\rho}\bar{u}_i^{\rho}\right) + \frac{\partial}{\partial x_i}\left(\bar{\rho}\tilde{u}_i\right) + \frac{\partial}{\partial x_i}\left(\tilde{\rho}\bar{u}_i^{\rho}\right) + \frac{\partial}{\partial x_i}\left(\tilde{\rho}\tilde{u}_i\right) = 0, \tag{B.4a}$$

$$\begin{aligned}
&\frac{\partial}{\partial t}\left(\bar{\rho}\tilde{u}_i\right) + \frac{\partial}{\partial t}\left(\tilde{\rho}\bar{u}_i^{\rho}\right) + \frac{\partial}{\partial t}\left(\tilde{\rho}\tilde{u}_i\right) \\
&+\frac{\partial}{\partial x_j}\left(\bar{\rho}\bar{u}_i^{\rho}\bar{u}_j^{\rho}\right) + \frac{\partial}{\partial x_j}\left(\bar{\rho}\bar{u}_i^{\rho}\tilde{u}_j\right) + \frac{\partial}{\partial x_j}\left(\bar{\rho}\tilde{u}_i\bar{u}_j^{\rho}\right) + \frac{\partial}{\partial x_j}\left(\bar{\rho}\tilde{u}_i\tilde{u}_j\right) \\
&+\frac{\partial}{\partial x_j}\left(\tilde{\rho}\bar{u}_i^{\rho}\bar{u}_j^{\rho}\right) + \frac{\partial}{\partial x_j}\left(\tilde{\rho}\bar{u}_i^{\rho}\tilde{u}_j\right) + \frac{\partial}{\partial x_j}\left(\tilde{\rho}\tilde{u}_i\bar{u}_j^{\rho}\right) + \frac{\partial}{\partial x_j}\left(\tilde{\rho}\tilde{u}_i\tilde{u}_j\right) \\
&= -\frac{\partial \bar{p}}{\partial x_i} - \frac{\partial \tilde{p}}{\partial x_i} + \frac{\partial \bar{\tau}_{ij}}{\partial x_j} + \frac{\partial \tilde{\tau}_{ij}}{\partial x_j} - \frac{\partial}{\partial x_j}\left\langle \rho u_i'' u_j'' \right\rangle .
\end{aligned} \tag{B.4b}$$

Now dismissing the second and higher order terms in relation to perturbations and subtracting the time-averaged equations, yield

$$\frac{\partial \tilde{\rho}}{\partial t} + \tilde{u}_i\frac{\partial \bar{\rho}}{\partial x_i} + \tilde{\rho}\frac{\partial \bar{u}_i^{\rho}}{\partial x_i} + \bar{u}_i^{\rho}\frac{\partial \tilde{\rho}}{\partial x_i} + \bar{\rho}\frac{\partial \tilde{u}_i}{\partial x_i} = 0, \tag{B.5a}$$

$$\begin{aligned}
&\bar{\rho}\frac{\partial \tilde{u}_i}{\partial t} + \bar{\rho}\bar{u}_j^{\rho}\frac{\partial \tilde{u}_i}{\partial x_j} + \bar{\rho}\tilde{u}_j\frac{\partial \bar{u}_i^{\rho}}{\partial x_j} + \tilde{\rho}\bar{u}_j^{\rho}\frac{\partial \bar{u}_i^{\rho}}{\partial x_j} \\
&+\left(\bar{u}_i^{\rho}\frac{\partial \tilde{\rho}}{\partial t} + \bar{u}_i^{\rho}\tilde{u}_j\frac{\partial \bar{\rho}}{\partial x_j} + \bar{u}_i^{\rho}\tilde{\rho}\frac{\partial \bar{u}_j^{\rho}}{\partial x_j} + \bar{u}_i^{\rho}\bar{u}_j^{\rho}\frac{\partial \tilde{\rho}}{\partial x_j} + \bar{u}_i^{\rho}\bar{\rho}\frac{\partial \tilde{u}_j}{\partial x_j}\right) \\
&+\left(\tilde{u}_i\frac{\partial \bar{\rho}}{\partial t} + \tilde{\rho}\frac{\partial \bar{u}_i^{\rho}}{\partial t} + \tilde{u}_i\bar{\rho}\frac{\partial \bar{u}_j^{\rho}}{\partial x_j} + \tilde{u}_i\bar{u}_j^{\rho}\frac{\partial \bar{\rho}}{\partial x_j}\right) \\
&= -\frac{\partial \tilde{p}}{\partial x_i} + \frac{\partial \tilde{\tau}_{ij}}{\partial x_j} - \frac{\partial}{\partial x_j}\left(\left\langle \rho u_i'' u_j'' \right\rangle - \overline{\rho u_i'' u_j''}\right).
\end{aligned} \tag{B.5b}$$

Multiplying Equation B.5a by $\bar{u}_i^{\rho}$ gives

$$\bar{u}_i^{\rho}\frac{\partial \tilde{\rho}}{\partial t} + \bar{u}_i^{\rho}\tilde{u}_j\frac{\partial \bar{\rho}}{\partial x_j} + \bar{u}_i^{\rho}\tilde{\rho}\frac{\partial \bar{u}_j^{\rho}}{\partial x_j} + \bar{u}_i^{\rho}\bar{u}_j^{\rho}\frac{\partial \tilde{\rho}}{\partial x_j} + \bar{u}_i^{\rho}\bar{\rho}\frac{\partial \tilde{u}_j}{\partial x_j} = 0. \tag{B.6}$$

Moreover, multiplying Equation B.3a by $\tilde{u}_i$ gives

$$\tilde{u}_i\bar{\rho}\frac{\partial \bar{u}_j^{\rho}}{\partial x_j} + \tilde{u}_i\bar{u}_j^{\rho}\frac{\partial \bar{\rho}}{\partial x_j} = 0. \tag{B.7}$$

Also, the time derivatives of the time-mean parts equal zero. Eventually, the linearised Navier-Stokes equations including the turbulence information are given as

$$\frac{\partial \tilde{\rho}}{\partial t} + \tilde{u}_i \frac{\partial \bar{\rho}}{\partial x_i} + \tilde{\rho} \frac{\partial \bar{u}_i^{\rho}}{\partial x_i} + \bar{u}_i^{\rho} \frac{\partial \tilde{\rho}}{\partial x_i} + \bar{\rho} \frac{\partial \tilde{u}_i}{\partial x_i} = 0, \tag{B.8a}$$

$$\begin{aligned} &\bar{\rho} \frac{\partial \tilde{u}_i}{\partial t} + \bar{\rho} \bar{u}_j^{\rho} \frac{\partial \tilde{u}_i}{\partial x_j} + \bar{\rho} \tilde{u}_j \frac{\partial \bar{u}_i^{\rho}}{\partial x_j} + \tilde{\rho} \bar{u}_j^{\rho} \frac{\partial \bar{u}_i^{\rho}}{\partial x_j} \\ &= -\frac{\partial \tilde{p}}{\partial x_i} + \frac{\partial \tilde{\tau}_{ij}}{\partial x_j} - \frac{\partial}{\partial x_j} \left(\left\langle \rho u_i'' u_j'' \right\rangle - \overline{\rho u_i'' u_j''} \right). \end{aligned} \tag{B.8b}$$

Bibliography

[1] Farassat, F. and Casper, J. H., "Towards an airframe noise prediction methodology: survey of current approaches," *AIAA Paper 2006-0210*, 2006.

[2] Karbon, K., Kumarasamy, S., and Singh, R., "Applications and issues in automotive computational aeroacoustics," *Tenth annual conference of the CFD Society of Canada (CFD 2002)*, 2002, pp. 394–396.

[3] Lighthill, M. J., "On sound generated aerodynamically. I. General theory," *Proceedings of the Royal Society of London. Series A. Mathematical and Physical Sciences*, Vol. 211, No. 1107, 1952, pp. 564–587.

[4] Tam, C. K. W., "Computational aeroacoustics: an overview of computational challenges and applications," *International Journal of Computational Fluid Dynamics*, Vol. 18, No. 6, 2004, pp. 547–567.

[5] Ewert, R. and Schröder, W., "Acoustic perturbation equations based on flow decomposition via source filtering," *Journal of Computational Physics*, Vol. 188, No. 2, 2003, pp. 365–398.

[6] Zhang, X. and Chen, X. X., "Linearised divergence equations for sound propagation," *AIAA Paper 2011-2930*, 2011.

[7] Zhang, X., Chen, X. X., Gill, J., and Huang, X., "Gradient Term Filtering for Stable Sound Propagation with Linearized Euler Equations," *AIAA Paper 2014-3306*, 2014.

[8] Agarwal, A., Morris, P. J., and Mani, R., "Calculation of sound propagation in nonuniform flows: suppression of instability waves," *AIAA Journal*, Vol. 42, No. 1, 2004, pp. 80–88.

[9] Özyörük, Y., Alpman, E., Ahuja, V., and Long, L. N., "Frequency-domain prediction of turbofan noise radiation," *Journal of Sound and Vibration*, Vol. 270, No. 4, 2004, pp. 933–950.

[10] Özyörük, Y. and Tester, B. J., "Assessment of a frequency-domain linearised Euler solver for turbofan aft radiation predictions and comparison with measurements," *Procedia Engineering*, Vol. 6, 2010, pp. 153–162.

[11] Özyörük, Y. and Tester, B. J., "Application of frequency-domain linearized Euler solutions to the prediction of aft fan tones and comparison with experimental measurements on model scale turbofan exhaust nozzles," *Journal of Sound and Vibration*, Vol. 330, 2011, pp. 3846–3858.

[12] Weng, C., Boij, S., and Hanifi, A., "The attenuation of sound by turbulence in internal flows," *The Journal of the Acoustical Society of America*, Vol. 133, 2013, pp. 3764–3776.

[13] Colonius, T. and Lele, S. K., "Computational aeroacoustics: progress on nonlinear problems of sound generation," *Progress in Aerospace Sciences*, Vol. 40, No. 6, 2004, pp. 345–416.

[14] Mitchell, B. E., Lele, S. K., and Moin, P., "Direct computation of the sound from a compressible co-rotating vortex pair," *Journal of Fluid Mechanics*, Vol. 285, No. 1, 1995, pp. 181–202.

[15] Colonius, T., Lele, S. K., and Moin, P., "Sound generation in a mixing layer," *Journal of Fluid Mechanics*, Vol. 330, No. 1, 1997, pp. 375–409.

[16] Freund, J. B., Lele, S. K., and Moin, P., "Direct simulation of a Mach 1.92 jet and its sound field," *AIAA Paper 1998-2291*, 1998.

[17] Freund, J. B., Lele, S. K., and Moin, P., "Numerical simulation of a Mach 1.92 turbulent jet and its sound field," *AIAA Journal*, Vol. 38, No. 11, 2000, pp. 2023–2031.

[18] Ran, H. and Colonius, T., "Numerical Simulation of the Sound Radiated from a Turbulent Vortex Ring," *International Journal of Aeroacoustics*, 2009, pp. 317–336.

[19] Lui, C. and Lele, S. K., "A numerical study of broadband shock noise," *AIAA Paper 2002-2530*, 2002.

[20] Rowley, C. W., Colonius, T., and Basu, A. J., "On self-sustained oscillations in two-dimensional compressible flow over rectangular cavities," *Journal of Fluid Mechanics*, Vol. 455, No. 2, 2002, pp. 315–346.

[21] Lui, C. and Lele, S. K., "Sound generation mechanism of shock-associated noise," *AIAA Paper 2003-3315*, 2003.

[22] Freund, J. B., Lele, S. K., and Moin, P., "Matching of near/far-field equations sets for direct computation of aerodynamic sound," *AIAA Paper 1993-4326*, 1993.

[23] Phillips, O. M., "On the generation of sound by supersonic turbulent shear layers," *Journal of Fluid Mechanics*, Vol. 9, No. 1, 1960, pp. 1–28.

[24] Powell, A., "Theory of vortex sound," *The Journal of the Acoustical Society of America*, Vol. 36, 1964, pp. 177–195.

[25] Doak, P. E., "Analysis of internally generated sound in continuous materials: 2. A critical review of the conceptual adequacy and physical scope of existing theories of aerodynamic noise, with special reference to supersonic jet noise," *Journal of Sound and Vibration*, Vol. 25, No. 2, 1972, pp. 263–335.

[26] Doak, P. E., "Analysis of internally generated sound in continuous materials: 3. The momentum potential field description of fluctuating fluid motion as a basis for a unified theory of internally generated sound," *Journal of Sound and Vibration*, Vol. 26, No. 1, 1973, pp. 91–120.

[27] Lilley, G. M., "On the noise from jets," *AGARD CP-131*, 1974, pp. 13.1–13.12.

[28] Goldstein, M. E., "The low frequency sound from multipole sources in axisymmetric shear flows. Part 2," *Journal of Fluid Mechanics*, Vol. 75, No. 01, 1976, pp. 17–28.

[29] Pridmore-Brown, D. C., "Sound propagation in a fluid flowing through an attenuating duct," *Journal of Fluid Mechanics*, Vol. 4, No. pt 4, 1958, pp. 393–406.

[30] Goldstein, M. E., "Aeroacoustics of turbulent shear flows," *Annual Review of Fluid Mechanics*, Vol. 16, No. 1, 1984, pp. 263–285.

[31] Goldstein, M. E., "An exact form of Lilley's equation with a velocity quadrupole/temperature dipole source term," *Journal of Fluid Mechanics*, Vol. 443, 2001, pp. 231–236.

[32] Curle, N., "The influence of solid boundaries upon aerodynamic sound," *Proceedings of the Royal Society of London. Series A. Mathematical and Physical Sciences*, Vol. 231, No. 1187, 1955, pp. 505–514.

[33] Williams, J. E. F. and Hawkings, D. L., "Sound generation by turbulence and surfaces in arbitrary motion," *Philosophical Transactions of the Royal Society of London. Series A, Mathematical and Physical Sciences*, Vol. 264, No. 1151, 1969, pp. 321–342.

[34] Pilon, A. R. and Lyrintzis, A. S., "Development of an improved Kirchhoff method for jet aeroacoustics," *AIAA Journal*, Vol. 36, No. 5, 1998, pp. 783–790.

[35] Singer, B. A., Lockard, D. P., and Lilley, G. M., "Hybrid acoustic predictions," *Computers & Mathematics with Applications*, Vol. 46, No. 4, 2003, pp. 647–669.

[36] Brentner, K. S. and Farassat, F., "Modeling aerodynamically generated sound of helicopter rotors," *Progress in Aerospace Sciences*, Vol. 39, No. 2-3, 2003, pp. 83–120.

[37] Gloerfelt, X., Bailly, C., and Juvé, D., "Direct computation of the noise radiated by a subsonic cavity flow and application of integral methods," *Journal of Sound and Vibration*, Vol. 266, No. 1, 2003, pp. 119–146.

[38] Brentner, K. S. and Farassat, F., "An analytical comparison of the acoustic analogy and Kirchhoff formulation for moving surfaces," *AIAA Journal*, Vol. 36, No. 8, 1998, pp. 1379–1386.

[39] Lyrintzis, A. S., "Surface integral methods in computational aeroacoustics -From the (CFD) near-field to the (Acoustic) far-field," *International Journal of aeroacoustics*, Vol. 2, No. 2, 2003, pp. 95–128.

[40] Uzun, A., Lyrintzis, A. S., and Blaisdell, G. A., "Coupling of integral acoustics methods with LES for jet noise prediction," *International Journal of aeroacoustics*, Vol. 3, No. 4, 2004, pp. 297–346.

[41] Colonius, T. and Freund, J. B., "Application of Lighthill's equation to a Mach 1. 92 turbulent jet," *AIAA Journal*, Vol. 38, No. 2, 2000, pp. 368–370.

[42] Zhang, X., Chen, X. X., Morfey, C. L., and Nelson, P. A., "Computation of spinning modal radiation from an unflanged duct," *AIAA Journal*, Vol. 42, No. 9, 2004, pp. 1795–1801.

[43] Leonard, A., "Vortex methods for flow simulation," *Journal of Computational Physics*, Vol. 37, No. 3, 1980, pp. 289–335.

[44] Cottet, G. H. and Koumoutsakos, P. D., *Vortex methods: theory and practice*, Cambridge University Press, 2000.

[45] Ould-Salihi, M. L., Cottet, G. H., and El Hamraoui, M., "Blending finite-difference and vortex methods for incompressible flow computations," *SIAM Journal on Scientific Computing*, Vol. 22, No. 5, 2001, pp. 1655–1674.

[46] Knio, O. M., Collorec, L., and Juvé, D., "Numerical study of sound emission by 2D regular and chaotic vortex configurations," *Journal of Computational Physics*, Vol. 116, No. 2, 1995, pp. 226–246.

[47] Guo, Y. P., "A model for slat noise generation," *AIAA Paper 1997-1647*, 1997.

[48] Guo, Y. P., "Prediction of flap side edge noise," *AIAA Paper 1999-1804*, 1999.

[49] Guo, Y. P., "Application of the Ffowcs Williams/Hawkings equation to two-dimensional problems," *Journal of Fluid Mechanics*, Vol. 403, 2000, pp. 201–221.

[50] Brown, C. E. and Michael, W. H., "Effect of leading edge separation on the lift of a delta wing," *J. Aero. Sci*, Vol. 21, No. 10, 1954, pp. 690–694.

[51] Howe, M. S., "Emendation of the Brown & Michael equation, with application to sound generation by vortex motion near a half-plane," *Journal of Fluid Mechanics*, Vol. 329, 1996, pp. 89–102.

[52] Howe, M. S., *Theory of vortex sound*, Vol. 33, Cambridge University Press, 2003.

[53] Howe, M. S., "Trailing edge noise at low Mach numbers," *Journal of Sound and Vibration*, Vol. 225, No. 2, 1999, pp. 211–238.

[54] Narayanan, S., Noack, B. R., and Meiburg, E., "Reduced-order dynamical modeling of sound generation from a jet," *AIAA Paper 2002-0073*, 2002.

[55] Leonard, A., "Computing three-dimensional incompressible flows with vortex elements," *Annual Review of Fluid Mechanics*, Vol. 17, No. 1, 1985, pp. 523–559.

[56] Eldredge, J. D., Colonius, T., and Leonard, A., "A vortex particle method for two-dimensional compressible flow," *Journal of Computational Physics*, Vol. 179, No. 2, 2002, pp. 371–399.

[57] Herbert, T., "Parabolized stability equations," *Annual Review of Fluid Mechanics*, Vol. 29, No. 1, 1997, pp. 245–283.

[58] Herbert, T. and Bertolotti, F., "Stability analysis of non-parallel boundary layers," *Bull. Am. Phys. Soc.*, Vol. 32, 1987.

[59] Piot, E., Casalis, G., Muller, F., and Bailly, C., "Investigation of the PSE approach for subsonic and supersonic hot jets. Detailed comparisons with LES and Linearized Euler Equations results," *International Journal of aeroacoustics*, Vol. 5, No. 4, 2006, pp. 361–393.

[60] Cheung, L. C. and Lele, S. K., "Acoustic radiation from subsonic and supersonic mixing layers with nonlinear PSE," *AIAA Paper 2004-363*, 2004.

[61] Hardin, J. C., "Introduction to Computational Aeroacoustics in Aerodynamics," *AIAA Professional Studies Series Short Course, Reno, NV*, 1992.

[62] Hardin, J. C. and Pope, D. S., "An acoustic/viscous splitting technique for computational aeroacoustics," *Theoretical and Computational Fluid Dynamics*, Vol. 6, No. 5, 1994, pp. 323–340.

[63] Shen, W. and Srensen, J., "Aeroacoustic modelling of low-speed flows," *Theoretical and Computational Fluid Dynamics*, Vol. 13, No. 4, 1999, pp. 271–289.

[64] Shen, W. Z. and Sorensen, J. N., "Comment on the aeroacoustic formulation of Hardin and Pope," *AIAA Journal*, Vol. 37, No. 1, 1999, pp. 141–143.

[65] Hardin, J. C. and Pope, D. S., "Sound generation by flow over a two-dimensional cavity," *AIAA Journal*, Vol. 33, No. 3, 1995, pp. 407–412.

[66] Ribner, H. S., *Aerodynamic Sound from Fluid Dilatations: A Theory of the Sound from Jets and Other Flows*, University of Toronto, Institute of Aerophysics, 1962.

[67] Crow, S. C., "Aerodynamic sound emission as a singular perturbation problem (Aerodynamic sound emission from compact eddy region by singular perturbation approach, discussing Lighthill and Ribner theories)," *Studies in applied mathematics*, Vol. 49, 1970, pp. 21–44.

[68] Ribner, H. S., "Comment on Aerodynamic Sound as a Singular Perturbation Problem [SC Crow, in Aerodynamic Noise, Arnold Goldburg, Ed. (American Institute of Aeronautics and Astronautics, New York, 1970), AIAA Reprint Series Vol. XI]," *The Journal of the Acoustical Society of America*, Vol. 49, 1971, pp. 1108–1108.

[69] Crighton, D. G., "Basic principles of aerodynamic noise generation," *Progress in Aerospace Sciences*, Vol. 16, No. 1, 1975, pp. 31–96.

[70] Lockard, D. P. and Morris, P. J., "Radiated noise from airfoils in realistic mean flows," *AIAA Journal*, Vol. 36, No. 6, 1998, pp. 907–914.

[71] Nallasamy, M., Hixon, R., and Sawyer, S., "Computed linear/nonlinear acoustic response of a cascade for single/multi frequency excitation," *AIAA Paper 2004-2998*, 2004.

[72] Huerre, P. and Monkewitz, P., "Absolute and convective instabilities in free shear layers," *Journal of Fluid Mechanics*, Vol. 159, 1985, pp. 151–68.

[73] Goldstein, M. E., *Aeroacoustics*, McGraw-Hill International Book Co., 1976.

[74] Möhring, W., Müller, E. A., and Obermeier, F., "Problems in flow acoustics," *Reviews of modern physics*, Vol. 55, No. 3, 1983, pp. 707–724.

[75] Dowling, A. P., Williams, J. E. F., and Goldstein, M. E., "Sound production in a moving stream," *Philosophical Transactions of the Royal Society of London. Series A, Mathematical and Physical Sciences*, Vol. 288, No. 1353, 1978, pp. 321–349.

[76] Ehlers, F. E. and Weatherill, W. H., *A harmonic analysis method for unsteady transonic flow and its application to the flutter of airfoils*, Vol. 3537, National Aeronautical and Space Administration, Scientific and Technical Information Branch, 1982.

[77] Verdon, J. M. and Caspar, J. R., "A linearized unsteady aerodynamic analysis for transonic cascades," *Journal of Fluid Mechanics*, Vol. 149, No. 1, 1984, pp. 403–429.

[78] Montgomery, M. D. and Verdon, J. M., *A three-dimensional linearized unsteady Euler analysis for turbomachinery blade rows*, Vol. 4770, National Aeronautics and Space Administration, Office of Management, Scientific and Technical Information Program, 1997.

[79] Verdon, J. M., "Linearized unsteady aerodynamic analysis of the acoustic response to wake/blade-row interaction," Tech. Rep. NASA/CR 2001-210713, 2001.

[80] Envia, E., "Application of a Linearized Euler Analysis to Fan Noise Prediction," *Fan-Gust Workshop*, Institute of Sound and Vibration Research, University of Southampton, U.K., 2002.

[81] Leneveu, R., Schiltz, B., Laldjee, S., and Caro, S., "Performance of a DGM scheme for LEE and applications to aircraft engine exhaust noise," *AIAA Paper 2008-2884*, 2008.

[82] Bailly, C. and Juvé, D., "Numerical solution of acoustic propagation problems using linearized Euler equations," *AIAA Journal*, Vol. 38, No. 1, 2000, pp. 22–29.

[83] Bogey, C., Bailly, C., and Juvé, D., "Computation of flow noise using source terms in linearized Euler's equations," *AIAA Journal*, Vol. 40, No. 2, 2002, pp. 235–243.

[84] Zhang, X., Chen, X., Morfey, C. L., and Tester, B. J., "Computation of fan noise radiation through a realistic engine exhaust geometry with flow," *AIAA Paper 2003-3267*, 2003.

[85] Tester, B. J., Gabard, G., and Özyörük, Y., "Influence of mean flow gradients on fan exhaust noise predictions," *AIAA Paper 2008-2825*, 2008.

[86] Zhang, X. and Chen, X. X., "Time-domain limitation of multimode propagation in an aeroengine duct," *Procedia Engineering*, Vol. 6, 2010, pp. 173–182.

[87] Arfken, G. B. and Weber, H. J., *Mathematical Methods for Physicists*, Academic press, 2005.

[88] Ribner, H. S. and Tucker, M., "Spectrum of turbulence in a contracting stream," Tech. Rep. NACA-TR-1113, 1953.

[89] Batchelor, G. K. and Proudman, I., "The effect of rapid distortion of a fluid in turbulent motion," *The Quarterly Journal of Mechanics and Applied Mathematics*, Vol. 7, No. 1, 1954, pp. 83–103.

[90] Hunt, J. C. R., "A theory of turbulent flow round two-dimensional bluff bodies," *Journal of Fluid Mechanics*, Vol. 61, No. 04, 1973, pp. 625–706.

[91] Goldstein, M. E., "Unsteady vortical and entropic distortions of potential flows round arbitrary obstacles," *Journal of Fluid Mechanics*, Vol. 89, No. Part 3, 1978, pp. 433–468.

[92] Patrick, S. M., Davis, C. M., and Atassi, H. M., "Acoustic radiation from a lifting airfoil in nonuniform subsonic flows," *ASME-PUBLICATIONS-FED*, Vol. 147, 1993, pp. 41–41.

[93] Atassi, H. M., Subramaniam, S., and Scott, J. R., "Acoustic radiation from lifting airfoils in compressible subsonic flow," *AIAA Paper 1990-3911*, 1990.

[94] Atassi, H. M., Fang, J., and Patrick, S., "Direct calculation of sound radiated from bodies in nonuniform flows," *Journal of fluids engineering*, Vol. 115, No. 4, 1993, pp. 573–579.

[95] Atassi, H. M., Dusey, M., and Davis, C. M., "Acoustic radiation from a thin airfoil in nonuniform subsonic flows," *AIAA Journal*, Vol. 31, No. 1, 1993, pp. 12–19.

[96] Scott, R., Atassi, H., and Susan-Resiga, F., "A new domain decomposition approach for the gust response problem," *AIAA Paper 2003-0883*, 2003.

[97] Pierce, A. D., "Wave equation for sound in fluids with unsteady inhomogeneous flow," *The Journal of the Acoustical Society of America*, Vol. 87, 1990, pp. 2292.

[98] Kierkegaard, A., Boij, S., and Efraimsson, G., "Simulations of the scattering of sound waves at a sudden area expansion," *Journal of Sound and Vibration*, Vol. 331, No. 5, 2012, pp. 1068–1083.

[99] Kierkegaard, A., Allam, S., Efraimsson, G., and Åbom, M., "Simulations of whistling and the whistling potentiality of an in-duct orifice with linear aeroacoustics," *Journal of Sound and Vibration*, Vol. 331, No. 5, 2012, pp. 1084–1096.

[100] Holmberg, A., *Aeroacoustic Characterization using Multiport Methods*, Ph.D. thesis, KTH, 2012.

[101] Holmberg, A., Kierkegaard, A., and Weng, C., "A Linearized Navier-Stokes Method Including Turbulence Damping," *AIAA Paper 2013-2167*, 2013.

[102] Trefethen, L., Trefethen, A., Reddy, S., Driscoll, T., et al., "Hydrodynamic stability without eigenvalues," *Science*, Vol. 261, No. 5121, 1993, pp. 578–584.

[103] Kim, J., "Control of turbulent boundary layers," *Physics of Fluids (1994-present)*, Vol. 15, No. 5, 2003, pp. 1093–1105.

[104] Duque-Daza, C. A., Baig, M., Lockerby, D. A., Chernyshenko, S., and Davies, C., "Modelling turbulent skin-friction control using linearized Navier–Stokes equations," *Journal of Fluid Mechanics*, Vol. 702, 2012, pp. 403–414.

[105] Farrell, B. F. and Ioannou, P. J., "Stochastic forcing of the linearized Navier–Stokes equations," *Physics of Fluids A: Fluid Dynamics (1989-1993)*, Vol. 5, No. 11, 1993, pp. 2600–2609.

[106] Lee, K. H., Cortelezzi, L., Kim, J., and Speyer, J., "Application of reduced-order controller to turbulent flows for drag reduction," *Physics of Fluids (1994-present)*, Vol. 13, No. 5, 2001, pp. 1321–1330.

[107] Viotti, C., Quadrio, M., and Luchini, P., "Streamwise oscillation of spanwise velocity at the wall of a channel for turbulent drag reduction," *Physics of Fluids*, Vol. 21, No. 11, 2009.

[108] Kierkegaard, A., Boij, S., and Efraimsson, G., "A frequency domain linearized Navier-Stokes equations approach to acoustic propagation in flow ducts with sharp edges," *The Journal of the Acoustical Society of America*, Vol. 127, No. 2, 2010, pp. 710–719.

[109] Kierkegaard, A., *Frequency Domain Linearized Navier-Stokes Equations Methods for Low Mach Number Internal Aeroacoustics*, Ph.D. thesis, KTH, 2011.

[110] Testud, P., Aurégan, Y., Moussou, P., and Hirschberg, A., "The whistling potentiality of an orifice in a confined flow using an energetic criterion," *Journal of Sound and Vibration*, Vol. 325, No. 4, 2009, pp. 769–780.

[111] Na, W., Boij, S., and Efraimsson, G., "Simulations of Acoustic Wave Propagation in an Impedance Tube Using a Frequency-Domain Linearized Navier-Stokes Methodology," *AIAA Paper 2014-2960*, 2014.

[112] Sharma, A., Chen, H.-n., and Shieh, C. M., "Linearized Navier-Stokes Analysis for Rotor-Stator Interaction Tone Noise Prediction," *AIAA Paper 2010-3744*, 2010.

[113] Wukie, N. A., Orkwis, P. D., Wojno, J., and Goerig, T., "Evaluation of a time-linearized Navier-Stokes method for booster tone noise analyses," *AIAA Paper 2014-2892*, 2014.

[114] Reynolds, W. C. and Hussain, A. K. M. F., "The mechanics of an organized wave in turbulent shear flow. Part 3. Theoretical models and comparisons with experiments," *Journal of Fluid Mechanics*, Vol. 54, No. 02, 1972, pp. 263–288.

[115] Bertolotti, F., Herbert, T., and Spalart, P., "Linear and nonlinear stability of the Blasius boundary layer," *Journal of Fluid Mechanics*, Vol. 242, 1992, pp. 441–474.

[116] Zuccher, S., *Receptivity and control of flow instabilities in a boundary layer*, Ph.D. thesis, Politecnico di Milano, 2001.

[117] Johnson, C. and HOFFMAN, J., *Computational Turbulent Incompressible Flow*, Springer-Verlag, New York, 2007.

[118] Schmid, P. J., "Nonmodal stability theory," *Annu. Rev. Fluid Mech.*, Vol. 39, 2007, pp. 129–162.

[119] Sharp, D. H., "An overview of Rayleigh-Taylor instability," *Physica D: Nonlinear Phenomena*, Vol. 12, No. 1, 1984, pp. 3–18.

[120] Brouillette, M., "The richtmyer-meshkov instability," *Annual Review of Fluid Mechanics*, Vol. 34, No. 1, 2002, pp. 445–468.

[121] Floryan, J., "On the Görtler instability of boundary layers," *Progress in Aerospace Sciences*, Vol. 28, No. 3, 1991, pp. 235–271.

[122] Naiman, H., *Analysis and design of quiet hypersonic wind tunnels*, Ph.D. thesis, Rutgers University-Graduate School-New Brunswick, 2010.

[123] Manera, J., Schiltz, B., Leneveu, R., Caro, S., Jacqmot, J., and Rienstra, S., "Kelvin-Helmholtz instabilities occurring at a nacelle exhaust," *AIAA Paper 2008-2883*, 2008.

[124] Alterman, Z., "Effect of surface tension on the Kelvin-Helmholtz instability of two rotating fluids," *Proceedings of the National Academy of Sciences of the United States of America*, Vol. 47, No. 2, 1961, pp. 224–227.

[125] Kirchhoff, G., "Ueber den Einfluss der Wrmeleitung in einem Gase auf die Schallbewegung," *Annalen der Physik*, Vol. 210, No. 6, 1868, pp. 177–193.

[126] Zwikker, C. and Kosten, C. W., *Sound absorbing materials*, Elsevier, 1949.

[127] Tijdeman, H., "On the propagation of sound waves in cylindrical tubes," *Journal of Sound and Vibration*, Vol. 39, No. 1, 1975, pp. 1–33.

[128] Peat, K. S., "A first aproximation to the effects of mean flow on sound propagation through cylindrical capillary tubes," *Journal of Sound and Vibration*, Vol. 175, No. 4, 1994, pp. 475–489.

[129] Ih, J. G., Park, C. M., and Kim, H. J., "A model for sound propagation in capillary ducts with mean flow," *Journal of Sound and Vibration*, Vol. 190, No. 2, 1996, pp. 163–175.

[130] Astley, R. J. and Cummings, A., "Wave propagation in catalytic converters: Formulation of the problem and finite element to solution scheme," *Journal of Sound and Vibration*, Vol. 188, No. 5, 1995, pp. 635–657.

[131] Willatzen, M., "Phase shift and attenuation characteristics of acoustic waves in a flowing gas confined by cylindrical walls," *Journal of Sound and Vibration*, Vol. 261, No. 5, 2003, pp. 791–804.

[132] Jeong, K.-W. and Ih, J.-G., "A numerical study on the propagation of sound through capillary tubes with mean flow," *Journal of Sound and Vibration*, Vol. 198, No. 1, 1996, pp. 67–79.

[133] Peat, K. S., "Convected acoustic wave motion along a capillary duct with an axial temperature gradient," *Journal of Sound and Vibration*, Vol. 203, No. 5, 1997, pp. 855–866.

[134] Peat, K. S. and Kirby, R., "Acoustic wave motion along a narrow cylindrical duct in the presence of an axial mean flow and temperature gradient," *The Journal of the Acoustical Society of America*, Vol. 107, 2000, pp. 1859–1867.

[135] Dokumaci, E., "An approximate dispersion equation for sound waves in a narrow pipe with ambient gradients," *Journal of Sound and Vibration*, Vol. 240, No. 4, 2001, pp. 637–646.

[136] Howe, M. S., *Acoustics of fluid-structure interactions*, Cambridge University Press, 1998.

[137] Lighthill, M. J., *On the energy scattered from the interaction of turbulence with sound or shock waves*, Mathematical Proceedings of the Cambridge Philosophical Society, Cambridge University Press, 1953.

[138] Kraichnan, R. H., "The scattering of sound in a turbulent medium," *The Journal of the Acoustical Society of America*, Vol. 25, No. 6, 1953, pp. 1096–1104.

[139] Cummings, A. and Chang, I.-J., "The transmission of intense transient and multiple frequency sound waves through orifice plates with mean fluid flow," *Revue de physique appliquée*, Vol. 21, No. 2, 1986, pp. 151–161.

[140] Noir, D. T. and George, A. R., "Absorption of sound by homogeneous turbulence," *Journal of Fluid Mechanics*, Vol. 86, No. 3, 1978, pp. 593–608.

[141] Howe, M. S., "On the absorption of sound by turbulence and other hydrodynamic flows," *IMA journal of applied mathematics*, Vol. 32, No. 1-3, 1984, pp. 187–209.

[142] Howe, M. S., "The dissipation of sound at an edge," *Journal of Sound and Vibration*, Vol. 70, No. 3, 1980, pp. 407–411.

[143] Howe, M. S., "The damping of sound by wall turbulent shear layers," *The Journal of the Acoustical Society of America*, Vol. 98, 1995, pp. 1723–1730.

[144] Bechert, D. W., "Sound absorption caused by vorticity shedding, demonstrated with a jet flow," *Journal of Sound and Vibration*, Vol. 70, No. 3, 1980, pp. 389–405.

[145] Leung, R. C. K., So, R. M. C., Wang, M. H., and Li, X. M., "In-duct orifice and its effect on sound absorption," *Journal of Sound and Vibration*, Vol. 299, No. 4, 2007, pp. 990–1004.

[146] Ashley, H. and Landahl, M., *Aerodynamics of wings and bodies*, Courier Dover Publications, 2012.

[147] Mikhail, M. N. and El-Tantawy, M. R., "The acoustic boundary layers: a detailed analysis," *Journal of computational and applied mathematics*, Vol. 51, No. 1, 1994, pp. 15–36.

[148] Cummings, A., "Transient and multiple frequency sound transmission through perforated plates at high amplitude," *The Journal of the Acoustical Society of America*, Vol. 79, 1986, pp. 942–951.

[149] Dokumaci, E., "On attenuation of plane sound waves in turbulent mean flow," *Journal of Sound and Vibration*, Vol. 320, No. 4, 2009, pp. 1131–1136.

[150] Knutsson, M. and Åbom, M., "Sound propagation in narrow tubes including effects of viscothermal and turbulent damping with application to charge air coolers," *Journal of Sound and Vibration*, Vol. 320, No. 1, 2009, pp. 289–321.

[151] Knutsson, M. and Åbom, M., "The effect of turbulence damping on acoustic wave propagation in tubes," *Journal of Sound and Vibration*, Vol. 329, No. 22, 2010, pp. 4719–4739.

[152] Scotti, A. and Piomelli, U., "Numerical simulation of pulsating turbulent channel flow," *Physics of Fluids*, Vol. 13, 2001, pp. 1367–1384.

[153] Comte, P., Haberkorn, M., Bouchet, G., Pagneux, V., and Aurégan, Y., *Large-Eddy Simulation of acoustic propagation in a turbulent channel flow*, Springer, 2006, pp. 521–528.

[154] Ronneberger, D. and Ahrens, C. D., "Wall shear stress caused by small amplitude perturbations of turbulent boundary-layer flow: an experimental investigation," *Journal of Fluid Mechanics*, Vol. 83, No. 03, 1977, pp. 433–464.

[155] Ahrens, C. and Ronneberger, D., "Acoustic attenuation in rigid tubes under turbulent flow conditions for various degrees of wall roughness (Acoustic attenuation calculation for turbulent flow in rigid tubes, determining critical flow velocity dependence on wall roughness and sound wave frequency)," *Acustica*, Vol. 25, 1971, pp. 150–157.

[156] Peters, M. C. A. M., Hirschberg, A., Reijnen, A., and Wijnands, A. P. J., "Damping and reflection coefficient measurements for an open pipe at low Mach and low Helmholtz numbers," *Journal of Fluid Mechanics*, Vol. 256, 1993, pp. 499–499.

[157] Allam, S. and Åbom, M., "Investigation of damping and radiation using full plane wave decomposition in ducts," *Journal of Sound and Vibration*, Vol. 292, No. 3, 2006, pp. 519–534.

[158] Munt, R. M., "Acoustic transmission properties of a jet pipe with subsonic jet flow: I. The cold jet reflection coefficient," *Journal of Sound and Vibration*, Vol. 142, No. 3, 1990, pp. 413–436.

[159] Dokumaci, E., "A note on transmission of sound in a wide pipe with mean flow and viscothermal attenuation," *Journal of Sound and Vibration*, Vol. 208, No. 4, 1997, pp. 653–655.

[160] Ingard, U. and Singhal, V. K., "Sound attenuation in turbulent pipe flow," *The Journal of the Acoustical Society of America*, Vol. 55, No. 3, 1974, pp. 535–538.

[161] Polifke, W., Poncet, A., Paschereit, C. O., and Dbbeling, K., "Reconstruction of acoustic transfer matrices by instationary computational fluid dynamics," *Journal of Sound and Vibration*, Vol. 245, No. 3, 2001, pp. 483–510.

[162] Polifke, W., "Numerical techniques for identification of acoustic multi-ports," *Advances in Aeroacoustics and applications, VKI lecture series, Brussels*, 2004.

[163] Föller, S., Kaess, R., and Polifke, W., "Reconstruction of the acoustic transfer matrices from large-eddy-simulations of compressible turbulent flows," *AIAA Paper 2008-3046*, 2008.

[164] Föller, S. and Polifke, W., "Identification of aero-acoustic scattering matrices from large eddy simulation. Application to a sudden area expansion of a duct," *Journal of Sound and Vibration*, Vol. 331, No. 13, 2012, pp. 3096–3113.

[165] Zhang, X., "SotonCAA Code," 2011.

[166] Wilcox, D. C., *Turbulence modeling for CFD*, Vol. 3, DCW industries La Caada, CA, 2006.

[167] Rienstra, S. W. and Hirschberg, A., *An introduction to acoustics*, Eindhoven University of Technology, 2003.

[168] Bechara, W., Bailly, C., Lafon, P., and Candel, S. M., "Stochastic approach to noise modeling for free turbulent flows," *AIAA journal*, Vol. 32, No. 3, 1994, pp. 455–463.

[169] Siefert, M., Delfs, J., and Caruelle, B., "Refraction and scattering in high Mach number boundary layers," *AIAA Paper 2011-2847*, 2011.

[170] Sijtsma, P., Oerlemans, S., Tibbe, T., Berkefeld, T., and Spehr, C., "Spectral broadening by shear layers of open jet wind tunnels," *AIAA Paper 2014-3178*, 2014.

[171] Smits, A. J. and Dussauge, J.-P., *Turbulent shear layers in supersonic flow*, Springer Science & Business Media, 2006.

[172] Favre, A. J., "The equations of compressible turbulent gases," Tech. rep., DTIC Document, 1965.

[173] Ronneberger, D. and Binder, G., "Response of wall turbulence to imposed unsteadiness," *EUROMECH Colloquia*, Vol. 272, 1991, p. 50.

[174] Nayfeh, A. H., "Effect of the acoustic boundary layer on the wave propagation in ducts," *The Journal of the Acoustical Society of America*, Vol. 54, No. 6, 1973, pp. 1737–1742.

[175] Temkin, S. and Temkin, S., *Elements of acoustics*, Wiley New York, 1981.

[176] Xun, H., *Adaptive mesh refinement for computational aeroacoustics*, Ph.D. thesis, University of Southampton, 2006.

[177] Watson, W. R. and Myers, M. K., "Inflow-outflow boundary conditions for two-dimensional acoustic waves in channels with flow," *AIAA journal*, Vol. 29, No. 9, 1991, pp. 1383–1389.

[178] Tam, C. K. and Dong, Z., "Wall boundary conditions for high-order finite-difference schemes in computational aeroacoustics," *Theoretical and Computational Fluid Dynamics*, Vol. 6, No. 5-6, 1994, pp. 303–322.

[179] Ashcroft, G. and Zhang, X., "Optimized prefactored compact schemes," *Journal of Computational Physics*, Vol. 190, No. 2, 2003, pp. 459–477.

[180] Thompson, K. W., "Time dependent boundary conditions for hyperbolic systems," *Journal of computational physics*, Vol. 68, No. 1, 1987, pp. 1–24.

[181] Hixon, R., Shih, S.-H., and Mankbadi, R., "Evaluation of boundary conditions for the gust-cascade problem," *Journal of Propulsion and Power*, Vol. 16, No. 1, 2000, pp. 72–78.

[182] Tam, C. K. W. and Webb, J. C., "Dispersion-relation-preserving finite difference schemes for computational acoustics," *Journal of Computational Physics*, Vol. 107, No. 2, 1993, pp. 262–281.

[183] Colonius, T., Lele, S. K., and Moin, P., "Boundary conditions for direct computation of aerodynamic sound generation," *AIAA journal*, Vol. 31, No. 9, 1993, pp. 1574–1582.

[184] Berenger, J.-P., "A perfectly matched layer for the absorption of electromagnetic waves," *Journal of computational physics*, Vol. 114, No. 2, 1994, pp. 185–200.

[185] Krank, B. and Efraimsson, G., "Evaluating stretched grids and introducing black hole layers as alternative non-reflecting buffer zone," *19th AIAA/CEAS Aeroacoustics Conference; Berlin; Germany; 27 May 2013 through 29 May 2013*, 2013.

[186] Ta'asan, S. and Nark, D. M., "An absorbing buffer zone technique for acoustic wave propagation," *AIAA, Aerospace Sciences Meeting and Exhibit, 33 rd, Reno, NV*, 1995.

[187] Richards, S., Zhang, X., Chen, X., and Nelson, P., "The evaluation of non-reflecting boundary conditions for duct acoustic computation," *Journal of Sound and Vibration*, Vol. 270, No. 3, 2004, pp. 539–557.

[188] Hixon, R., "Prefactored small-stencil compact schemes," *Journal of Computational Physics*, Vol. 165, No. 2, 2000, pp. 522–541.

[189] Hu, F., Hussaini, M., and Manthey, J. L., "Low-dissipation and low-dispersion Runge-Kutta schemes for computational acoustics," *Journal of Computational Physics*, Vol. 124, No. 1, 1996, pp. 177–191.

[190] Hixon, R., "Prefactored compact filters for computational aeroacoustics," *AIAA, Aerospace Sciences Meeting and Exhibit, 37 th, Reno, NV*, 1999.

[191] Kennedy, C. A. and Carpenter, M. H., "Comparison of several numerical methods for simulation of compressible shear layers," Tech. Rep. NASA Techical Paper 3484, 1997.

[192] Richardson, L. F. and Gaunt, J. A., "The deferred approach to the limit. Part I. Single lattice. Part II. Interpenetrating lattices," *Philosophical Transactions of the Royal Society of London. Series A, containing papers of a mathematical or physical character*, 1927, pp. 299–361.

[193] Roache, P. J., "Perspective: a method for uniform reporting of grid refinement studies," *Journal of Fluids Engineering*, Vol. 116, No. 3, 1994, pp. 405–413.

[194] Roache, P. J., "Quantification of uncertainty in computational fluid dynamics," *Annual Review of Fluid Mechanics*, Vol. 29, No. 1, 1997, pp. 123–160.

[195] Celik, I. B., Ghia, U., Roache, P. J., et al., "Procedure for estimation and reporting of uncertainty due to discretization in {CFD} applications," *Journal of fluids {Engineering-Transactions} of the {ASME}*, Vol. 130, No. 7, 2008.

[196] Farassat, F., *Theory of noise generation from moving bodies with an application to helicopter rotors*, National Aeronautics and Space Administration, 1975.

[197] Hoepffner, J., "Spatial/temporal stability analysis of the mixing layer," 2014.

[198] Morris, P. J., "The spatial viscous instability of axisymmetric jets," *Journal of Fluid Mechanics*, Vol. 77, No. 03, 1976, pp. 511–529.

[199] Michalke, A., "Survey on jet instability theory," *Progress in Aerospace Sciences*, Vol. 21, 1984, pp. 159–199.

[200] Haber, L. C., *Investigation of Dynamics in Turbulent Swirling Flows Aided by Linear Stability Analysis*, Ph.D. thesis, Virginia Polytechnic Institute and State University, 2003.

[201] Munt, R. M., "The interaction of sound with a subsonic jet issuing from a semi-infinite cylindrical pipe," *Journal of Fluid Mechanics*, Vol. 83, No. 04, 1977, pp. 609–640.

[202] Gabard, G. and Astley, R. J., "Theoretical model for sound radiation from annular jet pipes: far-and near-field solutions," *Journal of Fluid Mechanics*, Vol. 549, No. 1, 2006, pp. 315–341.

[203] Özyörük, Y., Dizemen, E., Aktürk, A., and Kaya, S., "A frequency domain linearized Euler solver for turbomachinery noise propagation and radiation," *AIAA Paper 2007-3521*.

[204] Smagorinsky, J., "general circulation experiments with the primitive equations: i. the basic experiment*," *Monthly weather review*, Vol. 91, No. 3, 1963, pp. 99–164.

[205] Kleissl, J., *Field experimental study of the Smagorinsky model and application to large eddy simulation*, Ph.D. thesis, Johns Hopkins University, 2004.

[206] Lilly, D. K., "The representation of small scale turbulence in numerical simulation experiments," *IBM Scientific Computing Symposium on Environmental Sciences*, 1967, pp. 195–210.

[207] Laughlin, P. M., *A Contribution to the Jet Noise Installation Problem*, Ph.D. thesis, University of Southampton, 2010.

[208] Redonnet, S. and Druon, Y., "Computational Aeroacoustics of Aft Fan Noises Characterizing a Realistic Coaxial Engine," *AIAA journal*, Vol. 50, No. 5, 2012, pp. 1029–1046.

[209] Mazumdar, S., Kimber, M. L., and Jana, A., "Quantification of Numerical Error for a Laminar Round Jet Simulation," University Lecture, 2013.

[210] Prasad, A. and Williamson, C. H. K., "The instability of the shear layer separating from a bluff body," *Journal of Fluid Mechanics*, Vol. 333, 1997, pp. 375–402.

[211] Pierce, A. D., *Acoustics: an introduction to its physical principles and applications*, American Institute of Physics, 1989.

[212] Weng, C., *Theoretical and numerical studies of sound propagation in low-Mach-number duct flows*, Ph.D. thesis, KTH Royal Institute of Technology, 2015.

[213] Menter, F. R., "Zonal two equation k-turbulence models for aerodynamic flows," *AIAA paper*, Vol. 1993-2906, 1993.

[214] Howe, M. S., "The interaction of sound with low Mach number wall turbulence, with application to sound propagation in turbulent pipe flow," *Journal of Fluid Mechanics*, Vol. 94, No. 04, 1979, pp. 729–744.

[215] Sack, S., Åbom, M., Schram, C. F., and Kucukcoskun, K., "Generation and scattering of acoustic modes in ducts with flow," *20th AIAA/CEAS Aeroacoustics Conference*, 2014, p. 55.

[216] Rice, E. J., "Spinning mode sound propagation in ducts with acoustic treatment," *The Journal of the Acoustical Society of America*, Vol. 56, No. S1, 1974, pp. S49–S50.

[217] Hanson, D. B., "Shielding of Prof-Fan cabin noise by the fuselage boundary layer," *Journal of Sound and Vibration*, Vol. 92, No. 4, 1984, pp. 591–598.

[218] Hanson, D. B. and Magliozzi, B., "Propagation of propeller tone noise through a fuselage boundary layer," *Journal of Aircraft*, Vol. 22, No. 1, 1985, pp. 63–70.

[219] Dierke, J., Ewert, R., and Delfs, J., "The Effect of a Boundary Layer on Engine Noise propagating to the Fuselage at Flight Conditions," *AIAA Paper 2013-2006*, 2013.

[220] Stern, F., "Chapter 7: Boundary Layer Theory," University Lecture, 2010.

[221] Cimbala, J. M., "The Turbulent Flat Plate Boundary Layer," University Lecture, 2015.

[222] Khamis, D. and Brambley, E. J., "Viscous effects on the acoustics and stability of a shear layer over a non-rigid wall," *J. Fluid Mech. (Under consideration for publication)*, 2016.